DEPARTMENT OF MECHANICAL AND AEROSPACE ENGINEERING

MECHANICAL BEHAVIOUR OF HIGH STRENGTH STRUCTURAL STEEL UNDER HIGH LOADING RATES

A thesis submitted for the degree of

Doctor of Philosophy

by

Aderinkola Adelabu Alabi

September 2019

ABSTRACT

Despite offering significant strength-to-weight advantages, high-strength structural steels with high yield-to-tensile ratio >0.90, such as S690QL and S960QL, are used only in limited offshore applications. This is due to the lack of material characterisation in regard to their mechanical behaviour (tensile and fracture behaviour), with little data available on the loading rates other than those typically experienced offshore when compared to the dataset available on low strength structural steels with a yield-to-tensile ratio <0.85.

The concern is that high-strength structural steels with high yield-to-tensile ratio obtain their strength at the expense of ductility and strain hardening capacity; properties which provide a sense of extra safety in avoidance of failure should service loads exceed yield. Owing to the fact that, the mechanical behaviour and performance of low strength structural steel is well known and established in the design codes and international standards, where most of the design codes relate the design formulae to low strength structural steel with Y/T ratio below 0.85, and yield strength up to 500 MPa for offshore design requirements. So, design codes that utilise these properties to deliver safety when using low strength structural steel with a yield-to-tensile ratio <0.85, may not currently be applicable for modern high strength structural steels.

In this research, a programme of mechanical testing combining the tensile and fracture toughness properties of modern HSS (S690QL and S960QL) with high yield-to-tensile ratio under high loading rates applicable to offshore scenarios is proposed and investigated. This is supported by finite element analysis on the fracture toughness of S690QL in order to determine the crack driving force and the effect of loading rates on the crack mouth opening displacement which cannot be estimated experimentally using rate dependent material model developed for S690QL. Material model for S690QL is developed at a range of strain rates using a rate-dependent method available in ABAQUS code in order to allow for the prediction of the flow stress at elevated loading based on the quasi-static test data.

The loading rates considered are those anticipated in offshore in-service conditions, up to 100 s^{-1} strain rates and K-rates up to the order of magnitude of 10^6 MPa√m/s. Results from the experimental tensile tests show that the strengths of the structural steel grades under consideration are relatively unaffected by the effect of loading rate when compared to low strength structural steel (mild steel), and this is predicted to be material dependent which

decreases as the nominal yield strength increases. Also, like other ferritic steel, a shift to a higher ductile-to-brittle transition temperature was observed as the loading rate increases with S690QL and S960QL, associated with a reduction in the fracture toughness value on the lower transition region.

Finally, the structural implication of dynamic loading on the mechanical behaviour of HSS, combining the tensile properties and fracture toughness data generated for S690QL on the FAD-based fracture engineering critical assessment (ECA) is assessed using CrackWISE® software in line with BS7910 and the results are presented in this research. The results from the assessment shows that proximity to failure by plastic collapse and fracture on the upper shelf decreases when the loading rate is increased, whereas on the lower shelf, the proximity to failure by fracture is increased for S690QL assessed. From these results, confidence and requirements regarding structural performance can be developed and re-evaluated in relevant codes and standards for these steel materials with high yield-to-tensile ratio, and high strength structural steel can exploit its strength, but not rely on its ability to deform or locally yield under extreme loading for offshore and marine applications.

ACKNOWLEDGEMENTS

LIST OF CONTENTS

LIST OF FIGURES

LIST OF TABLES

LIST OF NOTATIONS

a	crack length (mm)
a_0	initial crack length (mm)
Δa	average stable crack extension (mm)
a_0/W	ratio of the initial crack length and specimen width
A_c	crack area
A	material constant
A_{cs}	cross-sectional area (mm^2)
B	specimen thickness (mm)
C	Johnson Cook strain rate sensitivity parameter
C_v	absorbed energy (J)
e	engineering strain
ε	true strain
E	Young's modulus of elasticity (MPa)
f	mathematical function of a_0/W
F	applied force (N)
G	energy release rate (N/mm)
k	gas constant, 1.38^{-23} JK^{-1}
K	stress intensity factor (MPa√m)
K_0	Weibull fitting parameter at the 63.2% cumulative failure probability
K_{Jc}	equivalent elastic-plastic stress intensity factor corresponding to J_c (MPa√m)
$K_{Jc(1T)}$	equivalent elastic-plastic stress intensity factor from 1T size specimen (MPa√m)
$K_{Jc(0.4)}$	equivalent elastic-plastic stress intensity factor from 0.4T size specimen (MPa√m)

$K_{Jc(med)}$	equivalent elastic-plastic stress intensity factor value at which the median K_{Jc} for 1T size specimens is 100 MPa√m
K_{mat}	equivalent elastic-plastic stress intensity factor corresponding to J_{m} (MPa√m)
K_r	failure by fracture on the Y-axis of failure assessment diagram
J	experimental equivalent of the crack tip J-integral (N/mm)
J_{el}	elastic component of J (N/mm)
J_{pl}	plastic component of J (N/mm)
J_{c}	critical J at onset of cleavage fracture (N/mm)
J_{m}	J at the first attainment of a maximum force (N/mm)
J_{IC} or $J_{0.2}$	initiation fracture toughness (N/mm)
L_g	gauge length, 50 mm
L_r	failure by plastic collapse on the X-axis of failure assessment diagram
n	strain-hardening exponent
N	strain-hardening exponent used by SINTAP
P_m	membrane stress in engineering critical assessment
P_b	bending stress in engineering critical assessment
Q_{tm}	thermal membrane stress in engineering critical assessment
Q_{tb}	thermal bending stress in engineering critical assessment
R-curve	resistance curve
R	yield stress ratio
T	test temperature (°C)
T_{27}	temperature corresponding to 27 J
T_0	reference transition temperature based on Master Curve at $K_{Jc(med)}$ equals to 100 MPa√m (°C)
$T_{0,m}$	mid transition temperature (°C)
$T_{0,i}$	reference transition temperature based on Master Curve at intermediate loading rate, 200 mm/s (°C)

$T_{0,d}$	reference transition temperature based on Master Curve at dynamic loading rate, 5400 mm/s (°C)
ΔT_0	transition temperature shift (°C)
s	engineering stress (MPa)
S	span between outer loading points in three-point bend test (mm)
W	specimen width (mm)
W_a	gauge area width of the tensile test specimen (8mm)
W_s	shoulder width of the tensile test specimen (25 mm)
U	total area under force (F) vs specimen displacement plot along load line (Nmm)
U_e	elastic component area under force (F) vs specimen displacement plot along load line (Nmm)
U_p	plastic component area under force (F) vs specimen displacement plot along load line (Nmm)
Y/T ratio	yield-to-tensile ratio
1T	1-inch (25 mm) size specimen
0.4T	10 mm size specimen
$\dot{\varepsilon}$	strain rate (s^{-1})
$\dot{\varepsilon}^*$	dimensionless strain rate
$\dot{\varepsilon}_0$	quasi-static strain rate (s^{-1})
$\dot{\varepsilon}_p$	equivalent plastic strain rate (s^{-1})
$\dot{\varepsilon}_{lg}$	estimated strain rate over gauge length (s^{-1})
$\dot{\varepsilon}_{avg}$	average strain rate calculated (s^{-1})
$\dot{K}$	stress intensity factor loading rate also known as K-rate (MPa√m/s)
$\dot{K}_I$	average stress intensity factor loading rate (MPa√m/s)
σ	true stress (MPa)
σ_u	ultimate tensile strength (MPa)
σ_y	yield strength (MPa)

σ_{ref}	reference stress defining L_r (MPa)
σ_{yd} or σ_d	dynamic yield strength (MPa)
σ_{yy}	stress in front of crack tip based on HRR stress field
σ_0	quasi-static yield strength
V	crosshead speed (mm/s)
δ	crack tip opening displacement (CTOD)
ρ_0	initial notch tip radius
ν	Poisson's ratio

ABBREVIATIONS

AC	accelerated cooled
CMOD	crack mouth opening displacement
CTOD	crack tip opening displacement
CVN	Charpy V-Notch
DBTC	ductile-to-brittle transition curve
DIC	digital image correlation
DIF	dynamic increase factor
ECA	engineering critical assessment
EDM	electrical discharge machined
FAD	failure assessment diagram
FEA	finite element analysis
HAZ	heat affected zone
HRR	Hutchinson-Rice-Rosengren stress field
HSE	health safety executive
HSS	high strength structural steels
HV	Vickers hardness
LLD	load line displacement

LSS	lower strength structural steel
N	normalised route
QS	quasi-static
QT	quenched and tempered
SENB	single edge notched bend
SINTAP	structural integrity assessment procedure for Europe
TMCR	thermomechanically controlled rolled
TMCP	thermomechanically controlled processed
UTS	ultimate tensile strength

Chapter 1   Introduction

1.1   Industrial background

For heavy steel structures used offshore, high strength structural steels (HSS) with nominal yield strength >500 MPa are often preferred to conventional low strength structural steel (LSS) for the special structural element designs, as they offer sectional weight reduction. In addition to the physical benefits of lighter weight structures, the introduction of HSS in offshore applications comes with considerable savings in fabrication cost and times due to smaller weld profiles required (*Commissions of the European Communities 1988; Billingham et al. 2003; Willms 2009*).

Historical trends of structural steel over the years prompted the development of modern steel grades, **Figure 1.1**, with improved mechanical properties, weldability and satisfactory fatigue performance. The development is necessitated in order to match the change in technological advancement, especially offshore development where there is need for structural designs tailored towards deep-water applications, harsh environmental conditions, and severe loading conditions without jeopardizing structural integrity (*Billingham et al. 2003*). For example, the Seven Borealis pipelay and heavy lifting vessel has a tapered mast made using Dillimax 690 HSS to absorb the load moment in order to be capable of operation in the harshest environments in the world and is the largest offshore mast crane to date, **Figure 1.2** (*Subsea 7*; *https://www.subsea7.com/content/dam/subsea7-corporate2018/Datasheets/Vessel/rigid-pipelay-heavy-lift/Seven%20Borealis.pdf.downloadasset.pdf*). Besides the usage of HSS for offshore developments, other sectors such as the construction industry (bridges and buildings), and off-highway equipment industry (fixed and mobile cranes, excavators, earthmoving, etc.,) have also benefited from the use of HSS materials when strength-to-weight ratio is important (*Commissions of the European Communities 1988; Brockenbrough, R. L. and Associates Inc., 1995; Willms 2009, Ban et al. 2011; Shi et al. 2014; Ban and Shi 2017, Hai et al. 2018*).
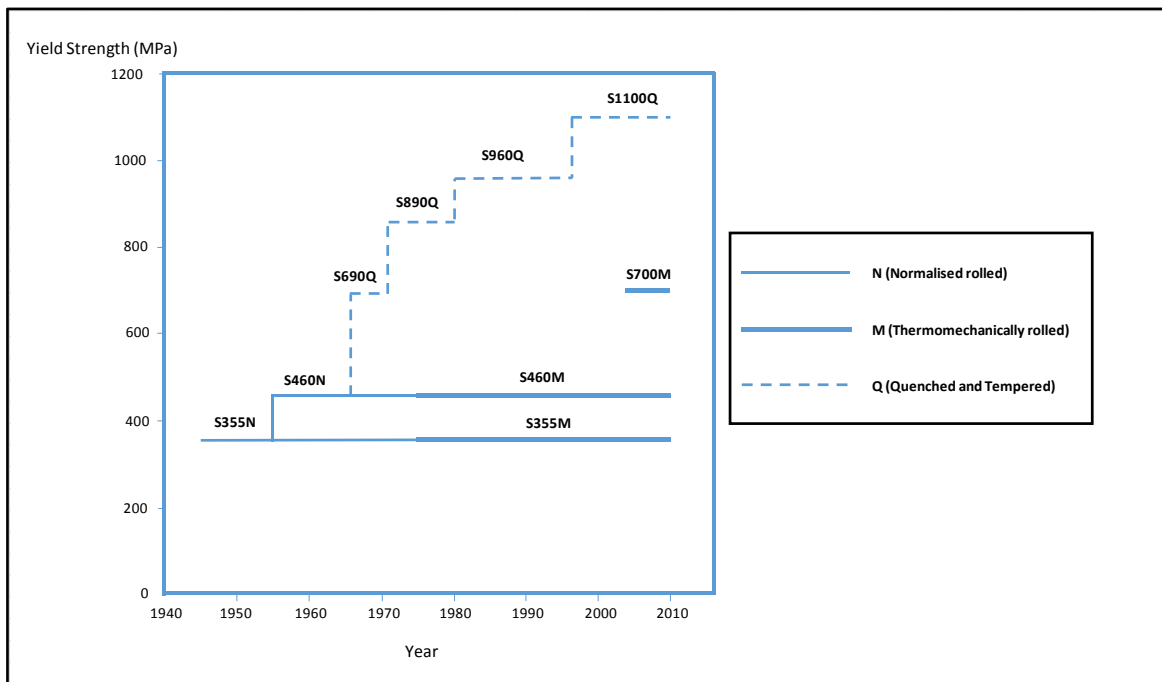
Figure 1.1   Historical development of high strength structural steel. Based on (*Willms 2009*)
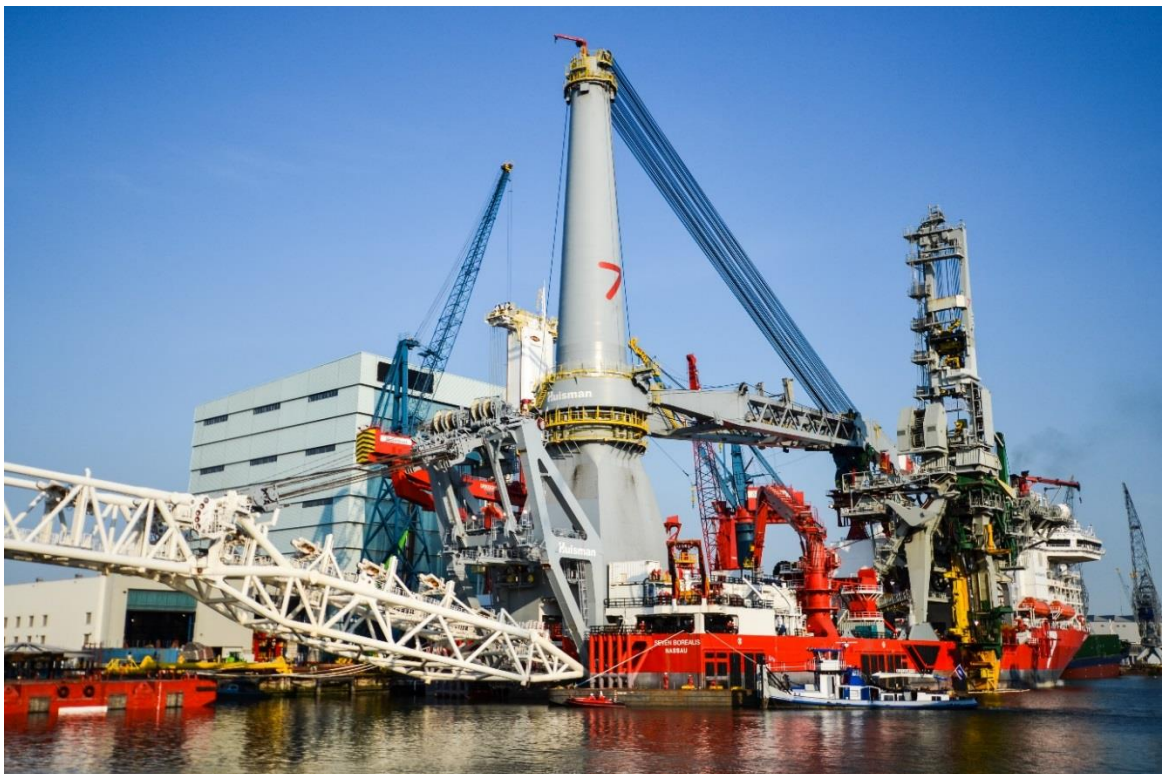
Figure 1.2   Largest offshore mast crane "Seven Borealis" built by Huisman Equipment for Subsea 7 (photo taken from http://flickr.com/photos/46853102@N00/7649921258)

As a result of the various benefits HSS provided (special element and architectural designs, cost reduction as well as improved safety where strength-to-weight is essential) over conventional LSS, more research has been tailored towards improving and understanding the mechanical properties and performance, production routes and microscale understanding of the constituent elements of HSS (*Billingham et al. 2003; Shi et al. 2014; Ban and Shi 2017*). Today, new generations of high performance HSS grades have evolved over the years through different production routes with finer grain microstructure that promotes higher strength and achieved with varying amount of chemical/alloy compositions (*Willms 2009*). The production routes such as Quenched and Tempered (QT), Thermomechanically Controlled Rolled (TMCR) or Accelerated Cooled (AC) routes and/or compositions have less effect on the ultimate tensile strength but an incremental effect on the yield strength and, consequently, the high yield-to-tensile ratio (Y/T) ratio.

The mechanical behaviour and performance of LSS is well known and established in the design codes and international standards. In fact, most of the design codes relate the design formulae to LSS with Y/T ratio below 0.85, and yield strength up to 500 MPa for most applications including offshore design requirements (*Billingham et al. 1997; Billingham et al. 2003; Shi et al. 2014*). The same level of confidence is yet to be achieved for HSS because of the concern that these HSS grades obtained their strength at the expense of ductility and strain-hardening capacity; properties which provide a sense of extra safety in avoidance of failure should service loads exceed yield. So, design codes that utilise these properties to deliver safety when using LSS with a Y/T ratio <0.85, may not currently be applicable for modern high strength steels (HSS).

An example of the approach to HSS is the American Petroleum Institute (API) practice which recommended a value for certain tubular joints with yield level of 66% (two-thirds) tensile strength when yield strength property ≤500 MPa (*API 2A-WSD 2014*). A re-evaluation conducted and incorporated into the newest edition of the standard suggested that a Y/T ratio of 0.80 for joints could be used provided that an adequate ductility is demonstrated in both heat affected zone (HAZ) and parent metal with 500 MPa $< \sigma_y \leq 800$ MPa (*API 2A-WSD 2014*). Also, Eurocode 3 (Design of steel structures), allows a Y/T value of up to 0.95 whereas the UK Annex of the same standard recommended 0.91 maximum (*Eurocode 3: 1-12 2007; UK National Annex, Eurocode 3: 1-12 2007*). To this end, a maximum Y/T ratio is imposed in the design codes and standards to ensure steel structures have adequate room to redistribute load

before major failure (*Bannister and Trail 1996; Bannister et al. 2000; Ban et al. 2011; Ban and Shi 2017*).

The requirements of Y/T ratios in accordance with design codes and regions, show how major international standards (especially for offshore applications) recommended a Y/T ratio in structural steels of no more than 0.85 which most modern HSS do not meet. This implies that, why it is essential to keep improving the mechanical properties of HSS grade through better metallurgy and production processes for offshore applications, it is essential to understand the possible in-service mechanical performance of HSS under critical loading rates when compared to what is known, understood and developed semi-empirically on the mechanical performance of conventional LSS having Y/T ratio <0.85. A large scale experimental and numerical analysis is required for HSS in order to characterise the possible in-service mechanical behaviour under different loading conditions, while taking into consideration uncertainties associated with the manufacturing technologies in different regions which may result in steel grade with quite different structural performance in-service.

One of the major issues with HSS is passing the fracture toughness requirements rather than passing the conventional Charpy V-Notch impact energy test. The higher the yield strength combines with thicker plate at lower service temperature, the bigger the issue is (*TNO report 2010*). Also, the rate of crack tip opening behaviour of HSS could be enhanced when Y/T ratio is in excess of 0.90 (*Bannister 1999; Bannister et al. 2000*). In the end, the fracture toughness of modern HSS needs to be demonstrated with a large-scale testing at different loading rates including the wide plate test which comes at high costs, long lead times because of lack of sufficient high load capacity test rig. In addition, the fatigue strength of HSS, especially at welded connections is still a research discussion, due to high residual stresses and the presence of initial defects and notches at welded connections, where the improvements with material strength in an unnotched base material are seen to reduce significantly for notched specimens (*Van Es et al. 2018*). However, crack initiation in welded connections is generally not regarded as being dependent on the yield strength (*Van Es et al. 2018*).

Also, integrity fracture performance of ferritic steels with Y/T ratios between 0.80 and 0.95 in structural designs such as pipelines, pressure vessels, bridge and building constructions, shows that high Y/T ratio does not necessarily signify poor mechanical or impact resistance (fracture) performance, but depends on a number of other factors (*Brockenbrough, R. L. and Associates Inc., 1995; Bannister and Trail 1996; Willms 2009; Bannister 1999; Bannister et al. 2000; Shi*

et al. 2014; Ban and Shi 2017). It was suggested that the Y/T ratio per se is not the only governing parameter that influences the plastic collapse of a steel component, other related characteristics such as strain-hardening exponent, ductile tearing resistance, and overall global deformation are important factors to take into account when considering the practicality of using high Y/T ratio as a measure of plastic capacity of a cracked component (*Bannister 1999*). Overall, fracture toughness properties of HSS are limited for offshore applications and many uncertainties are associated with the manufacturing technologies which may not be reflected in existing research findings on HSS. Thus, there is need for more larger scale fracture toughness tests on HSS representative of offshore in-service conditions (Table 2.4).

The successful application of HSS with high Y/T ratio in some offshore applications, like the Seven Borealis **(Figure 1.2)**, bridges and buildings construction – Samuel Beckett Bridge at Dublin **(Figures 1.3 and 1.4)**, can be translated to mean that HSS can exploit its strength, but not rely on its ability to deform or locally yield under extreme loading for offshore and marine applications. **Figure 1.3** (*Cutter et al. 2011*), shows the schematic design of the Samuel Beckett Bridge at Dublin where a high-tensile DILLIMAX 690 water quenched and tempered fine-grained structural steel delivered by Dillinger Hütte GTS was selected for the design of the cap and pylon (slender designs at ultra-high loadings), as shown in a close view in **Figure 1.5**.
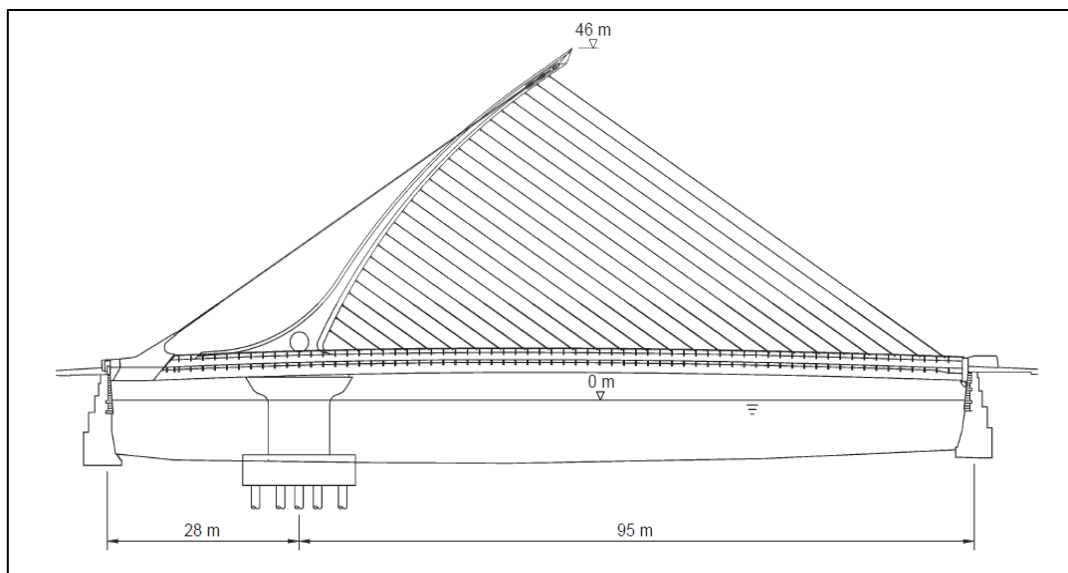
Figure 1.3   Design schematic and elevation of Samuel Beckett Bridge, Dublin (*Cutter et al. 2011*)

Figure 1.4   Samuel Beckett Bridge, Dublin (*Photo: S.M. Tunli – tunliweb.no*)

Figure 1.5   Samuel Beckett Bridge, Dublin pylon and cap close view (*Dillinger Hütte, Hollandia B.V.*)

Therefore, as confidence in the structural and mechanical performance of HSS grades is established, as well as the mechanical properties of HSS become more understood and improved in standards, the experimental programme supported by finite element analysis in this research can serve as fundamental data to theoretically or semi-empirically simulate the performance of offshore and marine structures with structural members made of HSS under possible in-service loading rate.

Hence, understanding the mechanical behaviour of HSS with Y/T ratio above 0.90 via characterising the tensile and fracture behaviour under loading rates representative of offshore conditions is being sought.

1.2   Research purpose

The knowledge gap on the mechanical behaviour of HSS with high Y/T ratio mentioned in section 1.1, indicates the limitation of HSS in terms of high Y/T ratio in excess of 0.90 compared to what is known and developed semi-empirically on the mechanical performance of conventional LSS having Y/T ratio <0.85, especially the fracture performance under high loading rates for offshore applications and designs. In this research, a perspective combining the tensile and fracture toughness properties of modern HSS under high loading rates applicable to offshore scenarios is proposed and investigated. The main aim of this research is to investigate and understand the tensile behaviour as well as the influence of high loading rate on the fracture performance of modern HSS with Y/T ratio >0.90 for an effective application of high strength structural steel in offshore structural members where reliability is important.

The HSS grades studied as agreed with the sponsor (Lloyd's Register Foundation) are S690QL and S960QL (designation and information about the steels are discussed in chapter 3). For comparison and loading rate sensitivity with different steel grades, tensile properties of S235 were tested experimentally under different loading rates which also include data from literatures. The experimental and FAD-based fracture engineering critical assessment carried out on the HSS grades under consideration with high Y/T ratio under high loading rates is expected to be useful for offshore users and marine engineers. It will also serve as basis to how actual mechanical properties of HSS under high loading rates could affect the structural integrity of an asset operating on the upper shelf to lower shelf regions of the ductile-to-brittle-transition curve (DBTC).

1.3   Research objectives

This research focuses on the following key objectives to achieve the research purpose aforementioned.

- Outlook on modern HSS, industrial application and limitation of high Y/T ratio that comes with HSS in the standards.

- Review of loading rate effects on the tensile properties and fracture toughness of ferritic steel to account for the in-service loading conditions representative of offshore scenarios.

- Investigate and characterise the change in tensile and fracture behaviours of HSS with Y/T ratio above 0.90 under different loading rates.

- Determine how the loading rates affect the transition regime on the ductile-to-brittle transition curve (DBTC) of HSS in order to determine the change in behaviour on the transition and lower regions of DBTC in terms of the transition temperature.

- Finally, conduct assessment of how actual properties (combination of the tensile and fracture toughness properties) of HSS under elevated loading rates could affect the structural integrity of an asset.

1.4   Summary of research methodology

This thesis concerns a systematic experimental and finite element analysis of the mechanical behaviour of HSS with high Y/T ratio under high loading rates. In order to understand the mechanical behaviour of these steel grades taking into account the structural response as experienced in offshore conditions with unavoidable crack-like defects or flaws, tensile and fracture toughness properties have been investigated. Invaluable experimental data at quasi-static (QS) and elevated loading rates (intermediate and dynamic) are generated for both tensile and fracture toughness properties using flat dog-bone shaped tensile, single edge notched bend (SENB) and Charpy V-Notch (CVN) test specimens. The data are used to characterise the tensile and fracture behaviour of the materials (S690QL and S960QL) under consideration.

Finite element analysis (FEA) has been employed to support the experimental work. The main purpose of the FEA is to allow for the prediction of crack driving force which cannot be

determined during the fracture toughness tests and to determine the influence of loading rate on crack mouth opening displacement using rate dependent model derived based on the experimental tensile test results. A quasi-static SENB model was developed and validated for this purpose and it is unchanged for the elevated loading rate analysis after validating the material model for S690QL. A linear static solver available in commercially FEA software ABAQUS (CAE) was used for all the analysis after comparison with the dynamic implicit solver results.

In order to satisfy the last objective listed in section 1.3, FAD-based fracture engineering critical assessment (ECA) was conducted. This is a rational consideration to define a conservative flaw acceptance criterion or in-service to evaluate the fitness-for-service (FFS) in the presence of flaws by combining the tensile and fracture toughness properties on a failure assessment diagram (FAD) as loading rate increases for the structural grades under consideration for appropriate recommendation. A flaw case was postulated to represent this on failure assessment diagram.

1.5   Structure of the thesis

The thesis is structured into two main parts and consists of 7 chapters in total. Chapter 1 introduces the research background and industrial needs with current situation of the mechanical behaviour of HSS with high Y/T ratio in the design codes and standards. Chapter 2 presents the general outlook of HSS and the structural implication of high Y/T ratio in industry. The literature survey on the effects of elevated loading rates on the mechanical properties, specifically, tensile and fracture toughness of ferritic steels is also discussed in Chapter 2. Chapter 3 describes the methodology and approach adopted for this research based on the review and knowledge gap identified in chapter 2, summarised in section 2.5. Experimental challenges of carrying out tests at high loading rates are also discussed in this chapter. FEA is introduced and validation methods used are discussed in this chapter.

The second part of this thesis focuses on the presentation and analysis of the results, finite element analysis, discussions and conclusion. In chapter 4, the experimental tensile test results S690QL and S960QL under high loading rate are presented. The tensile behaviour of HSS are compared to low strength structural steel, data from literatures as well as with the existing empirical equation. This is supported by material model FEA developed for S690QL. Chapter 5 concerns the experimental fracture toughness test results and the discussion on the influence

of loading rate on the lower region of ductile-to-brittle transition curve (DBTC) of S690QL and S960QL. The tearing resistance (R) curves obtained for S690QL at quasi-static and elevated loading rates are presented in chapter 5. Model generation, results and validation to describe the finite element analysis carried out on fracture behaviour of S690QL make the final part of chapter 5 before concluding remarks.

The discussion in Chapter 5 also evaluates the Charpy V-Notch results compared to when a fatigue pre-cracking is introduced in a Charpy-sized SENB specimen to calculate the fracture toughness of a steel material for an effective engineering critical assessment. The results highlight the importance of carrying out a proper fracture toughness test to describe the real impact resistance of ferritic steel at high loading rates.

Chapter 6 is concerned with the structural implication of dynamic loading on the mechanical behaviour of HSS, bringing together the tensile properties and fracture behaviour in the FAD-based fracture engineering critical assessment (ECA) by plotting the behaviour on the failure assessment diagram (FAD). A flaw case was proposed and discussed to represent a real time scenario. Lastly, Chapter 7 provides the main conclusions drawn from the research, future work and recommendations. It is important to mention that each of the chapters presented in this thesis has a concluding remark with the exception of chapters 1 and 7.

1.6   Contribution to new knowledge

1. Improve understanding of the possible in-service integrity performance of modern HSS with high Y/T ratio >0.90 especially for offshore applications as follows:

   - Mechanical response of high strength structural steels (HSS) with Y/T ratio >0.90 is less sensitive to the effect of loading rate due to the finer-grain size microstructure and a higher yield strength achieved via the QT processing route when compared to the low strength structural steels (LSS) with low Y/T ratio <0.85.

   - In the absence of high strain rate test data, quasi-static test data of S690QL and S960QL can be used to characterise its tensile behaviour up to 4 s^{-1} strain rates (typical strain rate an offshore/marine structure can be subjected to in-service) at room temperature.

- In terms of fracture toughness, Master Curve reference transition temperature T_0 for full thickness (1T specimen), and Charpy-size specimen (0.4T) data with an average value of a_0/W=0.52 for S690QL are -108 °C and -116 °C, respectively, under quasi-static loading conditions.

- A possible loading rate-induced temperature shift in the ductile-to-brittle transition curve of about 30.8 °C and 45.6 °C may be experienced by S690QL at intermediate (K-rate equals 10^4 MPa√m.s^{-1}) and dynamic (K-rate equals 10^6 MPa√m.s^{-1}) loading rates, respectively, when the yield strength of S690QL is taken as 817 MPa.

- The transition temperature T_0 estimated from the conventional Charpy V-Notch impact energy test is not conservative when compared to a T_0 calculated from a pre-cracked Charpy-size SENB specimen.

2. Contribution to standards by improving the overall understanding and acceptance of modern HSS for different applications and hence, improve sustainability by avoiding depletion of natural resources due to low consumption of raw materials.

3. Recommendation on the structural implication of dynamic loading on the mechanical behaviour of HSS for offshore practice, bringing together the tensile properties and fracture behaviour on the FAD-based fracture engineering critical assessment (ECA).

4. Suggestion of the best way to fit impact loading test data generated from Instrumented Charpy test results using Charpy-sized pre-cracked SENB impact test specimens for HSS, because of the ringing effect that is caused by imbalance between the internal and external forces during impact loading. To generate a sufficiently smooth data trace from a load and load line displacement (LLD) graph generated from Instrumented Charpy Impact test results, it is important to first fit through the linear (elastic) part of the data using the experimental fracture toughness data at equivalent temperature under quasi-static loading conditions, before using a curve fitting technique such as a spline or polynomial to generate a fit through the plastic region of the dynamic data. This will aid estimation of cleavage initiation point under impact loading.

1.7 List of publications based on the programme of work done

1.7.1 Published journal papers

- Alabi, A., A., Moore, P., L., Wrobel, L., C., Campbell, J., C., He, W., (2018). "*Tensile behaviour of S690QL and S960QL under high strain rate*" Journal of Constructional Steel Research 150 (2018) 570-580 https://doi.org/10.1016/j.jcsr.2018.08.009

- Alabi, A., A., Moore, P., L., Wrobel, L., C., Campbell, J., C., He, W., (2018), "*Influence of loading rate on the fracture toughness of high strength structural steel*" ECF22 - Loading and Environmental effects on Structural Integrity, Procedia Structural Integrity 13 (2018) 877–885 https://doi.org/10.1016/j.prostr.2018.12.166

1.7.2 Conference presentations and papers

- Alabi, A., Moore, P.L., Wrobel, L.C., He, W. and Tinkler, M., (2017). "*The Effect of Strain Rate on the Tensile Behaviour of High Strength Steel*", 14th International Conference on Fracture, Rhodes, Greece.

- Alabi, A., Moore, P.L., Wrobel, L.C., Campbell, J.C. and He, W., 2018 "*Influence of Loading Rate on the Fracture Toughness of High Strength Structural Steel*", 22nd European Conference on Fracture, Belgrade, Serbia.

- Alabi, A., (2018). "*Mechanical Behaviour of High Strength Structural Steel (HSSS) under High Loading Rates (S690QL and S960QL)*", NSIRC 2018 Annual Conference, TWI Ltd, Cambridge, UK.

- Alabi, A., A., Moore, P., L., Kulka, R., Wrobel, L., C., Campbell, J., C., He, W., (2018). "*Mechanical properties of high yield-to-tensile ratio high strength steels under service loading and the structural implication*" 1st International Conference on Structural Integrity for Offshore Energy Industry (SI 2018) Conference proceedings Aberdeen, UK, ISBN 978-1-9996144-1-6.

Chapter 2   Literature Review

2.1   Introduction

An outlook on the modern high strength structural steels (HSS), which include the requirements of Y/T ratios in accordance with design codes and regions and the production processes are presented in this chapter (section 2.2). Examples of offshore applications till date and a review of the structural implication of high Y/T ratio on the mechanical properties (tensile, fracture, fatigue and weldments) of HSS are also discussed in section 2.2.

In section 2.3, a brief description of tensile and fracture toughness properties of steel is introduced as a means of investigating and understanding the mechanical behaviour of HSS under consideration in line with the knowledge gap at different loading rates. This is followed by a detailed review of the effects of loading rates on the tensile and fracture toughness properties of ferritic steels, in order to appraise the effects of possible high loading rate on strength and impact resistance properties of HSS during offshore in-service conditions as presented in section 2.4.

The emerging research gap in terms of the tensile and fracture toughness properties of HSS with high Y/T ratio under possible offshore loading rates is summarised in Section 2.5.

2.2   Outlook on modern high strength structural steel

2.2.1   Overview

High strength structural steels (HSS) with nominal yield strengths in excess of 500 MPa offer numerous benefits ranging from potential structural weight reduction through reduced material usage (sustainability), cost effectiveness (economy), development of special aesthetic and elegant designs with reduced structural sections (architecture) and safety (when strength-to-weight ratio is important). They are increasingly used in a range of steel structures including the construction industry (bridges and buildings), off-highway equipment industry (fixed and mobile cranes, excavators, earthmoving etc.), offshore and marine industries. Today, many offshore structures such as jackets, topsides, jack-up structure legs, rack, pinions, offshore wind, wave energy converter etc., have successfully been fabricated and installed using high strength structural steels with nominal yield strength between 400 MPa and 800 MPa

34

(*Billingham et al. 2003; SSAB offshore brochure 2019; SSAB media 2019*). However, few studies on the mechanical behaviour of HSS with high Y/T ratio in excess of 0.90 under high loading rates have been reported for offshore applications, especially in terms of strength and fracture toughness (*Wiesner and MacGillivray 1999; HSE report 1999; HSE report 2001; Burdekin et al. 2004; Choung et al. 2013; Walters and Przydatek 2014*).

2.2.2   Production routes of HSS

The usage of HSS in special structural designs (slender structures) has enabled more research to be expended in improving its constituents' chemical composition and production routes over three decades. Metallurgical developments and steel production techniques have simultaneously progressed (*Healy and Billingham 1995; Billingham et al. 1997; Billingham et al. 2003; Willms 2009; Ban et al. 2011*). Combination of alloying elements and heat treatment helps to attain smaller grain size which results in a higher strength, and combination of other mechanical properties such as ductility, toughness and weldability. To achieve a good combination of strength and toughness in modern HSS, production routes such as Thermo-mechanically controlled rolled (TMCR), quenched and tempered (QT) are employed to promote a finer grain size (*Healy and Billingham 1995; Bannister and Trail 1996; Willms 2009; Ban et al. 2011*).

Traditionally, alloying elements such as carbon and manganese added to steel increase the nominal yield strength, with detrimental effects on the fabrication properties of steels, in particular, weldability. To avert this effect, carbon contents in modern HSS grades are limited, along with a high degree of cleanliness and typical sulphur and phosphorus levels of <0.005% and <0.010% respectively, implemented for good toughness and through-thickness homogeneity (*Healy and Billingham 1995*). To compensate for the strength reduction in limiting the carbon contents, micro-alloying elements such as niobium, vanadium, titanium are introduced to facilitate precipitation strengthening, or solid solution using traditional elements such as nickel, chromium, manganese, silicon and molybdenum (*Healy and Billingham 1995, Billingham et al. 2003*).

Conventional low strength steel grades with yield strength up to 460 MPa can be produced via a normalised (N) route heated slightly above the temperature (about 800-900 °C, depending on the carbon content) where its ferritic-pearlitic structure totally transforms to austenite followed by slow cooling in air (*Bannister and Trail 1996; Willms 2009*). Thermo-mechanically

controlled rolling (TMCR) of the plates after casting then ensures a finer grain size in the steel. Although TMCR gives a good combination of strength and toughness with higher yield strength up to 700 MPa attainable, today, the highest nominal yield strength steels up to 1300 MPa are achievable via the quenched and tempered (QT) route (*SSAB Technology 2011*) as shown in **Figure 2.1**. The process can be completed via Accelerated Cooling or Thermo-mechanically controlled processed (AC/TMCP) if thicker steel plates are required. QT consists of a rolling process followed by heating above the austenite transformation temperature followed by rapid cooling in water (or oil) plus subsequent tempering to improve the toughness.

These production processes, and/or compositions have less effect on the ultimate tensile strength but an incremental effect on the yield strength, consequently resulting in high Y/T ratio for HSS (*Healy and Billingham 1995; Billingham et al. 2003*). For instance, S690QL structural steel (grade under consideration) delivered according to *BS EN 10025:6: +A1 (2009)* required a minimum yield strength of 690 MPa and maximum tensile strength of 940 MPa for thicknesses between 3 mm and 50 mm in quenched and tempered condition. This implies that the nominal yield strength can be increased and improved during production if needed for various applications where strength-to-weight ratio is important.

It can therefore be said that the final nominal yield strength and Y/T ratio value depends on the manufacturing process, chemical composition, thickness and the plate manufacturer which are determined by the production routes and controlled by the nature and volume fraction of the microstructural phases present (*Healy et al. 1995*). Only nominal yield strengths up to 960 MPa are standardised to date (*BS EN 10025:6: +A1: 2009*). **Table 2.1** summarises the different processing routes for the production of modern HSS.

Table 2.1   Steel processing routes for production of high strength structural steels, based on (*Billingham et al. 2003; SSAB Technology 2011*)

Process routes	Strength/thickness limit
Normalised	Usually <450 MPa for 50 mm plate
Thermo-mechanically controlled rolled (TMCR)	Thickness restriction especially at higher strengths, typically up to 550 MPa at 40 mm
Accelerated cooled (TMCP)	Improved properties compared to TMCR but thickness restriction at higher strengths

Quenched & Tempered (QT)	Alloyed route – no real thickness restriction but expensive and costly to weld, and up to 1300 MPa is attainable.
Casting	Usually alloyed because of lack of processing capacity
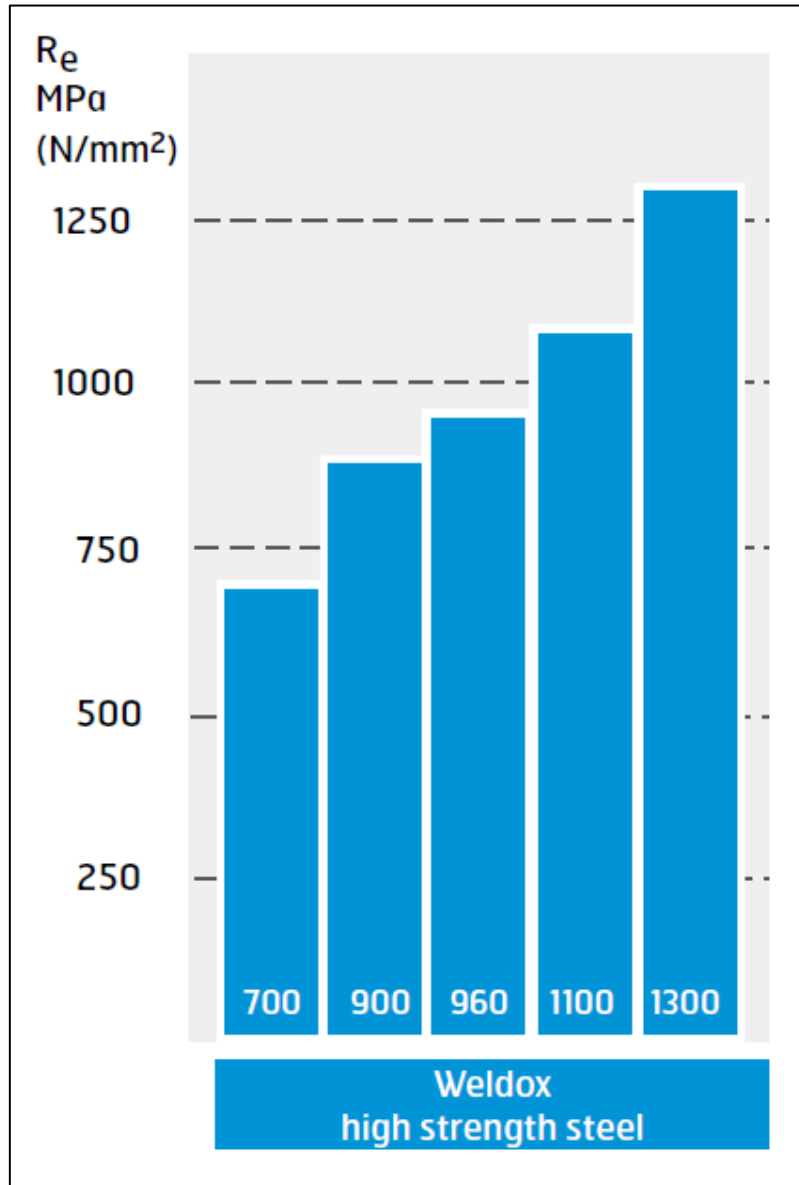
Figure 2.1   Weldox high strength structural steel grades to date (*SSAB Technology 2011*)

2.2.3   Limitation of high Y/T ratio in the design codes and standards

Modern production routes for high strength structural steels, such as TMCP, TMCR and QT, deliver higher yield strengths, but with only moderate effect on the ultimate tensile strength

resulting in a higher Y/T ratio as the yield strength increases (*Bannister and Trail 1996*). The high Y/T ratio, however, means a low strain-hardening capacity – a property that gives a sense of extra safety in avoidance of failure should service loads exceed yield (*Billingham et al. 2003*). The limitation of Y/T ratio by imposing a maximum Y/T ratio to ensure steel structures have adequate room to redistribute load before major failure as shown in **Table 2.2**, is a representation of different regions with different Y/T ratio values. For instance, Eurocode 3 (Design of Steel Structures) recommended the highest Y/T ratio limit of about 0.95, but the UK annex of the same standard suggested a limit of 0.91. Although ANSI/AISC 360-16 gives a value of 0.90, a maximum nominal yield strength of 450 MPa is recommended for the Y/T ratio value when carrying out plastic analysis.

The requirements in terms of Y/T ratio in various design codes have generally limited HSS usage due to insufficient understanding of its mechanical performance in-service. Hence, there is the need for research to be expended in understanding the mechanical performance of HSS with high Y/T ratio by simulating as close as possible the in-service loading conditions.

Table 2.2   Treatment of Y/T ratio in accordance with various design codes and regions.

Code	Region	Y/T ratio Limitation	Applications
API 2A-WSD	America	0.67 *0.80	Tubular joints, $500 \text{ N/mm}^2 < \sigma_y \le 800 \text{ N/mm}^2$
ISO 19902	International	0.90	Tubular Members (Offshore)
BS 5950 (Buildings)	Europe	0.84	All components
EC3 (Buildings, bridges and other steel structures)	Europe	**0.91/0.95	All components $(\varepsilon_{UTS} \ge 15\sigma_y/E)$
ANSI/AISC 360-16 (Buildings)	America	0.90	Grade up to 450 MPa beams
GL Rules IV – Industrial Services, Part 6 – Offshore Technology (Structural Design)	Europe	[a]0.87/0.93 [b]0.85/0.90	Steel Structures $t \le 16$ mm $t > 16$ mm $(\sigma_y > 360 \text{ N/mm}^2)$

AS 4100-1998 (Steel Structures)	Australia	0.83	Up to 450 MPa for plastic design ($\varepsilon_{ST} \geq 6\sigma_y/E$)
GB/T 19879-2015	Asia	0.80 0.83	Steel Plate for building, (Q345GJ) (Q390GJ, Q420GJ or Q460GJ grades)
GB50017-2003 (Ban et al. 2011)	Asia	0.83	Plastic Design ($\varepsilon_{UTS} \geq 20\sigma_y/E$)
GB50011-2010 (Ban et al. 2011)	Asia	0.85	Plastic designs
NS 3472 (NPD) (Offshore)	Europe	0.83	All components
DnV (Offshore)	Europe	0.85 0.75	Except tubular joints Tubular joints ($\sigma_y >$500 N/mm^2)

Notes:

*New Y/T ratio for joints provided adequate ductility is demonstrated in both HAZ and parent metal.

**Recommended Y/T ratio in the UK National Annex to Eurocode 3

[a, b] Recommended Y/T ratio for Normalised / Normalised rolled steels with 255 MPa $< \sigma_y \leq$ 360 N/mm^2 conditions.

ε_{ST} is the strain at the end of the yield plateau.

2.2.4   Offshore applications of HSS

The introduction of HSS in offshore applications, **Table 2.3**, came from the need to reduce weight and constructional cost, because of the immense size of offshore structures and drilling rigs (Figure 1.2) (*Healy et al. 1995; Billingham et al. 2003, SSAB offshore brochure 2019*). The lack of confidence on the performance of HSS in relevant design codes (Table 2.2), has limited its usage due to a reduced plastic deformation margin largely debated by designers as a concern (*Healy et al. 1995, Billingham et al. 1997, Ban et al. 2011, Ban and Shi 2017*).

However, in recent years, due to the advancement in offshore technology tailored towards deep-water applications, harsh environmental conditions, severe loading conditions, etc., and the need for a greener and cleaner energy in the form renewable energy (offshore wind farm), the needs to improve mechanical properties, weld properties, and to increase the strength-to-weight ratio of low strength steels arose (*Billingham et al. 2003, SSAB media 2019*).

Today, they are increasingly used in various offshore applications such as, offshore and marine cranes, launch and recovery systems, topsides and pylons. They are also used for ocean energy equipment like offshore wind, wave energy converter, tidal and stream converter (*SSAB media 2019*). For instance, major HSS steel grade manufacturer SSAB (*SSAB offshore brochure 2019*) has seen an increasing demand for its high strength steel in marine and offshore applications in recent decades due to the benefits of these steel grades offer towards the marine, offshore, and the energy segments.

According to SSAB, application of Strenx® 700 and the top end grades of Strenx® performance steel with yield strengths between 960-1300 MPa in selected part of offshore structures, can provide weight reduction opportunities of 30% and 50%, respectively, allowing for many cost and performance advantages (*SSAB offshore brochure 2019*). Typical HSS offering for offshore and marine applications is shown in **Figure 2.2.** It should be noted from **Figure 2.2** that only yield strength up to 960 MPa is standardised till date.

	Yield Strength [MPa]	Thickness interval [mm]	Impact toughness L = Longitudal T = Transversal [J/ DegC]	Elongation [A80 %]	Welding properties [CET max / CEV max][1]		Standards Classification Conformity
Strenx 620 OME	620	4.8–130³	69J [-40] L 69J [-40] T	15	−30mm (30)−100 mm (100)−130 mm	0,38/0,57 0,39/0,58 0,41/0,67	DNV-GL NV E620² DNV-GL VL E620² LR EH62² ABS EQ70
Strenx 700E	700 650 650	4−53 (53)−100 (100)−160	69J [-40] T	14	−5mm (5)−30 mm (30)−60 mm (60)−100 mm (100)−130 mm (130)−160 mm	0,34/0,48 0,32/0,49 0,36/0,52 0,39/0,58 0,41/0,67 0,43/0,73	EN 10025-6 S 690 QL
Strenx 700 OME	690	4,8 – 130	69J [-40] L 69J [-40] T	14	−30mm (30)−100 mm (100)−130 mm	0,38/0,57 0,39/0,58 0,41/0,67	DNV-GL NV E690² DNV-GL VL E690² LR EH69² ABS EQ70
Strenx 700F	700 650 650	4− 53 (53)−100 (100)−130	27J [-60] T	14	−30mm (30)−100 mm (100)−130 mm	0,38/0,57 0,39/0,58 0,41/0,67	EN 10025-6 S 690 QL1
Strenx 900E	900 830	4−53 (53)−100	27J [-40] T	12	4−80 mm (80)−100 mm	0,39/0,58 0,41/0,63	EN 10025-6 S 890 QL
Strenx 900F	900 830	4−53 (53)−80	27J [-60] T	12	4−80 mm (80)−100 mm	0,39/0,58 0,41/0,63	EN 10025-6 S 890 QL1
Strenx 960E	960 850	4−53 (53)−100	40J [-40] T	12 10	4−(35) mm 35−100 mm	0,38/0,58 0,41/0,67	EN 10025-6 S 960 QL
Strenx 1100E	1100	4−(5) (5)−40.0	27J [-40] T	8 10	− (5) mm 5−(8) mm 8−(15) mm 15−(40)	0,37/0,57 0,38/0,58 0,39/0,62 0,42/0,73	
Strenx 1100F	1100	4−(5) (5)−40.0	27J [-60] T	8 10	5−(8) mm 8−(15) mm 15−(40) mm	0,40/0,70 0,40/0,70 0,42/0,73	
Strenx 1300E	1300	4−10	27J [-40] T	8	4−10 mm	0,43/0,67	
Strenx 1300F	1300	4−10	27J [-60] T	8	4−10 mm	0,43/0,67	

1) CET = C + (Mn+Mo)/10 + (Cr+Cu)/20 + (Ni)/40 CEV = C + Mn/6 + (Cr+Mo+V)/5 + (Ni+Cu)/15
2) Max thickness 80 mm for DNV-GL and LR

Figure 2.2   Strenx® performance steel offering for offshore and marine applications
(*SSAB offshore brochure 2019*)

Table 2.3   Typical high strength structural steels used offshore (*Billingham et al. 2003*).

Strength/Grade (MPa)	Process route	Applications
350 (X52)	Normalised	Structures
	TMCP	Structures and pipelines
450 (X65)	Q & T	Structures
	TMCP	Pipelines
550 (X80)	Q & T	Structures and moorings
	TMCP	Pipelines
650	Q & T	Jack-ups and moorings
750	Q & T	Jack-ups and moorings
850	Q & T	Jack-ups and moorings

2.2.5 Structural implication of Y/T ratio on structural integrity design

In engineering terms, the Y/T ratio provides the basis for measuring the plastic deformation (strain-hardening) capacity of a material, and normally increases as the static yield strength increases. Y/T ratio is related to the strain-hardening exponent (*n*) used to qualify the plastic deformation performance of a metal (*Bannister and Trail 1996; Bannister 1999*). Usually, a higher Y/T ratio leads to a decrease in yield point elongation (Lüders Plateau) and a decrease in the strain-hardening exponent (*Bannister and Trail 1996*). It means that steels with low Y/T ratios, typically in the range 0.5 to 0.85, associated with conventional low and medium strength steels have a high strain-hardening exponent (extra safety margin). Modern HSS which is associated with high Y/T ratios in excess of 0.90, exhibits a low strain-hardening exponent.

In principle, in designs (conventional design approach) based on elastic loading, i.e. stresses kept below yield, the strain-hardening characteristics beyond yield should not matter strongly in the design concept. The approach has guided the elastic structural design methodologies where the working stress is usually taken as a proportion of the yield stress, with typical values around 60% of yield strength in normal loading and up to 80% in severe loading (*Healy et al. 1995*). The concept ensures that load resistance falls within the linear region of the stress-strain curve of the component, making the Y/T ratio irrelevant in practice for such elastic cases. The plastic design concept, on the other hand, is incorporated for additional safety precaution in steel structures where the structure is able to locally yield and redistribute load (work hardening) without major failure or total collapse. In this case, the Y/T ratio becomes applicable in the post-yield behaviour of steel, and can be said to be the parameter which represents the ability of a material to withstand plastic loading (*Bannister and Trail 1996*).

The possible structural implication of high Y/T ratio on the mechanical behaviour of modern HSS based on literature review relevant to this study are discussed in the following sub-sections.

2.2.5.1 Tensile properties

Compared to conventional LSS, modern HSS possesses a different stress-strain characteristic and generally has high Y/T ratios, and reduced ductility, **Figure 2.3** (*Ban and Shi 2017*). These characteristics results in a high Y/T ratio (mostly above 0.90) with reduced elongation, percentage reduction in area, and low strain-hardening capacity (factors that contribute to the lack of confidence in the design codes for HSS usage). Designing with HSS must exploit its

strength, but not rely on its ability to deform or locally yield under extreme loading for its special structural designs in general and offshore applications. The tensile properties of various steel grades with Y/T ratio between 0.55 and 0.99 in terms of yield strength, percentage elongation and percentage reduction in area are presented in **Figures 2.4 and 2.5** (*Ban et al. 2011; Ban and Shi 2017*).
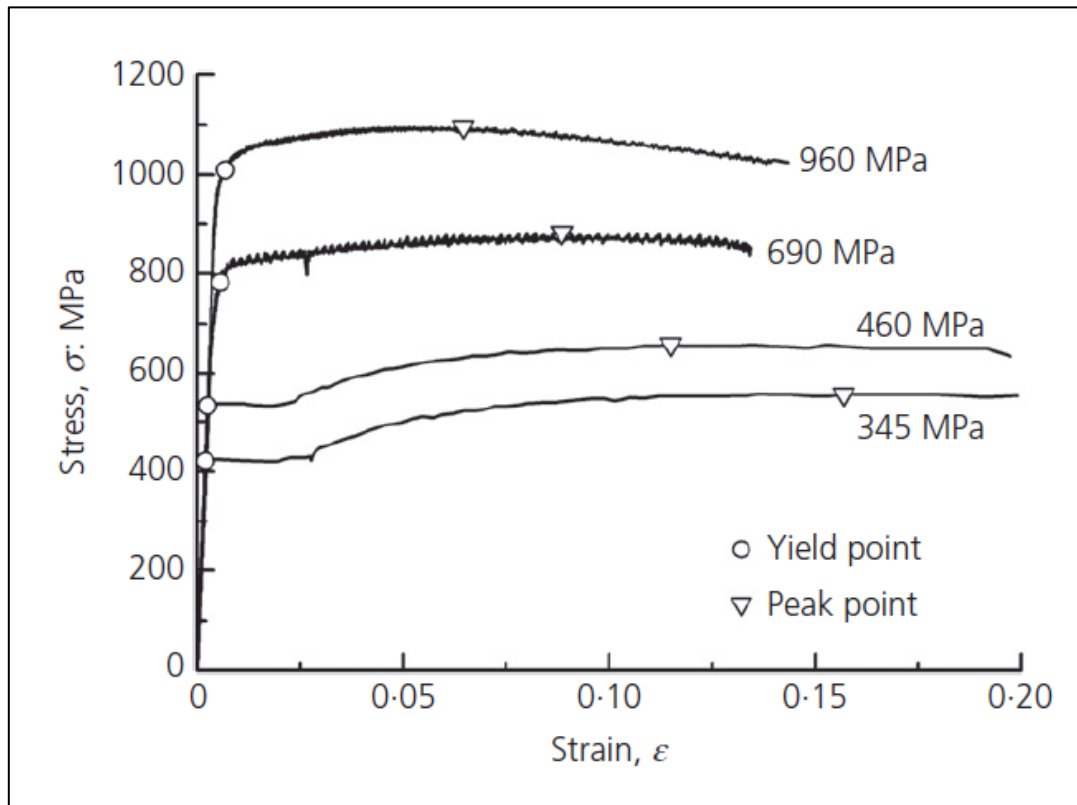
Figure 2.3   comparison of stress-strain curves for various steel grades (*Ban and Shi 2017*)
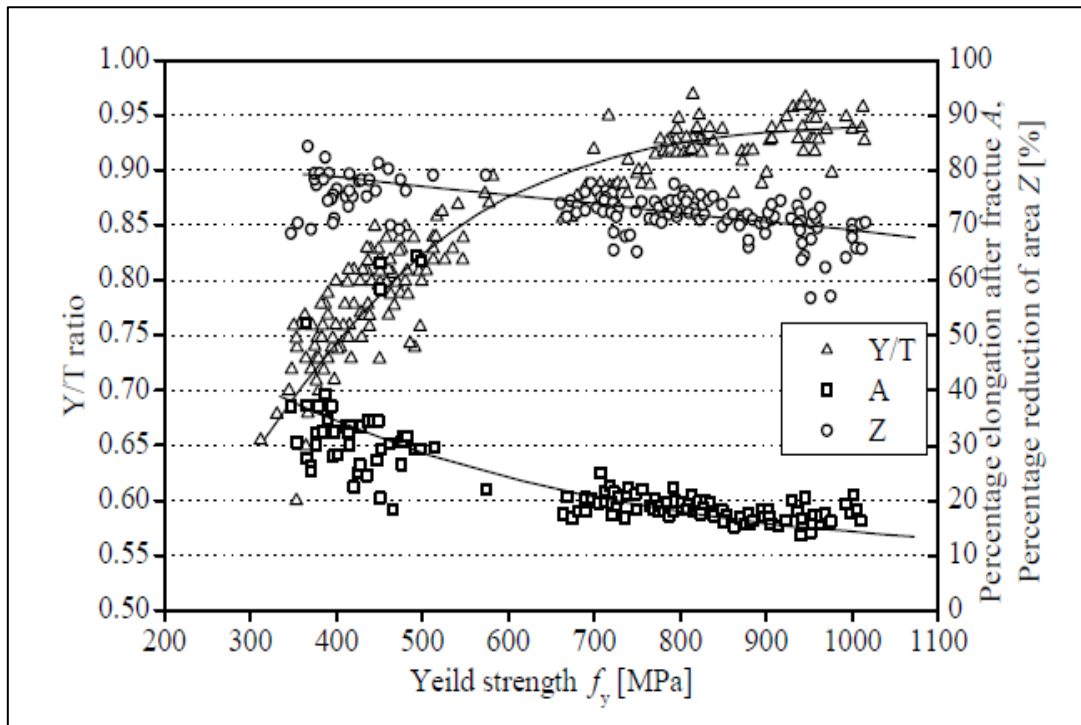
Figure 2.4   Comparison of material properties of 4 different European steels (*Ban et al. 2011*)
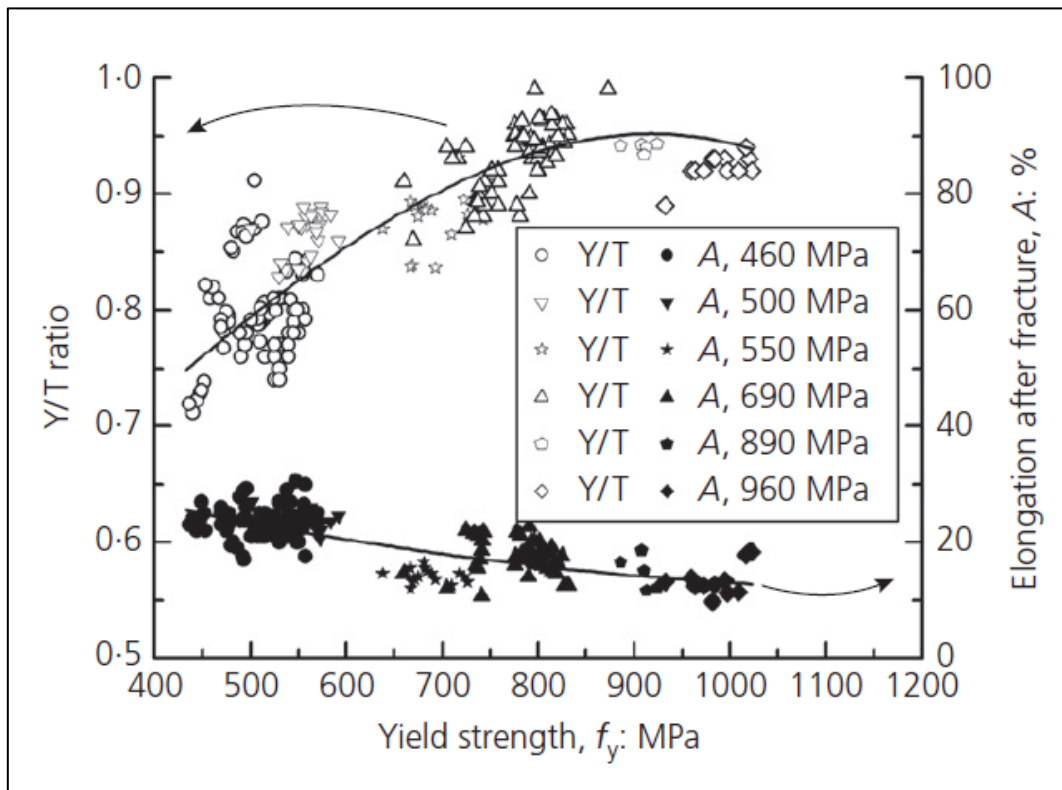
Figure 2.5   Summary of tension coupon test results of HSSs (*Ban and Shi 2017*)

2.2.5.2 Fracture behaviour

In terms of fracture behaviour, the presence of cracks modifies the shape of the stress-strain curve, whereas the strain-hardening exponent (*n)* influences fracture behaviour (*Bannister and Trail 1996*). The rate of crack tip opening behaviour is seen to be enhanced when Y/T ratio is in excess of 0.90, and in thin plates where failure mechanism is affected by both thickness and notch geometry (*Bannister 1999*). This is demonstrated by the work of Bannister (*Bannister 1999; Bannister et al. 2000*) where within elastic strain of 0.2% in the elastic region, no logical influence of Y/T ratio on the amount of crack opening, independent of notch depth was observed, **Figure 2.6**. An enhanced and higher crack tip opening displacement was obtained at a higher applied strain of 1% for a deep notch thin plate as compared to thicker steel plates, illustrated in **Figure 2.7**. The work by Tagawa (*Tagawa et al. 2014*) supports Bannister (*Bannister 1999*) observation, which suggested that crack tip opening behaviour is sensitive to Y/T ratio of a material, and that the shape of the crack tip blunting is a function of the strain-hardening properties and hence Y/T ratio. The effect of loading rate, however, is more pronounced on the low strength steel grades with low Y/T ratio, where high strength steel with high Y/T ratio exhibits less loading rate sensitivity depicted by the shift in transition temperature and yield strength amplification (*Wiesner and MacGillivray 1999*).
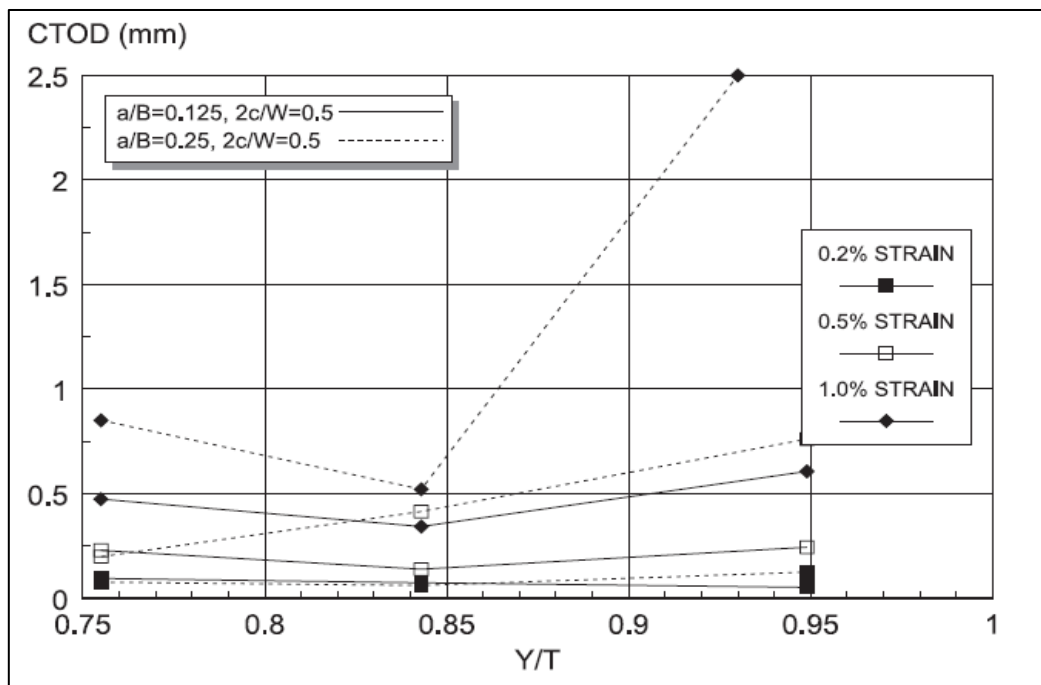
Figure 2.6   Effect of Y/T ratio on crack tip opening displacement at three levels of applied strain for 12mm plate (*Bannister 1999*)
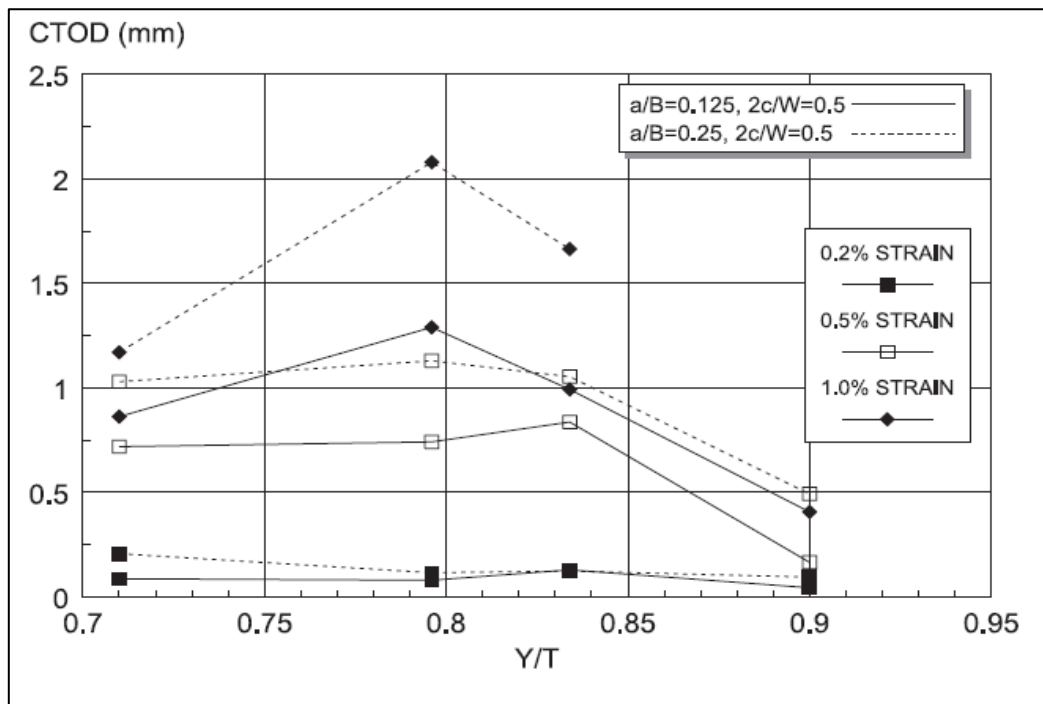
Figure 2.7   Effect of Y/T ratio on crack tip opening displacement at three levels of applied strain for 25mm plate (*Bannister 1999*)

Note: *a/B* is the ratio of crack depth and plate thickness while *2c/W* is the ratio of crack length and plate width.

2.2.5.3 Fatigue and weldments

It is important to mention that the fatigue performance of both parent and welded HSS indicates that the general performance of HSS is as good as the medium strength steels, where crack initiation in welded connections are generally not regarded as being dependent on the yield strength (*Billingham et al. 2003; Van Es et al. 2018*). However, more data are required before confident predictions of the fatigue performance of HSS with high Y/T ratio can be made (*Billingham et al. 2003*).

In the case of weldments (welded connections), factors like stress-strain characteristics of the parent material, weld material and heat affected zone (HAZ) have more effect than the Y/T ratio of the parent and weld materials because of the occurrence of weld mis-match and modified toughness in the HAZ (*Bannister 1999*). Research on HSLA-100 steel shows that even with low strain-hardening capacity that accompany high Y/T ratio, an undermatched weld can still achieve higher strength, and whether overmatched or undermatched welds is achieved, a remarkable tolerance to misalignment, lack of fusion defects and undercuts was observed

46

(*Dexter and Ferrell 1995*). These properties are not studied in this research and have been proposed for future work.

2.3   Mechanical properties

2.3.1   Overview

In view of the aforementioned structural implication of high Y/T ratio in HSS, mechanical properties in terms of tensile strength and fracture toughness parameters relevant to this study are introduced in this section to support the research objectives in section 1.3. The variables including different testing methods, key parameters, and the available guidelines up to the current date are presented in sub-sections 2.3.2 to 2.3.5. This is important in connection to the effect of loading rate on the tensile and fracture behaviour discussed in section 2.4 of this chapter.

The common and perhaps well-established method of determining the ability of a steel material to withstand load or deformation in terms of strength is via tension test. Fracture mechanics concept on the other hand, involves the study of material resistance in the presence of flaw or crack-like defects under different loading conditions similar to the same constraint that a steel structure might be subjected to in-service. Finally, the relevance of fracture-based engineering critical assessment (ECA) to this study is briefly introduced in sub-section 2.3.2 and discussed in detail in chapter 6.

2.3.2   Fracture toughness – an overview

While structural failures can be catastrophic, fracture mechanics based ECA in structural integrity assessment has helped to offset some of the potential catastrophic accidents that may have occurred in-service. Fracture toughness property is a measure of a material resistance to deformation and failure in the presence of flaws or crack-like defects under applied load (*Wallin 2011*). A value of fracture toughness can serve as a yardstick for characterising fracture behaviour, assessing and evaluating the criticality of structural performance in the presence of flaws or crack-like defects (*Zhu and Joyce 2012*).

Fracture mechanics based ECA serves as a quality assurance which is used to support design and fabrication principles, and in-service, to underpin fitness-for-purpose ability of most engineering steel structures, such as fixed offshore structures, heavy lifting equipment, nuclear,

pressure vessels, pipelines, automotive, ship and aircraft structures. Therefore, fracture toughness testing and analysis has been a very important subject for various engineering applications where fracture toughness values of most ferritic steels are largely affected by loading rates, as discussed in detail in section 2.4.3.

Structural integrity assessment of engineering steel structures depends on a number of factors, material properties (fracture toughness/yield strength), applied stress (loading) and flaws (geometry, size position or orientation). It is important to select the right parameter to define the fracture toughness of a ferritic steel under different loading conditions, geometry and constraints. These parameters can be used to characterise deformation behaviour of ferritic steel as a measure of fracture toughness under linear-elastic or elastic-plastic conditions, **Figure 2.8**, discussed briefly in the sub-sections 2.3.2.1 to 2.3.2.3. In a fracture toughness test, two elements describe the fracture behaviour in a steel material – the driving force and the material resistance. The driving force is the combination of flaw size and loading conditions while the material resistance is the ability of the material to resist the propagation of these flaws and cracks or ability to withstand deformation (*Wallin 2011*). In a nutshell, deformation process of a steel grade determines which fracture toughness parameter to use as a measure of fracture toughness or material resistance.
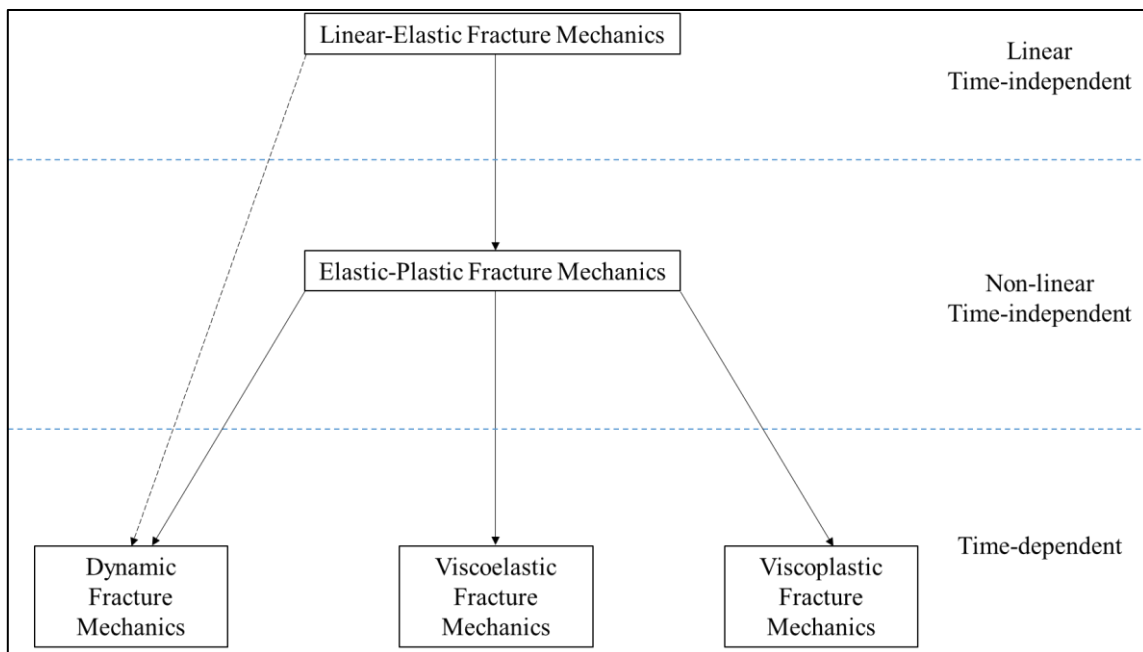
Figure 2.8   Summary of fracture mechanics classification tree (*Anderson 2005*)

2.3.2.1 Energy release rate (*G*) and stress intensity factor (*K*)

Stress intensity factor (*K*) and its equivalent partner, the energy release rate (*G*), have successfully been used to describe linear-elastic fracture behaviour in a brittle material. The *G* parameter originally defined as crack extension force tendency postulated by Griffith, is now known as energy release rate. The work of Griffith gave the background to crack formation by extending the idea behind the theorem of minimum energy (in which change from non-equilibrium state to equilibrium state decreases with net energy) to formulate a new criterion of rupture (*Griffith 1921*). The extended theorem means that the formation of a crack or crack growth occurs only when the total energy decreases or remains constant. This inferred that critical fracture is the point at which crack growth occurs under equilibrium conditions with no net change in total energy (*Anderson 2005*). However, since energy release rate postulated by Griffith depends on the change of potential energy due to crack formation or growth, its application is only valid for linear-elastic materials.

A more convenient approach to the energy release rate was developed by Irwin based on the energy theory of Griffith (*Anderson 2005*). The new concept defined energy release rate as a measure of energy available for an increment of crack growth as given in Eq. (2.1) and expanded to Eq. (2.2) when applied in an infinite plate (assuming width $\gg 2a$), as in the case of $2a$ as the crack length (*Anderson 2005*).

$$G = -\frac{d\prod}{d\mathrm{A}} \qquad\qquad (2.1)$$

$$G = \pi\sigma^2 a/E \qquad\qquad (2.2)$$

where, $\prod$ = potential energy

         A = is the crack area

         E = Young's modulus of elasticity

         σ = the stress

         a = is the crack length.

The stress intensity factor (*K*) on the other hand, was developed to characterise crack tip conditions in a linear-elastic state. It was assumed that stress close to the crack tip varies with

$1/\sqrt{r}$ for each mode of loading regardless of the configuration of the cracked body, and will therefore be convenient to approximate the stress intensity around the crack tip by a single parameter or factor ($k\sqrt{2\pi}$) (*Wallin 2011*). However, to take into account different geometries of the cracked component, a dimensionless constant (*Y*) was introduced, Eq. (2.3)

$$K = Y\sigma\sqrt{(\pi a)} \tag{2.3}$$

where,

Y is the dimensionless constant (e.g. *Y* = 1.12 for edge cracked body when crack length is *a*, and *Y* = 1 for embedded crack body when crack length is 2*a*)

Comparing Eqs. (2.2) and (2.3), stress intensity factor and energy release rate are essentially equivalent for a linear-elastic fracture behaviour defined in Eq. (2.4)

$$G \cdot E = K^2 \tag{2.4}$$

Although the application of *K* is more accurate for linear-elastic conditions, it can be extended to elastic-plastic conditions by the use of simple plasticity corrections when moderate crack-tip-yielding occurs, and the size of the crack tip yielding can be evaluated by use of either Irwin's approach or strip-yield model (*Anderson 2005*). These are beyond the scope of this work and not discussed.

2.3.2.2 Crack tip opening displacement (CTOD)

Another fracture toughness parameter, crack tip opening displacement (CTOD) evolved due to the limitation of using stress intensity factor (*K*) for elastic-plastic conditions in structural integrity assessment. CTOD (δ), formerly known as Crack Opening Displacement (COD), was introduced by Wells in the 1960s at the British Welding Research Association, now The Welding Institute (TWI), when he tried to extend the stress intensity factor approach to crack tip yielding conditions in the elastic-plastic region (*Wells 1969*).

Wells' postulation came from the observation made on a notched bar test specimen, where crack blunting prior to fracture was noticed when plastic deformation changes the initial sharp crack to a blunted crack resulting in a finite displacement at the original crack tip. This means that CTOD can be estimated by solving the physical displacement created as a result of blunting at the crack tip using Irwin's estimate of crack tip plasticity, Eq. (2.5)

$$\delta = \frac{4}{\pi} \frac{K^2}{\sigma_y E} \tag{2.5}$$

Consequently, this knowledge led to the development of a mathematical relationship between CTOD, stress intensity factor K and energy release rate G, where an appropriate fracture toughness parameter is no longer valid for linear-elastic fracture behaviour using Irwin's model of crack tip plasticity given in Eq. (2.2) and strip-yield model (proposed by Dugdale) as Eq. (2.6).

$$\delta = \frac{K^2}{m\sigma_y E} \tag{2.6}$$

It should be noted that the strip-yield model assumes plane stress conditions and a non-hardening material where m is a dimensionless constant ($m = 1$ for plane stress and $m = 2$ for plane strain), σ_y is the yield strength and δ represents the CTOD.

2.3.2.3 J-Integral

The J-integral can be viewed as both an energy parameter as well as a stress intensity factor, which can simply be defined as the energy release rate in a non-linear elastic material that contains flaws or cracks (*Anderson 2005*). J-integral was developed by James Rice (*Rice 1968*), who showed that a line integral around the crack tip can be used to define the non-linearity experienced in an elastic material. As discussed in section 2.3.2.1, where the energy release rate G holds for a linear-elastic condition, J-integral was seen as an equivalent to the energy release rate for non-linear elastic materials and the same definition holds, only that G is replaced by J to describe the non-linearity in elastic materials. Also, it should be noted that the energy release rate is defined in terms of the crack area and not crack length, as presented in Eq. (2.7).

$$J = -\frac{d\Pi}{dA} \tag{2.7}$$

The similarity between J and G means there is a unique relationship between stress intensity factor (K) and J for linear-elastic scenario. The expression in Eq. (2.4) when G is replaced by J can then be rewritten as Eq. (2.8)

$$J = \frac{K^2}{E} \tag{2.8}$$

Therefore, relating Eq. (2.6) and Eq. (2.8) to give Eq. (2.9) means *J*-integral and CTOD can be linearly related in elastic-plastic conditions.

$$J = m\sigma_y\delta \qquad\qquad\qquad (2.9)$$

It is worth pointing out that in order to fulfil the research purpose, *J*-integral and CTOD have been employed as the fracture toughness parameters for characterising the fracture behaviour of the HSS under consideration at both the quasi-static and elevated loading rates with emphasis on *J*-integral. This is because the materials (S690QL and S960QL) show an elastic-plastic behaviour, and the use of stress intensity factor (*K*) is not appropriate to evaluate the material resistance as mentioned in section 2.3.2.1.

2.3.3 *Fracture toughness testing methods*

The fracture toughness test methodology in structural analysis or engineering application uses different well-established types of fracture mechanics test coupons to determine a fracture toughness value or material resistance. This concept is used to define the material property against deformation, damage or total collapse in the presence of a crack under applied load.

The specimens are designed to simulate the same crack tip constraint a structural member might be subjected to in a real scenario through fatigue pre-cracking to introduce sharp crack/notch after Electron Discharge Machining (EDM) notching. During testing, the material resistance or behaviour is studied to analyse the critical toughness values above which deformation or failure could occur. The testing method(s) to be used for each material grade will depend on a set of results or information needed for analysis and characterisation where the behaviour of most metallic materials is described by three factors, the fracture behaviour, the strength and deformation behaviour with constraint effect of the geometry (*Zhu and Joyce 2012*).

The commonly used fracture toughness test specimens are single edge notched bend (SENB), compact tension (CT) and single edge notch tension (SENT) specimens. For the purpose of this research, SENB test specimens are preferred to SENT and CT because of the higher crack tip constraint they provide over SENT (i.e. conservative fracture toughness); and ease of machining and testing over CT. The standard SENB specimen is a notched bar taken from a steel material and tested in a three-point bending. Its configuration has three main characteristic dimensions, crack length (*a*), thickness (*B*) and width (*W*), with standard test span of 4*W* as shown in **Figure 2.9**.

Usually, the thickness (*B*) is the full thickness of the as received material, and (*W*) is the dimension in the direction of the notch. Before testing, the specimens are fatigue pre-cracked from a machined notch whose depth varies with testing standards but is typically a depth of half the specimen width. Most importantly, the orientation and location of the notch is an important factor to take into account owing to the fact that microstructure and mechanical properties of engineering materials are often sensitive to direction, especially during fracture toughness measurement of weld material. Specifically, the orientation of the specimen's notch should match the flaw being assessed. During the test, the load-point displacement and/or crack mouth opening are measured for the estimation of fracture toughness values using the fracture toughness parameters earlier discussed.

SENT test specimens are often preferred in the pipeline industry due to the lower crack tip constraint, and consequently higher values of fracture toughness (*Moore 2015*). The design of CT test specimens on the other hand is similar to that of SENBs because it has three main characteristic dimensions (*B, W, a*) as SENB, **Figure 2.10**. It would be worth noting that even though it consumes less material than SENB, it is more expensive to machine and complex to test because of the requirement of higher testing machine capacity (*Moore 2015*). Moreover, even though CT is always loaded in tension, the crack tip condition is always bending, and this gives a high constraint factor, where it experiences up to 80% bending load and 15% tension load (*Wallin 2011*).
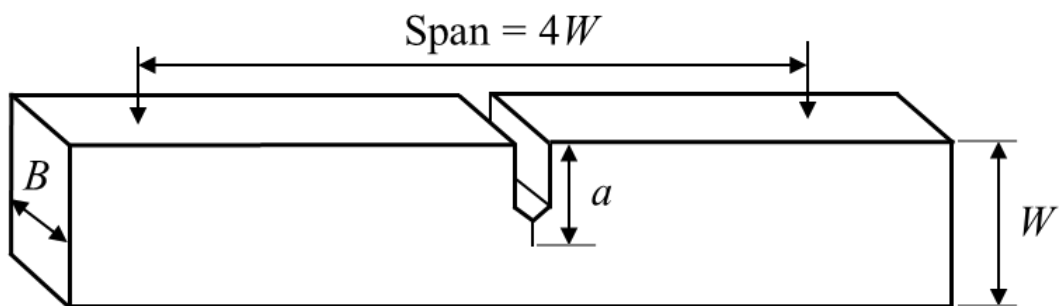
Figure 2.9   Standardised single edge notched bend (SENB) test specimen
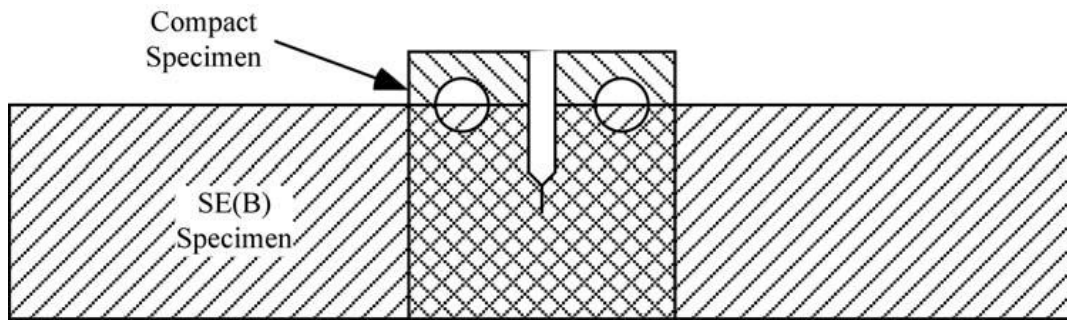
Figure 2.10   Profiles of SENB and CT specimens with same in-plane characteristic dimensions (*W, a*)

2.3.4   Fracture toughness test standards

So far, the experimental methods and techniques used to generate characterisation data of fracture behaviour have successfully contributed to the advancement of fracture mechanics as an engineering discipline in assessing the structural integrity of an asset. It has helped to determine how a crack initiates, propagates, and also to investigate the fracture behaviour of each structural member whether brittle or ductile in nature. Various standards are available for the standardisation of these procedures, discussed as follows.

2.3.4.1 ASTM

The American Society for Testing and Materials (ASTM) standard is one of the most widely used fracture toughness test standards in the world and has evolved continually as technology advances. The first of its fracture toughness test standards is ASTM E399, which was developed to determine plane strain fracture toughness K_{IC} of metallic materials under predominantly linear-elastic conditions (*ASTM E299 2013*). Due to the limitation of ASTM E399 for elastic-plastic conditions, ASTM E1820 was developed to cater for elastic-plastic fracture toughness measurements.

ASTM E1820 is a more generalised standard for the measurement of *K*, CTOD and *J*-integral fracture toughness parameters. Other ASTM standards that have evolved include ASTM E1921, which helps to define fracture toughness parameters based on transition curve for ferritic steels using a Master Curve approach to determine a reference temperature T_0. ASTM E1290 was essentially developed to evaluate CTOD parameter but has now been withdrawn (*Zhu and Joyce 2012*). Another important standard developed by ASTM is the ASTM STP1130

(Rapid Load Fracture Testing), which originated from the need to develop standards to determine fracture toughness under rapid load conditions (*ASTM STP1130 1992*).

2.3.4.2 BSI

The British Standard Institution (BSI) is another standard organization whose standards are widely used in the UK, Europe and worldwide. The first of its fracture toughness test standards was BS 6729, later replaced by BS 7448 (*Wiesner and MacGillivray 1999*). BS 7448 standard is divided into four parts, and gives procedures for fracture toughness testing at quasi-static and dynamic loading conditions for metallic materials to determine both single point toughness and tearing resistance curves. Part 2 is for weld materials which is now superseded by ISO 15653. The part 3 which has been used in this research, extended the procedures for determining fracture toughness of metallic materials from rates of increase in stress intensity factor of up to 2.5 MPa$\sqrt{m}$s^{-1} at quasi-static, up to 3000 MPa$\sqrt{m}$s^{-1} for dynamic loading conditions, corresponding to machine crosshead rates of about 0.02 to 100 mm/s respectively (*Wiesner and MacGillivray 1999; Zhou 2007*).

2.3.4.3 ISO

The main International Standard Organization (ISO) test method is ISO 12135, the generalised testing standard which is the ISO equivalent of ASTM E1820. BS EN ISO 15653 is the fracture toughness standard developed for weld testing and its development was based on BS 7448: Part 2 which it supersedes. The standard gives detailed procedures for determining fracture toughness of welds and detailed guidance on specimen configuration, especially how to prepare notch weld fracture toughness specimen but builds on ISO 12135 (*Moore 2015*). Another important standard relevant to this study is the BS ISO 26843, which is a standard to measure fracture toughness at impact loading rates using pre-cracked Charpy-type test pieces (*BS ISO 26843 2015*).

Overall, the use of a fracture toughness test standard depends on individual perspective and client requirements as there are only a few distinctions between these standards. ASTM is often preferred for use by ASME, because it gives lower values of CTOD compared to ISO or BS methods, which are normally preferred in the UK and Europe, especially in the oil and gas industry (*Moore 2015*).

2.3.5 Tensile properties

The common and perhaps the well-established method to quantify the mechanical response of ferritic steel in terms of strength is the tensile test. Results from these tests have been used to select steel grades for different engineering applications over the years. Also, tensile tests have been used to successfully predict the mechanical behaviour of materials under any form of loading which have made the test an important part of engineering development, design and application (*Davis 2004*).

The characteristic stress-strain curve of a ductile material, **Figure 2.11**, has two main parts – the elastic and plastic regions. Since yield strength of ferritic steel is often the primary concern, the linear-elastic region helps to predict the mechanical response of a steel grade under applied loads without losing its original shape or form. This term is called the elastic deformation, whereas the plastic deformation occurs immediately after yielding. The point at which ferritic steel does not recover its original form when load is removed is the first point at which plastic deformation begins. However, the stress at which plastic deformation starts depends on how accurately the strain is measured at small strain (*Davis 2004*).

In order to avoid discrepancies in measurement, 0.2% offset stress has been adopted to describe the onset of plasticity as a measure of the yield strength of a particular steel grade by constructing a straight line parallel to the linear portion of the stress-strain curve. The test standards used to carry out the tests are mentioned in chapter 3.
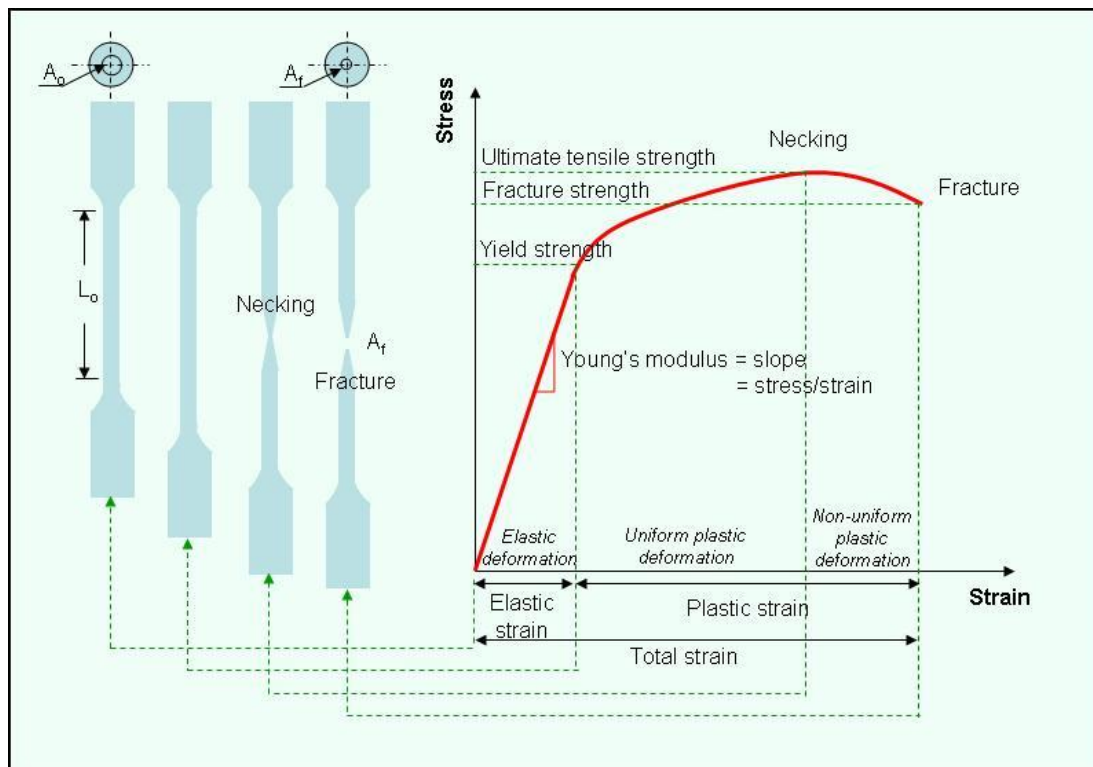
Figure 2.11   Stress-strain relationship under uniaxial tensile loading (*Faridmehr et al. 2014*)

2.4   Loading Rate

2.4.1   *Overview*

The effect of loading rates is generally known to affect the mechanical properties, especially the tensile properties and the fracture toughness of most ferritic steels (*Wiesner and MacGillivray 1999*). The loading rate effect on the mechanical properties of steel is predicted to be specifically dependent on a particular steel grade, with the sensitivity depending on the nominal yield strength (*HSE 1999; Wallin 2011*). Loading rate affects steel resistance and its structural response, which makes it very important to characterise a particular steel grade behaviour against the in-service loading conditions.

The degree of sensitivity, however, differs with LSS showing a high rate of sensitivity when compared to quenched and tempered high strength low alloyed (HSLA) steels, which are relatively unaffected (*Francis et al. 1978*). Typical examples of engineering loading rates which serve as the basis for the loading rates considered in this research expressed in terms of strain rate and stress intensity factor loading rate are given in Table 2.4. These values are taken

from the information given by (*Wiesner and MacGillivray 1999; Burdekin et al. 2004; Walters and Przydatek 2014*), and should be used as estimates only since the exact values will depend largely on loading configuration, local geometry, and flaw dimensions.

The effect of loading rate on the fracture toughness is more sensitive to temperature and the rate of change of the crack tip stress intensity factor loading rate ($\dot{K}$) rather than the overall strain rate ($\dot{\varepsilon}$) of the material in a cracked component (*Francis et al. 1978*). It is important to mention that whilst the fracture mechanical loading rate is mostly approximated and expressed in terms of stress intensity factor loading rate for linear elastic conditions, the loading rates in structural engineering are usually considered in terms of strain rates. The use of the strain rate to determine a single effective loading rate value in a cracked specimen could lead to a crude estimation in a real scenario (*Wallin 2011*). Hence, the use of stress intensity factor loading rate as a means of expressing fracture mechanical loading rate. However, a relationship exists between $\dot{K}$ *and* $\dot{\varepsilon}$, Eq. (2.10), for a cracked component within the elastic region just outside of the crack tip plastic zone (*Burdekin et al. 2004*).

$$\dot{\varepsilon} = \frac{2\sigma_y \, \dot{K}}{E \, K} \qquad\qquad (2.10)$$

During high loading conditions, the effects of material inertia and strain rate sensitivity play an important role in the fracture behaviour of the material, which varies largely from that obtained under quasi-static conditions (*Xu and Li 2011*). In the transition region, inertia effect (the imbalance created by high loading between internal and external forces when increased to the internal temperature is partly contributed by external forces) dominates fracture behaviour and beyond that, inertia effects can be ignored (*Johnson and Cook 1983*). That is, at the transition region, transition time can be used to identify if the fracture behaviour of materials is dynamic or quasi-static in nature (*Xu and Li 2011*). A schematic representation of the effect of loading rates on the strength and fracture behaviour of ferritic steel is presented in **Figure 2.12**.

Table 2.4   Typical strain rates in some engineering components (*Wiesner and MacGillivray 1999; Burdekin et al. 2004; Walters and Przydatek 2014*)

Applications	Strain Rate, $\dot{\varepsilon}$ (s^{-1})	Stress Intensity Factor Loading Rate, $\dot{K}$ (MPa√m/s)
Storage tanks, buried pipelines, pressure vessels	10^{-6} to 10^{-4}	10^{-2} to 1
Self-weight, wind and wave loading	10^{-4} to 10^{-2}	1 to 10
Bridges, cranes and earthmoving	10^{-2} to 0.1	10 to 10^3
Earthquake loading and marine collision	0.1 to 10	100 to 10^4
Land transport and aircraft undercarriage	10 to 1000	10^3 to 10^6
Explosion and ballistics	10^4 to 10^{6+}	10^7 to 10^{10+}

Figure 2.12   Schematic representation of the sources of loading rate effect on the tensile and fracture toughness properties.

2.4.2 Effect of loading rate on the tensile behaviour of ferritic steel

Since loading rates in structural engineering are usually considered in terms of strain rates (section 2.4.1), the effect of loading rate during tensile testing is mostly expressed by strain rate. This is so because the stress-strain distributions during tension tests are uniform and the induced plasticity adiabatic heating occurs uniformly (*Wallin 2011*), unlike the non-uniformity of stress-strain distributions which varies largely in front of the crack tip due to the presence of crack during fracture toughness tests. Owing to this fact, it is better to express the effect of loading rate in terms of strain rate during a tension test of an unnotched specimen.

The major strain rate effect on the tensile properties of steel is the amplification of the yield and tensile strengths, considered as a positive strain rate dependence (*Wiesner and MacGillivray 1999*) which comes mainly from material strengthening (*Wallin 2011*). On the other hand, the increment could result in a shift in the ductile-to-brittle transition curve (DBTC), leading to a reduced fracture toughness value at the lower shelf as a result of material strengthening during high strain rate conditions. This is considered as a negative strain rate dependence (*Wiesner and MacGillivray 1999; Wallin 2011*). The behaviour of carbon steels at high strain rates shows that both the upper and lower yield stresses and strains increase with increasing strain rates (*HSE report 1999*). However, the ultimate stress and strain are less sensitive at high strain rates, whereas the strain at the initiation of strain-hardening is seen as the most sensitive parameter to the effect of strain rate, **Figure 2.13** (*HSE report 1999*).

On the degree of sensitivity to the effect of strain rate on the yield strength, the results reported by the Steel Construction Institute (*HSE report 2001*) show that strain rate sensitivity is low for high strength grades. The same observation was highlighted by Bomel Ltd (*HSE report 1999*). It was observed that higher steel grades with nominal yield strength between 560 MPa and 690 MPa have their lower yield strength properties reduced by less than 10% when compared to lower steel grades with yield strength between 300 MPa and 380 MPa with an increase in the lower yield strength of up to 20-30% at the same 10^{-1} s^{-1} strain rate. This is because when nominal yield strength of steel increases, the strain rate effect on the yield strength becomes less significant as compared to lower yield strength steel grades, shown in **Figure 2.14**. In **Figure 2.14**, A36 represent the ASTM steel grade with nominal yield strength of 250 MPa, and A514 is the quenched and tempered ASTM grade with nominal yield strength of approximately 760 MPa (*HSE report 2001*) which is similar to the steel grade under consideration in this research.
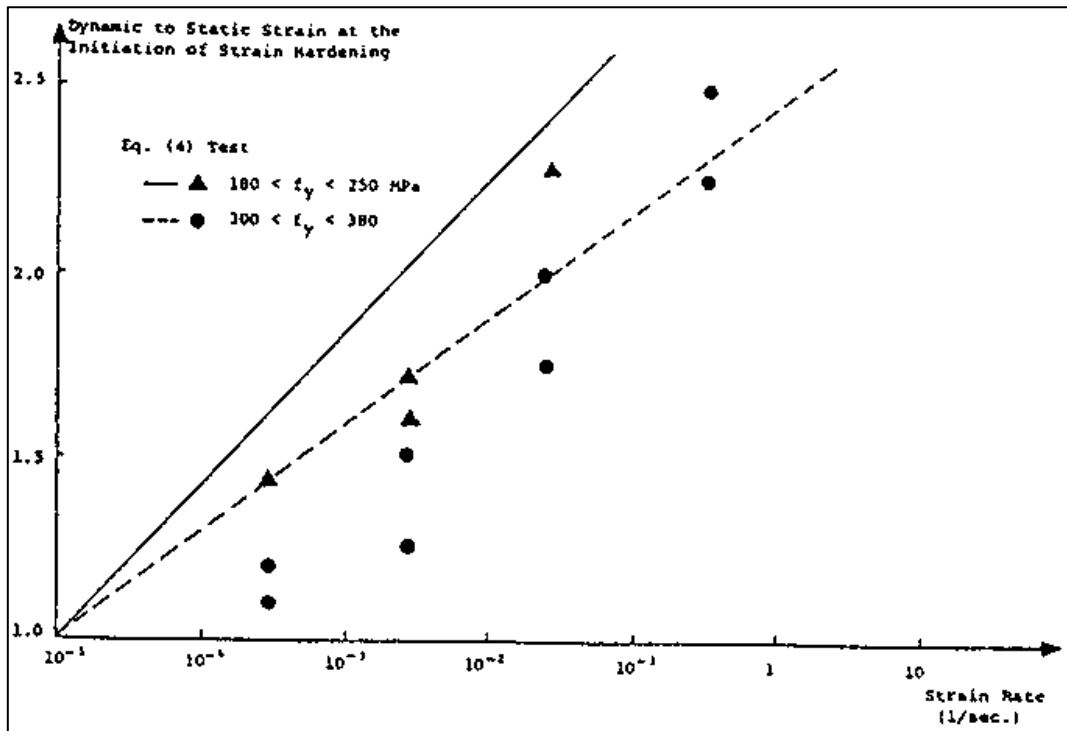
Figure 2.13   Effect of strain rates on strain at the initiation of strain hardening for steels at different yield strengths (*HSE report 1999*).
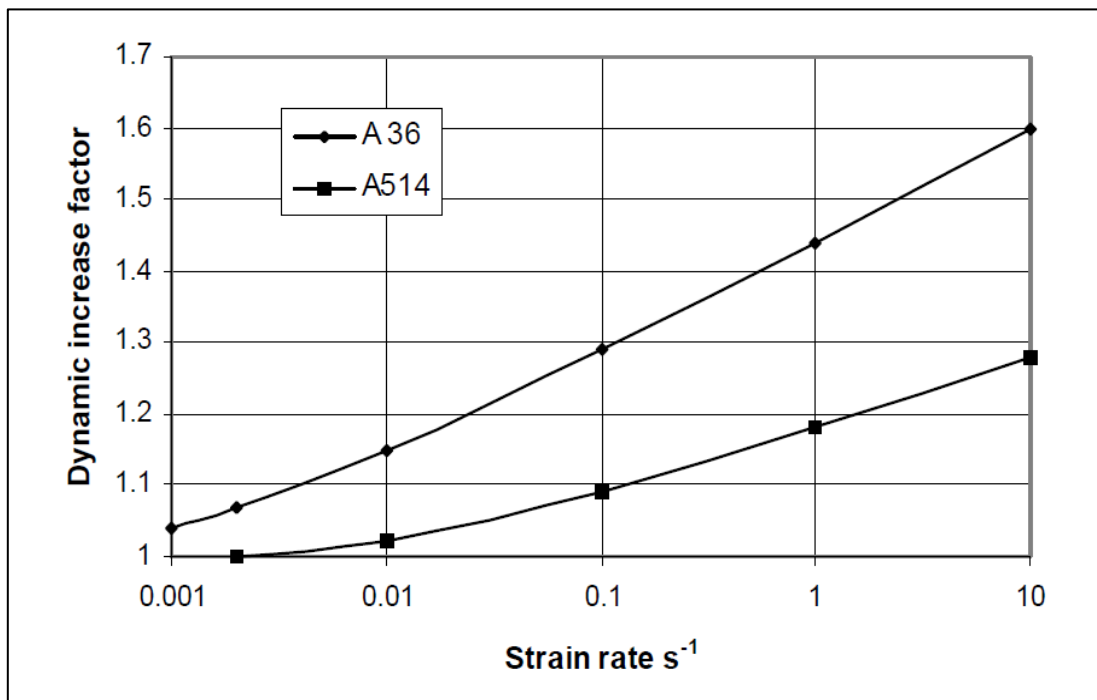
Figure 2.14   Dynamic increase factor on the yield strength of low (A36) and high strength steel (A514) versus strain rate (*HSE report 2001*)

An important aspect of the effect of strain rate on the tensile properties of ferritic steels is the temperature dependence. The effect of high strain rate and consequently, the dynamic amplification on yield strength is temperature dependent, being increased at lower temperature (*NagarajaRao et al. 1966; Campbell and Ferguson 1970; Priest 1977; Francis et al. 1978; Wiesner and MacGillivray 1999; HSE report 1999; HSE report 2001; Breuk 2003; Burdekin et al. 2004; Wallin 2011; Choung et al. 2013;Walters and Przydatek 2014*). For instance, the expression on the right-hand side of Eq. (2.11) (*Burdekin et al. 2004*), shows the temperature dependency on nominal yield strength due to high loading rates.

$$\sigma_{ys}(T, \dot{\varepsilon}) = \sigma_o + S\left\{\frac{1}{T}\frac{\ln\left(A/\dot{\varepsilon}_{static}\right)}{\ln\left(A/\dot{\varepsilon}\right)} - \frac{1}{293}\right\} \qquad (2.11)$$

where, σ_{ys} is the yield strength at temperature (T) and strain rate ($\dot{\varepsilon}$), σ_0 is the quasi-static yield strength at room temperature (T = 293K) under quasi-static loading, $\dot{\varepsilon}_{static}$ is the quasi-static strain rate taken as 5×10^{-5} s^{-1}, S is a parameter to be fitted using test data and A is a material constant. Typical value for A is taken as 10^8 and value for S can be taken as 60000 ±1000 MPaK for a wide range of ferritic steels in the absence of test data valid for temperatures below ambient and strain rate up to 1000 s^{-1}.

A typical example of the effect of increasing strain rate on a full stress-strain curves is illustrated in **Figure 2.15** for a 20 Mn Mo Ni 55 pressure vessel steel. From the figure, higher stress-strain curves were observed as the strain rates increase, and as a result of the amplification, an increased susceptibility to the formation of upper yield strength behaviour is noticed (*Wiesner and MacGillivray 1999*). Whether this trend will be noticed for the steel grades under consideration is a point of discussion in this research.
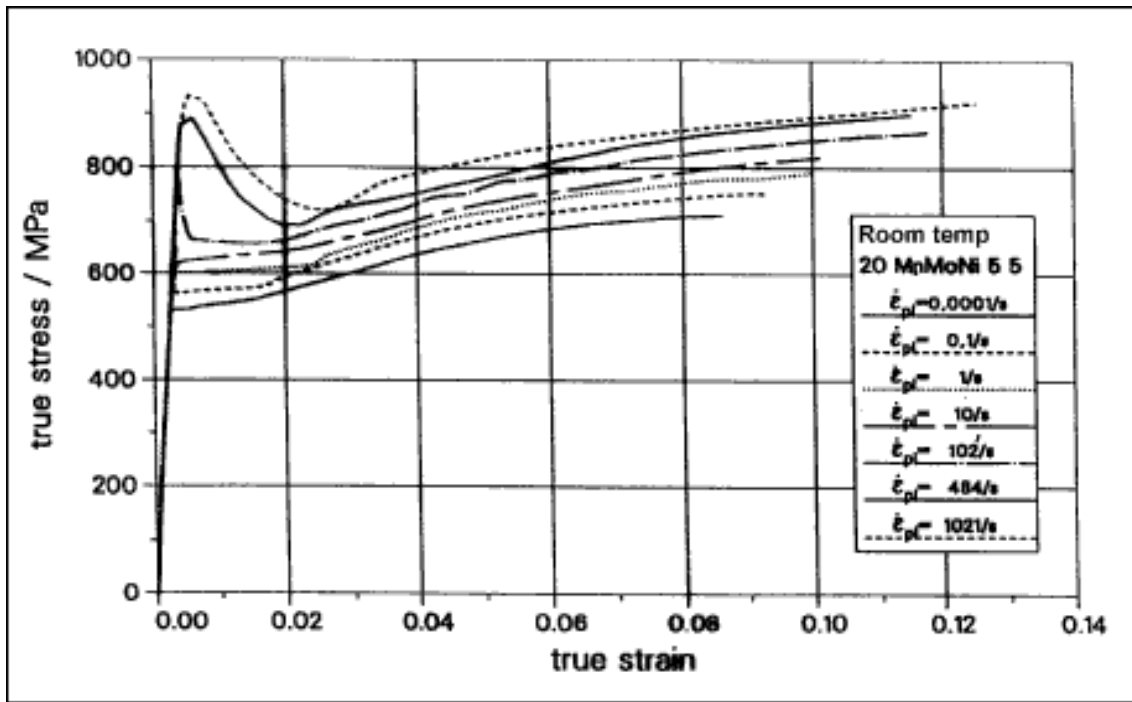
Figure 2.15   ESIS Round-Robin dynamic stress-strain curves (*Wiesner and MacGillivray 1999*)

Also, the earlier work by the Steel Structure Committee (SSC 275) (*Francis et al. 1978*) on ship steels with yield strengths ranging from 275 MPa to 690 MPa further illustrated the effect of strain rate and temperature on nominal yield strength of these steels. The work showed how the yield strength of a particular ferritic steel grade under high strain rate is linearly related to the logarithm of the strain rate and inversely proportional to the absolute temperature as expressed in Eq. (2.12). The dynamic yield strength was observed to be equal to the static yield strength plus a factor which causes an increase (or decrease) in the tensile properties called the dynamic over stress. The dynamic over stress is temperature dependent and implies that at low temperature, the dynamic over stress increases owing to the effects of strain rate but decreases with thermal softening at high temperature.

$$\sigma_{yd} = \sigma_y\,(T, \dot{\varepsilon}) \approx \frac{\ln(\dot{\varepsilon})}{T} \qquad\qquad (2.12)$$

This is explained by the mechanism of thermal activation of dislocations over short-range barriers (*Campbell and Ferguson 1970; Burdekin et al. 2004*). Since a dislocation is obstructed in its movement by the interstitial atoms (such as, carbon, nitrogen, boron or hydrogen) or grain boundaries in steel, it means that a higher force is required to overcome this obstruction. A stress (flow stress) is required to sustain plastic deformation by moving dislocations via both

63

short and long-range barriers, with its magnitude depending on the temperature (*Burdekin et al. 2004*).

Over short-range barriers, there exists an initial stress large enough to enable dislocations to move past these barriers without the aid of thermal fluctuations associated with yield stress at absolute zero temperature. It follows that at stresses greater than the initial stress, the barriers are ineffective, and the strain rate is then controlled by a different mechanism (dissipative mechanism), such as the interaction of dislocations with electrical and thermal waves in the crystal lattice (*Campbell and Ferguson 1970*). If deformation is thermally activated as shown in **Figure 2.16**, the effective stress σ^* is strain rate and temperature dependent due to short-range barriers that can be cut or passed by thermal activation, which is characterised by activation enthalpy, Eq. (2.13) (*Burdekin et al. 2004*).
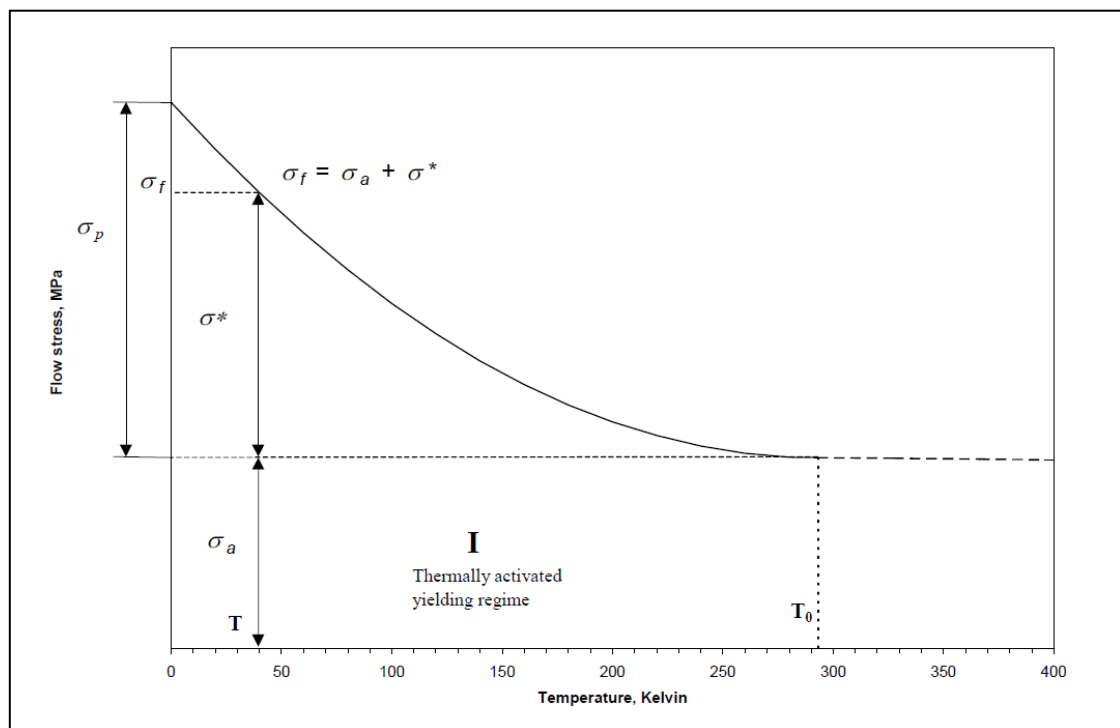
Figure 2.16   Flow stress partitions of an effective stress and internal stress with temperature of interest less than 300 K (*Burdekin et al. 2004*).

The value of flow stress can therefore be characterised varying from a maximum value $(\sigma_p + \sigma_a)$ to an athermal internal stress value σ_a at temperature T_0. At athermal (long range barriers) condition, the increased amplitude of atomic thermal vibrations produces an effective vibration of the dislocation line, and this permits it to cut through barriers that could not be bypassed by the stress alone, and, thus σ_a is not temperature or strain rate sensitive (*Burdekin et al. 2004*).

64

Since effective stress is a function of activation enthalpy, it follows that, from Eq. (2.14), flow stress as a function of strain rate and temperature can therefore be written as Eq. (2.15).

$$H = kT \ln(A/\dot{\varepsilon}) \tag{2.13}$$

$$\sigma^* = \sigma_p \left(1 - \frac{H}{H_0}\right)^{\frac{1}{1-m}} \tag{2.14}$$

$$\sigma_f = \sigma_a + \sigma_p \left\{1 - \frac{kT \ln(A/\dot{\varepsilon})}{H_0}\right\}^{\frac{1}{1-m}} \tag{2.15}$$

where, H = activation enthalpy

H_0 = the activation enthalpy associated with local barriers in Joules

σ_f = flow stress (MPa)

σ_a = internal stress (MPa)

σ_p = the Peierls stress at T=0, K

k = the gas constant, 1.38E^{-23} JK^{-1}

m = is an integer

It is important to mention that temperature rise is inherent at high strain rates owing to the short time available to conduct the heat generated during plastic work deformation in which there is no significant local heat exchange with the environment (adiabatic effect). Whereas, at low or quasi-static strain rates, the heat conduction time increases and thus, operates solely on a non-adiabatic condition because of the available time for heat conduction, leading to a lower rise in temperature (*Breuk 2003*). Considering this fact, the strength model developed by Johnson-Cook (*Johnson and Cook 1983, 1985*) shows that in all cases (strain rates at 1 s^{-1}, 10 s^{-1}, and 100 s^{-1}), the adiabatic stress-strain curve increases to a maximum and then decreases with

increasing strain. At strain rates beyond approximately 0.1 s^{-1}, adiabatic deformation dominates (*Breuk 2003*).

In summary, the effect of loading rates on the tensile properties of ferritic steel is predicted to be material dependent which is associated with the manufacturing process, chemical composition, thickness and microstructure. The degree of sensitivity, however, decreases as the nominal yield strength increases with low alloyed HSS relatively unaffected by the effect of strain rate (*Francis et al. 1978*).

2.4.3 *Influence of loading rate on the fracture behaviour of ferritic steel*

Often, an understanding of the fracture behaviour of steel during experimental testing at different loading regimes helps to prevent some of the potential catastrophic accidents during in-service conditions. It is, therefore, imperative to ascertain the influence of loading rates on the fracture toughness of ferritic steel. A single fracture toughness value (critical value) is assumed to control the fracture behaviour of a material (*Wallin 2011*). The value describes the crack initiation and subsequent propagation behaviour of the material (the driving force and the material resistance). The driving force is a function of material flaw size and loading conditions, while the material resistance is the ability of the material to resist propagation of these flaws or cracks. From study (*Bannister and Trail 1996*), strain-hardening exponent (*n*) influences fracture toughness where crack opening is enhanced by a high Y/T ratio and, hence, low strain-hardening capacity (*Bannister 1999*).

The effect of loading rates on the fracture behaviour of ferritic steel comes mainly from the material strengthening and adiabatic heating in the plastic region in front of the crack (*Wallin 2011*), schematically represented in Figure 2.12. Since fracture behaviour has a close relationship with plastic deformation behaviour of material near the crack tip, **Figure 2.17**, cleavage fracture toughness is significantly affected by material strengthening because of the increasing effect on yield and ultimate strengths (*Wallin 2011*). In some cases, ductile fracture is considered to have a positive rate dependence with an enhancement of dynamic ductile fracture toughness, however this factor is considered negligible when performing structural analysis (*Walters and Przydatek 2014*). Cleavage fracture toughness of ferritic steels generally reduces in value with increasing loading rate (a negative rate dependence) (*Wiesner and MacGillivray 1999, Wallin 2011*).

The mechanism of brittle fracture is mainly controlled by the stress state in front of the crack, and less affected by adiabatic heating because its initiation is in the region of high stresses where the plastic strains are relatively small, further away from the crack tip (*Wallin 2011*). This implies that the yield strength and strain-hardening properties of ferritic steel have an effect on the cleavage fracture toughness resistance. Mechanistically, the reduction in cleavage fracture toughness is associated with the increase in yield strength at high loading rates, which elevates the crack tip stresses such that the critical conditions in the crack tip region are reached at lower levels of remote load than under static conditions (*Wiesner and MacGillivray 1999*).
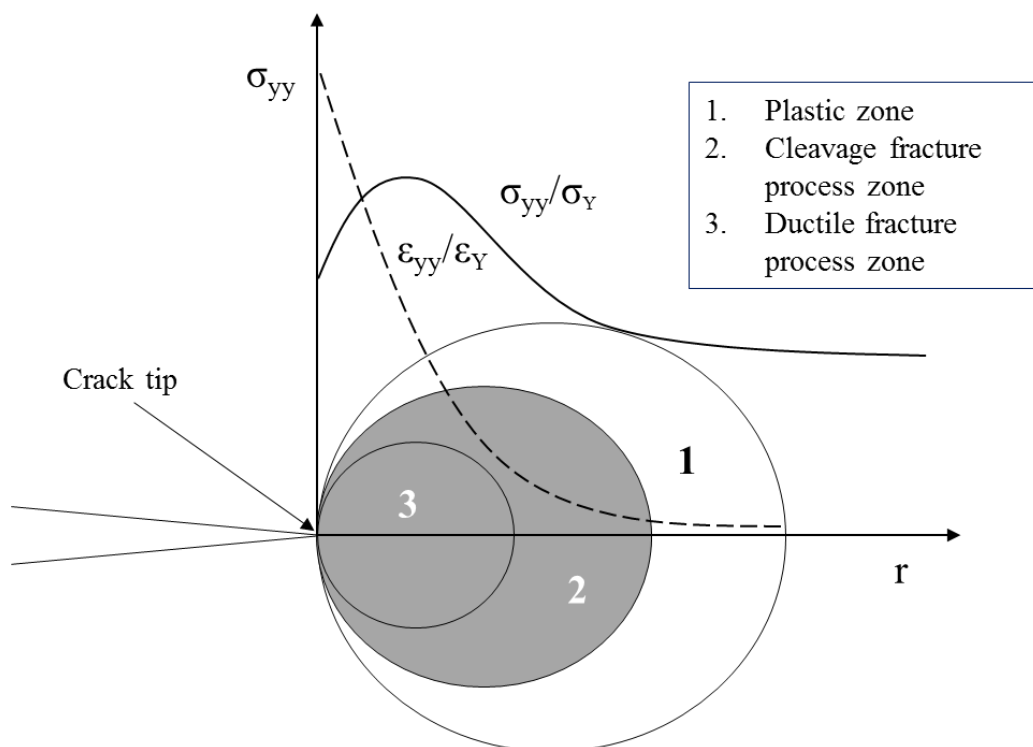
Figure 2.17   Schematic representation of different fracture process zone sizes (*Anderson 2005; Wallin 2011*)

A significant impact may be experienced on the ductile-to-brittle-transition curve where a cleavage fracture toughness value may drop up to 80% from the measured toughness at quasi-static conditions. The effect of loading rates on the difference in the dynamic and quasi-static fracture toughness values for a ferritic steel relies mainly on the material's deformation properties, and the brittle fracture process remaining the same, but the difference in fracture toughness predicted to be material dependent (*Wallin 2011*).

Thus, the effect of loading rate must be accounted for in the estimation of cleavage fracture toughness resistance of high strength structural steel (HSS) with high Y/T ratio above 0.90. The one common effect of loading rate on the fracture toughness of most ferritic steels is the change in the transition temperature with a shift to a higher fracture transition temperature (Francis *et al. 1978; Wiesner and MacGillivray 1999; HSE report, OTO 1999; Burdekin et al. 2004; Wallin 2011; Walters and Przydatek 2014; Gotoh 2015*). The extent of the shift is, however, highly dependent on the strength level of the steel grade (*Wiesner and MacGillivray 1999; HSE report, OTO 1999*). Perhaps this is one of the reasons why toughness requirements must be adjusted accordingly, in respect to the yield strength of the steel for normal or extreme loading conditions (*Shoemaker 1981*).

The effect of high loading rate is more pronounced for the lower strength steel grade, whereas, high strength steel exhibits a lower loading rate sensitivity depicted by the shift in temperature (*Wiesner and MacGillivray 1999*). It is important to mention that increasing loading rate may not necessarily mean an increase in ductile toughness at the upper shelf (*Wiesner and MacGillivray 1999*). A low Y/T ratio could lead to a decrease in ductile initiation than those observed at quasi-static condition, like the ferritic carbon steel pipe (typically A106 Grade B or A333 Grade 6) reported by (*Wiesner and MacGillivray 1999*).

The general trend shows that the effect of loading rate on the fracture toughness of ferritic steels was more concerned on defining the fracture transition temperature shift ΔT to a higher temperature value using an empirical approach, **Figure 2.18,** where there is a possibility of cleavage fracture toughness reduction at high loading rate on the ductile-to-brittle transition curve (DBTC) (*Burdekin et al. 2004*). The upper region of the curve means that the materials exhibit an elastic-plastic behaviour with ductile mode of failures, whereas the lower shelf indicates a brittle mode of failure with a possible reduction at elevated loading rate. As such, the approach is more concerned with the lower transition region and lower shelf of the curve.

Hence, the introduction of a statistical method to describe the fracture characteristics in the transition region based on the reference transition temperature T_0, called the Master Curve (*Wallin and Mahidhara 1997*). This forms the basis and background upon which the ASTM 1921 testing standard (*ASTM 1921-15a$^{\varepsilon 1}$*) was based. The concept has been applied to a wide range of yield strengths from 200 to 1000 MPa to predict ΔT_0, Eq. (2.16), as a result of loading rate induced temperature shift (*Wallin and Mahidhara 1997*).

68

$$\Delta T_0 = \frac{T_0 \cdot \ln(\dot{K}_I)}{\Gamma - \ln(\dot{K}_I)} \tag{2.16}$$

The function Γ is the loading rate effect fitting parameter given in Eq. (2.17), and $\dot{K}_I$ is the average loading rate of the elevated rate tests.

$$\Gamma = 9.9 \cdot exp\left[\left(\frac{T_0 + 273.15}{190}\right)^{1.66} + \left(\frac{\sigma_y^{T_0}}{722}\right)^{1.09}\right] \tag{2.17}$$
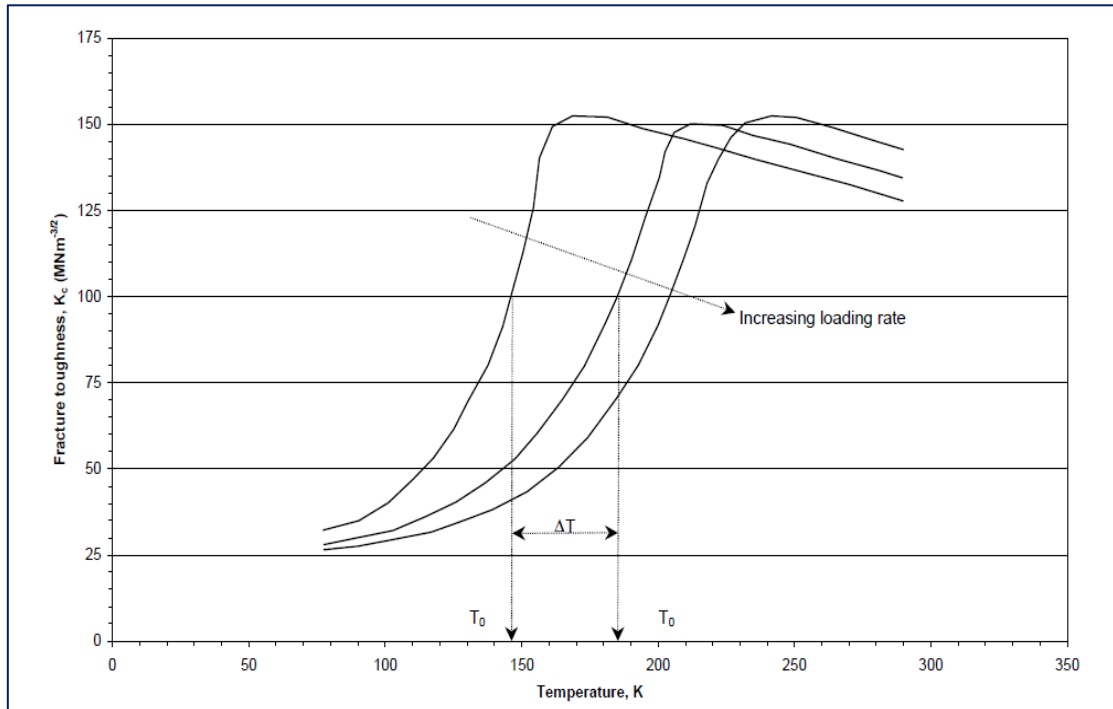
Figure 2.18   General trends of strain rate effects on fracture toughness transition curve of ferritic steels (*Burdekin et al. 2004*).

2.4.4   *Effect of strain rate on weldments*

One of the most important factors considered for improved mechanical properties of HSS is the weldability. An effective way of joining steel plates together by welding without formation of flaws is very important to offshore applications. However, high loading rates could have a huge impact on the structural response of welded components. Therefore, there is a need to consider the effect of dynamic loading around the weld regions. Investigations carried out (*HSE report 1999*) on the effect of high strain rate on weldments (typical ship weld material) indicated a decrease in toughness with decreasing test temperature.

The observations on the review done on weld materials with strength range 400-800 MPa suggested that there is a significant reduction in toughness with increasing loading rates, more pronounced in the temperature region between -20 °C and +20 °C, which is the typical design temperature range for many marine structures (*HSE report 1999*). Also, increased strain rates or decreased test temperatures cause the yield strength of the weld material to increase. This is similar to the effect of strain rate and temperature on mild steel tensile properties investigated by the Steel Construction Institute (*HSE report 2001*), where high loading rates increased the tensile properties and it was observed that the tensile properties of weld material were significantly higher than that of parent materials. Although there is a similar effect of strain rate on tensile properties with that of parent materials, overall, the prediction of these effects on weldments had been inexact (*HSE report 2001*).

2.5   Knowledge gap

High strength structural steel (HSS) with yield strength >690 MPa in selected part of structures for offshore applications have demonstrated the potential benefits of weight reduction opportunities of up to 50%, allowing for many cost and performance advantages emerging from the use of high performance steel grade towards offshore, marine and energy segments where reliability is important. To maximise these benefits and increase the usage of HSS in the offshore, marine and energy industries, appropriate understanding of the possible mechanical or structural response in terms of strength and fracture toughness at critical loading rates, and low temperature needs to be available in line with what is known about LSS.

After describing the requirements of Y/T ratios in accordance with design codes and regions, which most modern HSS do not meet, and the structural implication of the Y/T ratio on the strength and fracture behaviour where there is tendency of an enhanced crack tip opening behaviour when Y/T ratio is in excess of 0.90, it was found that more emphasis has been placed on the strength parameter more often for building and bridge constructions other than offshore applications.

In order to complement the existing literature and to provide understanding to the fracture behaviour of HSS with high Y/T ratios >0.90 representative of offshore and marine in-service loading condition (such as those given in **Table 2.4** where there is a chance of reduced ductility at dynamic loading rates), this thesis reports a perspective combining the strength and fracture toughness properties of modern HSS under high loading rates applicable to offshore scenarios

left unexplored from the past researches. *J*-integral is considered as the fracture toughness parameter in this thesis because of its robustness theoretically and ease of calculation to determine crack driving force numerically for structural assessments. However, the measured CTOD values for S690QL and S960QL are summarised in the appendix for information purpose.

Since the degree of sensitivity to the effect of loading rates on low strength carbon steels is high compared to quenched and tempered and High Strength Low Alloyed (HSLA) steels (similar to the grade under consideration), which are relatively unaffected as reported in the literature, a comprehensive experimental programme (tension and fracture toughness tests) at different loading rates was designed for the purpose, and it is supported by finite element analysis.

In addition, in order to overcome crude estimation in a real scenario as reported in the literature by the use of strain rate to determine a single effective loading rate value in a cracked specimen, stress intensity factor loading rate for linear elastic conditions has been employed for the fracture toughness tests using SENB test specimens. For the tensile tests, loading rate is expressed in terms of strain rate in this thesis for the HSS grades under consideration. The present research work is expected to be useful for offshore users as well as to serve as basis to how actual mechanical properties of HSS under high loading rates could affect the structural integrity of an asset. This will contribute to understanding the mechanical performance of HSS in design practices with confidence for marine, offshore and energy segments.

Chapter 3   Methodology

3.1   Materials

3.1.1   Overview

In this chapter, the experimental methods used to provide understanding and characterisation data are described based on the knowledge gap identified in chapter 2. The finite element analysis method is also introduced in this chapter. The materials studied are S690QL (WELDOX 700 EZ) and S960QL (WELDOX 960 HZ) with high Y/T ratios of about 0.95. The materials are typical high strength structural steel grades used in offshore applications and supplied by Huisman Equipment, Netherlands from storage. The as-received delivery properties of these steel grades were in accordance with BS10025:6 (*BS EN 10025:6: +A1: 2009*) with the delivery condition in terms of chemical composition from the mill certificate summarised in **Tables 3.1 and 3.2** for S690QL and S960QL, respectively.

These structural steel grades were delivered in quenched and tempered conditions which satisfied the -40 °C or -60 °C minimum impact energy requirement of 27 J in the transverse direction for S690QL and S960QL, respectively. It should be noted that the chemical and microstructural analyses of these materials were carried out to ascertain the chemical compositions given in the mill certificate which is presented and discussed in chapter 4. The steel grade designation for S690QL and S960QL stands for the following:

S = Structural Steel,

690/960 = Minimum Yield Strength (MPa),

Q = Quenching and Tempering (Production process),

L = Low Notch Toughness Testing Temperature (Impact energy at minimum temperature).

Table 3.1   Delivery chemical composition conditions for S690QL from the mill
certificate

Elements	Mass percent (%) (m/m)
Carbon (C)	0.13
Silicon (Si)	0.30
Manganese (Mn)	1.20
Phosphorous (P)	0.009
Sulphur (S)	0.001
Chromium (Cr)	0.25
Molybdenum (Mo)	0.151
Boron (B)	0.001
Aluminium (Al)	0.05
Copper (Cu)	0.01
Niobium (Nb)	0.022
Vanadium (V)	0.031
Nickel (Ni)	0.08
Titanium (Ti)	0.011
Nitrogen (N)	0.003
*EW	0.42
+C14	0.277

*CEV(EW) = C+MN/6+(CR+MO+V)/5+(NI+CU)/15

+C14 = CET = C+(MN+MO)/10+(CR+CU)/20+NI/40

Table 3.2   Delivery chemical composition conditions for S960QL from the mill certificate

Elements	Mass percent (%) (m/m)
Carbon (C)	0.16
Silicon (Si)	0.21
Manganese (Mn)	1.37
Phosphorous (P)	0.009
Sulphur (S)	0.001
Chromium (Cr)	0.25
Molybdenum (Mo)	0.487
Boron (B)	0.002
Aluminium (Al)	0.048
Copper (Cu)	0.01
Niobium (Nb)	0.015
Vanadium (V)	0.02
Nickel (Ni)	0.07
Titanium (Ti)	0.007
Nitrogen (N)	0.002
*EW	0.55

*CEV(EW) = C+MN/6+(CR+MO+V)/5+(NI+CU)/15

3.1.2 S690QL structural steel grade

According to BS10025:6 (*BS EN 10025:6: +A1: 2009*) for S690QL grade, 690 MPa means the minimum yield strength and 940 MPa represents the maximum tensile strength for a nominal thickness ≥ 3 mm and ≤ 50 mm. It means that the nominal yield strength can be increased and, since the production route and/or chemical compositions have less effect on the tensile strength, the production routes, in this case QT (see section 2.2.2), have an incremental effect on the nominal yield strength when there is a need to increase yield strength above the specified

minimum yield strength given in the standard. This process results in a higher Y/T ratio. It should also be noted that the as-received S690QL plate is supplied in 25 mm thickness and the qualification mechanical properties from the mill certificate are given in **Table 3.3**.

Table 3.3   Delivery mechanical property conditions for S690QL from the mill certificate

Elements	Specimen position	Direction	Specimen type	Temp (°C)	Test results
Tensile test	Top end	Transvers	Rectangular		$\sigma_{y(0.2)}$ = 807 MPa, UTS = 841 MPa % Elongation = 17
Impact test	Top end	Transvers	Charpy- V 10 x 10	-40	Average of 226 J
Z-test	Top end		Diameter = 6		Average of 71%

3.1.3   S960QL structural steel grade

Unlike the S690QL grade, the as-received plate condition of S960QL was delivered in 60 mm thickness. The minimum yield strength and the maximum tensile strength for the nominal thickness of >50 mm and ≤100 mm, which corresponds to the delivery condition of S960QL under consideration, is not stated in BS10025:6 (*BS EN 10025:6: +A1: 2009*). However, the minimum yield strength for the nominal thickness ≤ 50 mm is 960 MPa and the maximum tensile strength given is 1150 MPa. The qualification delivery mechanical properties from the mill certificate are summarised in **Table 3.4**.

Table 3.4   Delivery mechanical property conditions for S960QL from the mill certificate

Elements	Specimen position	Direction	Specimen type	Temp (°C)	Test results
Tensile test	Top end	Transvers	Round		$\sigma_{y(0.2)}$ = 928 MPa, UTS = 983 MPa % Elongation = 19

Impact test (1/4 T)	Top end	Transvers	Charpy- V 10 x 10	-60	Average of 157 J
Z-test	Top end		Diameter = 10		Average of 66%

3.2 Experimental study

3.2.1 Overview

The method used to describe the experimental work on the steel grades under consideration is divided into two parts. The first part, which is intended to assess the as-received properties in terms of the chemical and microstructural conditions, is presented and discussed in chapter 4. The second part concerns the approach used to determine tensile and fracture toughness properties at quasi-static and high loading rates in order to characterise the mechanical performance of S690QL and S960QL under possible in-service conditions. This includes tension, fracture toughness and conventional Charpy V-Notch impact tests.

Also, since S960QL was delivered in 60 mm thickness, a hardness traverse through thickness test was performed to study the homogeneity of the material taken 5 mm apart from the top edge to bottom edge. The results of the hardness traverse test are presented in chapter 5.

3.2.2 Tension tests

A program of tensile testing was developed to provide understanding and characterisation data for the two high strength structural steel grades (S690QL and S960QL) under consideration, at a range of loading rates an offshore structure might be subjected to (**Table 2.4**). The data generated at quasi-static conditions were compared with that of low strength structural steel (S235 and S355) with Y/T ratio <0.85 and data from literatures. Tensile properties of S235 were generated at a range of strain rates same as HSS (S690QL and S960QL) under consideration, whereas S355 data was taken from TWI archives for comparison with low strength and high strength steels at quasi-static loading rates.

For the purpose of easy machining, comparison and setup during quasi-static and high loading rate tension tests, flat dog-bone shaped tensile specimens were employed. The choice of a flat dog-bone specimen was informed due to the recommended specimen geometry for the high-

speed dynamic fast jaw grip hydraulic machine. Specimens were prepared from the S690QL and S960QL high strength structural steel plates, with load axis aligned with the rolling direction. The choice of taking the samples in the rolling (parallel) direction was made because it is more conservative (with slightly lower differences in the yield stress) compared to samples taken in the transverse (perpendicular) direction (*Breuk 2003*).

In order to make sure that the collapse load falls within the machine capacity (100 kN), the ratio between the width of the gauge area ($W_a = 8$ mm) and the shoulder width ($W_s = 25$ mm) was set at <0.33. For easy comparison in the change of the mechanical behaviour over a range of strain rates, the aspect ratio (ratio between the width and the 3 mm specimen thickness) was kept constant. The tensile specimen has a constant gauge length of 50 mm and width length of 25 mm for all the tests.

Tests were carried out at crosshead speeds of 0.008 mm/s (quasi-static) and up to 167 mm/s (elevated loading rate) using displacement control method at ambient temperature. This is equivalent to about 0.0002 s^{-1} and 4 s^{-1} strain rates, respectively, calculated after the tests from the measurements taken from the extensometer attached to the specimens during the test. Also, a test was carried out at 5000 mm/s (dynamic loading rate) with help of digital image correlation. This is summarised in **Table 3.5** with main focus on the order of magnitude, because factors close to unity in front of the order of magnitude tend to have less effect on the mechanical properties (*Walters and Przydatek 2014*). Therefore, in this research as summarised in **Table 3.5** and based on **Table 2.4**, the loading rates in terms of strain rates are defined as follows:

1.   Quasi-static (QS) loading rate at 0.0002 s^{-1}

2.   Elevated loading rates at between 0.04 and 4 s^{-1}

3.   Dynamic loading rate at 100 s^{-1}

It should be noted that the strain rate was estimated before the test to give an understanding of the target strain rate over the parallel length as given by BS standard (*BS EN ISO 6892: 2009*), and after the test based on the change in length and time in order to confirm the average strain rate as given in Eqs. (3.1) and (3.2), respectively. In this research, a comparison between QS and dynamic results is being sought, so the gauge length equals the parallel length because of

the specimen geometry design for high loading rate tests on the VHS test machine (section 3.2.2.3).

$$\dot{\varepsilon}_{Lg} = \frac{V_g}{L_g} \qquad\qquad (3.1)$$

$$\dot{\varepsilon}_{avg} = \frac{\varepsilon}{t} \qquad\qquad (3.2)$$

where

$\dot{\varepsilon}_{Lg}$ is the estimated strain rate over the gauge length before test;

$\dot{\varepsilon}_{avg}$ is the actual calculated average strain rate after the test;

ε is the change in length $= (\varepsilon_{final} - \varepsilon_{original})$;

V_g is the constant crosshead speed;

L_g is the gauge length = 50 mm

t is the time at fracture

Table 3.5 Summary of tension tests at a range of loading rates in terms of strain rates

Crosshead speed (V_g) (mm/s)	Estimated strain rate ($\dot{\varepsilon}_{Lg}$) using Eq. (3.1) (s^{-1})	Average strain rate ($\dot{\varepsilon}_{avg}$) using Eq. (3.2) (s^{-1})
0.008	1.7×10^{-4}	2×10^{-4} (0.0002)
1.67	3.3×10^{-2}	4×10^{-2} (0.04)
8.33	1.7×10^{-1}	2×10^{-1} (0.2)
50	1×10^{0}	1×10^{0} (1)
166.67	4×10^{0}	4×10^{0} (4)
5000	1×10^{2}	0.98×10^{2} (~100)

3.2.2.1 Quasi-static and elevated tension tests

Tests conducted under standard loading condition (quasi-static) using a displacement control method on an Instron B909 testing machine at ambient temperature were in accordance with BS standard (*BS EN ISO 6892: 2009*). The specimen photograph and dimension of the test

specimen employed at quasi-static and up to 4 s^{-1} strain rates are shown in **Figures 3.1** and **3.2**, respectively. From **Table 3.5** above, tests at 0.008 mm/s crosshead speed refer to the standard or QS loading rate tests. The same method was employed for the tension tests at crosshead speed above 0.008 mm/s up to 166.67 mm/s, with high level of detail using the same VHS Instron testing machine. This test speed range is considered to be an elevated loading rate in this thesis. The test-setup uses a load cell (attached and calibrated with the testing machine), and an extensometer is attached to the specimen gauge length to measure accurately the stress-strain characteristic of the material.

At the end of each test, both cross-section reduction and gauge length extension were measured. The engineering stress-strain characteristics were converted to true stress-strain characteristics using Eqs. (3.3) and (3.4).

$$\varepsilon = ln(1 + e) \tag{3.3}$$

$$\sigma = s(1 + e) \tag{3.4}$$

where, ε and σ represent the true strain and true stress, respectively. s and e denote the engineering stress and strain results from the experiments.

The same formulae were used to estimate the true stress-strain characteristics of S235, S690QL and S960QL under elevated and dynamic loading rates.
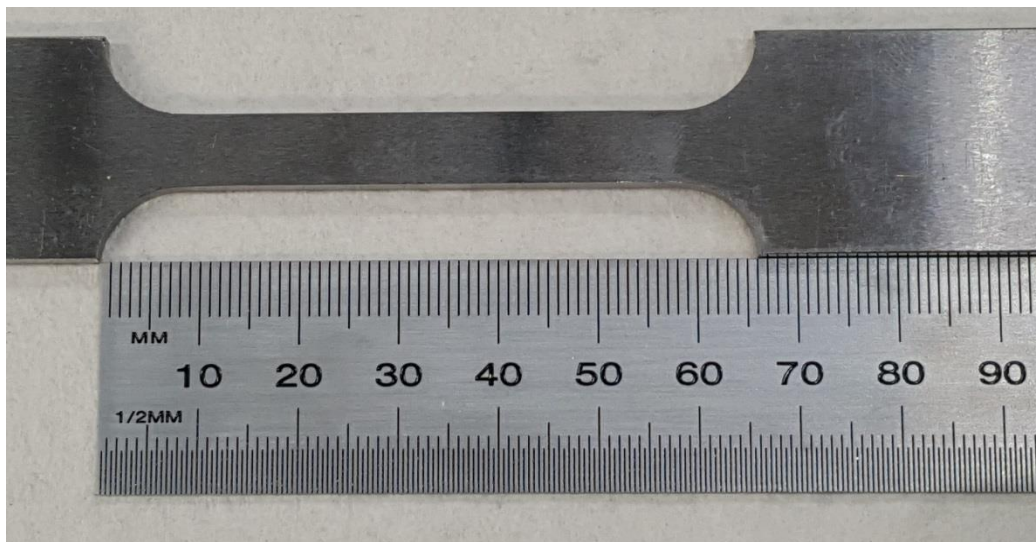
Figure 3.1   Photograph of the flat dog-bone shaped tensile specimen.
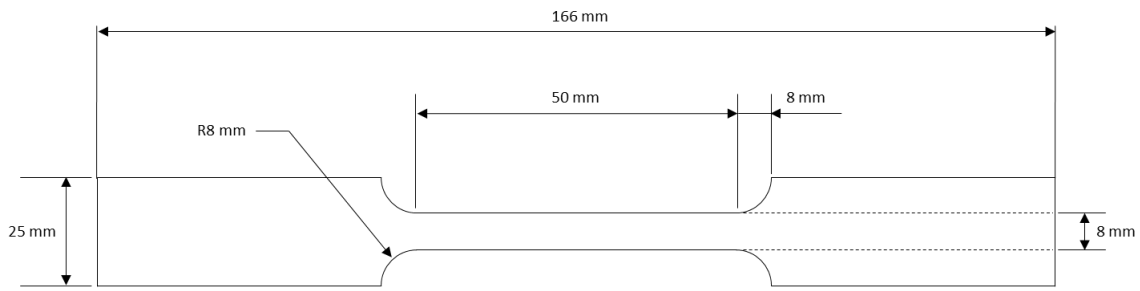
Figure 3.2   Tension test specimen dimension used at QS and elevated loading rates.

3.2.2.2 Dynamic tension tests

In this thesis, tension tests conducted at a crosshead speed of 5000 mm/s with equivalent strain rate of about 100 s^{-1} are referred to as dynamic tension tests (Table 3.5). For the purpose of clarity, the specimen geometry requires one end to be longer, **Figure 3.3**, because of the testing machine requirement discussed in section 3.2.2.3.
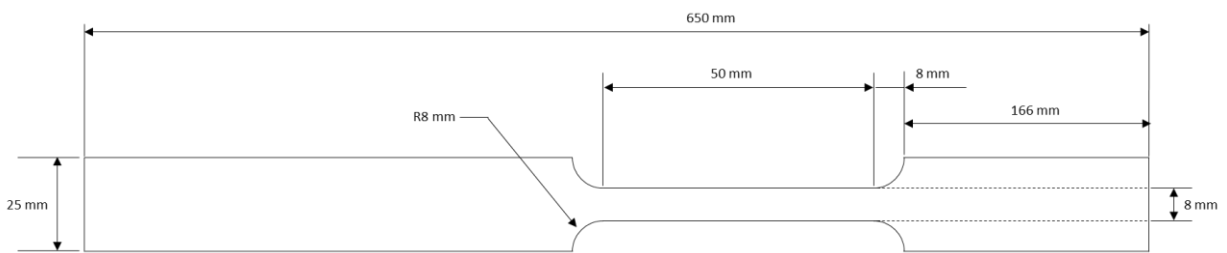
Figure 3.3   Dynamic tension test specimen dimension used at 100 s^{-1}.

3.2.2.3 Test setup and procedures at dynamic loading rates

Dynamic tests require a specialised machine capable of high-speed loading and data recording along with skilled and experienced personnel for the experimental procedures and setup. This has made dynamic testing over the years very expensive and, as such, has made quasi-static testing conditions generally accepted for design purposes. This is why most offshore and marine structures such as ships and fixed structures are often designed for quasi-static loading conditions, despite the fact that there are occasions when dynamic loading such as impact from ship collision or dropped objects could affect the response of the structure. It is therefore imperative to quantify the mechanical response in terms of in-service loading conditions since structures do not always operate under quasi-static loading conditions.

To bridge this gap, tests were carried at critical loading rate scenarios an offshore crane may experience in-service. Tests were carried out at room temperature on an Instron VHS 160

dynamic test machine, **Figure 3.4**. The machine is a specialised dynamic testing machine with capacity of 100 kN with crosshead speed up to 20 m/s, utilising advanced servo-hydraulic and control technologies alongside patented FastJaw gripping techniques. The gripping techniques require one end of the flat tensile specimen to be longer than the other in order to give room for travel. All tests were performed at TWI Ltd, Cambridge.

To maintain accuracy and precision at strain rates above 10 s^{-1}, high speed recording equipment is required. The use of a high-speed Digital Image Correlation (DIC) system has proven to be a suitable option for the measurement of the strain profile experienced by the specimen under high loading conditions. Since the purpose of the test is to determine the effects of dynamic loading rates in terms of strain rate, DIC was employed with the VHS high speed test machine.

The DIC system is calibrated to measure within a certain measuring volume which takes a trigger pulse from the VHS test machine to start the camera and data logger. The DIC system requires a high-speed camera to capture about 70,000 frames/sec for a number of data points along the gauge length of the specimen. The camera setup (field of view used, frame rate and stand-off distance) all contribute to the number of data points. The setup of the test machine and schematic representation of the DIC system is shown in **Figures 3.5 and 3.6**, respectively.

To achieve the required overall precision, it is noteworthy that the experience of the technician plays an important role. Whilst the use of DIC at dynamic loading rates required skilled and experienced personnel, the test-setup and accuracy at strain rate below 10 s^{-1} also require a well calibrated machine, experienced personnel and accurate stress-strain measurements with the use of an extensometer attached to the specimen gauge length.

Figure 3.4   Instron VHS 160 dynamic test machine with capacity of 100 kN and speed up to 20 m/s. Courtesy of TWI Ltd.

Light source

High speed right camera

High speed left camera

Tensile specimen with speckle pattern
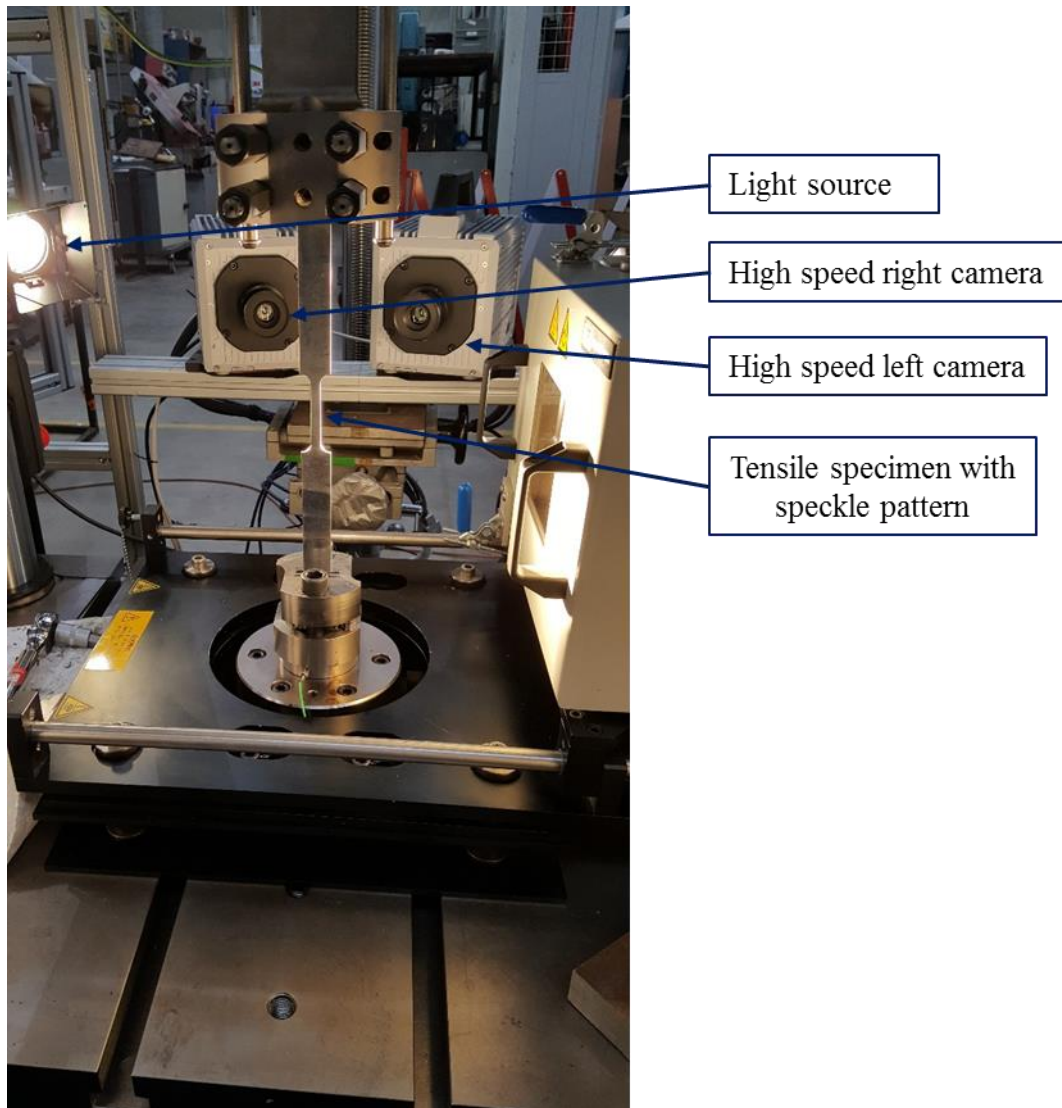
Figure 3.5   DIC system setup with the VHS test machine with view from behind (facing the camera). Courtesy of TWI Ltd.
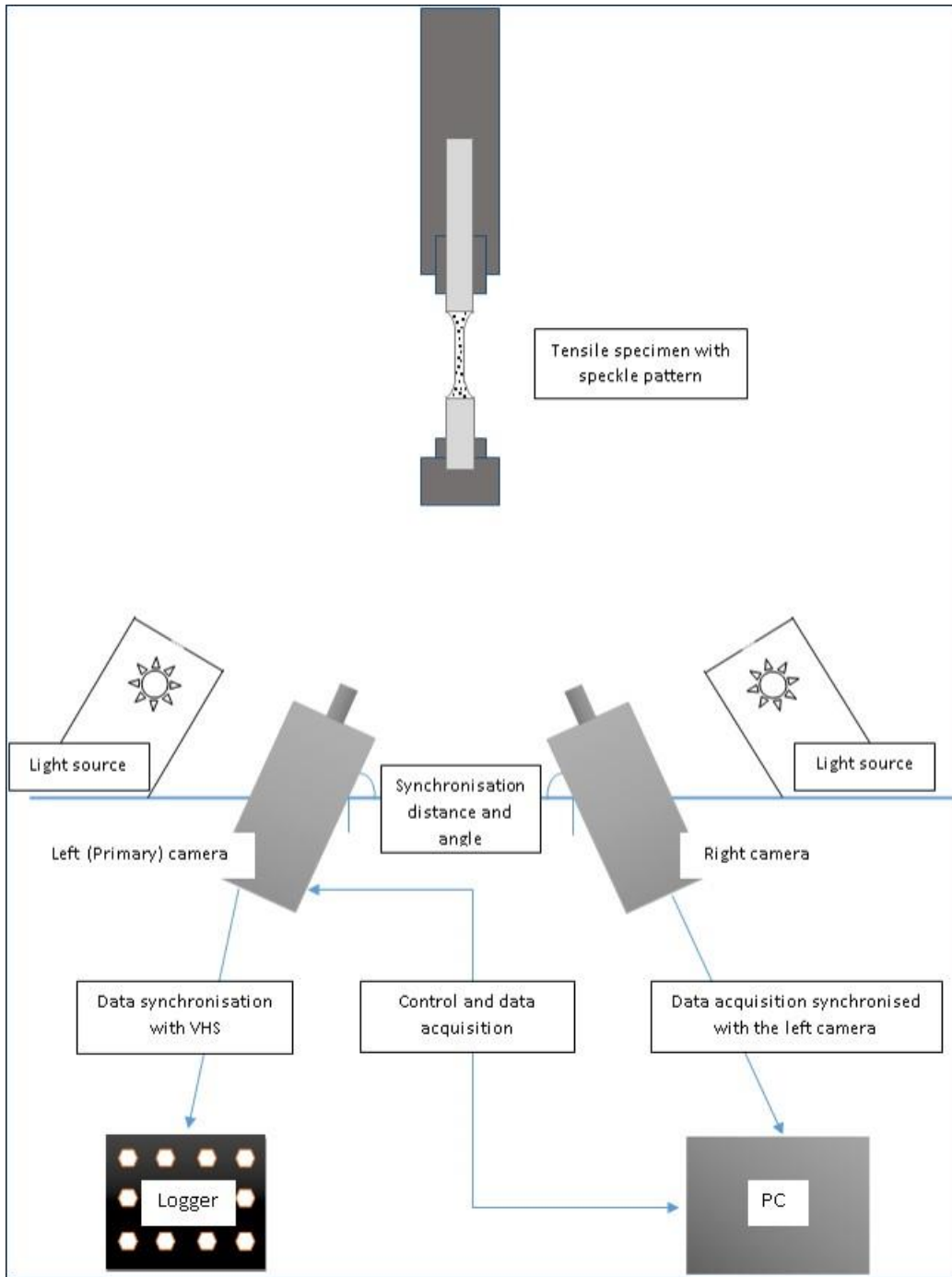
Figure 3.6   A simple schematic representation of the DIC setup and framework with the
VHS machine.

3.2.3   Fracture toughness test programme

Single edge notched bend (SENB) specimens were employed for the purpose of investigating the fracture behaviour of S690QL and S960QL at different loading rates. The reason for choosing SENB over other fracture toughness test specimen designs is discussed in section 2.3.3, which is based on an optimisation of specimen machining and conservatism of test results. A square cross-section with thicknesses and widths ($B=W$) = 25 mm and 10 mm for standard and Charpy-sized specimens, respectively, were prepared and tested to BS 7448:1 (*BS 7448-1 1991*) in the case of quasi-static condition. Whereas, at elevated and dynamic loading rates, BS 7448:3 (*BS 7448-3 2005*) and BS ISO 26843:2015 (*BS ISO 26843 2015*) were used, respectively.

Each of the specimens was taken at a ¼ depth of full thickness of the plate and EDM (electrical discharge machined) notch through thickness in the Y-X orientation, **Figure 3.7**. All the specimens are fatigue pre-cracked, **Figure 3.8** with nominal value of the ratio of the initial crack length and specimen width (a_0/W) equal to 0.5, loading span (S) of 40 mm, and initial and final fatigue load of 3.5 kN and 2 kN, respectively. For S690QL, two datasets were generated using the standard specimen configuration ($B=W=25$ mm) and a Charpy-sized pre-cracked SENB specimen ($B=W=10$ mm), **Figures 3.9 and 3.10**, respectively, whereas only Charpy-sized SENB pre-cracked specimens ($B=W=10$ mm) were tested for S960QL due to available test materials.
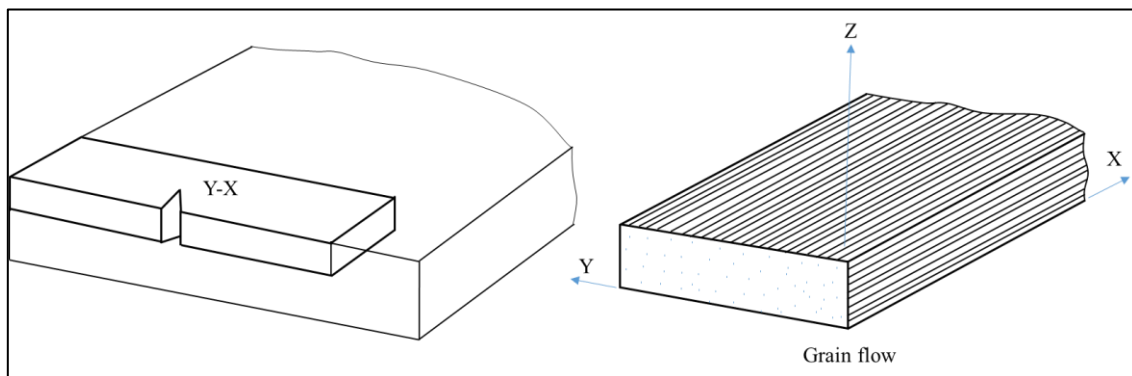
Figure 3.7   Y-X orientation for basic fracture plane identification for a plate or rectangular section.
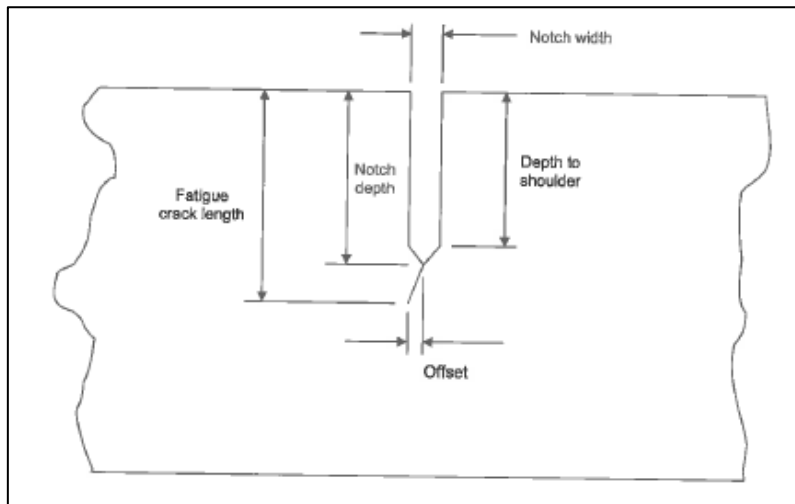
Figure 3.8   Schematic representation of EDM Notch and Fatigue pre-cracking
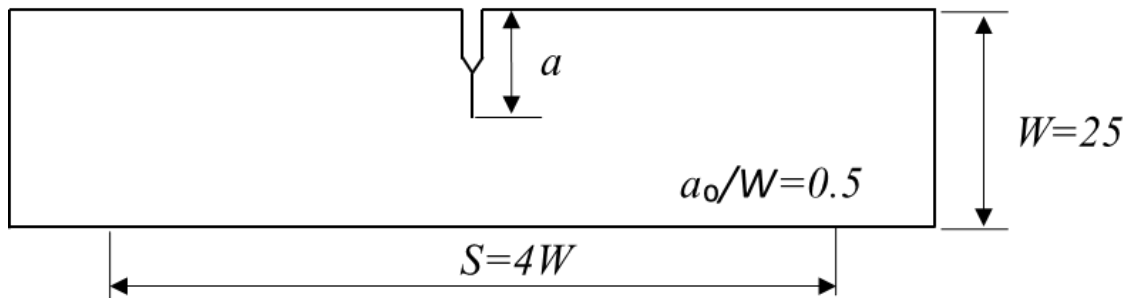
Figure 3.9   Standard SENB test specimen geometry used at quasi-static loading rate.
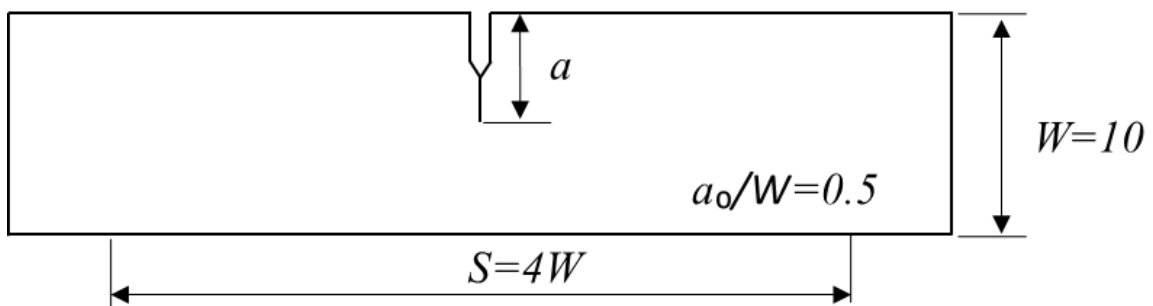
Figure 3.10   Charpy-sized SENB test specimen geometry used at quasi-static, intermediate and dynamic loading rates

Tests were done at a range of loading rates using a displacement control method summarised as follows:

1. Standard or quasi-static (QS) at 0.005 mm/s;

2. Intermediate at 200 mm/s;

3. High or dynamic at 5400 mm/s loading rates.

The test temperatures are between ambient (23 °C) and -120 °C. For the quasi-static loading rate, tests are done at 23 °C, -100 °C and -120 °C temperatures. The selected temperatures cover the fracture behaviour of S690QL and S960QL at upper shelf and lower shelf on the ductile-to-brittle transition curve (DBTC). Two clip gauges were used to measure the crack mouth opening displacement as well as load line displacement mounted on the integral knife edges during tests at both ambient and low temperatures, **Figures 3.11 and 3.12**, respectively. An environmental chamber was utilised at -100 °C and -120 °C to achieve a uniform test temperature on the specimen, monitored using a thermocouple attached to the specimen during the tests.

The same test set up was used during the intermediate loading rate tests while, at high loading rate tests, an Instrumented Charpy test method was used on 10 mm thick specimens, discussed further in section 3.2.4. In terms of the fracture mechanical loading rate expressed as K-rate, if the QS K-rate is within the range 0.5 to 3 MPa√m/s, then the test method given by BS EN 7448-1 was carried out. The intermediate loading rate was carried out in accordance with BS 7448-3 (*BS 7448-3 2005*). An order of magnitude of equals to about 1 MPa√m/s was achieved at the 0.005 mm/s test speed and about 10^4 MPa√m/s for 200 mm/s. It is important to mention that an average elastic stress intensity factor loading rate (K-rate) was estimated by fitting the linear part of the data describing the stress intensity factor-time trace.

Striker

SENB test specimen

Knife edge

Roller/Support

Clip gauges
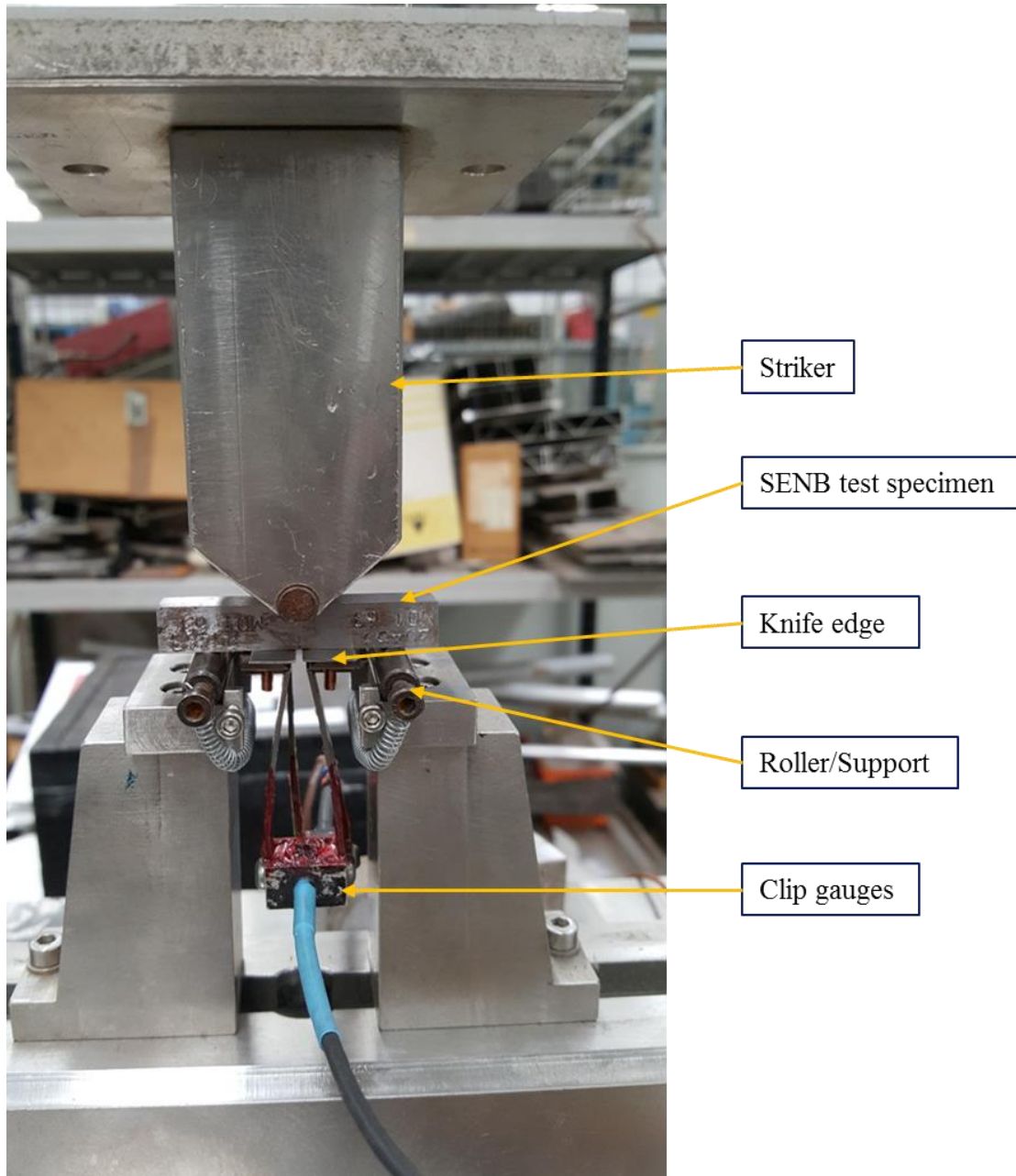
Figure 3.11   Quasi-static and intermediate SENB fracture toughness test set up at ambient temperature. Courtesy of TWI Ltd.
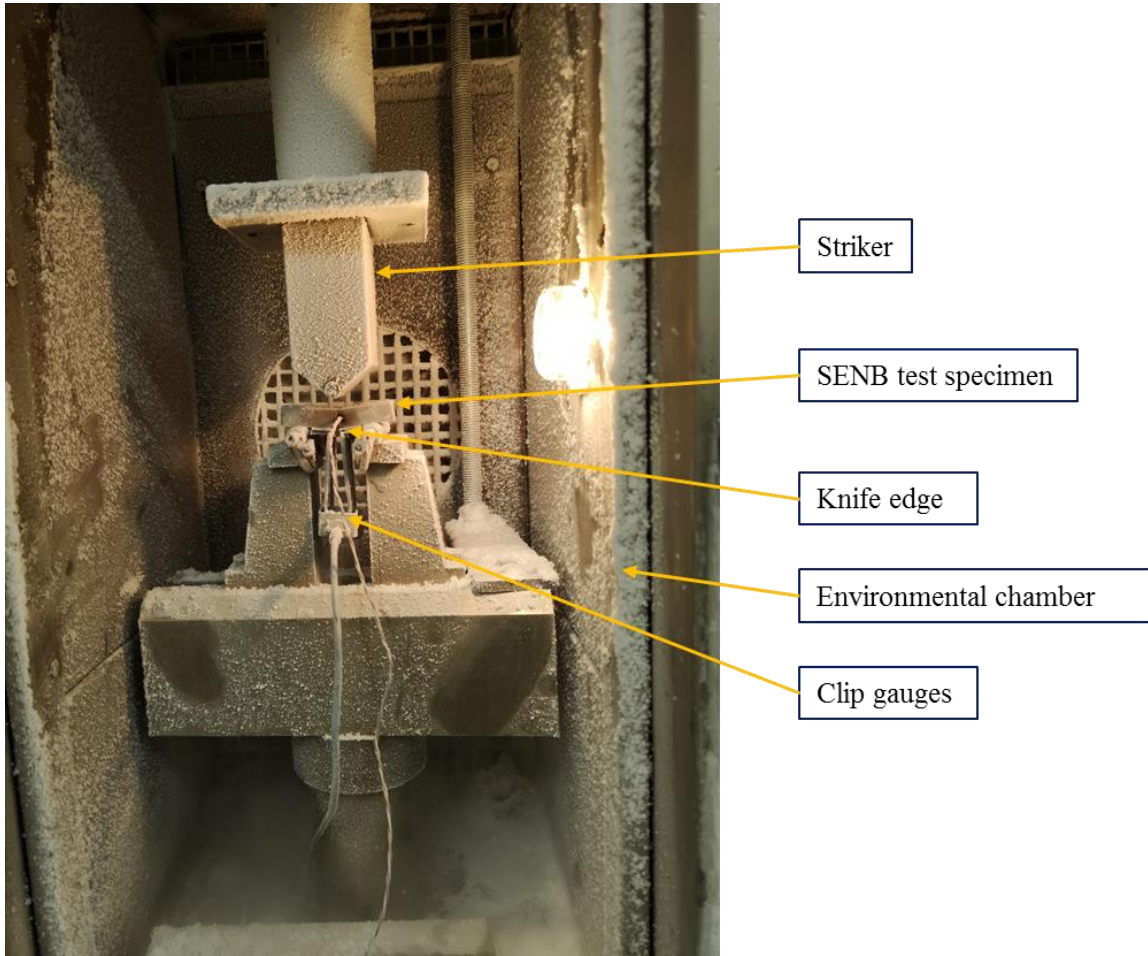
Figure 3.12   Quasi-static and intermediate SENB fracture toughness test set up at low temperature in an environmental chamber. Courtesy of TWI Ltd

A single point *J*-integral and CTOD fracture toughness value was estimated but with emphasis on *J* given as given in Eq. (3.5) for bend specimens. The results describing the values of CTOD are presented in the appendix.

$$J = J_{el} + J_{pl} \tag{3.5}$$

where

$$J_{el} = \left[\frac{FS}{BW^{1.5}} \times f\left(\frac{a_0}{W}\right) \right]^2 \frac{1-v^2}{E} \tag{3.6}$$

$$J_{pl} = \frac{2U_p}{B(W-a_0)} \tag{3.7}$$

J_{el} and J_{pl} represent the elastic and plastic component, respectively. U_p is the plastic component area under the force versus specimen displacement plot along the load line as shown in **Figure 3.13**.

The measured J values for this research are divided into two, J_c and J_m, representing the critical J at the onset of brittle crack extension (brittle fracture) and value of J at the first attainment of a maximum force (ductile tearing), respectively. Each measured value of J_c at cleavage initiation is converted to an equivalent elastic-plastic stress intensity factor K_{Jc} in accordance with ASTM E1921 (*ASTM E1921-15$^{\varepsilon 1}$, 2016*) using Eq. 3.8,

$$K_{Jc} = \sqrt{\frac{J_c E}{1 - v^2}} \qquad\qquad (3.8)$$

where,

$\qquad$ K_{Jc} = equivalent elastic-plastic stress intensity factor (MPa√m)

$\qquad$ J_c = critical J at onset of cleavage initiation (N/mm)

$\qquad$ E = Young's Modulus (GPa)

$\qquad$ v = Poisson's ratio
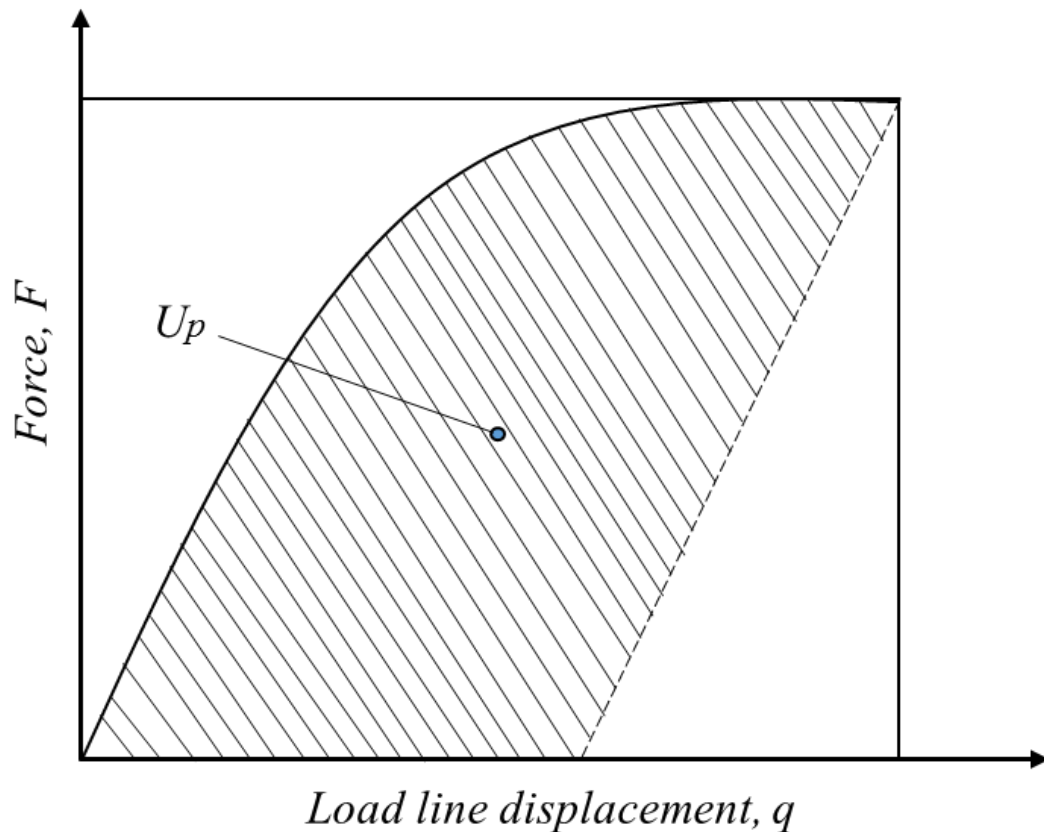
Figure 3.13   Definition of U_p for the determination of J

3.2.4   Conventional Charpy tests and instrumented Charpy-sized SENB dynamic fracture toughness tests

3.2.4.1 Overview

Offshore and marine structures such as ships and fixed structures are often designed for quasi-static loading conditions, and there are occasions when dynamic loading such as impact loading could affect the response of the structure. Although, dynamic test requires specialised machines (high speed recording equipment), skilled and experienced personnel for the experimental procedures which is very expensive; a number of standardised qualitative methods have been used over the years which include the conventional Charpy V-notch (CVN) and Pellini drop-weight tests to qualify the property of material under dynamic or impact loading. CVN has been employed most often during fabrication and design stages to establish the impact resistance of most ferritic steels under dynamic loadings. The results of such tests do not really give insight into the deep mechanism of failure and, as such, proper fracture toughness tests were required.

Therefore, in order to simulate the possible loading rates that offshore and marine structures could be subjected to in-service as described in **Table 2.4**, fracture toughness tests were done at intermediate and high/dynamic loading rates. A conventional CVN impact test was also carried out to establish the impact resistance in terms of absorbed energy for S690QL and S960QL.

3.2.4.2 Charpy V-notch impact test

Charpy V-Notch (CVN) specimens were prepared and tested to BS 148-1 at a range of temperatures between ambient 23 °C and -100 °C in order to estimate the T_{27} and T_0, corresponding to the transition temperature at 27 J impact energy and mid transition temperature, respectively. Specimens were taken in the rolling direction with the V-notch perpendicular to it (where the notch is through the thickness of the plates) and also in the direction parallel to it (where the notch is in the rolling/longitudinal direction). For S690QL steel plate, the notch geometry in both directions has been studied, whereas only the notch in the transverse direction was tested for S960QL. This is to establish if there is any significant difference in the T_{27} and T_0 for the HSS under consideration.

The V-notch has an included angle of 45°, a depth of 2 mm, and a root radius of 0.25 mm, **Figure 3.14** as recommended by BS EN ISO 148-1:2010. For the S960QL plate with 60 mm thickness, the specimens were taken within 2 mm and 17 mm of the upper surface to identify any through-thickness effect. A hardness traverse through thickness test showed no significant difference between the upper and lower surfaces. A total number of 11 and 12 coupons were tested when notch is in the transverse and longitudinal direction, respectively, for S690QL. For S960QL in the transverse direction, 12 coupons in total were tested. For both materials, a 450 J capacity Zwick testing machine calibrated to a 2 mm striker head is used. At the end of the test, the absorbed energy, crystallinity and lateral expansion were measured, and the data curve fitted using a *tanh* function given in Eq. (3.9).

$$C_v = A + B \tanh\left(\frac{T-T_0}{C}\right) \qquad (3.9)$$

where,

C_v represents the absorbed energy

T_0 is the mid transition temperature

A is the energy corresponding to T_0

A+B represents the upper shelf energy

C is the measure of the slope of the transition.
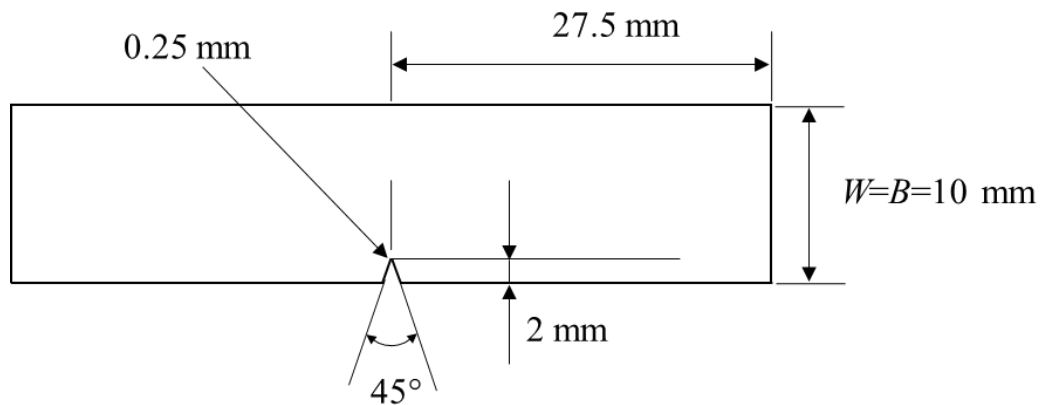
Figure 3.14   Charpy V-notch impact test geometry.

3.2.4.3 Instrumented Charpy-sized SENB fracture toughness test

There are limitations in capturing the crack tip constraint behaviour using a CVN test method. Most often, results from CVN tests are used in proxy to a quasi-static fracture toughness test. A fracture toughness test with high crack tip constraint at impact loading will help to better understand and provide a better understanding of fracture behaviour at dynamic loading. For this purpose, a similar CVN geometry has been employed called Charpy-sized SENB specimen. The only difference is that a Charpy-sized SENB specimen (10mm x 10mm x 55mm) is fatigue pre-cracked with nominal crack depth $(a_0/W) = 0.5$ and has similar geometry to the fracture toughness test geometry used under quasi-static loading conditions, **Figure 3.10**.

Measurement of the fracture toughness was in accordance with BS ISO 26843 and tests were done on a Zwick PSW750 Instrumented testing machine, **Figure 3.15**. The machine is an automated machine capable of measuring the load-displacement graph as well as the absorbed energy at a range of temperatures. Since, for this research, a comparison between quasi-static and dynamic results is sought, so a similar temperature range and specimen geometry has been used throughout this study for all the loading rates (section 3.2.3).

Also, the test set up and results are highly dependent on the striker configuration, and so tests were undertaken at different striker heights (angle) to generate a resistance curve, as well as at

different striker edge radii to determine the influence of striking edge radius on the toughness of S690QL and S960QL. This is discussed in detail in the sub-section 3.2.4.4.
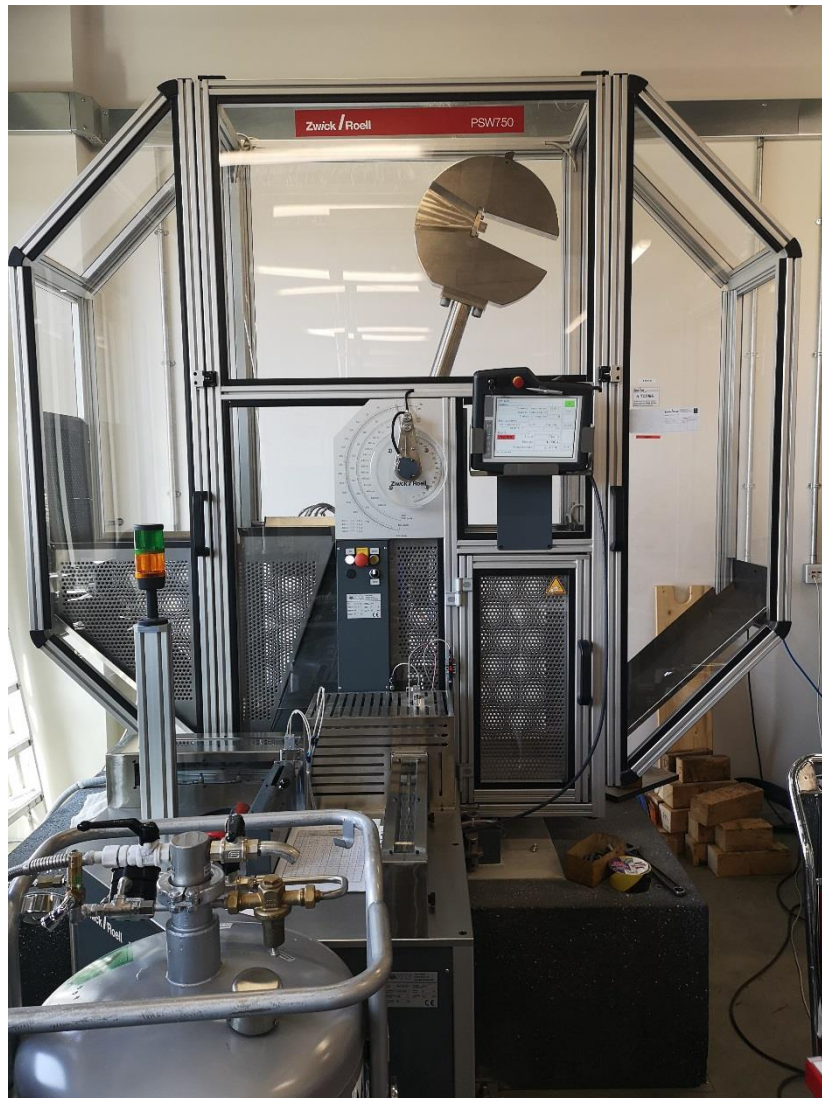
Figure 3.15   Zwick PSW750 Instrumented Charpy test machine. Courtesy of TWI Ltd.

3.2.4.4 Influence of striking edge radius on the absorbed energy and maximum load using Instrumented Charpy pre-cracked specimens.

The Instrumented Charpy (IC) testing method is similar to the conventional non-instrumented Charpy (CVN) impact energy test. In an IC test, the force-displacement curve is recorded which can be used to determine the critical fracture toughness value provided that a sharp crack (fatigue pre-cracked) is introduced in the specimen for high crack tip constraint. Different striking configurations of 2 mm (ISO 148/14556) and 8 mm (ASTM E23) can influence the results of Instrumented Charpy testing.

It is important to mention that the differences between 2 mm and 8 mm radius strikers are insignificant in terms of absorbed energy for S690QL tested using the Instrumented pre-cracked Charpy specimen with an average value of around 95 J recoded at ambient temperature for both strikers. However, a significant difference was observed for S960QL with average values of absorbed energy of 73 J and 64 J recorded using 2 mm and 8 mm, respectively.

Also, in terms of maximum load, a significant difference is observed. A difference of up to 2.2 kN is observed when the 8 mm striker radius is used for S690QL, **Figure 3.16**. The present work corroborated the study and observation made by Lucon (*Lucon 2008*) in which an 8 mm striker gives a significantly higher value than a 2 mm striker when the toughness of the material is increased. For S960QL with lower toughness, **Figure 3.17**, the difference is not as high when compared to S690QL in terms of maximum load. In summary, the effect of striker configuration is significant for the maximum load, with the 8 mm striker providing consistently higher values and effect is predicted to be material-dependent, which tends to increase with material toughness. To increase the level of conservatism, subsequent low blow tests used to generate the R-curve at dynamic loading for S690QL were conducted on the IC testing machine with the 2 mm striking configuration. This is discussed further in the next section (3.2.5).
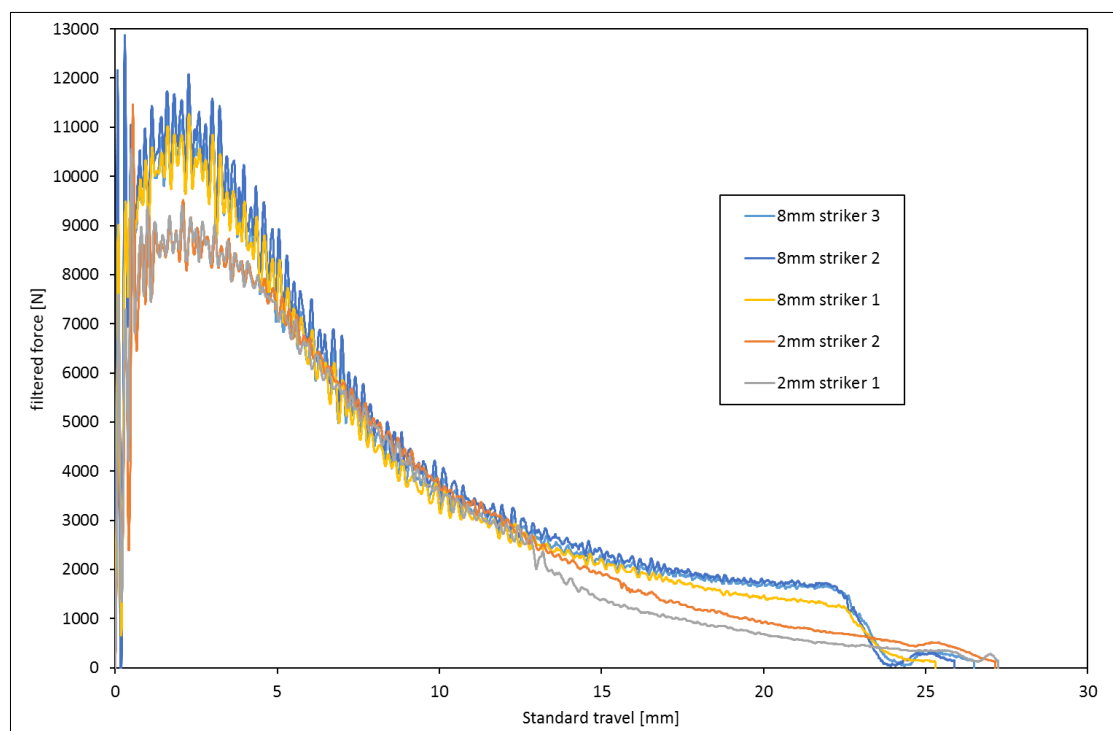
Figure 3.16   Effect of striker configuration on Instrumented pre-cracked Charpy test for S690QL
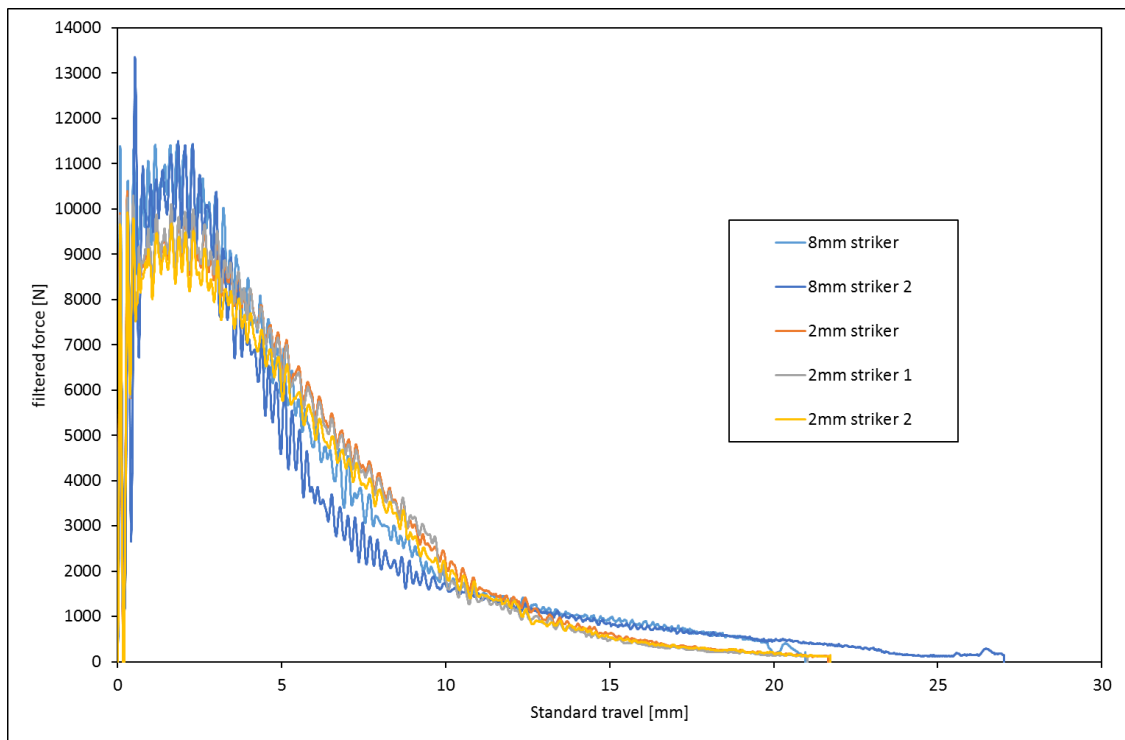
Figure 3.17   Effect of striker configuration on Instrumented pre-cracked Charpy test for S960QL

3.2.5 Low blow testing

Determination of resistance curves under impact loading is very challenging when using multiple specimen methods where Charpy-size specimens are often used for the purpose. The test procedure called the low blow testing method requires limiting the extent of pendulum hit in order to have sufficient ligament to produce a certain stable crack extension, and not sufficient to fully break the specimen (*BS ISO 26843: 2015*).

In this research, the method was used to generate the *J*-R curve presented in section 5.5 in chapter 5. The main factor to consider in order to limit the extent of hit by the striker, is to decrease the angle of rise of the pendulum. At full speed, the angle of rise of the IC testing machine is 160° (Figure 3.15). The angle of rise considered for this work is between 25° and 45° which gives an array of chevrons, **Figure 3.18**. It is observed that as the angle of rise increases, the crack mouth opening increases, and at around 40°, the pendulum hit is sufficient to fully break the specimen. Therefore, based on this study, the angle of rise for HSS with yield strength >690 MPa to generate a valid *J*-R curve using low blow testing method should be considered at angle of rise <40° until an angle is reached where a certain stable crack extension

can be produced. The data in terms of absorbed energy for S690QL and S960QL are presented in the appendix.

Figure 3.18   Low blow Instrumented pre-cracked Charpy tests at different angle of pendulum rise from 25° (LHS) to 40° (RHS) with 5° increments for S690QL.

3.2.6   Challenges of carrying out tests at high loading rates

3.2.6.1 Use of VHS machine and DIC

High loading rate tests require specialised machines capable of high-speed loading and data recording (DIC) alongside skilled and experienced personnel for the experimental procedures, setup and DIC calibration. The test set-up was challenging due to the requirements for accuracy and precision and calibration with the Digital Image Correlation (DIC) as discussed in sub-section 3.2.2.3. Manufacturing a 3 mm flat tensile specimen which requires one end longer than the other (Figure 3.3) from 25 mm and 60 mm thick plates was a herculean task. This was successfully done at the test house, a subsidiary of TWI Ltd, with the help of the experienced technicians.

As described in section 3.2.2.3, a V6 data is exported after the test for a post-test analysis which was done using GOM correlate software. GOM correlate is a digital image correlation (DIC) and evaluation software for materials research and component testing. The imported images in the form of V6 are extracted automatically providing a quick and easy access to all result data sets for complete evaluation. The test samples in **Figures 3.19 and 3.20**, shows a full strain field analysis on the flat specimen under uniaxial loading conditions considered in this research. It demonstrates the strain effects which are analysed on the full surface of the specimen and displayed by the load and strain profile to the left in **Figures 3.19 and 3.20**. A virtual extensometer (similar to what was employed under QS conditions) was attached to the specimen in order to extract the strain profile on the sample at every stage of the test until fracture, for S690QL and S960QL, **Figures 3.19 and 3.20**, respectively. The figures show the reading from the load cell signal which is synchronised with the DIC data. The extracted data are then exported in an excel file for post processing.

The load characteristics extracted was converted to stress based on the area of the specimen at 24 mm^2 which is kept constant for all the tension tests in this thesis. Due to the imbalance between the internal and external forces during high loading problems, the load signal as expected was noisy due to stress wave propagation developed during the test. To reduce the noise in the data, the moving average technique in the Matlab software was employed as a curve fitting technique. The fitting method was used to generate an average data from the processed data extracted from the excel file. The data from the curve fitting were then used to quantify the effect of strain rate at 100 s^{-1} for the S690QL and S960QL steels under consideration and (S235) as a low strength steel representation. The processed data extracted from GOM correlate represents the engineering stress and engineering strain. The results are the converted to true stress and true strain using Eqs. (3.3) and (3.4), respectively.
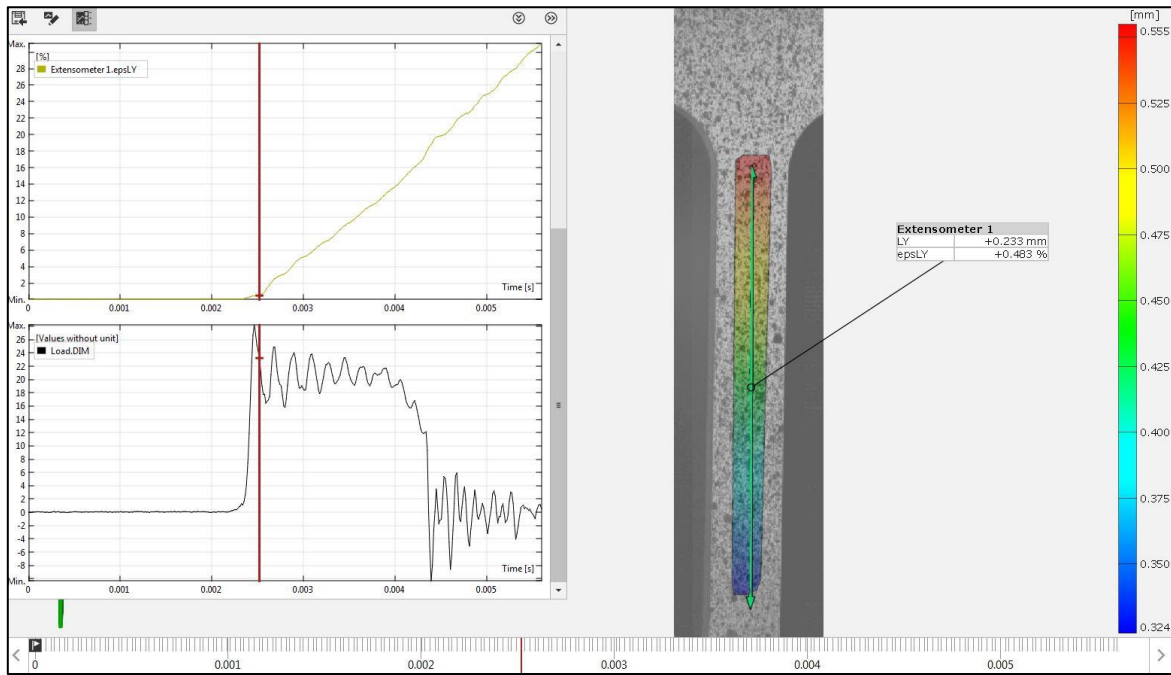
Figure 3.19   GOM Correlate interface showing the DIC results of tension tests at 100 s^{-1}
strain rates for S690QL.
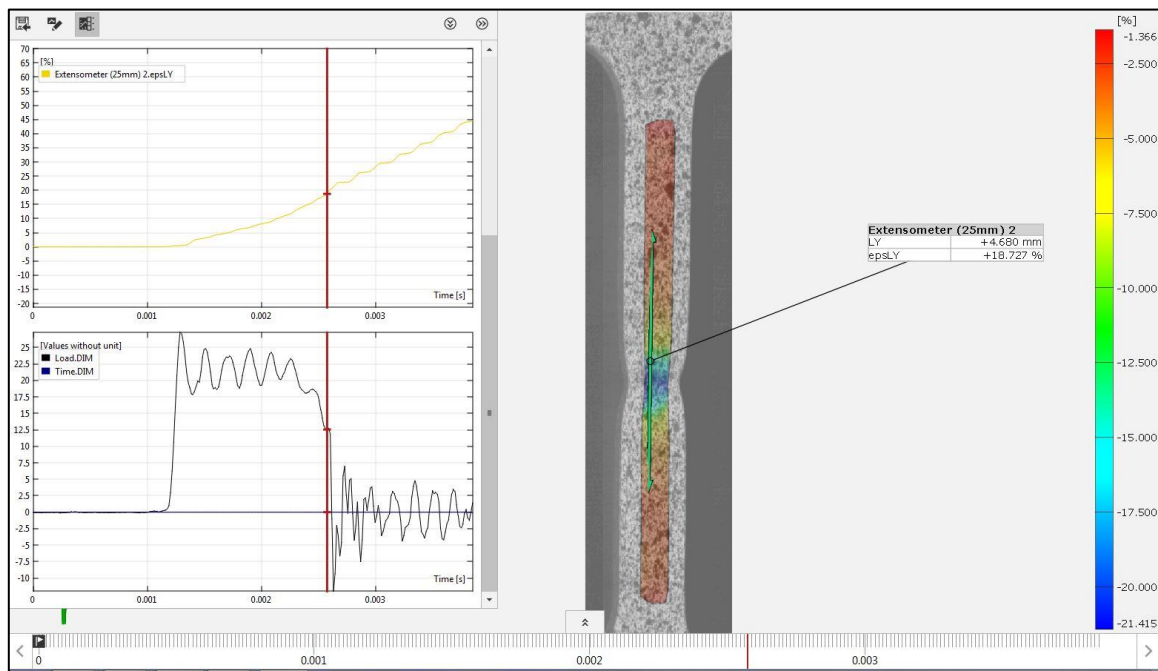
Figure 3.20   GOM Correlate interface showing the DIC results of tension tests at 100 s^{-1}
strain rates for S960QL after necking.

Also, in terms of fracture toughness tests, the processed results for S690QL on VHS calibrated with the DIC using Charpy-sized pre-cracked SENB specimens are compared to results from Instrumented Charpy (IC) testing using the same test specimens at ambient temperature, **Figure 3.21**. The tests were carried out at an impact loading speed of 5.4 m/s on both machines. As far as the test data on VHS machine is concerned, the two important factors that contribute to a decrease in the maximum load are due to the striking edge radius, as well as the configuration of the pendulum striker which impacts the specimen. On the Instrumented Charpy test machine calibrated to an ASTM 8 mm striker, the configuration of the pendulum striker is released at an angle. Whereas on a VHS machine calibrated to an ISO 2 mm striker, the striker is released perpendicularly to the specimen.

Owing to the fact, the IC test machine seems to give accurate traces in accordance with a Type IV diagram type of a typical force-time trace at impact loading (*ASTM E1820 -15a, BS ISO 26843: 2015*), the results from the Instrumented Charpy (IC) test machine was used to characterise the fracture behaviour of S690QL and S960QL at ambient and low temperatures presented in chapter 5.
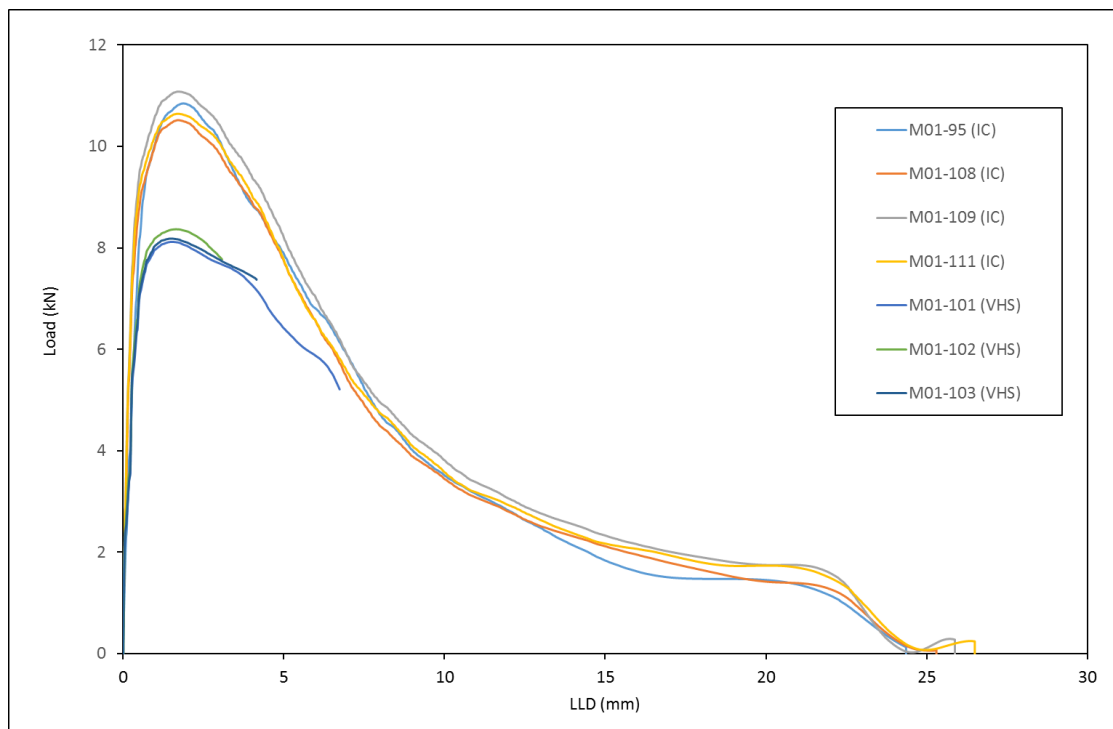
Figure 3.21   Comparison between results from VHS calibrated with DIC and Instrumented Charpy test machines for S690QL

3.3 Numerical Study

This section introduces finite element analysis (FEA) carried out in this thesis to support the experimental test results data. The main purpose of the FEA is to allow for the prediction of crack driving force which cannot be determined during the fracture toughness tests and the effect of loading rates on the crack mouth opening displacement using rate dependent material model developed for S690QL. A material model simulating the tension test of S690QL at different loading rates was developed using rate dependent model in commercially available ABAQUS software, version 6.14 (*Simulia, 2014*). The material model was validated with the experimental data and compared using the Modified Ramberg-Osgood (RO) power law (*Ramberg and Osgood 1943*) data, discussed further in section 4.5. The input data for the material model as well as the experimental tension test results used for the analysis are presented in chapter 4. The results from the material model are then used in the fracture toughness finite element analysis.

To predict the crack driving force and assess the effect of loading rate on the crack mouth opening displacement for S690QL at every load increment, a three-dimensional quarter (1/4) symmetric model was developed to represent the experimental SENB fracture toughness tests and validated (described in section 3.3.2). The model was used to assess the crack mouth opening displacement and to determine the crack driving force useful for structural assessments. The key features of the material model and fracture toughness model are described in sections 3.3.1 and 3.3.2, respectively. Validation of the fracture toughness SENB model is discussed in section 3.3.2.1. For clarity, further discussion on the FEA analysis of the fracture toughness SENB model are presented in section 5.7, and this includes the results from the model which are compared with the experimental test results presented in chapter 5.

3.3.1 Material model

Simulations of the tension test results have been performed to describe the material flow stress behaviour at quasi-static, elevated and dynamic loading rates using von Mises flow rule and isotropic hardening condition available in the ABAQUS code. A rate dependent model was developed. The use of Johnson Cook (JC) material rate dependent model has not been employed in this thesis because it requires the understanding of the hardening parameter as well as temperature effect in the form of tension tests at elevated temperature which are carried out in this work as input data in the ABAQUS code.

On the other hand, the yield stress ratio to define the materials yield behaviour requires the knowledge of the dynamic and quasi-static yield stress from the experiments. In this case, the yield stress ratio assumes that the shapes of hardening are identical at different loading rates, which are a function of the equivalent plastic strain rate ($\dot{\varepsilon}_{pl}$) given as Eq. 3.10.

$$\sigma = \sigma_0 R(\dot{\varepsilon}_{pl}) \qquad\qquad\qquad (3.10)$$

where:

R represents the yield stress ratio (taken as the ratio of the dynamic and quasi-static yield stress generated from the tension tests using Eq. (4.2)

σ is the yield stress for a non-zero plastic strain rate

σ_0 is the static yield stress.

The FE model has the same specimen geometry used for the experimental study. Imposed displacement has been applied to the end of the specimen and the boundary conditions applied in the simulations were in accordance with the experiments as shown in **Figure 3.22,** where the other end was fixed. A C3D8R linear hexahedral element type was used for the simulations, with a total number of elements equal to 4392 as there is no significant difference when the number of elements is increased. S690QL properties in terms of true stress and effective plastic strain from the quasi-static tensile test data has been used in the model, and compare to Ramberg Osgood material law hardening behaviour.
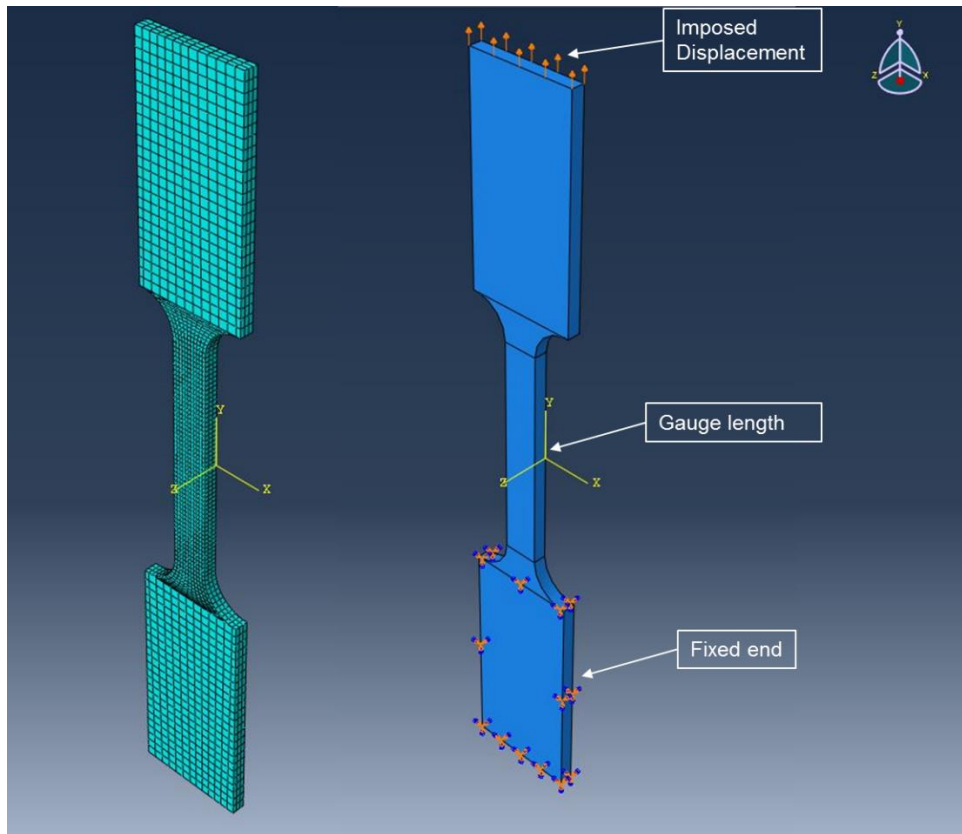
Figure 3.22   Tensile FE model and boundary conditions

3.3.2   Fracture toughness SENB model

A three-dimensional FE model was generated with the ratio of initial crack length and width (a_0/W) taken as a mean value of 0.52. The choice of $a_0/W = 0.52$ was informed due to differences in the values of a_0, with marginal difference in the experimental results due to the curved thumbnail shaped crack front which cannot be the same for all specimens. Also, to aid convergence, the SENB was modelled with an initial notch tip radius (ρ_0) of 2.5μm.

A quarter (1/4) symmetric model was developed to represent the quasi-static experimental SENB test specimen geometries with imposed displacement (DY), boundary conditions (DX) and the mesh arrangement shown in **Figure 3.23** at room and low temperatures. The summary of the three-dimensional finite element model is given in **Table 3.6**.
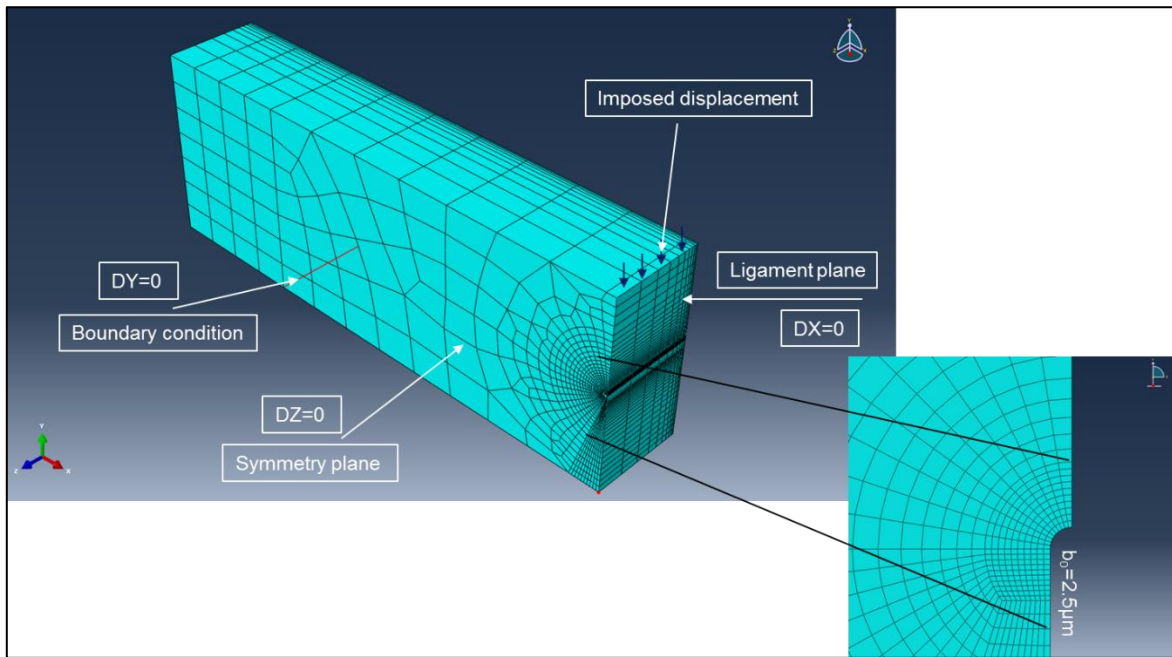
Figure 3.23   SENB FEA model and boundary conditions used.

Table 3.6   Summary of the finite element model used

Loading condition	DY (mm) @ ambient temp	DY (mm) @ low temp	DX (mm)	Notch tip radius (ρ_0) (µm)	Number of elements	Element type
Quasi-static	2.5	1.5	0	2.5	19140	C3D20R
Elevated	-	1.5	0	2.5	19140	C3D20R

3.3.2.1 Fracture toughness SENB FEA model validation

- A weighted crack-front average *J*-integral (J_{avg}) value for each load increment was calculated from the model and verified using the analytical formulae Eq. (3.11) given by BS 7448-4.

$$U_p = U - U_e \qquad (3.11)$$

where, U and U_e represent the total area and the elastic component area respectively, under a plot of force versus specimen displacement plot along the load line. The elastic component area (U_e) is given as Eq. (3.12) for SENB.

$$U_e = \frac{F \times q_e}{2} \qquad (3.12)$$

$$q_e = \frac{F(1-v^2)}{EB_{eff}} \times \left(\frac{S}{W-a}\right)^2 \times \left[1.193 - 1.980\left(\frac{a}{W}\right) + 4.478\left(\frac{a}{W}\right)^2 - 4.443\left(\frac{a}{W}\right)^3 + 1.739\left(\frac{a}{W}\right)^4\right] \quad (3.13)$$

where, B_{eff} = B

- The second method used to validate the model at quasi-static condition is the use of theoretical HRR (Hutchinson, Rice and Rosengren) stress field using Eq. (3.14) (*Shih, 1983*). HRR is used to characterise crack-tip stresses and strains in nonlinear material using *J*-integral. In this thesis, the stress field variation in the model has been compared with the theoretical stress field from HRR equation as a means of validating the model at quasi-static condition.

$$\sigma_{ij} = \sigma_0 \left(\frac{EJ}{\alpha \sigma_0{}^2 I_n r}\right)^{\frac{1}{n+1}} \tilde{\sigma}_{ij}(n, \theta) \quad (3.14)$$

where σ_{ij} is the asymptotic crack tip stress field

                 σ_0 is the yield stress

                 E is the Young modulus

                 J represents *J*-integral

                 α is material constant

                 n is strain hardening exponent

                 r is the distance from the crack tip along the centre line

                 $\tilde{\sigma}_{ij}$ is dimensionless function of n and θ

                 I_n is an integration constant that depends on n

The HRR stress field input data used to validate the model is summarised in **Table 5.12** in chapter 5. After validating the model at quasi-static using the above methods, the three-dimensional ¼ SENB FE model was unchanged at elevated loading analysis, but a rate dependent material model was incorporated in the analysis. The load line displacement loading

condition (DY) was applied in conjunction with the time period of the analysis (Δt) to achieve the load line velocity used during the experiment.

3.4   Chapter summary

This chapter summarises the experimental methods and finite element analysis employed in this thesis. In order to simulate the change in mechanical behaviour that the materials under consideration (S690QL and S960QL) might experience in-service, experimental tensile tests were designed at a range of loading rates from 0.008 mm/s to 5000 mm/s using a displacement control method. A material model was developed and validated in comparison with Ramberg Osgood material law hardening behaviour.

Also, since the major effect of loading rate on the ductile-to-brittle transition curve is a shift from a lower temperature to higher temperature, the test temperatures considered for the fracture toughness tests are between ambient and -120 °C, and the loading rate conditions are summarised as follows:

1. Standard or quasi-static (QS) at 0.005 mm/s;

2. Intermediate at 200 mm/s;

3. High or dynamic at 5400 mm/s loading rates.

Assuring comparability, Charpy-sized single edge notched bend (SENB) specimens using a square cross-section with thickness (B) and width (W) = 10 mm, and $a_0 / W = 0.5$ were employed for the purpose of investigating the fracture behaviour of S690QL and S960QL at different loading rates. Data were also generated at QS loading rate using a standard SENB configuration when (B) and width (W) = 25 mm in order to establish the difference between using a Charpy-sized SENB specimen and a standard SENB specimen at ambient and low temperatures for S690QL steel delivered in 25 mm thickness. This is followed by discussing the challenges faced when carrying out tests at high loading rates and the influence of striking radius on the absorbed energy and maximum load of S690QL and S960QL as compared with experimental data from VHS machine.

A three-dimensional ¼ SENB FE model for S690QL was developed for quasi-static fracture behaviour and validated with the experimental test data, theoretical HRR stress field and the

analytical method in BS7448-4. The same model was unchanged for the dynamic analysis where a rate dependent model was incorporated in the analysis using the yield stress ratio method available in ABAQUS code.

Chapter 4   Tensile Behaviour of S690QL and S960QL under High Loading Rate

4.1   Introduction

This chapter is divided into three parts. The first part concerns the as-received plate condition of S690QL and S960QL in terms of the chemical composition. In the second part, the experimental test results and discussion of the quasi-static, elevated and dynamic tensile properties of S690QL and S960QL at ambient temperature are presented. The results describe the as-received tensile properties of S690QL and S960QL at a range of strain rates from quasi-static (0.0002 s^{-1}) up to high/dynamic (~100 s^{-1}). The strain rate range extends over the primary strain rate range encountered in offshore or marine in-service conditions (Table 2.4).

The as-received tensile property results of low strength structural steel grade, S235, at quasi-static condition up to 100 s^{-1} strain rate, and S355 at only quasi-static loading condition are also presented in the second part, for comparison to the S690QL and S960QL tensile behaviour and sensitivity to the effect of strain rate in terms of engineering yield strength (taken as 0.2% proof strength throughout this thesis), Y/T ratio and strain hardening parameters. It should be noted that S355 tensile data under QS loading rate are taken from the TWI database and not tested. In this thesis, S235 and S355 are referred to as conventional low strength structural/mild steel.

Finally, in order to support the experimental results and to simulate the material flow stress behaviour at quasi-static and elevated loading rate, finite element analysis was carried out on S690QL and validated using the von Mises flow rule and isotropic hardening available in the ABAQUS code in conjunction with Ramberg Osgood power law tensile properties.

4.2   Chemical composition of S690QL and S960QL under consideration

The chemical compositions of S690QL and S960QL structural steels investigated in this thesis are summarised in **Tables 4.1 and 4.2** for a consideration of the carbon content and micro-alloying elements used to achieve the smaller grain size with improved toughness via the QT production route mentioned in section 2.2.2.

Table 4.1   Chemical composition of S690QL plate delivered in 25 mm thickness

Elements	Mass percent (%) (m/m)
Carbon (C)	0.14
Silicon (Si)	0.29
Manganese (Mn)	1.19
Phosphorous (P)	0.008
Sulphur (S)	<0.002
Chromium (Cr)	0.25
Molybdenum (Mo)	0.15
Nickel (Ni)	0.084
Boron (B)	0.0017
Aluminium (Al)	0.054
Copper (Cu)	0.008
Niobium (Nb)	0.016
Vanadium	0.031
Titanium (Ti)	0.011
Nitrogen (N)	0.002
Oxygen	<0.001

Table 4.2   Chemical composition of S960QL plate delivered in 60 mm thickness

Elements	Mass percent (%) (m/m)
Carbon (C)	0.16
Silicon (Si)	0.21
Manganese (Mn)	1.39
Phosphorous (P)	0.008
Sulphur (S)	<0.002
Chromium (Cr)	0.25
Molybdenum (Mo)	0.49
Nickel (Ni)	0.077
Boron	0.0019
Aluminium	0.051
Copper (Cu)	0.010
Niobium (Nb)	0.013
Vanadium	0.021
Titanium (Ti)	0.007
Nitrogen (N)	0.002
Oxygen	<0.001

4.3   Quasi-static tensile properties of S690QL and S960QL

4.3.1   Uniaxial tensile test results of S690QL and S960QL

Initial uniaxial tensile tests at room temperature were carried out on S690QL to determine how material geometry and/or cross-sections affect the overall plastic deformation (uniform and localised) under the quasi-static condition as shown in **Figure 4.1**, using designations M01 and M02 to represent samples with cross sectional areas of 24 mm^2 and 38 mm^2, respectively. Within the elastic limit, no notable change is observed but a significant difference is noticed in the plastic work. Although for low cross-sectional area (M01) a reduced value of about 20% in

the strain-hardening exponent (n) compared to high cross-sectional area (M02) is obtained as shown in **Table 4.3**, there is a similarity in the plastic work shape prior to necking. A low cross-sectional area gave enhanced percentage reduction in area after necking (non-uniform plastic work deformation or local elongation). The Y/T ratio in **Table 4.3** is taken as the ratio of the 0.2% proof stress and ultimate tensile strength from the engineering stress-strain curve. Also, the linear fit from the logarithmic relationship of the true stress-strain curve ($\sigma=K\varepsilon^{n}$) where σ is the stress, ε is the strain, n is the strain-hardening exponent and K is the strength coefficient, represents the value of the strain-hardening exponent used for the analysis. These definitions and approach to determining the values of Y/T ratio and n have been employed in this thesis.

The result means that elongation and reduction in area are a measure of different responses in the mechanical behaviour of a material and should not be generalized as a means of measuring ductility. Uniform plastic elongation is highly influenced by plastic work hardening, whereas reduction in area is a representation of a local plastic work deformation before fracture. As such, reduction in area is influenced by the necking process and is the most structure-sensitive ductility factor in detecting quality changes in a material's behaviour after necking (*Loveday et al. 2004; Davis 2004*). Therefore, the extent of plastic work deformation does not only depend on the strain-hardening curve but also depends on the specimen geometry and the shape (cross sections) prior to necking formation.

Table 4.3   Effect of specimen geometry on strain-hardening exponent (n)

Specimen No	CSA* (mm^2)	Strain-hardening exponent (n)	Y/T ratio	Strain rate (s^{-1})
M01	24	0.044	0.956	2×10^{-4}
M02	38	0.053	0.955	2×10^{-4}

*CSA is cross-sectional area

Based on the knowledge of the initial tensile testing results, specimens with a cross-sectional area of 24 mm^2 are used for all subsequent tests at quasi-static and high/dynamic loading rates, so that comparisons could be made at different loading rates. A total of number of 18 specimens were tested for S690QL where a total number of 24 specimens were tested for S960QL.
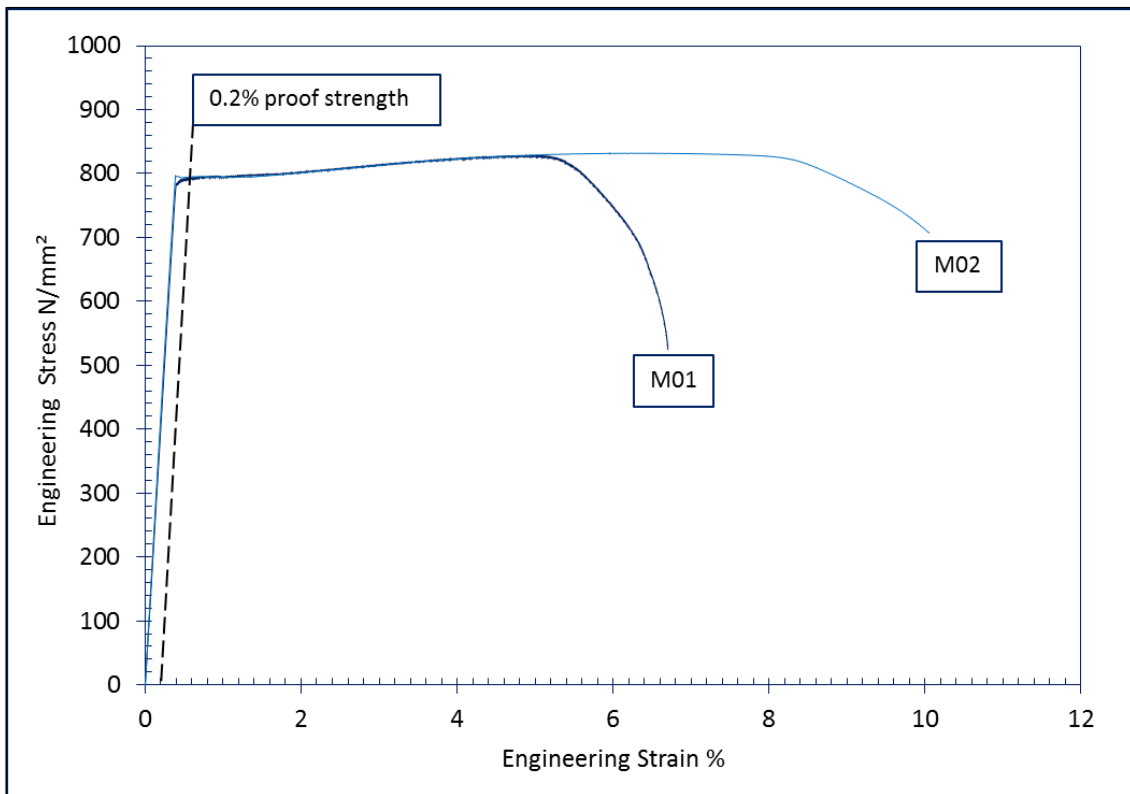
Figure 4.1　　　Effect of specimen geometry on S690QL at quasi-static loading condition.

The quasi-static engineering stress-strain tensile properties at room temperature are summarised in **Table 4.4** for S690QL and S960QL. The true stress-strain characteristics are presented in **Figure 4.2** where the true stresses for S690QL and S960QL are 821 MPa and 917, MPa, respectively.

Table 4.4　　　Quasi-static engineering stress-strain characteristics of S690QL and S960QL

Materials	0.2% Yield Strength (N/mm²)	UTS (N/mm²)	Y/T ratio	Elongation (%)	Strain hardening exponent (*n*)
S690QL	816.9	848.8	0.96	12.89	0.046
S960QL	905.5	952.9	0.95	13.18	0.054
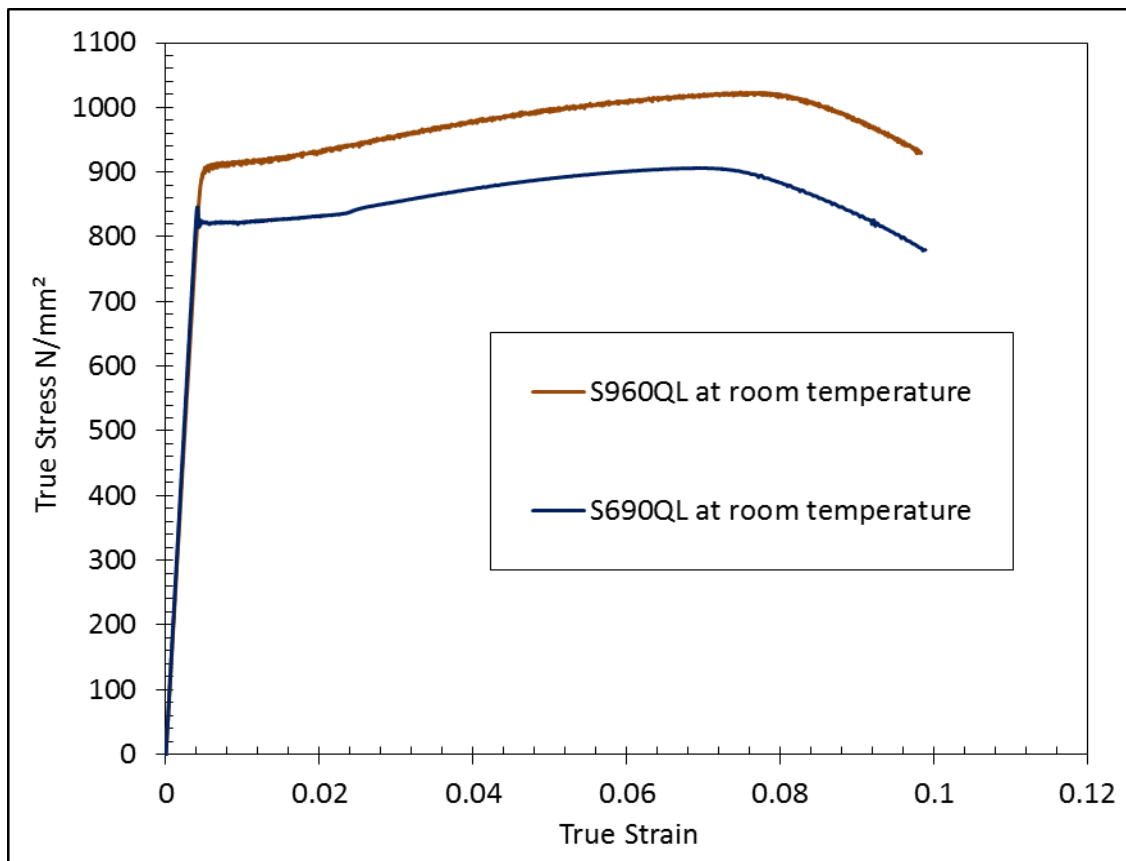
Figure 4.2 Quasi-static (0.0002 s^{-1}) true stress-strain curve for S690QL and S960QL

4.3.2 *Tensile properties of S235 and S355 under quasi-static loading conditions*

The stress-strain characteristics of S235 and S355 representing a low Y/T ratio low strength structural steel grade are shown in **Figure 4.3**. The tensile properties of both steel grades are summarised in **Table 4.5**.

Table 4.5 Quasi-static engineering tensile properties of S235 and S355

Materials	0.2% Yield Strength (N/mm^2)	UTS (N/mm^2)	Strain hardening exponent (n)	Y/T ratio
S235	232.2	328.7	0.144	0.71
S355	420.5	585.0	0.176	0.72
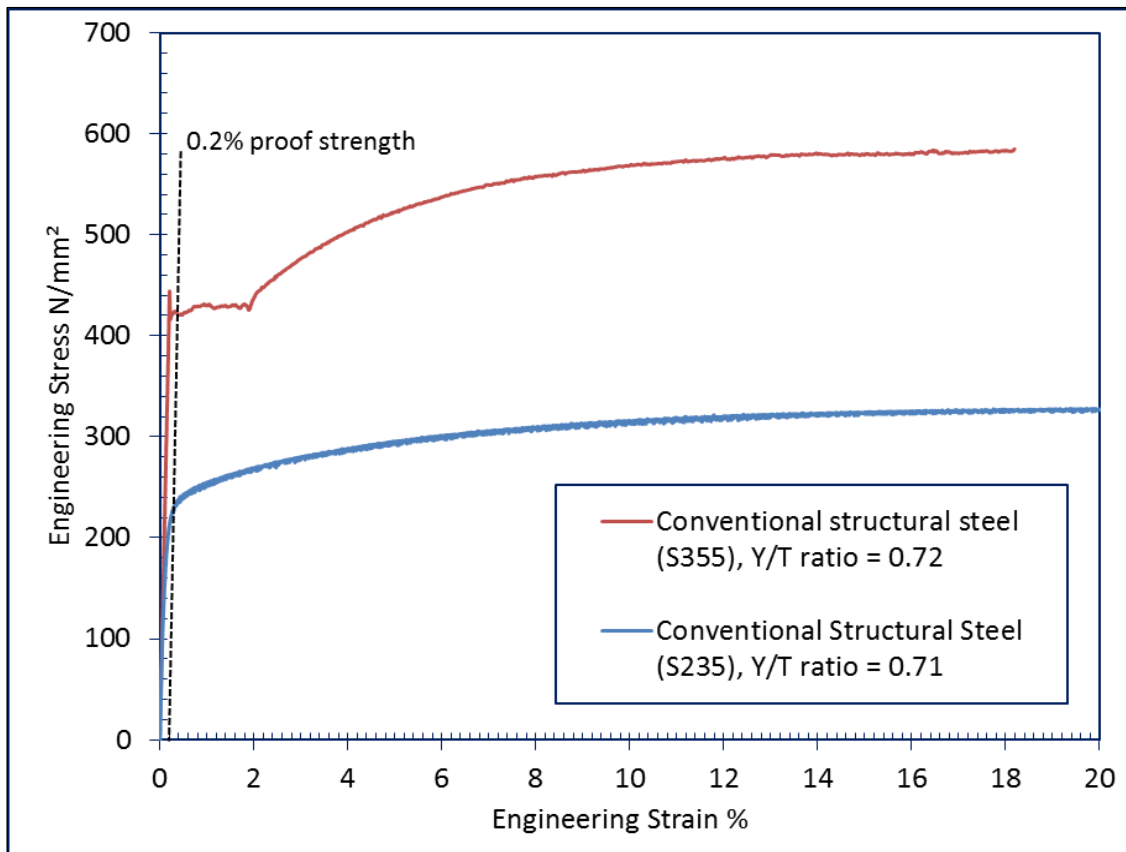
Figure 4.3   Quasi-static engineering stress-strain characteristics of S235 and S355

The results of HSS (S690QL and S960QL) in terms of strain-hardening exponent (n) show that LSS (S235 and S355) have higher values when compared to HSS at quasi-static conditions, part of the requirements that has limited the usage of HSS. However, HSS brings a higher strength level than LSS when a strength-to-weight ratio is important as shown in **Figure 4.4**, when compared to conventional LSS (S235 and S355).
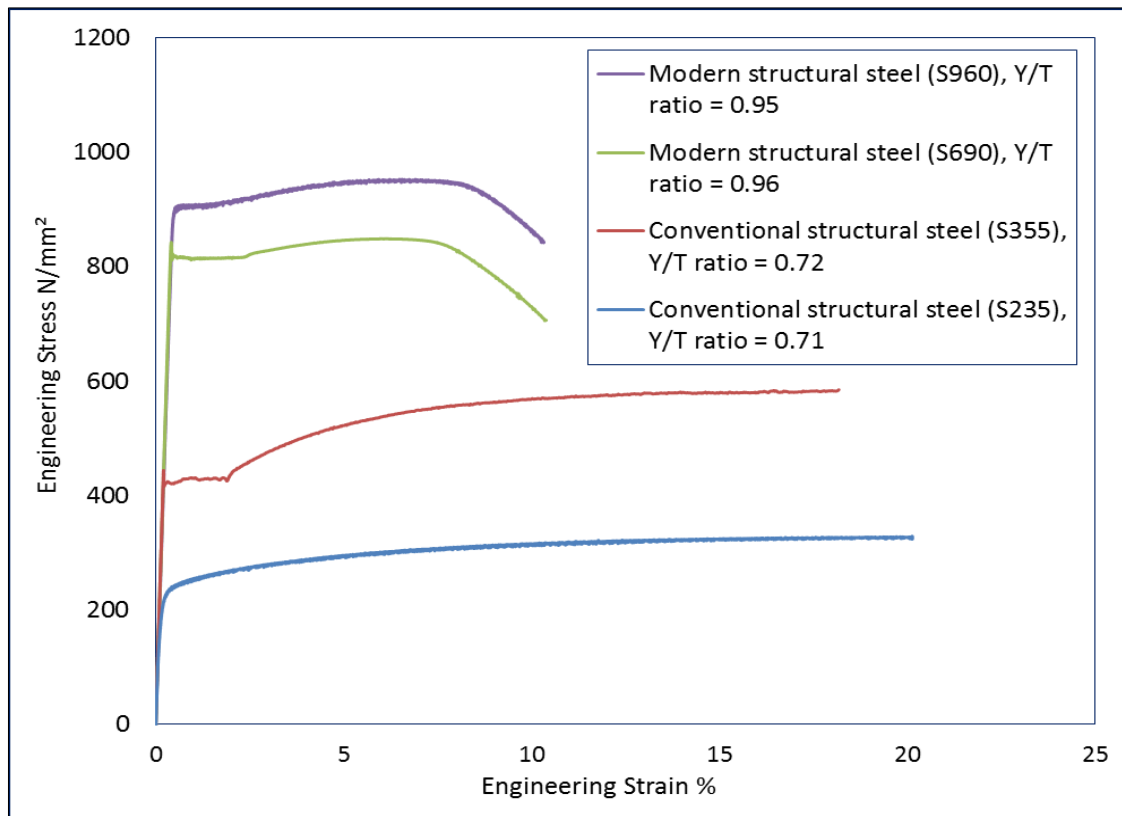
Figure 4.4   Stress-strain characteristics of modern QT high strength structural steel and conventional low strength structural steel grades.

In the following sections, the tensile behaviour of S690QL and S960QL are characterised in order to understand and simulate the possible in-service tensile behaviour. The results are compared to data from literatures at different strain rates for different grades. Also, the results are compared to the prediction from empirical methods based on Johnson Cook (1983 and 1985) given as Eq. (4.1) and the work of Burdekin et al. (2004) given in Eq. (2.11).

$$F = 1 + C \ln(\dot{\varepsilon}^*) \qquad\qquad (4.1)$$

where:

F   represents the flow stress increase factor σ_d/σ_0 (N/mm^2)

σ_d is the dynamic yield stress (N/mm^2)

σ_0 is the quasi-static yield stress (N/mm^2)

C   is the material sensitivity parameter

$\dot{\varepsilon}^*$ is the dimensionless strain rate $\dot{\varepsilon}_p/\dot{\varepsilon}_0$

$\dot{\varepsilon}_p$ represents the equivalent plastic strain rate s^{-1}

$\dot{\varepsilon}_0$ is the reference strain rate taken as 0.0002 s^{-1}

4.4   Characterisation of S690QL and S960QL at high loading rate

4.4.1   Overview

Despite offering significant strength-to-weight advantages, high-strength structural steels, such as S690QL and S960QL, are used only in limited offshore applications. This is due to the lack of material characterisation in regard to their tensile behaviour, with little data available on loading rates other than those typically experienced offshore. The concern is that high strength structural steels with high Y/T ratio >0.90 are obtained at the expense of ductility and strain-hardening capacity, **Figure 4.4**. In this section, the effects of loading rates in terms of strain rate are discussed, and the results are compared against the performance of conventional low strength steel (S235 tested) and data from literatures.

For clarity, since the loading rates in structural engineering are usually considered in terms of strain rates (*Wallin 2011*), the tensile test results in this context are expressed in terms of strain rates as described in sub-section 3.2.2 and summarised in **Table 3.5** based on the understanding from literature, **Table 2.4**. Whilst the fracture mechanical loading rate is mostly expressed in terms of stress intensity factor loading rate for linear elastic conditions, the use of the strain rate to determine a single effective loading rate value in a cracked specimen could lead to a crude estimation in a real scenario (*Wallin 2011*). Therefore, the use of stress intensity factor loading rate as a means of expressing fracture mechanical loading rate has been employed in this thesis for fracture toughness tests only.

4.4.2   Dynamic tensile test results

Comprehensive uniaxial tensile tests were performed to characterise the tensile behaviour of S690QL and S960QL high strength structural steel plates at high strain rates up to 100 s^{-1}. The dynamic tensile test results for S690QL and S960QL are shown in **Figures 4.5 and 4.6**, respectively. The graphs show the full true stress-strain behaviour up to fracture from the QS condition up to 100 s^{-1} strain rates. The results show no significant effect when the loading rate

increases in terms of strain rate ($\dot{\varepsilon}$) from 0.04 s⁻¹ up to 100 s⁻¹ on the tensile properties of S690QL and S960QL. It is worth pointing out that, in **Figures 4.5 and 4.6**, the material exhibits a peak in the yield strength at low strains which becomes more obvious as the strain rate increases, and this is not considered in the analysis as 0.2% proof stress was taken as the yield strength for all configurations.
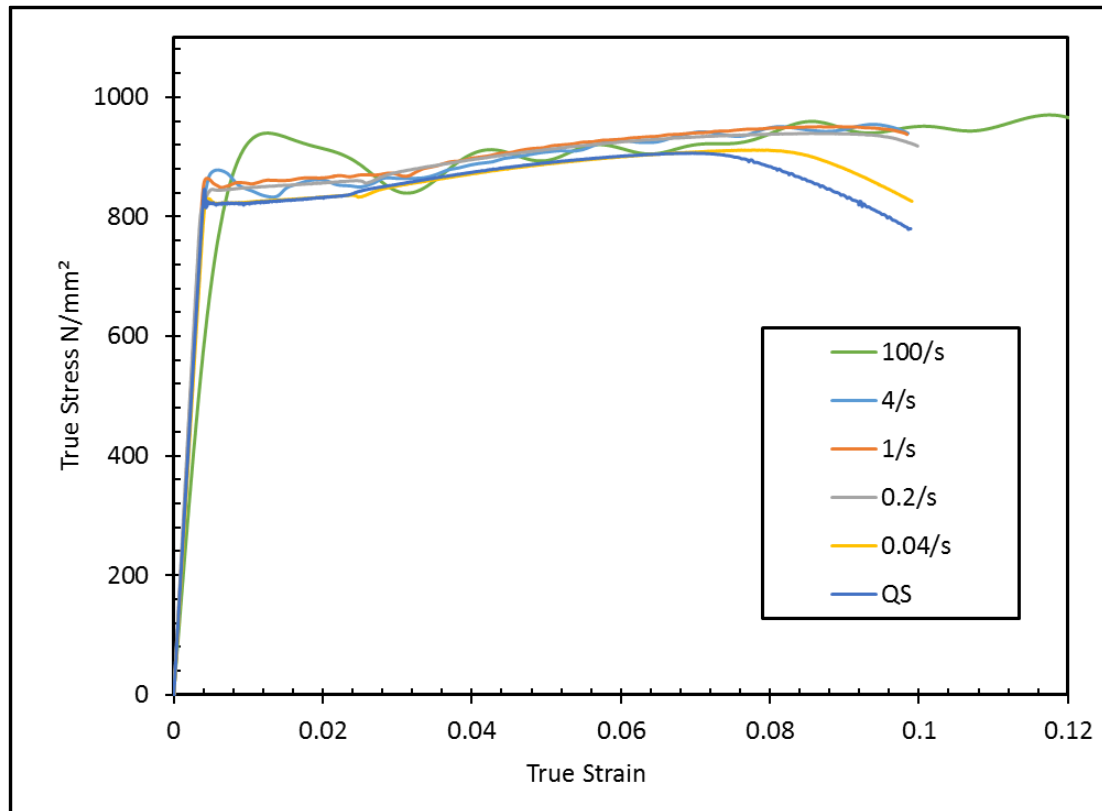
Figure 4.5   Full true stress-strain behaviour of S690QL from QS up to 100 s⁻¹ strain rates.
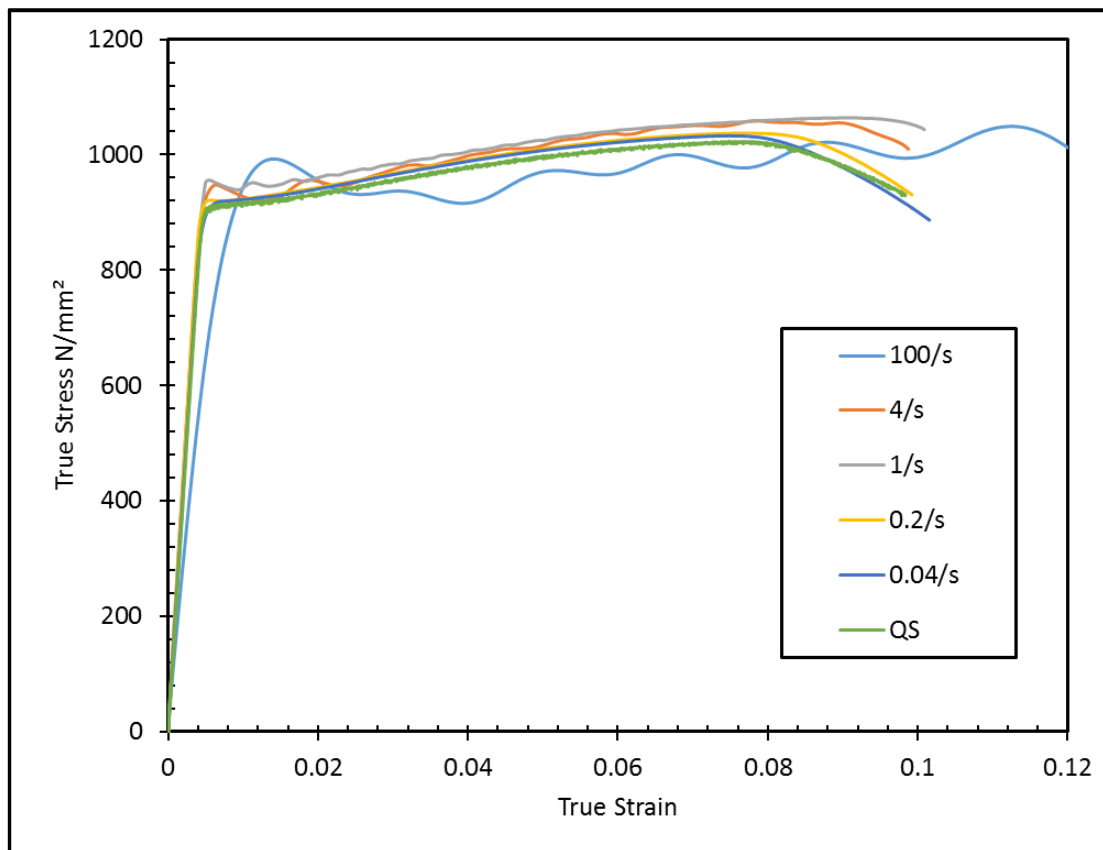
Figure 4.6   Full true stress-strain behaviour of S960QL from QS up to 100 s^{-1} strain rates.

Dynamic tensile test results of S235 representing the structural steel grade with low Y/T ratio <0.85, is shown in **Figure 4.7**. The results as shown in **Figure 4.7**, show that low strength steel grade is more sensitive to the effect of loading rates than HSS (S690QL and S960QL) considered in this research.
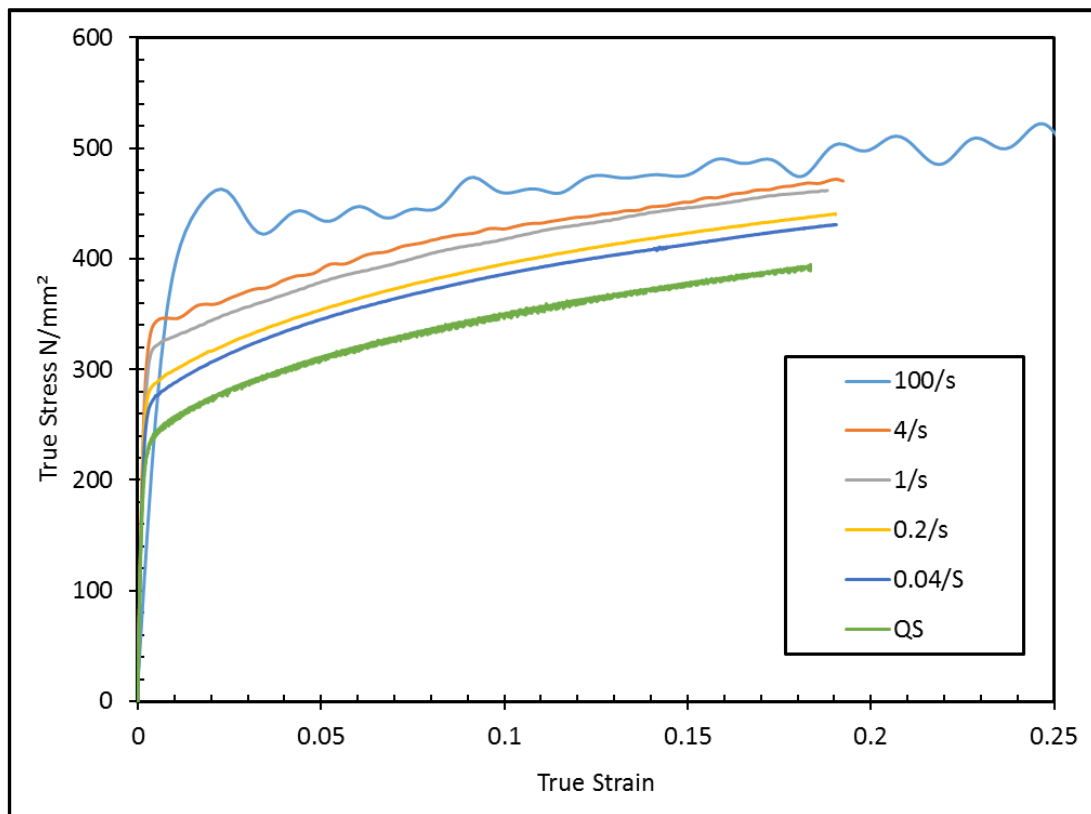
Figure 4.7   Full true stress-strain behaviour of S235 from QS up to 100 s^{-1} strain rates.

Information regarding offshore structures' in-service scenarios under normal and high strain rate conditions revealed that time at maximum force could be around 1.3 s and 0.25 s, respectively. For the tension tests carried out, the corresponding time to maximum force and fracture at 1 s^{-1} strain rate (the critical strain rate considered for offshore cranes) falls around 0.10 s and 0.12 s, respectively for both S690QL and S960QL. This is slightly lower but similar in order of magnitude to those given by (*Walters and Przydatek 2014*) for offshore structures. Based on this understanding more emphasis will be given to strain rates between QS and 4 s^{-1}, however discussion will still include the strain rate at 100 s^{-1}.

Tables 4.6 and 4.7 present data obtained from the tensile tests at QS up to 100 s^{-1} strain rates for S690QL and S960QL, respectively. The coefficient of variation (CV), defined as a ratio of the standard deviation over the mean value from the tests demonstrates good repeatability between the tests for the materials under consideration where for strain rates at 0.2 s^{-1} and 100 s^{-1} for S690QL, the highest CV for yield strength and ultimate tensile strength were observed. It is important to mention that from Table 4.7 for S960QL, variation is observed in the test at QS and 0.04 s^{-1} data. This is due to the hardness variation and the position where the test specimen is manufactured from as there is a limited test material delivered in 60 mm thickness

119

for S960QL. However, the data from test 1 does compare well with the tensile properties reported in the test certificate (Table 3.4) under QS conditions when the test specimen is taken close to the surface. Also, in terms of degree of sensitivity, the results from the two tests are representation of the effect of strain rate which is relatively unchanged as strain rate increases.

The tensile test results data of S235 to represent LSS with low Y/T ratio at QS up to 100 s^{-1} strain rates are presented in **Table 4.8** where 6 specimens were tested. The degree of sensitivity to the effect of strain rates is discussed further in the next sub-section 4.4.3, where the test results from this work are compared to the data taken from literatures at different loading rates to ascertain the dynamic amplification factor due to strain rate effect.

Table 4.6   Quasi-static and dynamic tensile testing results at different strain rates for S690QL

Strain rate	0.2% Yield Strength (N/mm^2)			UTS (N/mm^2)		
	Test 1	Test 2	CV %	Test 1	Test 2	CV %
0.0002 (QS)	810.1	816.9	0.6	843.7	848.8	0.4
0.04	809.3	817.5	0.7	843.5	848.2	0.4
0.2	816.9	840.0	2.0	850.0	871.5	1.8
1	838.1	846.7	0.7	868.4	877.0	0.7
4	878.7	866.5	1.0	890.4	877.9	1.0
100	861.5	887.3	2.1	868	881.0	1.1

Table 4.7   Quasi-static and dynamic tensile testing results at different strain rates for S960QL.

Strain rate	0.2% Yield Strength (N/mm^2)			UTS (N/mm^2)		
	Test 1	Test 2	CV %	Test 1	Test 2	CV %
0.0002 (QS)	905.8	845.4	4.9	952.9	912.6	3.1
0.04	911.0	860.8	4.0	962.6	919.7	3.2
0.2	915.0	903.7	0.9	965.9	951.9	1.0
1	942.4	944.0	0.1	982.5	984.9	0.2

4	935.6	936.7	0.1	980.5	976.0	0.3
100	955.6	958.6	0.3	938.0	955.9	1.3

Table 4.8   Quasi-static and dynamic tensile testing results at different strain rates for S235

Strain rate (s^{-1})	0.2% Yield Strength (N/mm^2)	UTS (N/mm^2)	Strain-hardening exponent (n)	Y/T ratio
0.0002 (QS)	232.2	328.7	0.144	0.706
0.04	266.6	356.9	0.137	0.747
0.2	281.3	365.0	0.131	0.771
1	317.7	384.7	0.118	0.826
4	340.0	390.4	0.101	0.871
100	382.3	379.9	0.071	1.006

4.4.3   Sensitivity of mild steel, S690QL and S960QL under high loading rate

The dependence of the dynamic increase factor (DIF), that is, the ratio of dynamic yield strength and quasi-static yield strength (σ_d/σ_0) on strain rate ($\dot{\varepsilon}$) in comparison with other data from literatures as well as the empirical method predictions is presented in **Figure 4.8**. The input data for the empirical prediction used in Eqs. (2.11) and (4.1) are summarised in **Tables 4.9 and 4.10**, respectively.

Test results and data presented in **Figure 4.8** shows how increase in strain rate amplifies the yield stress, with the degree of sensitivity dependent on the nominal yield strength. The results of HSS (S690QL and S960QL) under consideration as compared to other data on the figure is a confirmation that strain rate sensitivity decreases as material strength increases. S690QL and S960QL are less sensitive to the effect of strain rate up to the loading rate considered in this thesis. The DIF as a result of the elevated strain rate on the yield stress of S235 tested with Y/T ratio <0.85 is high, whereas, the degree of sensitivity of S690QL and S960QL with Y/T ratio >0.95 is relatively unaffected by the strain rate effect. About 66% dynamic amplification was observed on the yield stress of low strength steel S235 from quasi-static to 100 s^{-1} strain rates

which is an equivalent of about 1.66 DIF as shown in **Figure 4.8**. In comparison with the prediction based on empirical equations, Johnson Cook prediction using Eq. (4.1) seems a better march with S690QL and S960QL test results. However, the prediction based on Burdekin et al. equation (Eq. 2.11) marches the test results of S235 reasonably well.

This effect (strain rate sensitivity) is less notable on the HSS (S690QL and S960QL) whose dynamic amplification effect on yield stress from QS to 100 s^{-1} is <10% and DIF of about 1.1 maximum, **Figure 4.8**. The test results of S690QL (σ_0 = 816.7 MPa) when compared to the data from HSE report 2001 where A514 (760 MPa) with a DIF of about 1.3 at 10 s^{-1} strain rates, further corroborate the fact that the degree of sensitivity of steel decreases with increasing nominal yield strength as described in sub-section 2.4.2. For clarity, the DIF used in **Figure 4.8**, represents the ratio of the dynamic engineering stress and quasi-static engineering stress.

Table 4.9   Input data in Eq. (4.1) based on Johnson Cook empirical method

Input parameter	S235	S690QL	S960QL
σ_0 (MPa)	232.2	816.7	905.8
Strain rate parameter (C)	0.0515	0.0070	0.0044
$\dot{\varepsilon}_0$ (s^{-1})	0.0002	0.0002	0.0002

Table 4.10   Input data in Eq. (2.11) based on (Burdekin et al. 2004) empirical prediction

Input parameter	S235	S690QL	S960QL
σ_0 (MPa)	232.2	816.7	905.8
Assumed material parameter S (MPaK)	50000	50000	50000
$\dot{\varepsilon}_{static}$ (s^{-1})	0.0002	0.0002	0.0002
A	10^8	10^8	10^8
T (K)	293	293	293
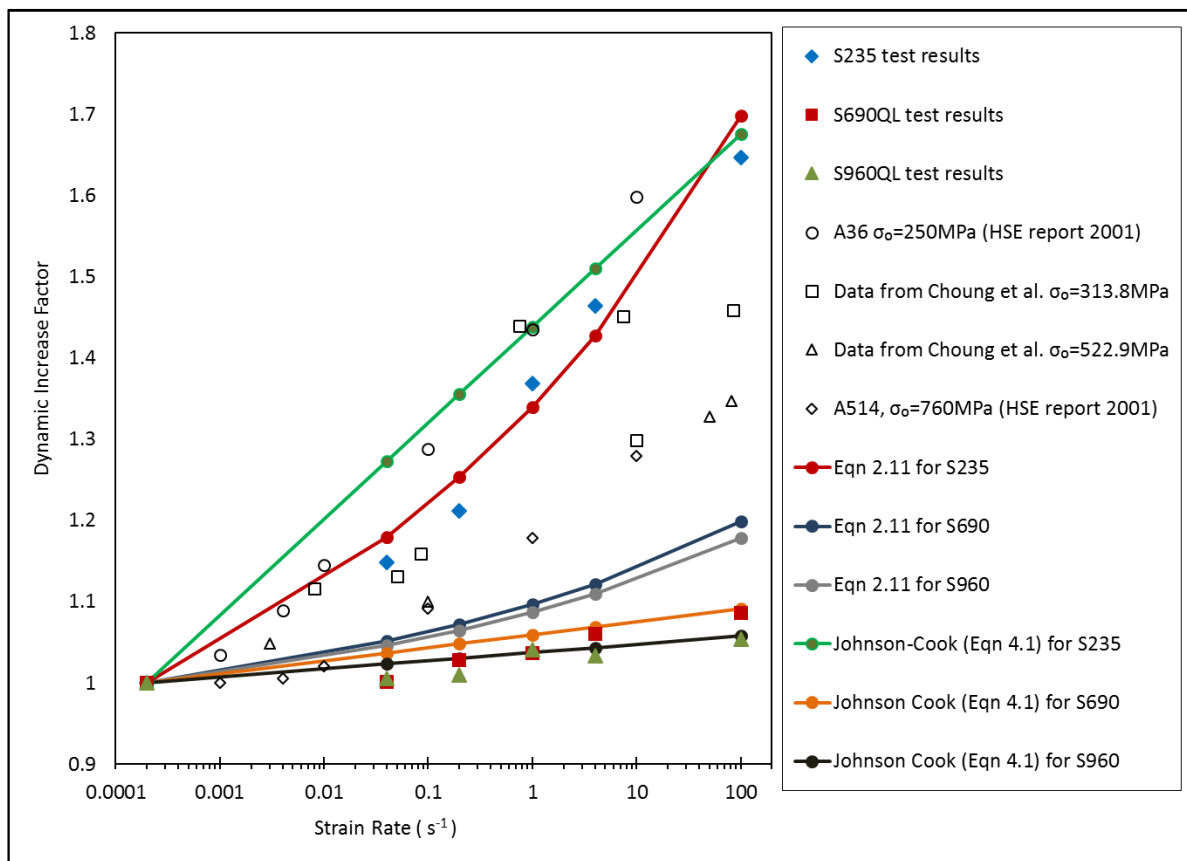
Figure 4.8   The effect of strain rate on the yield stress of S690QL and S960QL in comparison with literatures and empirical equation predictions from QS condition up to 100 s^{-1}

It could be said that strain rate sensitivity depends on the nominal yield strength with the degree of sensitivity of ferritic steels decreasing as the nominal yield strength increases. Therefore, it means that a reduced degree of strain rate sensitivity is expected as a result of a combination of metallurgical effects (finer-grain size microstructure, chemical compositions and production route). A higher number of dislocations are expected during plastic deformation resulting in a higher flow stress. Further restriction of the dislocation motion via grain size reduction creates a higher dislocation density. Higher dislocation density impedes the free mobility of dislocations, and thus reduces the degree of sensitivity of HSS to increased loading rates. For this reason, the metallurgical and production techniques used to achieve the strength level of S690QL and S960QL were studied and discussed in section 4.4.5.

Another important inference is the effect of strain rate on the strain at the beginning of strain hardening observed as the most sensitive parameter to the effect of strain rate. This is also observed in the conventional low strength structural steels with Y/T ratio <0.85, and sensitivity

to strain rate usually tends to decrease at room and low temperatures as the plastic strain increases (*Choung et al. 2013*). About 22% and 15% differences in strains between QS and 4 s^{-1} loading rates were recorded at the beginning of strain hardening, which decreases to about 1.7% and 0.75% at 5% plastic strain for S690QL and S960QL, respectively. This implies that strain rate sensitivity decreases as the plastic strain increases at ambient temperature.

Since yield strength is linearly related to the logarithm of the strain rate (*Francis et al. 1978*), it follows that a semi-logarithmic graph can be used to represent the flow stress increase factor dependence on dimensionless strain rate, **Figures 4.9 and 4.10**, given in Eq. (4.1) (Johnson Cook 1985; *Breuk 2003*).
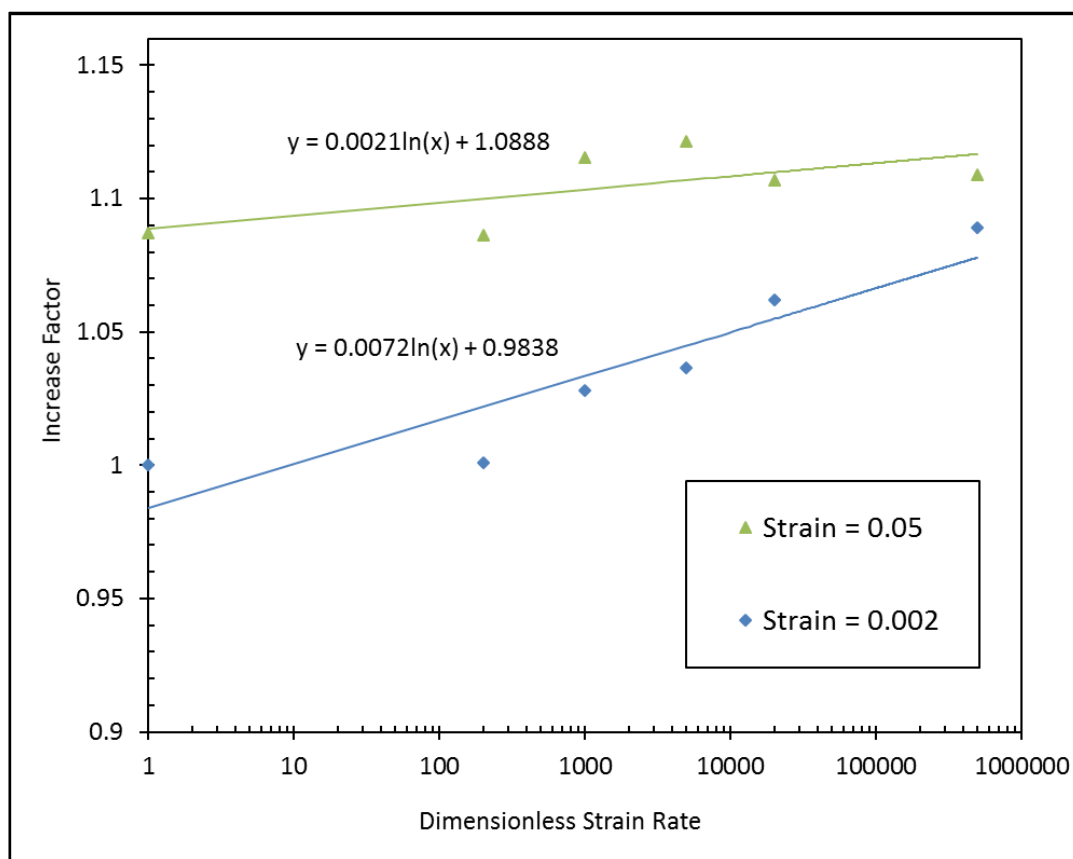
Figure 4.9   Flow stress increase factor (σ_d/σ_0) dependence on the dimensionless strain rate $\dot{\varepsilon}_p/\dot{\varepsilon}_0$ for S690QL. Reference strain $\dot{\varepsilon}_0$ taken as 2×10^{-4} s^{-1}.
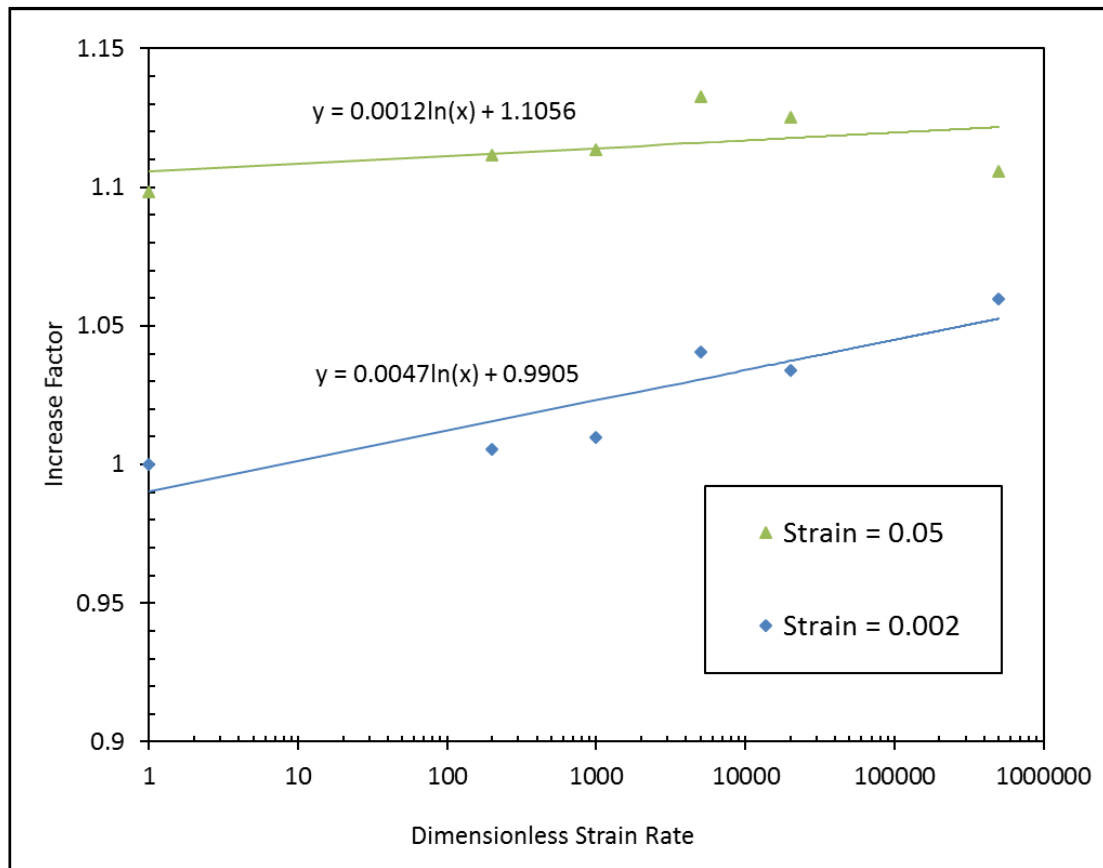
Figure 4.10   Flow stress increase factor (σ_d/σ_0) dependence on the dimensionless strain rate $\dot{\varepsilon}_p/\dot{\varepsilon}_0$ for S960QL. Reference strain $\dot{\varepsilon}_0$ taken as 2×10^{-4} s^{-1}.

Regression equations, which describe the relationships between DIF and strain rates, were produced from the experimental data obtained from the tests. Eqs. (4.2) and (4.3) can be used to extrapolate the true stresses beyond 100 s^{-1} if needed but this is out of the scope of this thesis and will not be discussed.

$$DIF = 0.007\ln(\dot{\varepsilon}) + 1.0439 \qquad\qquad (4.2)$$

$$DIF = 0.0044\ln(\dot{\varepsilon}) + 1.0293 \qquad\qquad (4.3)$$

4.4.4   Effect of loading rates on Y/T ratio and strain-hardening exponent

The Y/T ratio only becomes relevant in the post-yield behaviour of steels, which represents the ability to withstand plastic loading and as a measure of deformation capacity. For designs based on elastic loading, i.e. stresses kept below yield, the strain-hardening characteristics beyond yield should not matter strongly in the design. **Figure 4.11** shows that the Y/T ratio for S235 grade mild steel increased from around 0.7 at quasi-static conditions, steadily up to around 1

125

at 100 s^{-1}. The S690QL and S960QL Y/T ratio kept fairly constant, ranging between 0.95 and 1 throughout the strain rate range tested.

Also, since the strain-hardening exponent (n) determines the plastic deformation performance of steel, the strain-hardening exponent was determined using the power law approach. A downward trend was observed on the n value of S235 as the strain rate increases from QS to 100 s^{-1}. This shows that there is tendency of a reduced n value at elevated strain rate similar to an offshore in-service loading condition. The higher n value reported under QS condition; a condition often considered for LSS usage above HSS in terms of plastic deformation capacity could mean a lower n value at higher strain rate. Whereas, for the HSS (S690QL and S960QL), n kept fairly constant at up to 4 s^{-1} strain rates but dropped at 100 s^{-1}, **Figure 4.12**.
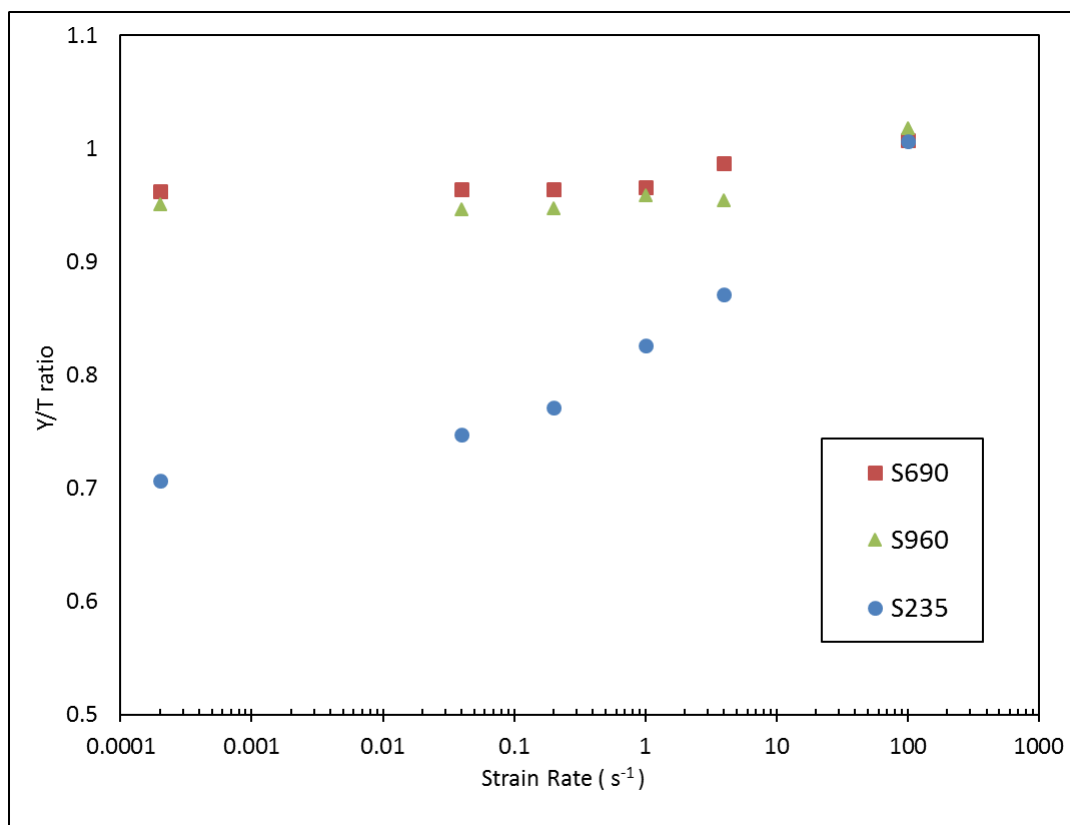
Figure 4.11   The effect of strain rate on the Y/T ratio of LSS (S235) and HSS (S690QL and S960QL).
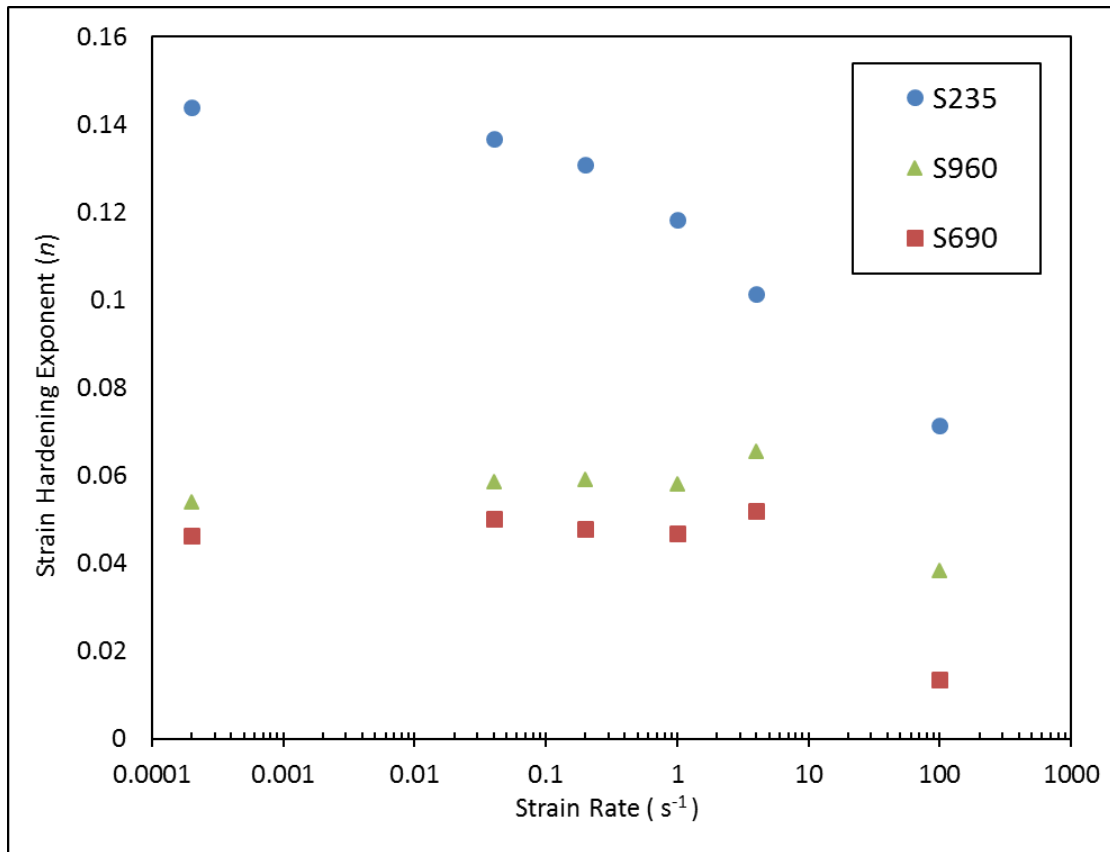
Figure 4.12   Effect of strain rate on the strain-hardening exponent (*n*) of LSS (S235) and HSS (S690QL and S960QL).

A relationship between Y/T ratio and *n* has been developed (*Bannister 1999; Bannister et al. 2000*). The expression in Eq. (4.4) provides a conservative lower bound fit for calculating *N* from Y/T ratio, **Figure 4.13**, where *N* represents strain-hardening exponent used by Structural Integrity Assessment Procedure for Europe (SINTAP). From **Figure 4.13**, it is important to point out that the materials *N* value may look the same, but they do not have the same tensile properties. S690QL, delivered in 25 mm thickness has nominal yield strength of about 817 MPa and 0.96 Y/T ratio, whereas S960QL delivered in 60 mm has nominal yield strength of about 906 MPa and Y/T ratio 0.95. This is important to point out because it would help the users to have clear information about the tensile performance of these steel grades with varying thickness delivery conditions.

$$N = 0.3[1 - (Y/T)] \qquad\qquad (4.4)$$
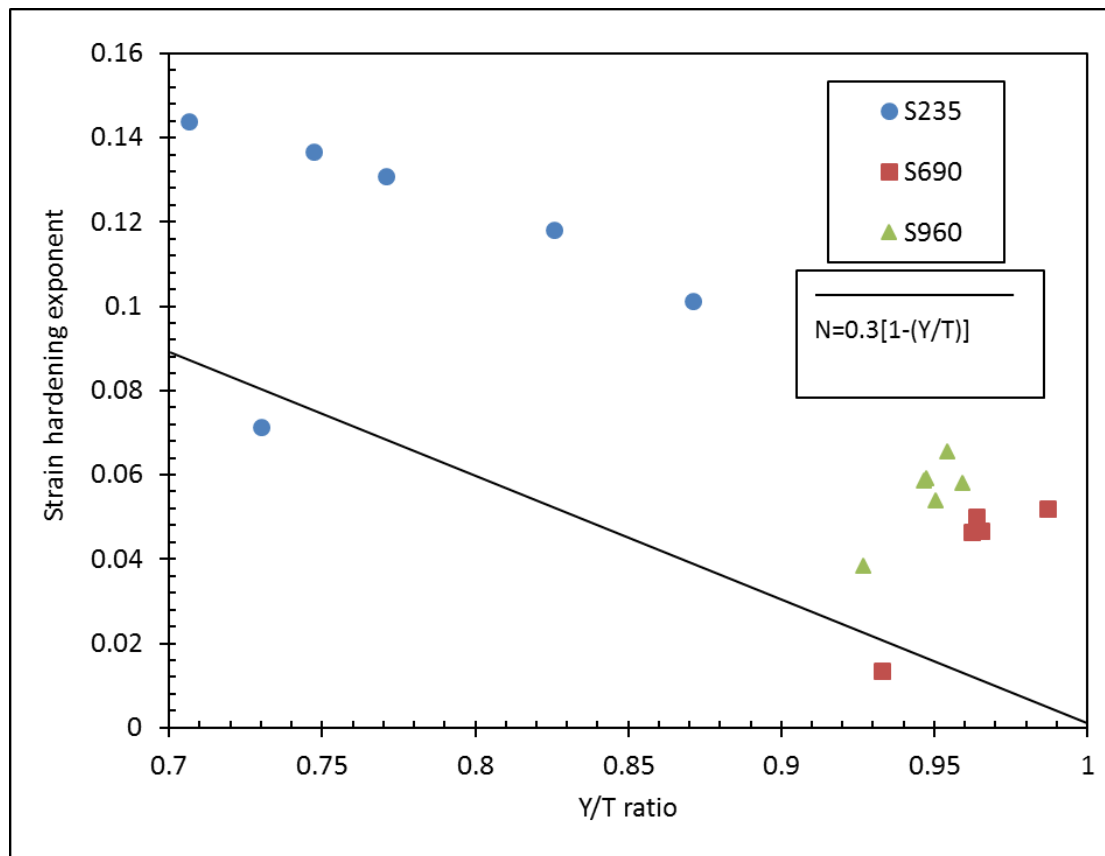
Figure 4.13   A conservative lower bound fit for calculating strain hardening exponent (N) from Y/T ratio using SINTAP approach, Eq. (4.4) (*Bannister et al. 2000*).

4.4.5   *Metallographic examination*

Traditionally, alloying elements such as carbon and manganese added to steel increase nominal yield strength, with detrimental effects on the fabrication properties of steels, in particular, weldability. To avert this effect, carbon content in modern steels is limited, along with a high degree of cleanliness and typical sulphur and phosphorus levels of <0.005% and <0.010%, respectively, implemented for good toughness and through-thickness homogeneity (*Healy and Billingham 1995*). Modern production routes such as Quenched and Tempered (QT), Thermomechanically Controlled Rolled (TMCR) or Accelerated Cooled (AC/TMCP) were developed to promote fine-grained and homogeneous structures with higher strength, thereby improving the combination of strength level and toughness in modern and high performance HSS. These production processes and/or compositions have less effect on the ultimate tensile strength but an incremental effect on the nominal yield strength, and consequently high Y/T ratio. The increase in nominal yield strength of steel predominantly achieved via alloying and

heat treatment, affects the degree of sensitivity to strain rate because of the fine-grain size achieved during the process.

Metallographic examination was carried out to determine to some extent the effect of grain size on the strain rate sensitivity. The metallographic examination shows a variation in grain size of the S690QL and S960QL under consideration as compared to S235. **Figure 4.14** shows the examination of impurities (high sulphur content) from S235 micrograph. On the other hand, S690QL and S960QL showed a fine-grained size structure and high degree of cleanliness with typical sulphur and phosphorus levels of <0.002% and <0.009%, respectively, **Figures 4.15 and 4.16**. There is no doubt that the tempered martensite structure, such as achieved in S690QL and S960QL quenched after austenising above room temperature and rapid cooling in water, would have a different degree of rate sensitivity compared to steel grades produced via a Normalised (N) heat treatment route, heated slightly above the temperature where its austenite totally changes to a ferritic-perlitic structure followed by slow cooling. It should be noted that the micrographs shown in **Figures 4.15 and 4.16** refer to as-received grain size material properties.
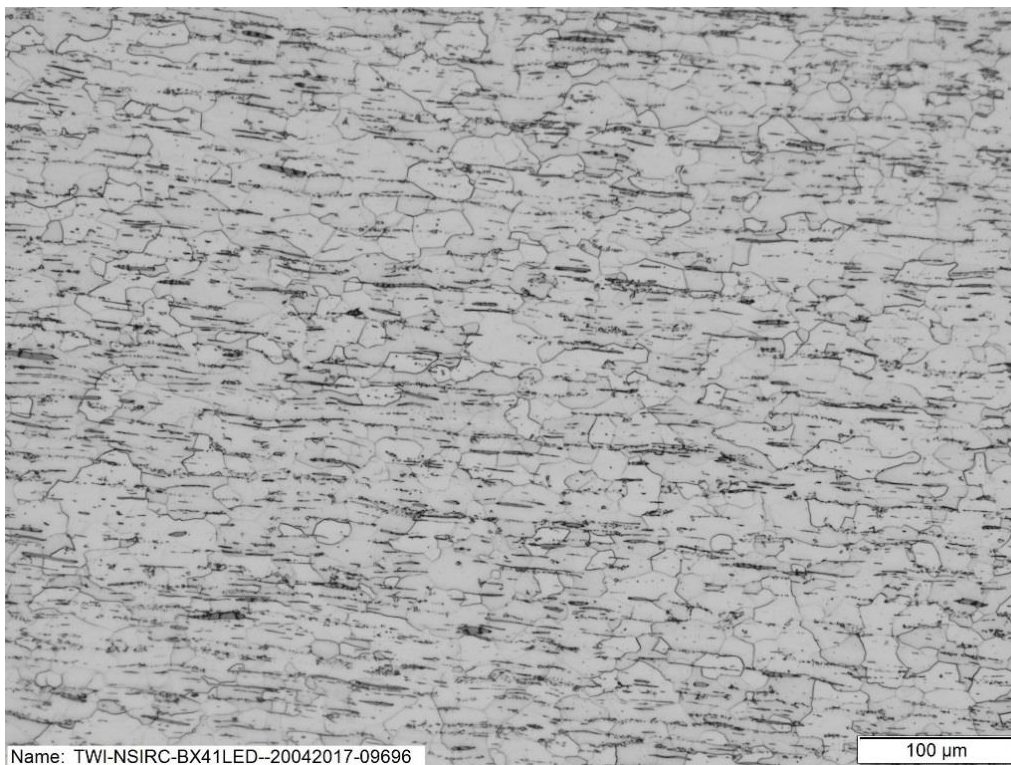
Figure 4.14   Micrograph of Mild Steel (S235) etched with 2% Nital.
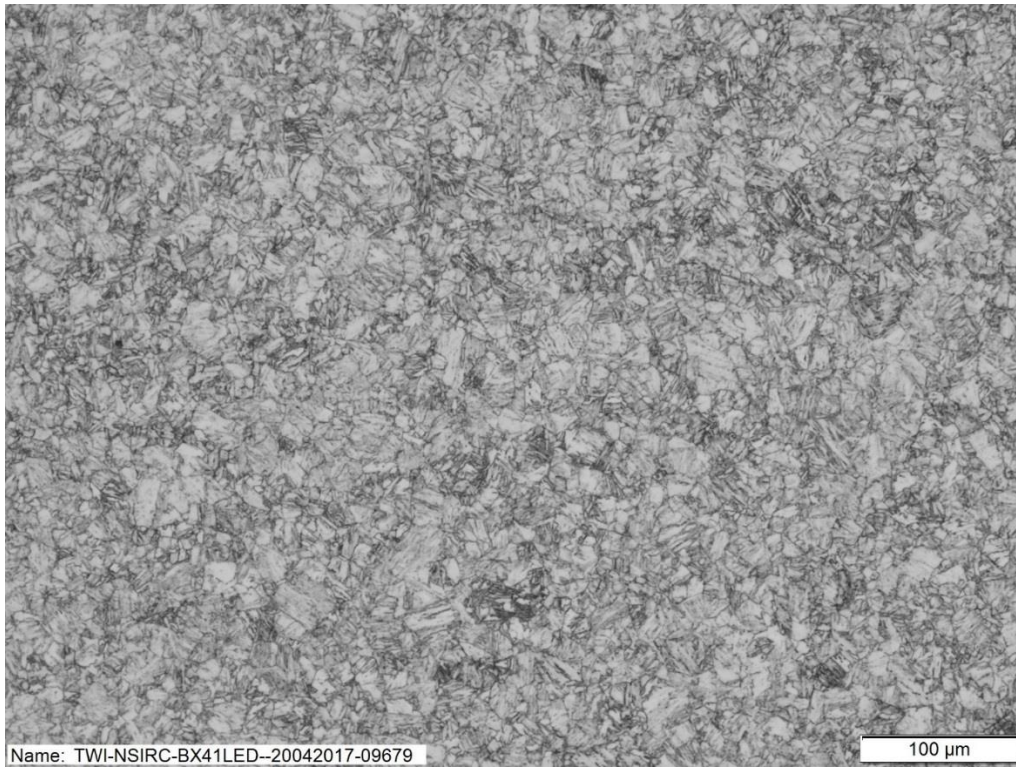
Figure 4.15   Micrograph of S690QL etched with 2% Nital.
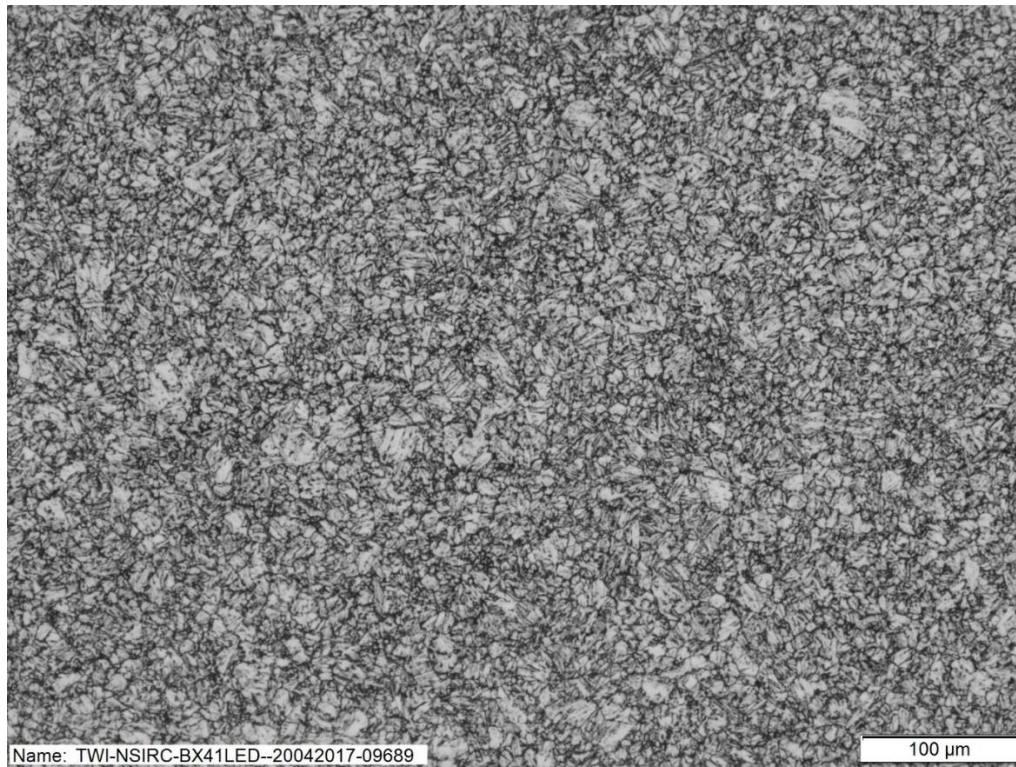
Figure 4.16   Micrograph of S960QL etched with 2% Nital.

The grain size was determined according to ASTM E112, as given in **Table 4.11**. From the results, the grain size varies from 0.021 mm to 0.008 mm; a larger grain size was observed in S235 while S960 has the smallest. Obviously, the production routes have an effect on the grain size which influences the strength level. Therefore, it can be said that among other factors the degree of strain rate sensitivity depends on the production routes, chemical compositions and consequently a finer-grained structure with less sensitivity is recorded when the nominal yield strength increases.

Table 4.11   Calculated grain size according to ASTM E112

Materials	ASTM grain size	Mean grain diameter (mm)
S235	8	0.021
S690	10	0.011
S960	11	0.008

4.5   Material model

As mentioned in section 3.3, the main purpose of the FE analysis is for the prediction of crack driving force and to determine the effect of loading rate on the rate of crack mouth opening displacement which cannot be determined during the experimental tests using rate dependent model derived from the experimental tension tests. To do this, a validated material model is required for the purpose. In this section, the results of the material model developed for S690QL is discussed and validated for further parametric study beyond the scope of this work.

A linear static analysis has been used in this study because the load case versus time shows a linear relationship and applying dynamic analysis does not change the results, **Figure 4.17**. The von Mises flow rule and isotropic hardening condition available in the ABAQUS code where the isotopic hardening behaviour assumes that S690QL has the same physical property when measured in different directions has been employed. An elastic-plastic FE model representing the exact tensile test specimen geometry was generated, with gauge length of 50 mm, **Figure 4.18**, assuming that the shapes of hardening are identical at different loading rates which are a function of the equivalent plastic strain rate ($\dot{\varepsilon}_{pl}$) given as Eq. (3.10).

To define the plastic and hardening properties, two methods were used. Firstly, the direct engineering stress-strain data obtained from the tension tests were converted to the true stress-true strain characteristics using Eq. (3.3) and (3.4). The true strain is then converted to equivalent plastic strain using Eq. (4.5).

$$\varepsilon_{pl} = \varepsilon - (s/E) \tag{4.5}$$

where, ε_{pl} is the equivalent plastic strain, ε and s represent the true strain and true strain, respectively, and E is the Young's Modulus.

The second method uses modified Ramberg-Osgood (RO) power law (*Ramberg and Osgood 1943*) to represent the tensile properties based on the experimental tensile data. The data were generated using Eq. (4.6). The first term on the right side represents the elastic part of the strain (σ/E), while the second term accounts for the plastic part $\alpha \frac{\sigma_0}{E} \left(\frac{\sigma}{\sigma_0} \right)^{n-1}$.

$$\varepsilon = \frac{\sigma}{E} + \alpha \frac{\sigma_0}{E} \left(\frac{\sigma}{\sigma_0} \right)^{n-1} \tag{4.6}$$

where $\alpha \frac{\sigma_0}{E}$ represents the yield offset taken as 0.002, $\sigma = 817$ MPa, $E = 212$ GPa and n is the RO hardening parameter derived from curve fitting, **Figure 4.19**. The summary of the input data is presented in **Table 4.12**

Table 4.12   Summary of input data to material model using direct experimental and RO data

Model	Displacement (mm)	Yield stress ratio (R)	Young's Modulus (E) GPa	Poisson's ratio (v)	Gauge length (mm)	Step time used
QS	5.20	1	212	0.3	50	1
1	5.17	1.044	212	0.3	50	0.1034
4	5.18	1.054	212	0.3	50	0.0311
100	9.50	1.076	212	0.3	50	0.0019

NB: The yield stress ratio (R) is calculated using Eq. (4.2) from curve fitting of the experimental data.
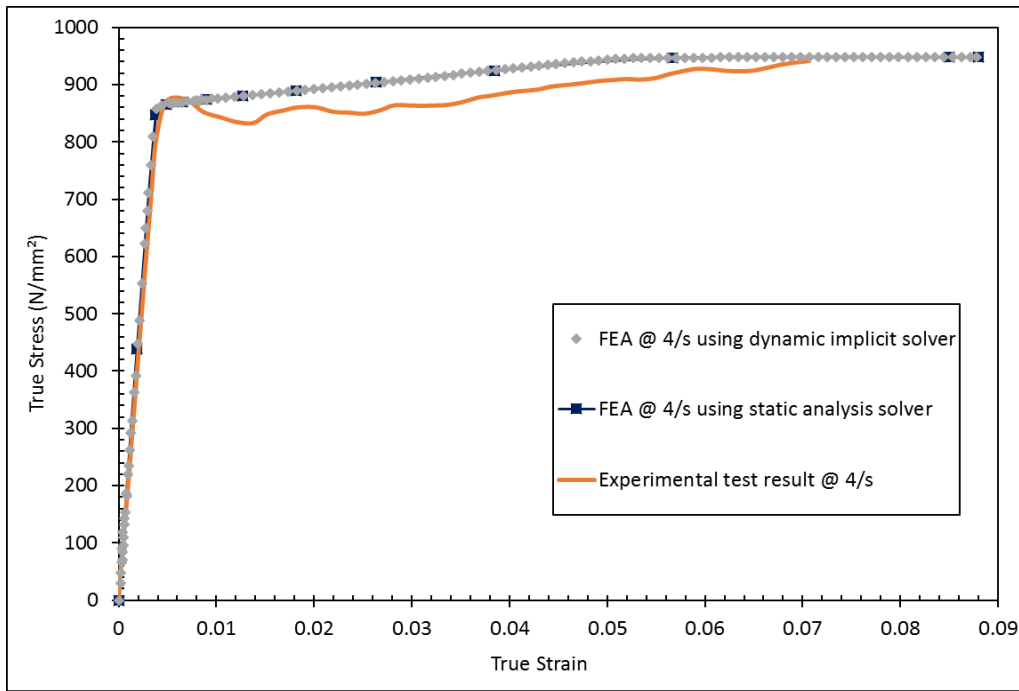
Figure 4.17   Comparison using dynamic implicit solver and static analysis method in ABAQUS code.
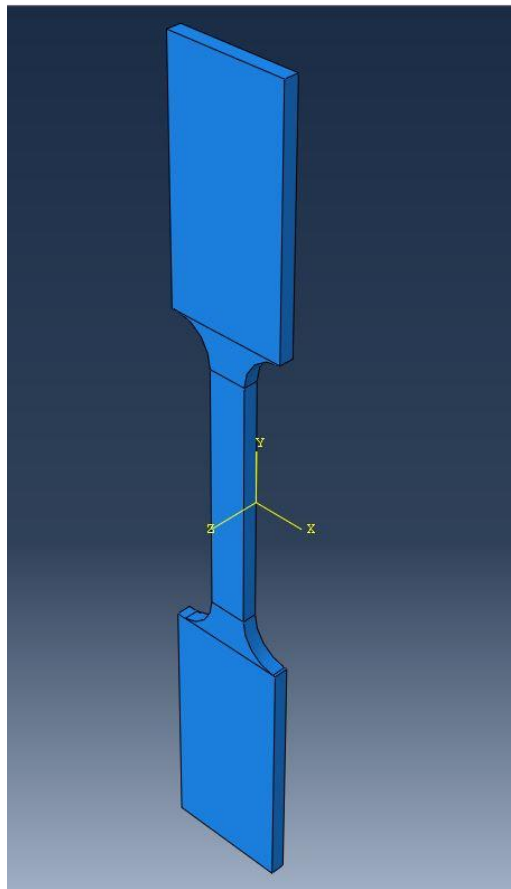
Figure 4.18   FEA tensile model generated with partitioning.

133
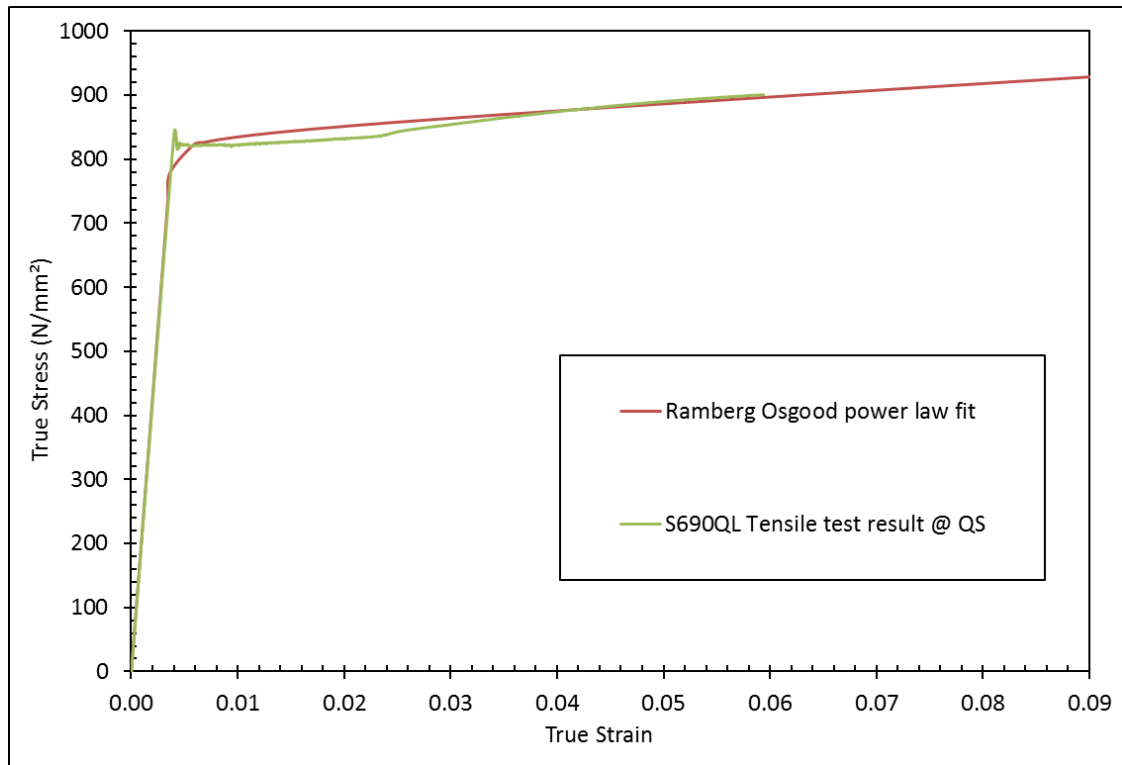
Figure 4.19   Stress-strain characteristics used for the FEA

4.5.1   *Results and Discussion*

Initial FEA results under quasi-static conditions show good agreement with the experimental results. The result compares well with the direct experimental tensile data and the RO power law for the true stress-true strain relationship as shown in **Figure 4.20**. Therefore, at elevated loading rate direct experimental tensile data and modified RO power law true stress-true strain relationship used for flow stress comparison.

At elevated loading rates, in this case 1 s^{-1} and 4 s^{-1} displacement (*DY*) up to UTS was applied in conjunction with the time period of the analysis (Δ) to achieve a crosshead speed (assuming a constant speed) of 50 mm/s and 167 mm/s, respectively, in accordance with the experimental tensile results as shown in **Figure 4.21**. The same load increments (about two hundred) were used throughout the numerical analysis including the quasi-static FEA.

Rate dependent yield stress ratios of 1.044 and 1.054, as given in Table 4.12 using Eq. (4.2) were used at 1 s^{-1} and 4 s^{-1}, respectively. The results using modified RO power law data is presented in **Figure 4.22** where the rate dependent input parameter was unchanged. The FEA results at QS, 1 s^{-1} and 4 s^{-1} from both datasets compare well with the experimental tensile test results with marginal difference observed in the flow stress at QS due to the appearance of

lüders plateau band in the QS experimental data which disappears as loading rate increases. Therefore, the material model for S690QL can be used to predict the flow stress at 10 s^{-1} which was not tested and above 100 s^{-1}, but care must be taken when using the model to predict beyond 100 s^{-1}.
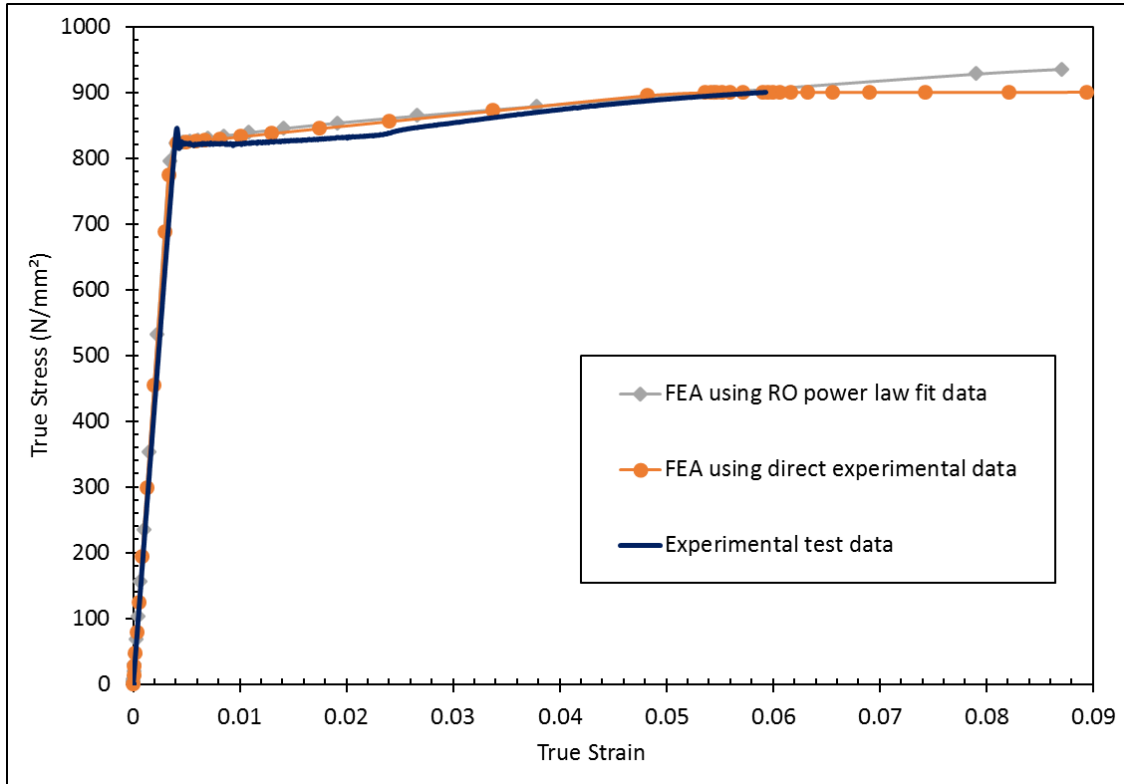
Figure 4.20   Quasi-static FEA true stress-strain results based on the direct experimental data and RO power law fit data.
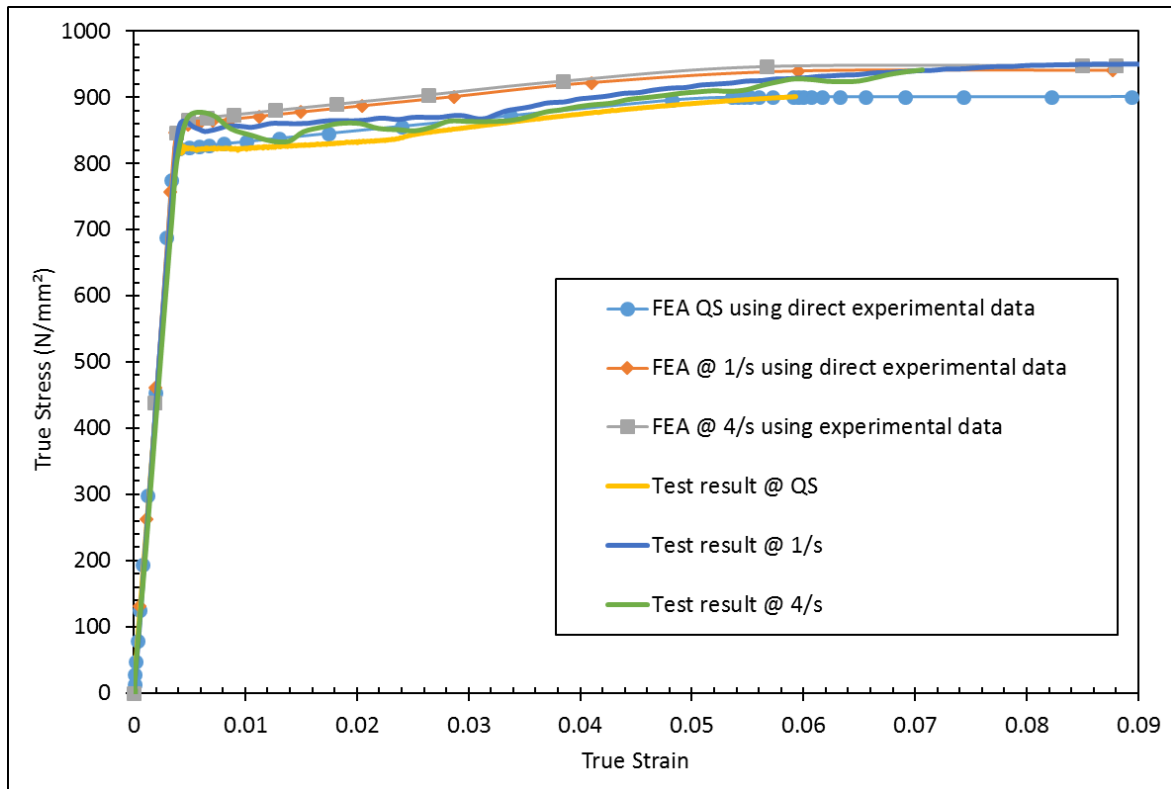
Figure 4.21   FEA results at QS and elevated loading rates using experimental tensile data.
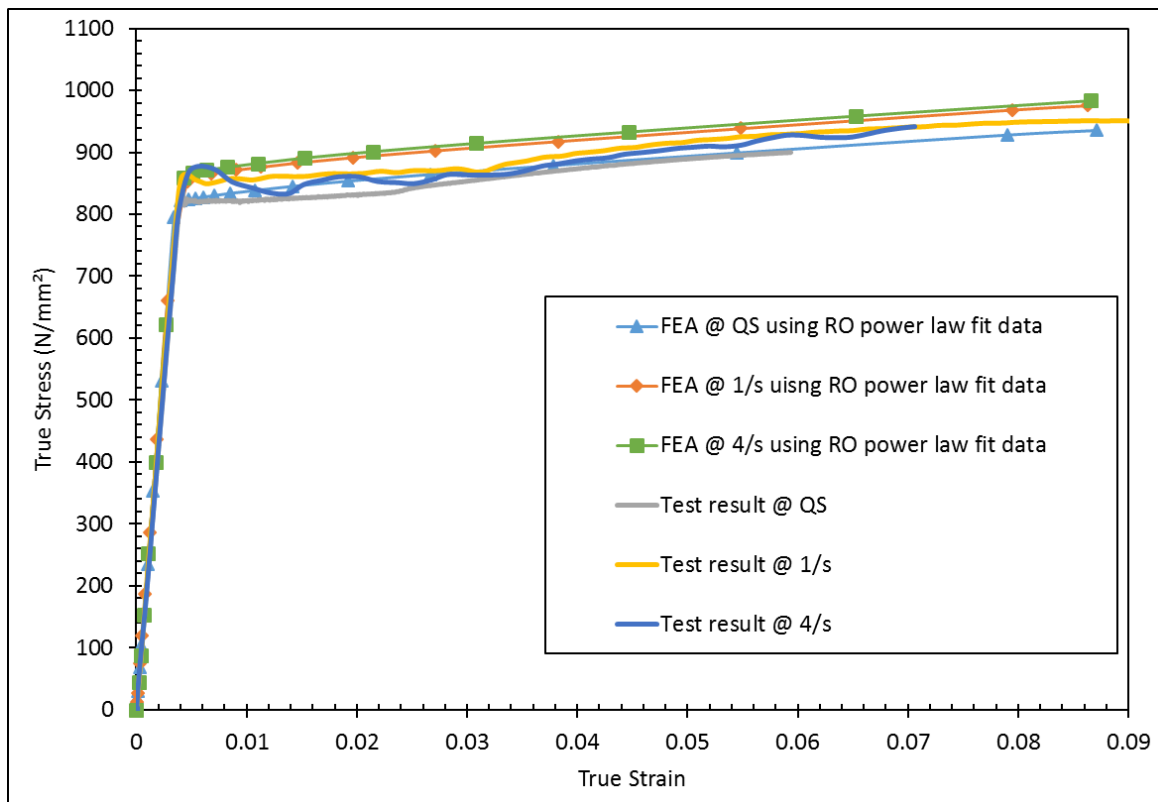
Figure 4.22   FEA results at QS and elevated loading rates using RO power law fit data

Since the results from the material model show some good agreement with the experimental tension test data, direct experimental tensile properties as material properties for S690QL were used for the subsequent fracture behaviour FEA as discussed in chapter 5.

4.6   Chapter summary

This chapter summarises the experimental tensile test results and the effect of loading rates in terms of strain rates on the tensile behaviour of S690QL and S960QL, which include a discussion on the quasi-static and dynamic tensile properties of S690QL and S960QL at ambient temperature. Finite element analysis using the von Mises flow rule and isotropic hardening condition available in the ABAQUS code is also presented in this chapter where a rate dependent model using yield stress ratio to define the materials yield behaviour was employed.

Loading rates from QS up to 100 s^{-1} strain rates were considered, representing the critical loading rate encountered in an offshore or marine in-service condition. The results show how the tensile properties of S690QL and S960QL with high Y/T ratio >0.90 change as a result of increasing loading rates. The results are compared to S235 (tested) and data from the literatures as a representation of other steel grades lower than HSS studied in this work and it was observed that S690QL and S690QL (HSS under consideration) show less sensitivity to the effect of loading rate up to 100 s^{-1} strain rates considered in this thesis. About 66% dynamic amplification was observed on the yield stress of low strength steel (S235) from quasi-static to 100 s^{-1} strain rates, whereas dynamic amplification effect on the yield stress from QS to 100 s^{-1} is <10% for S690QL and S960QL.

It goes to say that finer-grained size microstructures were associated with a reduced degree of strain rate sensitivity associated with HSS. The degree of strain rate sensitivity in their tensile properties, therefore, depends on the production routes, chemical compositions and microstructure. The tensile performance of HSS under quasi-static conditions gives a reasonably accurate prediction of its behaviour under high loading up to 4 s^{-1} strain rates without requiring any specialist tensile testing for its characterisation. Thus, in the absence of high strain rate test data, quasi-static test data of S690QL and S960QL can be used to characterise its tensile behaviour up to 4 s^{-1} strain rates at ambient temperature.

As the experimental tensile test results show that S690QL and S960QL are relatively unaffected by the effect of structural loading rate from quasi-static up to 100 s^{-1} strain rates, fracture toughness values at different structural loading and temperature conditions encountered in primary offshore structural applications would help to better understand the mechanical response and performance of these materials even in the presence of flaws. Further research is required to establish the Ductile-to-Brittle Transition Curve (DBTC) of these materials (S690QL and S960QL) where a shift from the upper shelf to lower shelf could be unsafe.

To this end, the next chapter concerns the experimental fracture toughness test results and discussion on the effect of loading rate on the mechanical behaviour of high strength structural steels with high yield-to-tensile ratio in addition to the finite element analysis.

Chapter 5   Influence of Loading Rate on the Fracture Toughness of S690QL and S960QL

5.1   Introduction

It is known that loading rates influence the fracture behaviour of most ferritic steels. High loading rates could change a stable ductile tearing behaviour to an unstable brittle fracture by altering the ductile-to-brittle transition curve, and an understanding of fracture behaviour of steel during experimental testing under different loading regimes helps to prevent some potential catastrophic accidents during in-service conditions. This is predicted to be material dependent, with low strength structural steels showing a larger loading rate sensitivity compared to high strength structural steels as discussed in chapter 4 in terms of strength.

This research has undertaken further experimental work and analysis concerning the effect of loading rates on the fracture toughness of S690QL and S960QL in order to better understand the mechanical performance of HSS with high Y/T ratio >0.95 at different loading rates, for use when sectional weight reduction of heavy steel structures used offshore is important. The results, analysis and discussion of the experimental fracture toughness test results of S690QL and S960QL at a range of stress intensity factor loading rate (K-rate) up to the order of magnitude of 10^6 MPa√m/s with emphasis on S690QL are presented in this chapter.

The results, analysis and discussion focus on the loading rates at quasi-static (QS), intermediate and high/dynamic loading rates for input in FAD-based fracture engineering critical assessments, presented in detail in chapter 6. Additionally, the discussion provides further information on the use of Charpy-sized SENB ($B=W=10$ mm) specimens with nominal a_0/W $=0.5$ to generate fracture toughness data at high loading rates. The results of a hardness traverse through thickness test are also presented in this chapter, in order to assess the significance of through-thickness properties on S960QL steel plates delivered in 60mm thickness as seen in variation of the tensile data presented in Table 4.7 in chapter 4 for S960QL.

The experimental results and discussion are supported by finite element analysis which was used to characterise the crack-tip stresses and strains in nonlinear static analysis in order to determine the crack driving force and crack mouth opening displacement which cannot be estimated during the fracture toughness tests. The model was validated as discussed in section 3.3.2.1.

5.2 Traverse through thickness hardness properties of S960QL

S960QL steel plates were supplied in 60 mm thickness, so a hardness traverse through thickness test was carried out to identify any through-thickness effect on the plate. Hardness can be correlated with yield strength, and it is necessary to ensure consistency between them when sub-size specimens are extracted from the plate taking into consideration the position of specimens are taken from. Tests were performed on a Vickers testing machine with Vickers load of 10 kg in accordance with BS EN ISO 6507-1:2005.

Indentation on the sample was taken from the top edge to bottom edge within 1 mm and then 5 mm apart along the thickness resulting in 13 total indentations as shown in **Figure 5.1**. The results show some variation from the top edge to bottom edge as shown in **Figure 5.2** but not significant. A large variation at the centreline of about 285 HV value is observed and the results are summarised in **Table 5.1**. This confirmed that sub-size 3 mm thick specimens extracted near the surface would be representative of the bulk tensile behaviour as discussed in chapter 4.

Table 5.1   Summary of the hardness traverse through thickness test results of S960QL

Indent No	HV (Vickers hardness)	Indentation location (from top edge to bottom edge) (mm)
1	330	+1
2	325	+5
3	326	+5
4	325	+5
5	314	+5
6	314	+5
7	285	+5 (centre)
8	330	+5
9	319	+5
10	326	+5
11	334	+5

12	334	+5
13	317	Near bottom edge
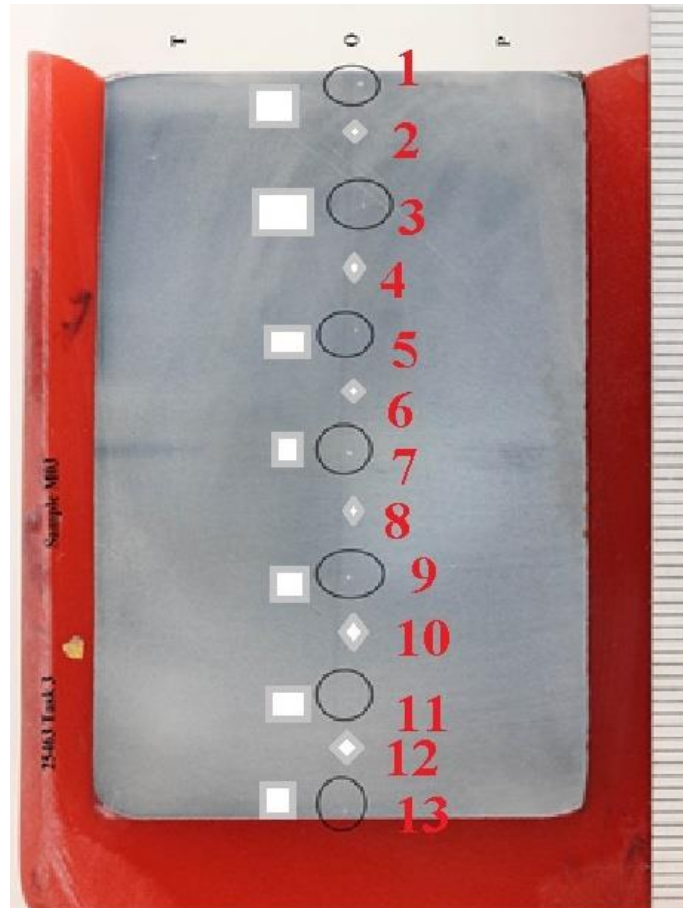
Figure 5.1   Indentation locations for the hardness traverse through thickness test for 60 mm thick S960QL steel plate.
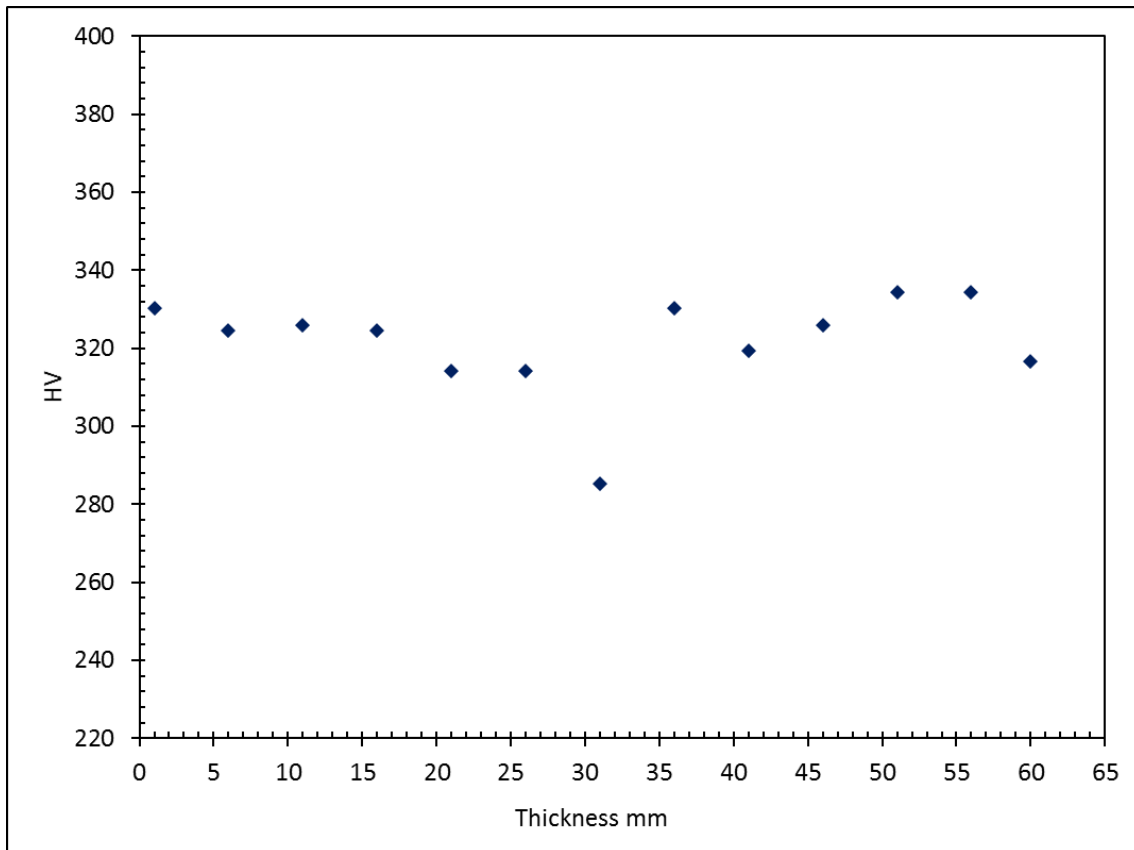
Figure 5.2   Hardness traverse through-thickness results for 60 mm thick S960QL steel plate.

5.3   Fracture toughness behaviour of S690QL and S960QL

5.3.1   *Quasi-static fracture toughness results of S690QL*

The experimental fracture toughness test results at ambient (23 °C) and low temperature (-100 °C and -120 °C) are presented and discussed here. The results describe tests carried out under quasi-static loading rate with a displacement control speed of 0.005 mm/s, corresponding to an average K-rate value of about 1 MPa√m/s over the range of tests carried out using a single point measurement method. A total number of 6 and 17 specimens at ambient and low temperatures were tested, respectively at QS loading conditions.

5.3.1.1 *Fracture toughness test results at ambient temperature*

The experimental fracture toughness results at ambient temperature for the standard SENB specimen configuration ($B=W=25$ mm) and a Charpy-sized pre-cracked SENB specimen ($B=W=10$ mm) for S690QL are presented in **Figures 5.3 and 5.4**, respectively. It is important

to mention that the minimal differences shown in the figures are due to the curved thumbnail shaped crack front during fatigue pre-cracking, as it is difficult to reproduce the exact crack front for all the specimens.

A single point value of J_m at the first attainment of a maximum force (ductile tearing), and the equivalent elastic-plastic stress intensity factor K_{mat} calculated using Eq. (5.1), were determined and summarised in **Table 5.2**. These values represent the size-dependent material resistance to crack propagation with an average J_m value of about 344 N/mm and 589 N/mm for $B=W=10$ mm and $B=W=25$ mm, respectively.

$$K_{mat} = \sqrt{\frac{J_m E}{1-v^2}} \tag{5.1}$$

where,

K_{mat} = equivalent elastic-plastic stress intensity factor (MPa$\sqrt{m}$)

J_m = the first attainment of a maximum force (ductile tearing) (N/mm)

E = Young's Modulus (GPa)

v = Poisson's ratio taken as 0.3 throughout this thesis

Table 5.2   Summary of the experimental fracture toughness results under quasi-static loading (V = 0.005 mm/s) at ambient temperature for S690QL

Specimen No	J_m (N/mm)	K_{mat} (MPa$\sqrt{m}$)	Specimen geometry (mm)	Initial crack length (a_0) (mm)	Maximum load (kN)
M01-63	333.32	279.31	$B=W=10$	5.169	7.52
M01-65	360.78	290.59	$B=W=10$	5.040	7.98
M01-66	337.21	280.94	$B=W=10$	5.199	7.45
M01-93	343.73	283.64	$B=W=10$	5.096	7.78
M01-122	567.75	364.53	$B=W=25$	13.088	43.55
M01-123	609.47	377.69	$B=W=25$	13.181	43.11
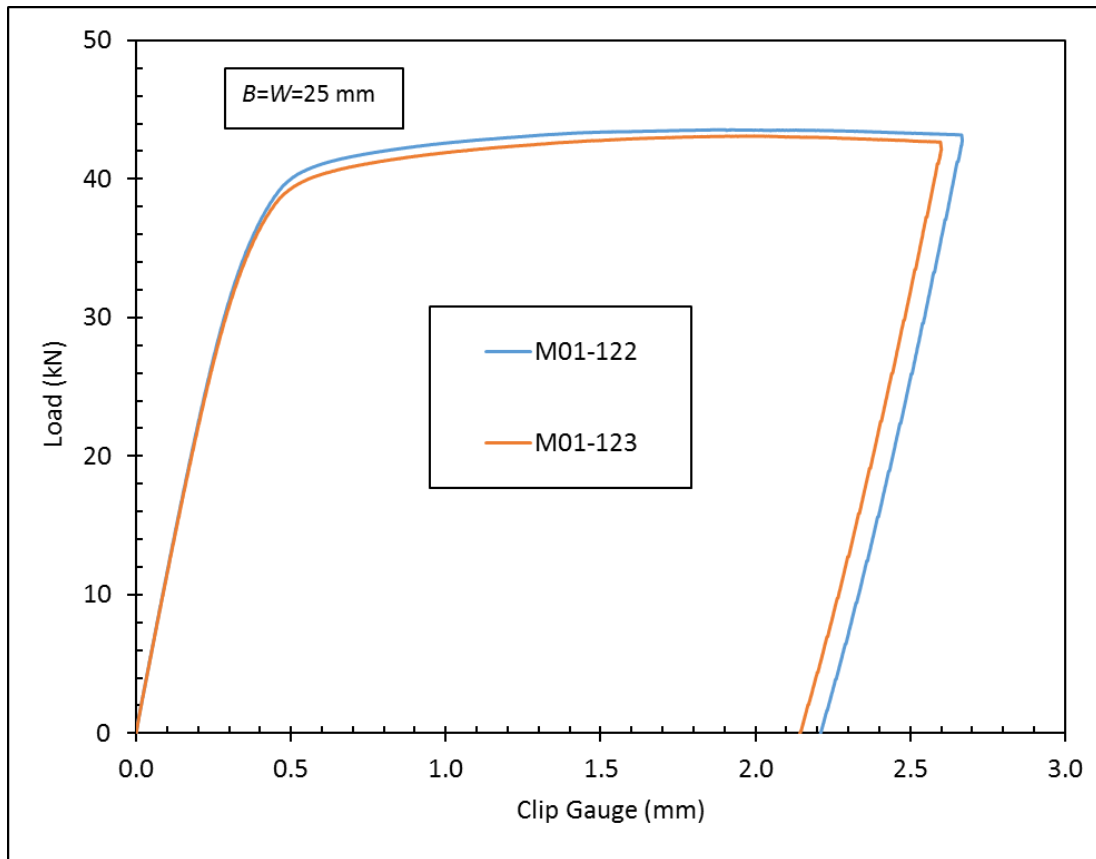
Figure 5.3   Load versus clip gauge displacement for S690QL at QS and ambient temperature for the standard SENB specimen configuration (*B=W*=25 mm)
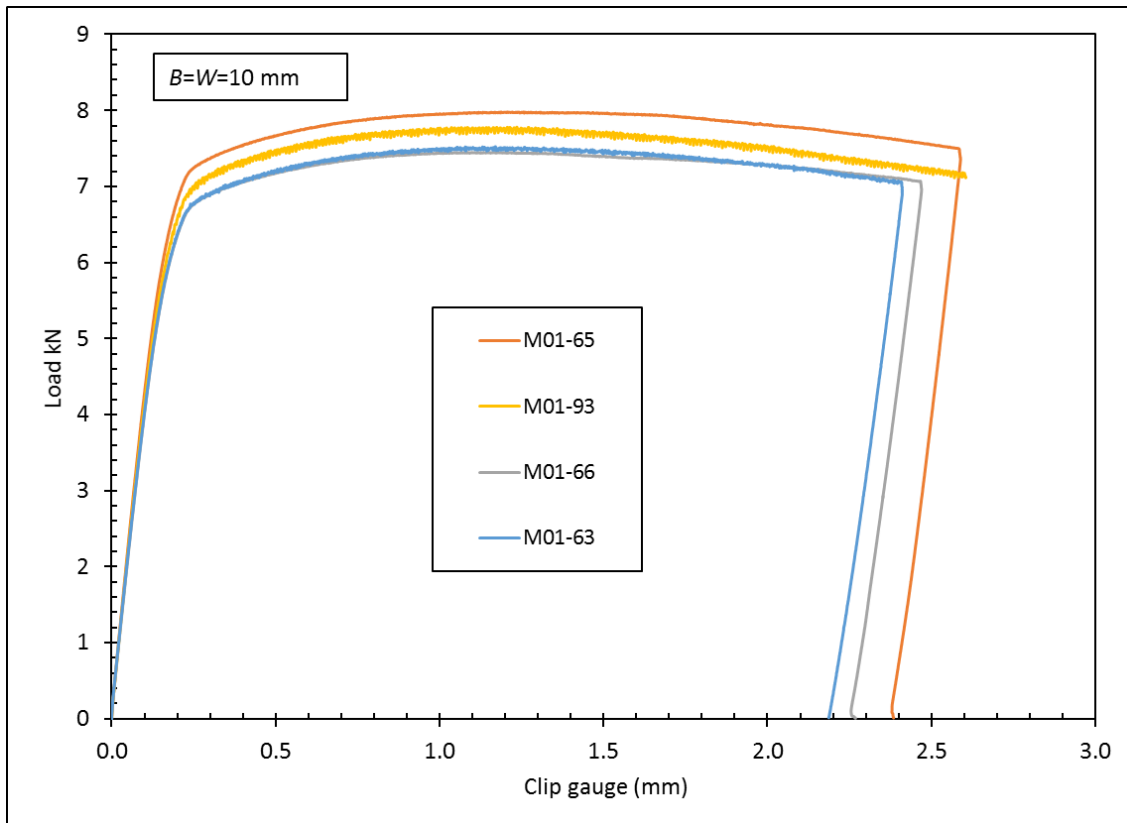
Figure 5.4   Load versus clip gauge displacement for S690QL at QS and ambient temperature for Charpy-sized pre-cracked SENB specimen (*B=W=*10 mm)

5.3.1.2 Fracture toughness test results at low temperatures

Quasi-static Charpy-sized SENB (*B=W=*10 mm) fracture toughness test results at low temperatures (-100 °C and -120 °C), plotting the load versus the clip gauge displacement are shown in **Figures 5.5 and 5.6**, respectively. All specimens tested at -120 °C failed by cleavage fracture with no ductile crack extension, ($\Delta a = 0$ mm). However, some of the results at -100 °C exhibit brittle crack extension where ductile tearing ($\Delta a \geq 0.2$ mm) precedes cleavage fracture after post-test examination of the fracture surface using optical microscopy, but failed before the first attainment of a maximum force.

All the standard SENB specimen configurations (*B=W=*25 mm) tested at -100 °C failed by cleavage fracture with no ductile tearing, ($\Delta a = 0$ mm) due to high crack tip constraint. The results of standard SENB specimen configurations (*B=W=*25 mm) are plotted in **Figure 5.7**. The experimentally measured single point fracture toughness J_c (critical J at the onset of brittle crack extension) for both Charpy-sized SENB (*B=W=*10 mm) and standard specimen configuration (*B=W=*25 mm) under quasi-static loading conditions and at low temperatures

are summarised in **Table 5.3**. The results from both configurations are important to compare how geometry configuration and loss of crack tip constraint could change the estimated reference transition temperature T_0 of S690QL under the quasi-static (QS) loading conditions.

On the lower shelf, a larger specimen thickness (25 mm) compared to 10 mm results in a lower fracture toughness at the same temperature (Table 5.3). The equivalent elastic-plastic stress intensity factor K_{JC} for 1T (1 inch) size specimens were estimated from the critical J at the onset of brittle crack extension and presented in **Table 5.3**. This is important in order to estimate the reference transition temperature T_0 at which K_{JC} value is 100 MPa$\sqrt{m}$ using a statistical method called Master Curve concept discussed further in section 5.4.2.

Table 5.3   Summary of fracture toughness test results under quasi-static loading (V= 0.005 mm/s) at low temperatures for S690QL

Specimen No	J_c (N/mm)	K_{JC} (1T) (MPa$\sqrt{m}$)	Specimen geometry (mm)	Test temperature (°C)	Initial crack length (a_0) (mm)	Fracture load (kN)
*M01-86	323.81	222.48	B=W=10	-100	5.156	8.54 (J_m)
M01-87	48.82	88.89	B=W=10	-100	5.123	7.64
M01-94	131.18	143.09	B=W=10	-100	5.093	8.31
M01-98	206.49	155.67	B=W=10	-100	5.094	8.57
M01-99	174.72	155.40	B=W=10	-100	5.112	8.58
M01-100	79.14	112.06	B=W=10	-100	5.168	7.77
M01-106	15.17	51.51	B=W=10	-120	4.954	5.59
M01-112	43.44	84.33	B=W=10	-120	4.989	8.07
M01-113	41.09	82.13	B=W=10	-120	5.278	7.15
M01-114	39.34	80.45	B=W=10	-120	5.202	7.30
M01-115	68.78	126.55	B=W=25	-100	13.313	38.54
M01-116	57.72	115.94	B=W=25	-100	13.271	36.50
M01-117	111.08	160.83	B=W=25	-100	13.280	43.34
M01-118	20.78	69.56	B=W=25	-100	13.239	23.87
M01-119	38.97	95.26	B=W=25	-100	13.196	31.11

M01-120	35.45	90.86	B=W=25	-100	13.151	29.15
M01-121	51.29	109.29	B=W=25	-100	13.317	34.93

*M01-86 specimen attains maximum load plateau with slow stable ductile tearing or crack extension (Δa) = 2.6 mm after post-test examination of the fracture surface using optical microscopy.
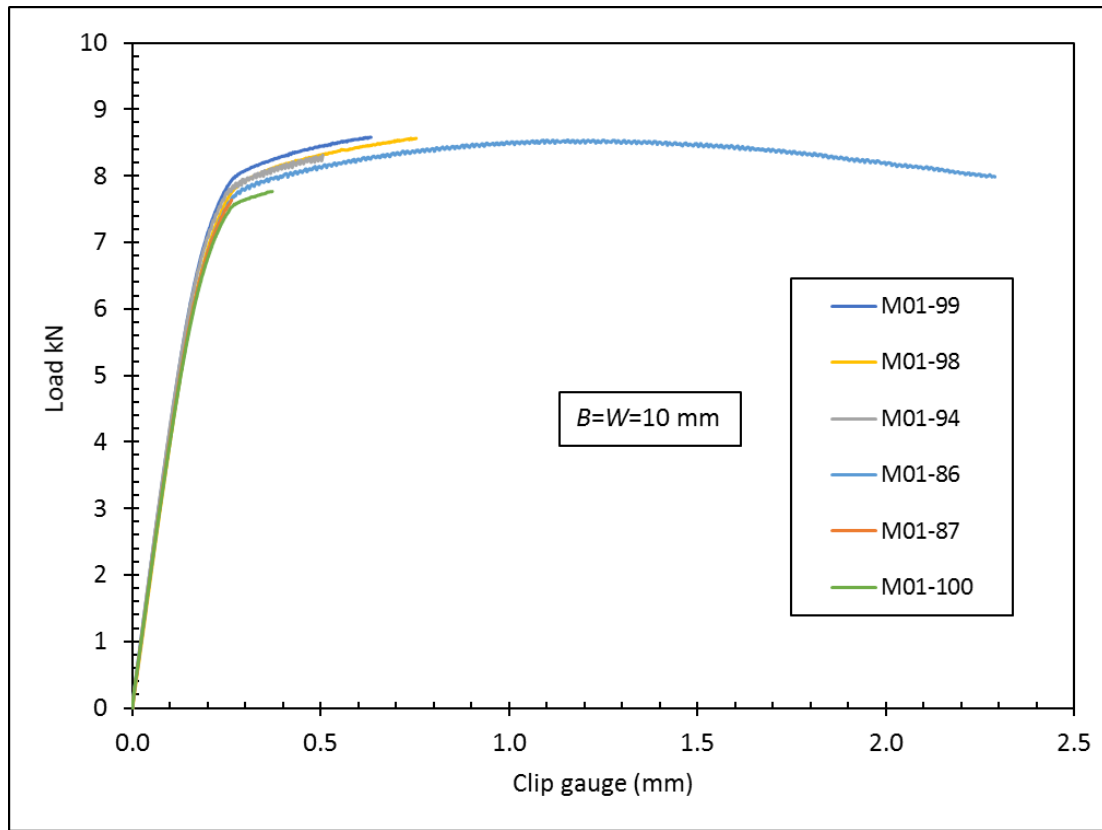
Figure 5.5   Load versus clip gauge displacement for S690QL under QS loading conditions tested at -100 °C for Charpy-sized pre-cracked SENB specimen (*B=W=*10 mm)
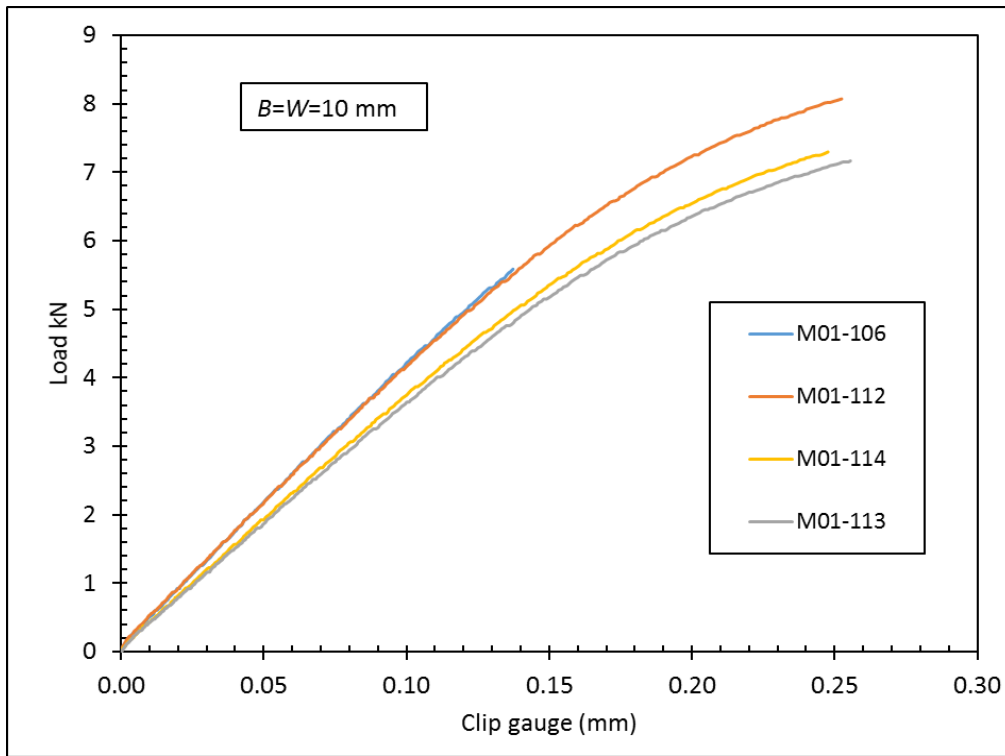
Figure 5.6   Load versus clip gauge displacement for S690QL under QS loading conditions
tested at -120 °C for Charpy-sized pre-cracked SENB specimen ($B=W=10$ mm)
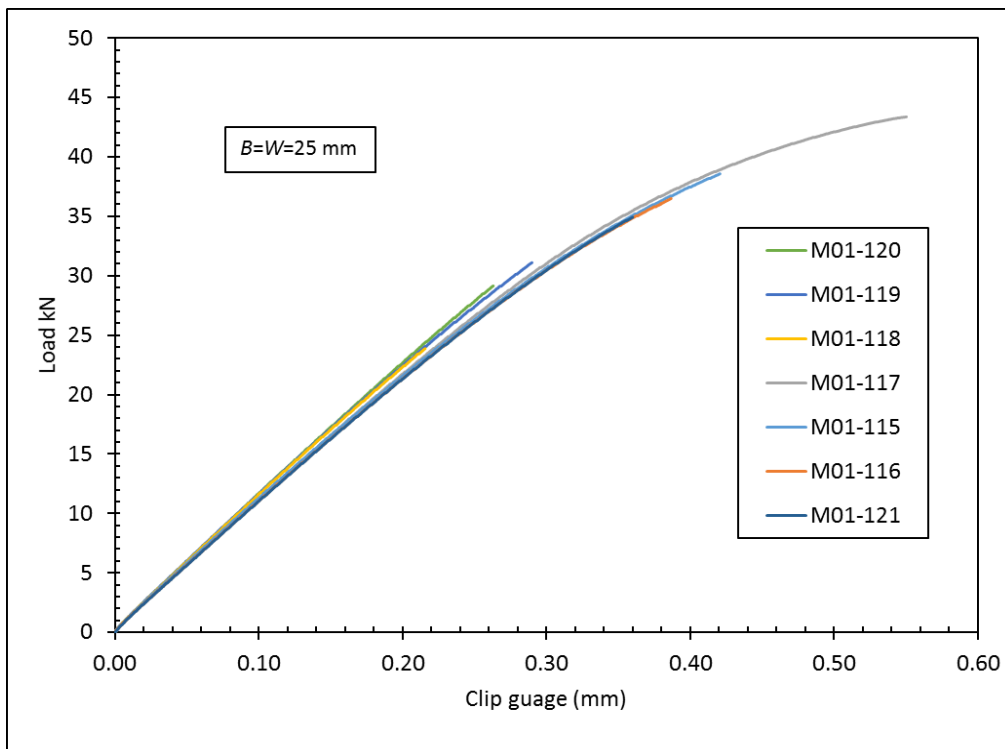
Figure 5.7   Load versus clip gauge displacement for S690QL under QS loading conditions
tested at -100 °C for the standard SENB specimen configuration ($B=W=25$ mm)

5.3.2 Quasi-static fracture toughness results of S960QL

The test method and analysis used for S690QL was unchanged for S960QL. Experimental fracture toughness results for only Charpy-sized pre-cracked SENB specimen ($B=W=10$ mm) at ambient (23 °C) and low temperature (-100 °C) are presented because of limited test materials. A total number of 7 and 6 specimens were tested at ambient and low temperatures, respectively, at QS loading conditions.

5.3.2.1 Fracture toughness test results at ambient temperature

The experimental results at ambient temperature for the Charpy-sized pre-cracked SENB specimens ($B=W=10$ mm) are presented in **Figure 5.8** and the fracture toughness data are summarised in **Table 5.4**.

Compared to the equivalent S690QL results with average K_{mat} value of 283.62 MPa√m (Table 5.2), the S960QL fracture toughness values for upper shelf behaviour are slightly lower with an average K_{mat} value of 250.62 MPa√m (Table 5.4) using Charpy-sized pre-cracked SENB specimen ($B=W=10$ mm).

Table 5.4 Summary of fracture toughness test results under quasi-static loading (V= 0.005 mm/s) at ambient temperature for S960QL.

Specimen No	J_m (N/mm)	K_{mat} (MPa√m)	Specimen geometry (mm)	Initial crack length (a_0) (mm)	Maximum load (kN)
M03-46	239.41	230.44	$B=W=10$	5.147	8.60
M03-48	275.29	247.10	$B=W=10$	5.078	8.84
M03-49	304.64	259.94	$B=W=10$	5.098	8.82
M03-60	281.89	250.05	$B=W=10$	5.240	8.29
M03-62	336.26	273.10	$B=W=10$	5.134	8.01
M03-63	283.44	250.73	$B=W=10$	5.244	8.29
M03-66	266.20	242.99	$B=W=10$	5.156	8.05
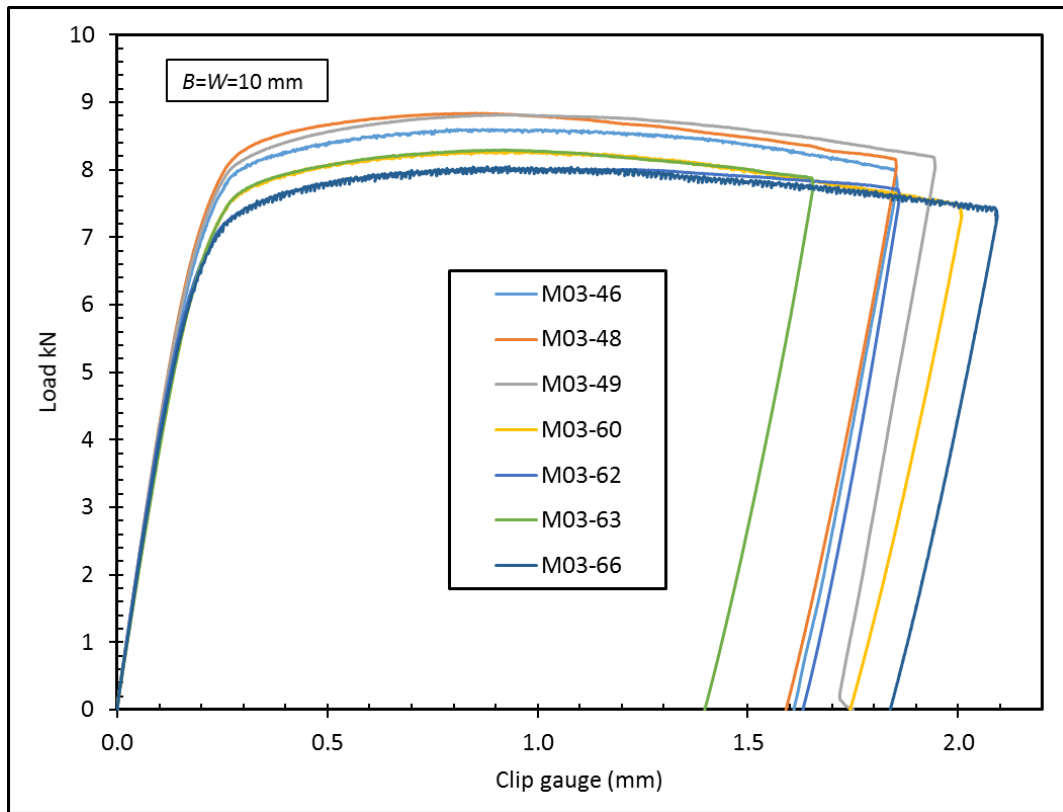
Figure 5.8   Load versus clip gauge displacement for S960QL at QS loading rate and
ambient temperature for Charpy-sized pre-cracked SENB specimen (*B=W*=10 mm)

5.3.2.2 Fracture toughness test results at low temperatures

All the quasi-static Charpy-sized SENB (*B=W*=10 mm) fracture toughness test results at low
temperature (-100 °C) failed by cleavage fracture with minimal ductile crack extension, ($\Delta a <$
0.2 mm) after post-test examination of the fracture surface using optical microscopy, but
fractured before the first attainment of a maximum force as shown in **Figure 5.9** and
summarised in **Table 5.5**. The values are similar to those obtained for S690QL.

Table 5.5   Summary of fracture toughness test results under quasi-static loading (V=
0.005 mm/s) at -100 °C for S960QL

Specimen No	J_c (N/mm)	K_{JC} (1T) (MPa√m)	Specimen geometry (mm)	Test temperature (•C)	Initial crack length (a_0) (mm)	Fracture load (kN)
M03-67	28.04	68.36	*B=W*=10	-100	5.147	6.55
M03-68	27.66	67.92	*B=W*=10	-100	5.163	6.66
M03-69	38.61	79.51	*B=W*=10	-100	5.098	7.92

M03-86	73.01	107.79	$B=W=10$	-100	5.177	8.11
M03-89	14.84	50.84	$B=W=10$	-100	5.089	5.23
M03-90	19.03	57.04	$B=W=10$	-100	5.142	5.54
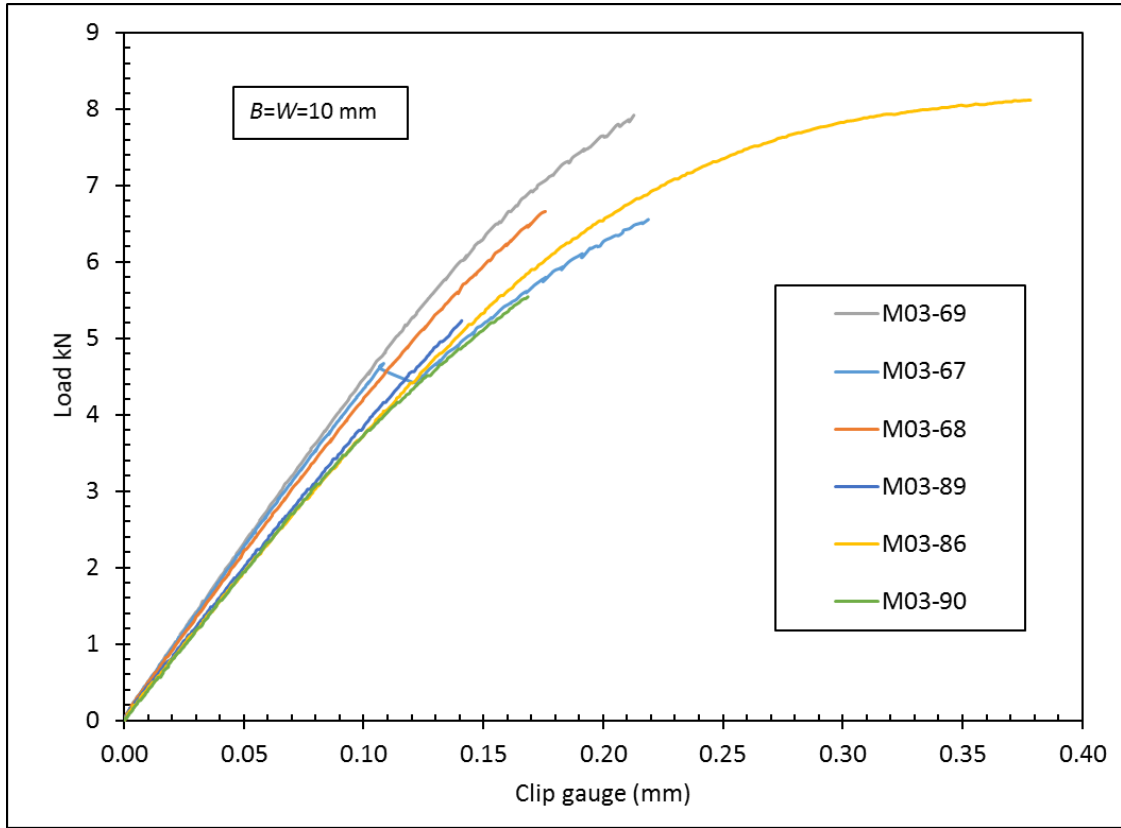
Figure 5.9   Load versus clip gauge displacement for S960QL under QS loading conditions tested at -100 °C for Charpy-sized pre-cracked SENB specimen ($B=W=10$ mm)

5.3.3   *Intermediate loading rate fracture toughness results for S690QL and S960QL*

In order to compare between QS and elevated loading rates results, the same Charpy-sized SENB ($B=W=10$ mm) specimens were used throughout for the intermediate and high/dynamic loading rate tests. The effect of loading rate on the fracture toughness of ferritic steels was mainly concerned with defining the fracture transition temperature shift (ΔT_0) in this thesis.

The results presented here describe how intermediate loading rates, carried out at a displacement control speed of 200 mm/s, corresponding to an average K-rate value of about 10^4 MPa√m/s over the range of tests, affect the fracture behaviour of S690QL and S960QL in the transition and lower shelf regions of the ductile-to-brittle transition region (DBTC) using

the Master Curve concept. Therefore, this sub-section is mainly concerned with the experimental fracture toughness results at low temperature (-100 °C) as summarised in **Tables 5.6 and 5.7**, for S690QL and S960QL, respectively under intermediate loading rates. A total number of 8 specimens each were tested for both materials (S690QL and 960QL) at low temperatures.

All specimens tested at -40 °C for S690QL exhibit ductile tearing with crack extension ($\Delta a \geq$ 0.2 mm) after post-test examination of the fracture surface using optical microscopy, but fractured before the first attainment of a maximum force. On the other hand, specimens tested at -40 °C for S960QL show first attainment of a maximum force before the end of the test. The results at -40 °C are important for the finite element analysis validation at elevated loading rates.

The full experimental results showing the plot of load versus clip gauge displacement at -100 °C tested at 200 mm/s are shown in **Figures 5.10 and 5.11**, for S690QL and S960QL, respectively. The fracture load at -100 °C for S690QL varies between 3.9 kN and 7.6 kN for intermediate loading as compared to 7.6 kN and 8.6 kN under QS loading rate. Although scattered, the results show how the fracture behaviour of S690QL could be affected by increasing loading rate.

Table 5.6   Summary of the fracture toughness test results at intermediate loading (V= 200 mm/s) tested at -100 °C for S690QL

Specimen No	J_c (N/mm)	K_{JC} (1T) (MPa√m)	Specimen geometry (mm)	Test temperature (°C)	Initial crack length (a_0) (mm)	Fracture load (kN)
M01-125	81.64	113.75	B=W=10	-100	5.141	7.62
M01-126	88.04	117.97	B=W=10	-100	5.019	6.96
M01-127	5.27	31.95	B=W=10	-100	5.111	4.07
M01-128	17.39	54.70	B=W=10	-100	5.206	5.20
M01-129	11.64	45.49	B=W=10	-100	4.992	4.58
M01-130	34.73	75.61	B=W=10	-100	5.259	5.69
M01-139	16.88	53.95	B=W=10	-100	4.955	4.62
M01-140	15.77	52.29	B=W=10	-100	5.081	3.89

Table 5.7   Summary of the fracture toughness test results at intermediate loading (V= 200 mm/s) tested at -100 °C for S960QL

Specimen No	J_c (N/mm)	K_{JC} (1T) (MPa√m)	Specimen geometry (mm)	Test temperature (°C)	Initial crack length (a_0) (mm)	Fracture load (kN)
M03-94	21.03	59.80	B=W=10	-100	5.066	4.77
M03-95	25.49	65.37	B=W=10	-100	5.256	4.59
M03-96	19.18	57.24	B=W=10	-100	5.041	4.48
M03-97	27.32	67.53	B=W=10	-100	5.002	3.89
M03-98	25.21	65.03	B=W=10	-100	5.067	4.36
M03-99	9.89	42.26	B=W=10	-100	5.363	3.50
M03-105	13.68	48.98	B=W=10	-100	5.044	4.75
M03-106	25.91	65.87	B=W=10	-100	5.038	4.37
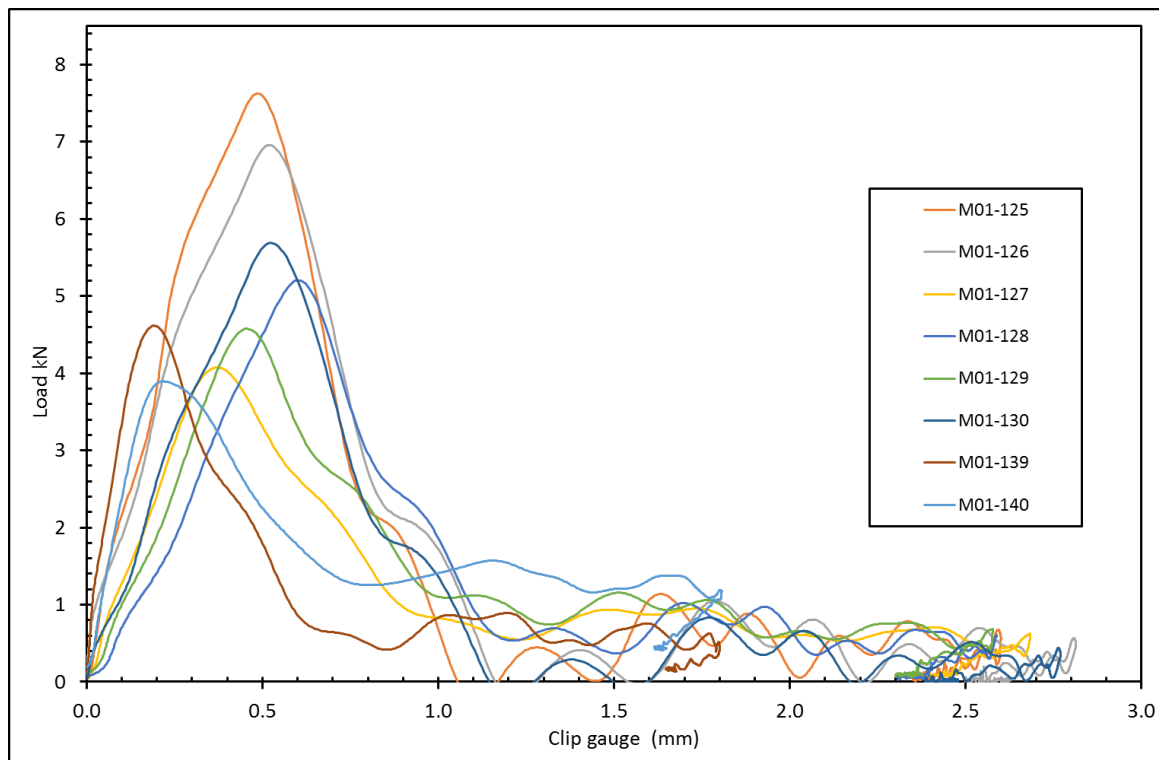
Figure 5.10   Load versus clip gauge displacement for S690QL at intermediate loading rate (V = 200 mm/s) tested at -100 °C for Charpy-sized pre-cracked SENB specimen (B=W=10 mm)
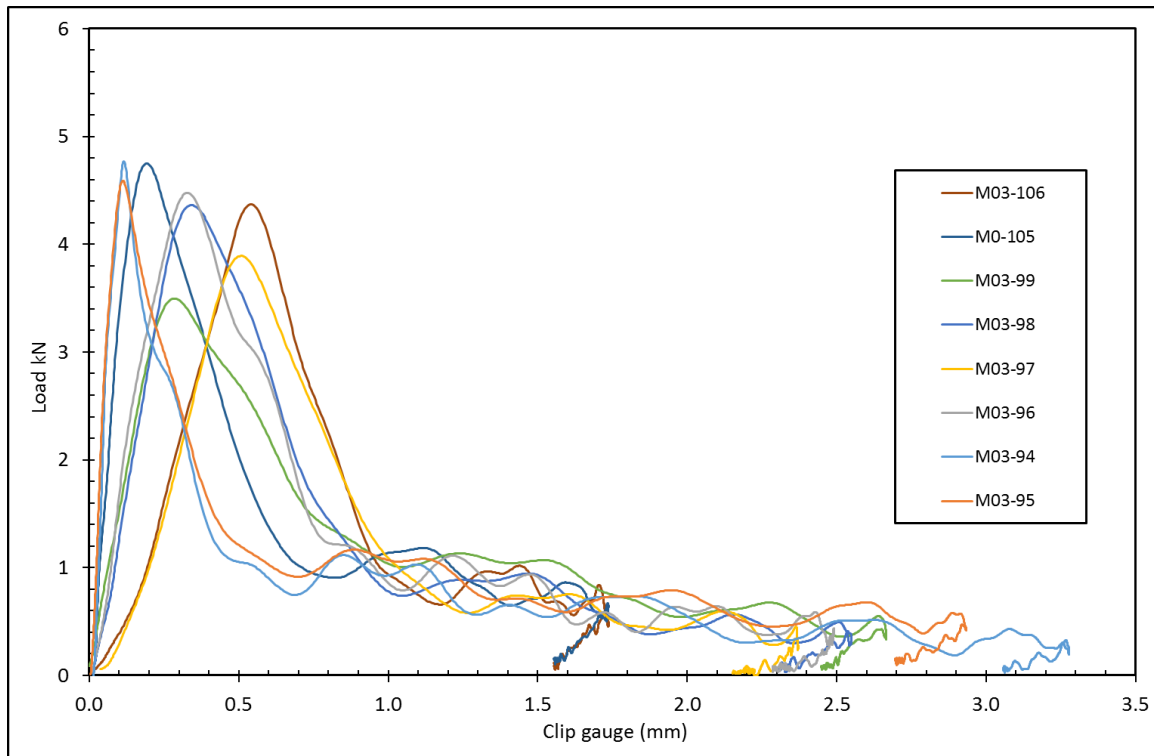
Figure 5.11   Load versus clip gauge displacement for S960QL at intermediate loading rate (V = 200 mm/s) tested at -100 °C for Charpy-sized pre-cracked SENB specimen (*B=W=10 mm*)

5.3.4   High/dynamic loading rate fracture toughness results for S690QL and S960QL

The Instrumented Charpy impact test results using the Charpy-sized pre-cracked SENB specimens which were tested at crosshead speed V_0 = 5400 mm/s, are summarised in **Table 5.8**, for S690QL at -100 °C for easy comparison with other loading rates at the lower region of the transition curve (DBTC). The crosshead speed corresponds to an average K-rate value of about 10^6 MPa√m/s over the range of tests. The raw data (force-time curve) are converted to force-displacement in accordance to ASTM E2298-15 by double integration. The graph of the load versus load point displacement is shown in **Figure 5.12**. All specimens tested at -100 °C failed by cleavage fracture with no crack extension (Δa = 0). A total number of 33 and 29 specimens were tested for S690QL and S960QL, respectively, at dynamic loading rates.

It should be noted that, at these loading rates and on the lower shelf region, all the experimental test results presented represent the test data from S690QL steel plate only at -100 °C. Due to the imbalance between the internal and external forces during high loading rates, significant oscillations were present in the test data during deformation. The experimentally measured

154

loads at fracture were a function of the position of cleavage fracture initiation relative to the peaks and troughs of the cyclic inertial forces acting on each test specimen in accordance with BS ISO 26843 and ASTM E2298-15.

Two sets of data are generated at the upper shelf (fully ductile regime) and were tested at ambient temperature for both S690QL and S960QL. Firstly, a test data was generated by varying the angle of strike such that it is sufficient to produce a certain stable crack extension as provided by BS ISO 26843 in order to determine the resistance curve. This requires a special test procedure discussed in section 3.2.5. The second test data generated are carried out using the same procedure for tests done at low temperatures, which is without varying the angle of strike.

The processed experimental results tested at ambient temperature by varying the angle of strike are shown in **Figure 5.13** for S690QL. A single point value of J_m at the first attainment of a maximum force (ductile tearing) and the equivalent elastic-plastic stress intensity factor K_{mat} are calculated using Eq. (5.1).

Table 5.8   Summary of the fracture toughness test results at dynamic loading (V= 5400 mm/s) tested at -100 °C for S690QL

Specimen No	J_c (N/mm)	K_{JC} (1T) (MPa√m)	Specimen geometry (mm)	Test temperature (°C)	Initial crack length (a_0) (mm)	Fracture load (kN)
M01-88	32.0	72.75	B=W=10	-100	5.179	5.66
M01-89	37.0	77.94	B=W=10	-100	5.260	6.54
M01-90	41.8	82.56	B=W=10	-100	5.188	7.35
M01-91	33.2	73.97	B=W=10	-100	5.153	6.25
M01-92	28.0	68.34	B=W=10	-100	4.941	5.66
M01-97	32.5	73.33	B=W=10	-100	5.099	5.96
M01-104	32.5	73.33	B=W=10	-100	5.219	5.82
M01-105	34.3	73.24	B=W=10	-100	5.179	6.08
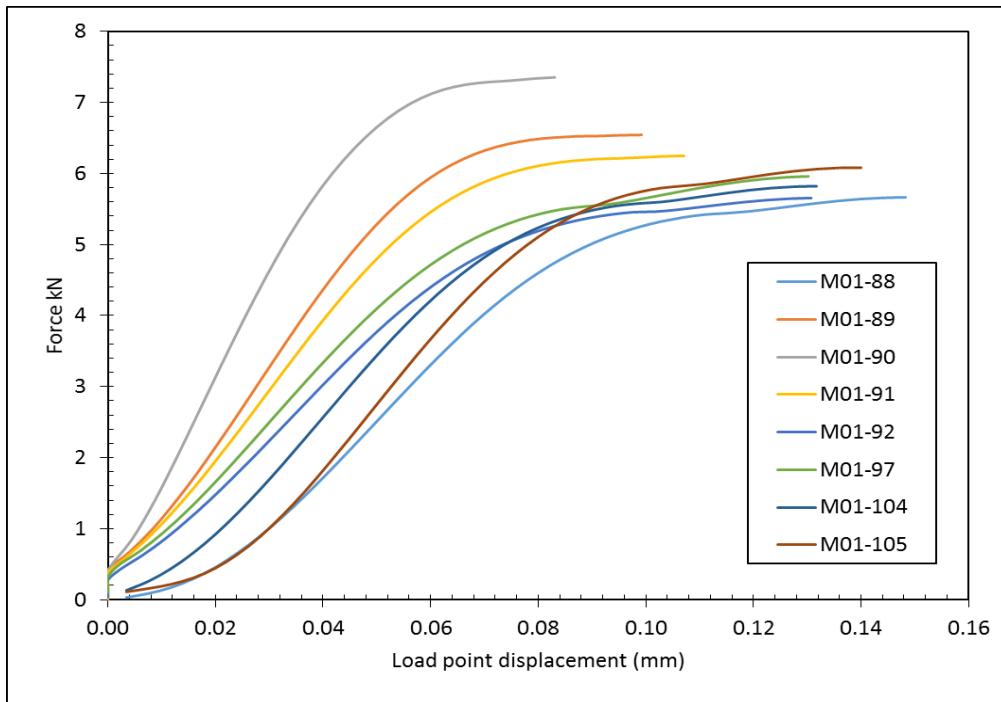
Figure 5.12   Load versus time for S690QL at dynamic loading rate (V = 5400 mm/s) tested at -100 °C for Charpy-sized pre-cracked SENB specimens (*B=W=*10 mm)
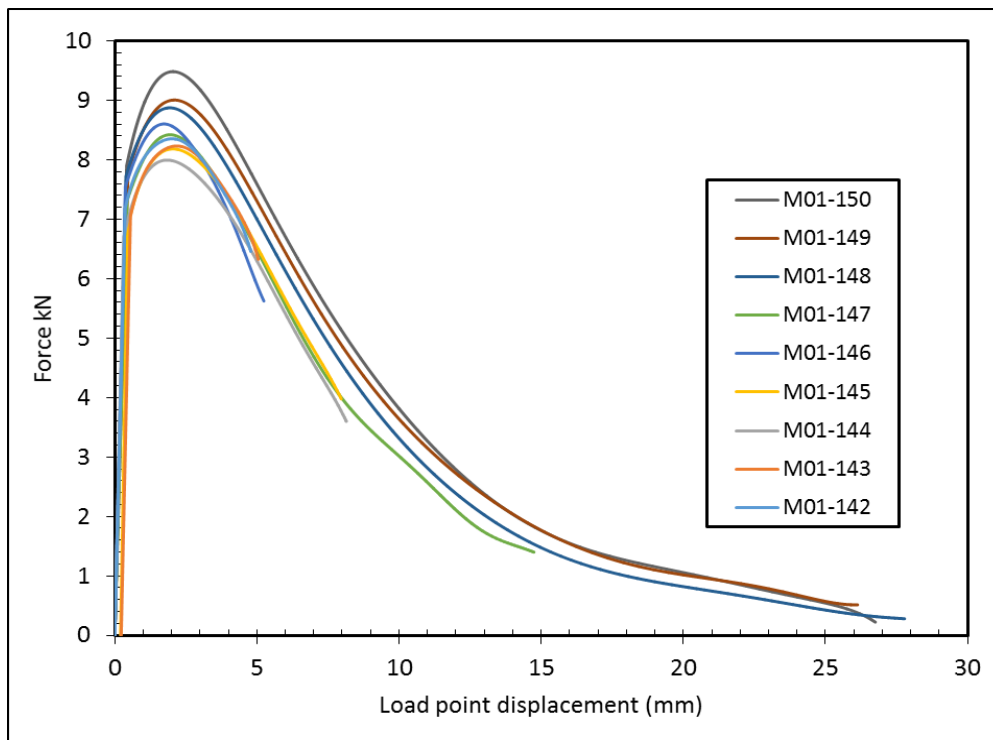
Figure 5.13   Low blow load versus load point displacement for S690QL at dynamic loading rate (V = 5400 mm/s) tested at ambient for Charpy-sized pre-cracked SENB specimen (*B=W=*10 mm)

Figure 5.14 shows the equivalent K_{JC} (1T) values of S690QL at K-rates of 1 MPa√m/s (QS), 10^4 MPa√m/s (intermediate) and 10^6 MPa√m/s (high/dynamic loading rates) tested at -100 °C. A decrease in toughness is observed as the loading rate increases from QS to intermediate, but kept fairly constant when the loading rate is increased further to high/dynamic loading rate. This effect (effect of loading rate) on the DBTC of S690QL is discussed further in section 5.4.
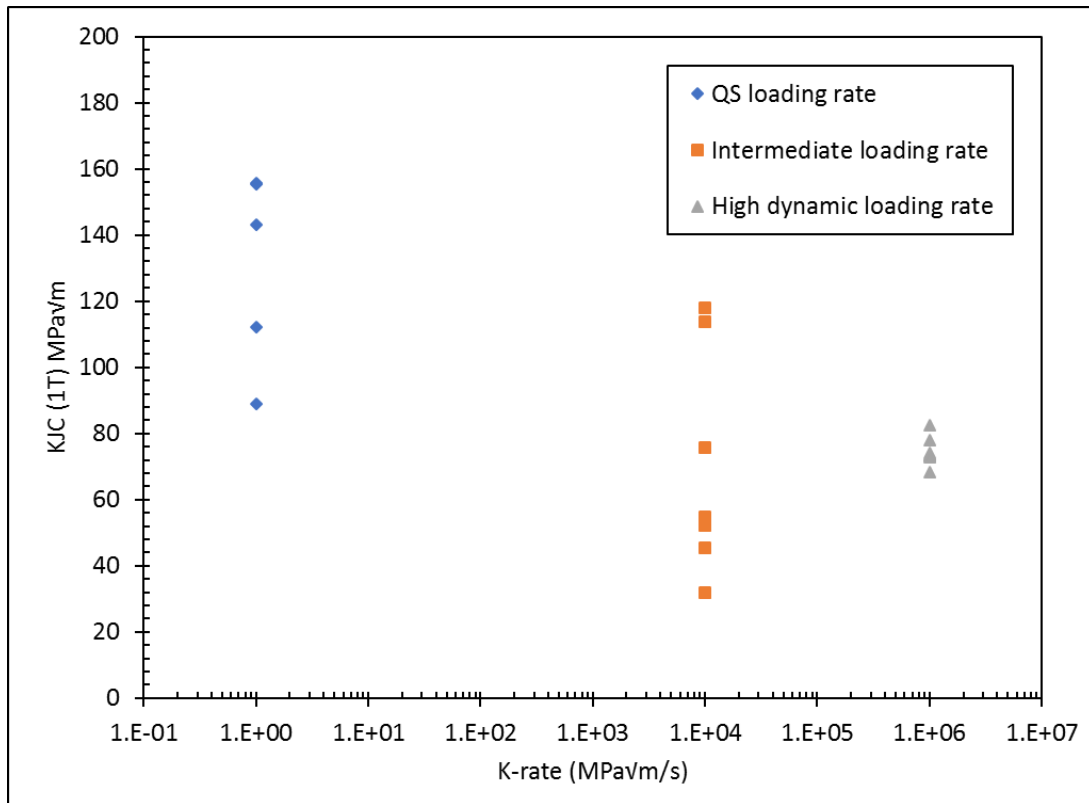
Figure 5.14   Comparison of the equivalent K_{JC} (1T) of S690QL under QS, intermediate and high dynamic loading rates tested at -100 °C for Charpy-sized pre-cracked SENB specimen ($B{=}W{=}10$ mm)

5.4   Effect of loading rate on the ductile-to-brittle transition curve of S690QL

The effect of loading rate on the fracture toughness of the steel grades under consideration is similar to other ferritic steels where the effect shifts the fracture transition temperature (T_0) to a higher temperature. A little or minimal effect is observed on the upper shelf fracture toughness with a possible fracture toughness reduction on the lower shelf of the ductile-to-brittle-transition curve (DBTC).

Since the main effect of loading rate on the fracture behaviour of ferritic steels is a shift to a higher fracture transition temperature as discussed in section 2.4.3, two approaches were used

to describe the change in the temperature. First, a *tanh* function is fit through the experimental fracture toughness data at QS, intermediate and dynamic loading rates using Eq. (5.2) to define the mid fracture transition temperature shift from QS to dynamic loading rates. The second approach used in this thesis is the Master Curve concept for the estimation of the reference transition temperature at each loading rate in accordance with the ASTM E1921 (*ASTM E1921-15a^{ε1}*) standard. The results are then used to predict the change in the fracture transition temperature from QS to dynamic loading rates.

$$J = A + Btanh((T - T_\mathrm{o})/C \qquad\qquad (5.2)$$

5.4.1 Tanh function fit predictions

The *tanh* function fit, **Figure 5.15,** shows a shift on the DBTC from a lower fracture transition temperature at 0.005 mm/s to a higher fracture transition temperature at intermediate loading rate. In this thesis, the essence of the fit is to show the real time change as result of induced loading rate on the DBTC with emphasis on the experimental fracture toughness test data of S690QL. This illustrates the two different influences (fracture toughness value and mid transition temperature) of dynamic loading on the lower shelf transition region and the upper shelf independently.

The transition temperature shift (ΔT_0) of about 32 °C was estimated for K-rate of order of magnitude of 10^4 MPa√m.s^{-1} for S690QL, as shown in **Figure 5.15**. A further increase in loading rate will shift the curve to a higher transition temperature. The fracture transition temperature shift estimated at K-rate of order of magnitude of 10^6 MPa√m.s^{-1}, **Figure 5.16** is about 41 °C. It is important to note that the transition temperature shift in this case corresponds to the mid transition temperature.
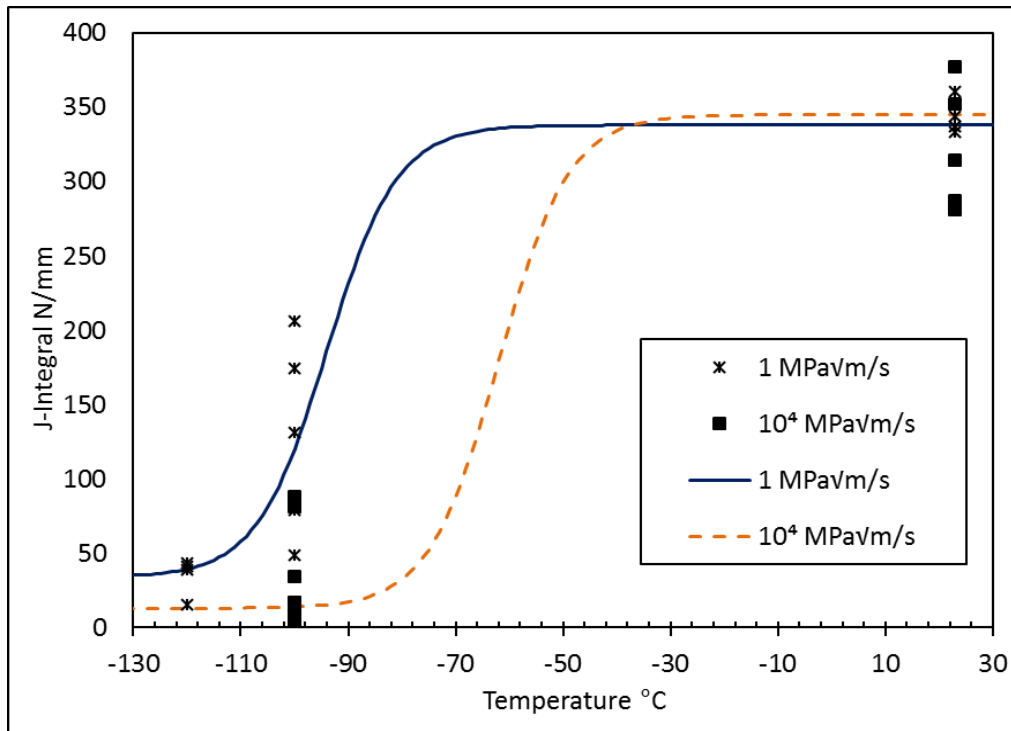
Figure 5.15   Effect of loading rate (increase in K-rate to 10^4 MPa√m.s^{-1}) on the ductile-to-brittle transition curve for S690QL
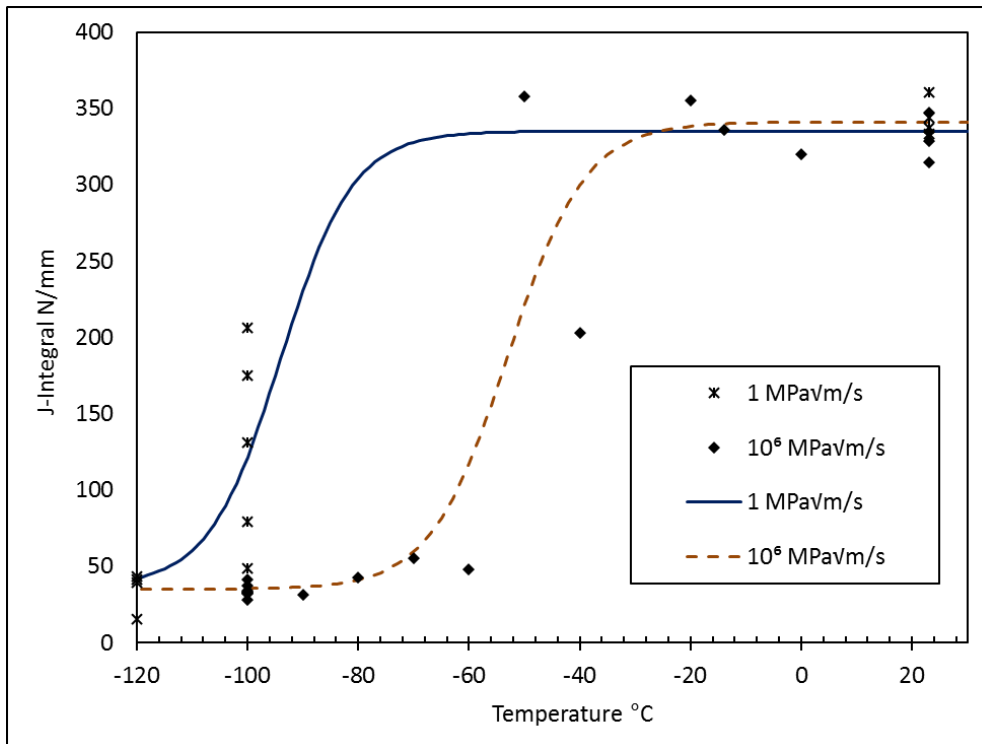
Figure 5.16   Effect of loading rate (increase in K-rate to10^6 MPa√m.s^{-1}) on the ductile-to-brittle transition curve for S690QL

The comparison using the prediction from ASTM E1921 requires the estimation of T_0 at QS loading rates using the Master Curve approach. Thus, the other way of measuring temperature shift as a result of elevated loading rates is the estimation of reference transition temperature based on the Master Curve at each loading rate as discussed in the next sub-section.

5.4.2 Master curve predictions

The Master Curve (MC) is a statistical method describing the fracture characteristics in the transition region based on the reference transition temperature T_0, and this forms the basis of the ASTM 1921 standard. The MC concept is only intended for describing ferritic steels fracture toughness behaviour in the transition region and lower region of the ductile-to-brittle transition curve (DBTC) where variability can be large. It takes into account temperature effect, scattered fracture toughness data in the transition region of the DBTC and specimen size effect. The concept has been applied to a wide range of yield strengths from 200 MPa to 1000 MPa to predict the change in the fracture transition temperature ΔT_0, using Eqs. (2.16) and (2.17), as a result of loading rate induced temperature shift (*Wallin and Mahidhara 1997*) as discussed in section 2.4.3.

Assuring comparability between QS and elevated loading rates (intermediate and high dynamic), the Charpy-sized pre-cracked SENB specimen has been considered for the determination of the reference transition temperature at intermediate ($T_{0,i}$) and high dynamic loading conditions ($T_{0,d}$). The experimental fracture toughness J_C data presented earlier at -100 °C and -120 °C have been considered for the estimation of Charpy-sized pre-cracked SENB QS reference transition temperature (T_0). Firstly, equivalent elastic-plastic stress intensity factors $K_{JC(1T)}$ for 1T size specimens are estimated after the J_C data have been converted to $K_{JC(0.4T)}$ using Eqs. (5.3) and (5.4), respectively. 1T represents specimen at 1 inch or approximately 25 mm size specimen and 0.4T represents a 10 mm size specimen. The Weibull scale parameters (K_0 and $K_{JC(med)}$) are determined using statistical analysis due to the scatter in the data. Then the reference transition temperature T_0 is estimated using Eq. (5.5).

$$K_{JC(1T)} = 20 + [K_{JC(0.4T)} - 20]\left(\frac{0.4}{1}\right)^{\frac{1}{4}} \tag{5.3}$$

and $K_{JC(0.4T)}$ given as

$$K_{JC(0.4T)} = \sqrt{J_C \frac{E}{1-v^2}} \qquad (5.4)$$

$$T_0 = T - \left(\frac{1}{0.019}\right) ln \left(\frac{K_{JC(med)} - 30}{70}\right) \qquad (5.5)$$

The estimated T_0 from both Charpy-sized pre-cracked SENB ($B=W=10$ mm) and standard SENB configuration ($B=W=25$ mm) specimens are -116 °C and -108 °C, respectively, **Figures 5.17 and 5.18** under QS conditions. The Master Curve theory should mean both datasets predict the same T_0, but it is important to mention that a difference of about 8 °C is observed due to the partial loss of crack-tip constraint. This effect is described by (*Joyce and Tregoning 2005*) and is not discussed in this thesis.

Therefore, only the T_0 values determined from data on Charpy-sized pre-cracked SENB specimens ($B=W=10$ mm) is used for the comparison in this thesis to avoid the crack-tip constraint effect bias on the dynamic effect comparison.
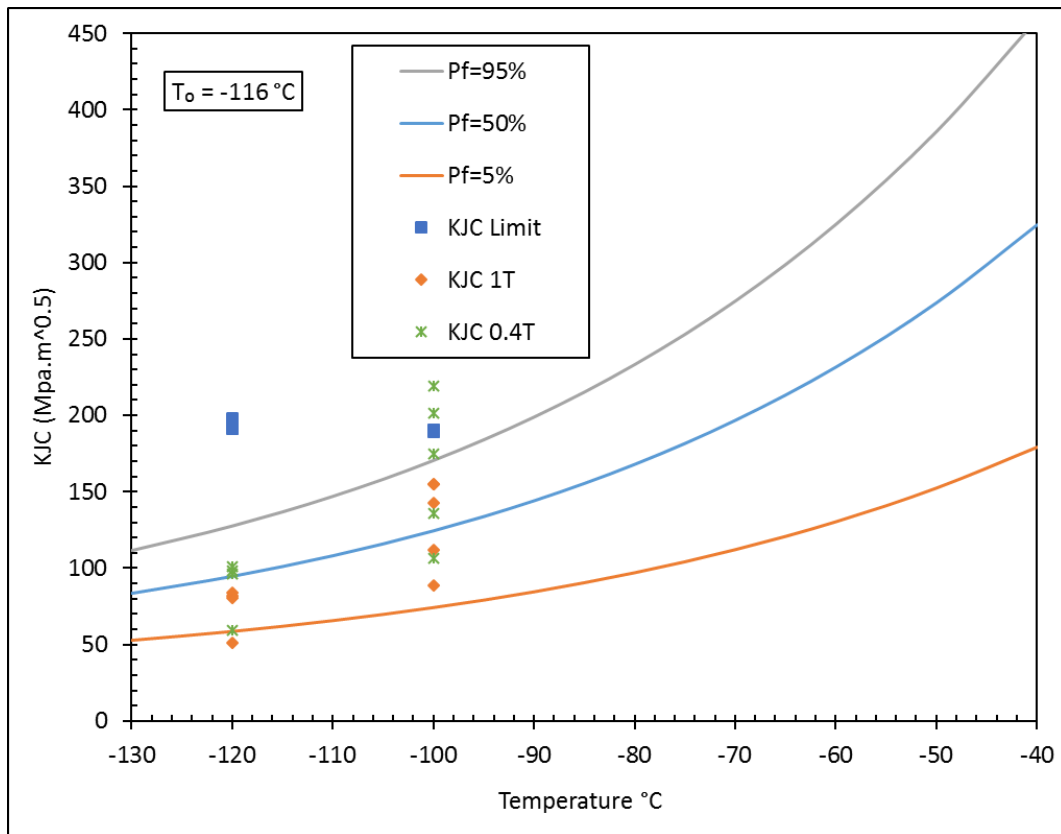
Figure 5.17   QS Master Curve for 1T specimens based on 0.4T (10 mm), average of $a_0/W=0.51$ data for S690QL
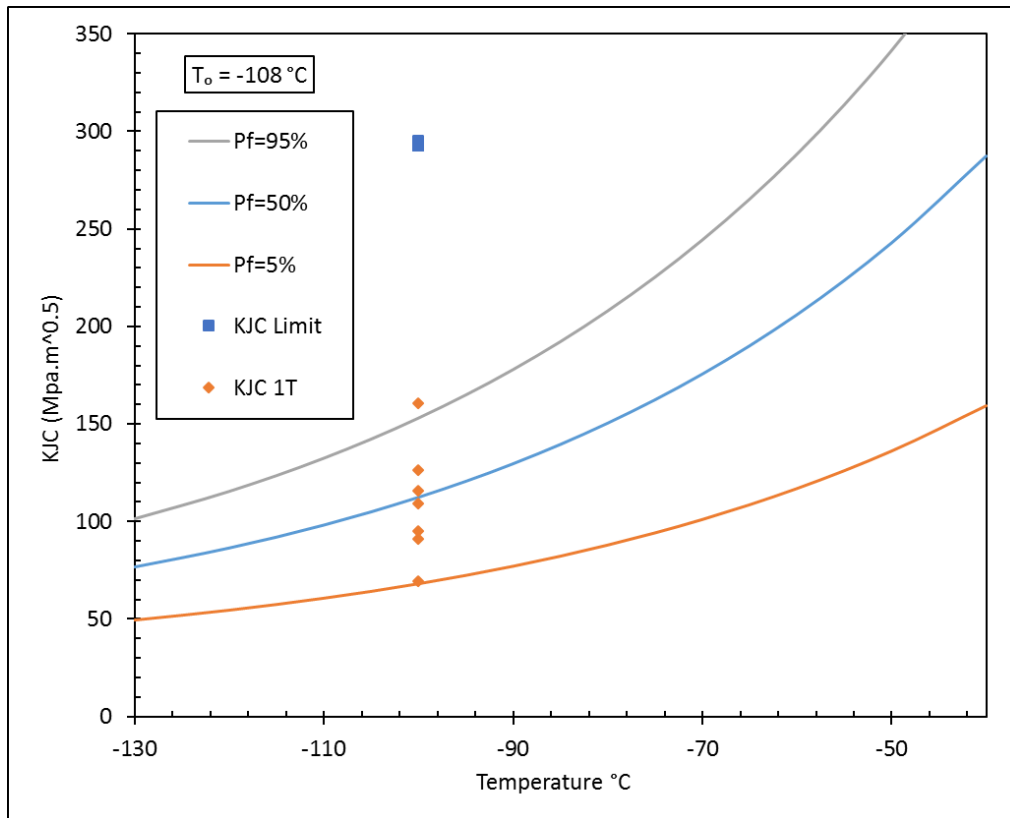
Figure 5.18   QS Master Curve for 1T specimens with nominal of a_0/W=0.52 for S690QL

The same approach using the Master Curve concept was used to estimate the reference transition temperature at intermediate ($T_{0,i}$) and high dynamic loading conditions ($T_{0,d}$) based on the experimental fracture toughness data generated at these loading rates. The reference temperatures $T_{0,i}$ and $T_{0,d}$ calculated are approximately -85.2 °C and -70.4 °C, respectively, as shown in **Figures 5.19 and 5.20**. An intermediate temperature shift $\Delta T_{0,i}$ of about 31 °C is observed for S690QL at K-rate of order of magnitude of 10^4 MPa√m/s (intermediate loading rate). A further dynamic temperature shift $\Delta T_{0,d}$ of about 45.6 °C was observed when the loading rate (K-rate) changes to 10^6 MPa√m/s (dynamic conditions) from 1 MPa√m/s K-rate (QS conditions).

A comparison has been made based on the prediction of the $\Delta T_{0,i}$ and $\Delta T_{0,d}$ in accordance with the ASTM 1921-15a standard. The prediction requires the prior knowledge of the estimated reference transition temperature T_0 at QS loading conditions. The predicted temperature shifts $\Delta T_{0,i}$ and $\Delta T_{0,d}$ are 22.9 °C and 39.5 °C, respectively. The results show a marginal difference in the temperature shift using Master Curve and the *tanh* function when compared to the prediction using ASTM 1921-15a based on QS T_0, **Table 5.9**. It is important to mention that the prediction based on ASTM 1921-15a standard, however, should be used for estimation only

as stated by the standard. The actual ΔT_0 for a given HSS material should be determined from a fracture toughness test which has been done in this thesis.

Table 5.9   Comparison of the transition temperature shift using different methods for S690QL using Charpy-sized pre-cracked SENB ($B{=}W{=}10$ mm) specimens.

Reference transition temperature method	QS Transition temperature T_0 (°C)	Intermediate loading condition ($T_{0,i}$ and $\Delta T_{0,i}$) (°C)		High/dynamic loading condition ($T_{0,d}$ and $\Delta T_{0,d}$) (°C)	
Master Curve (Experimental data)	-116**	$T_{0,i}$	-85.2	$T_{0,d}$	-70.4
		$\Delta T_{0,i}$	31	$\Delta T_{0,d}$	45.6
Tanh function DBTC fit	-94*	$T_{0,i}$	-62	$T_{0,d}$	-53
		$\Delta T_{0,i}$	32	$\Delta T_{0,d}$	41
ASTM E1921 prediction based on T_0	-116**	$T_{0,i}$	-93.1	$T_{0,d}$	-76.5
		$\Delta T_{0,i}$	22.9	$\Delta T_{0,d}$	39.5

Note:

* represents the mid-transition temperature using *Tanh* function fit.

** represents the Master Curve concept reference transition temperature corresponding to the median toughness equals to 100 MPa√m.
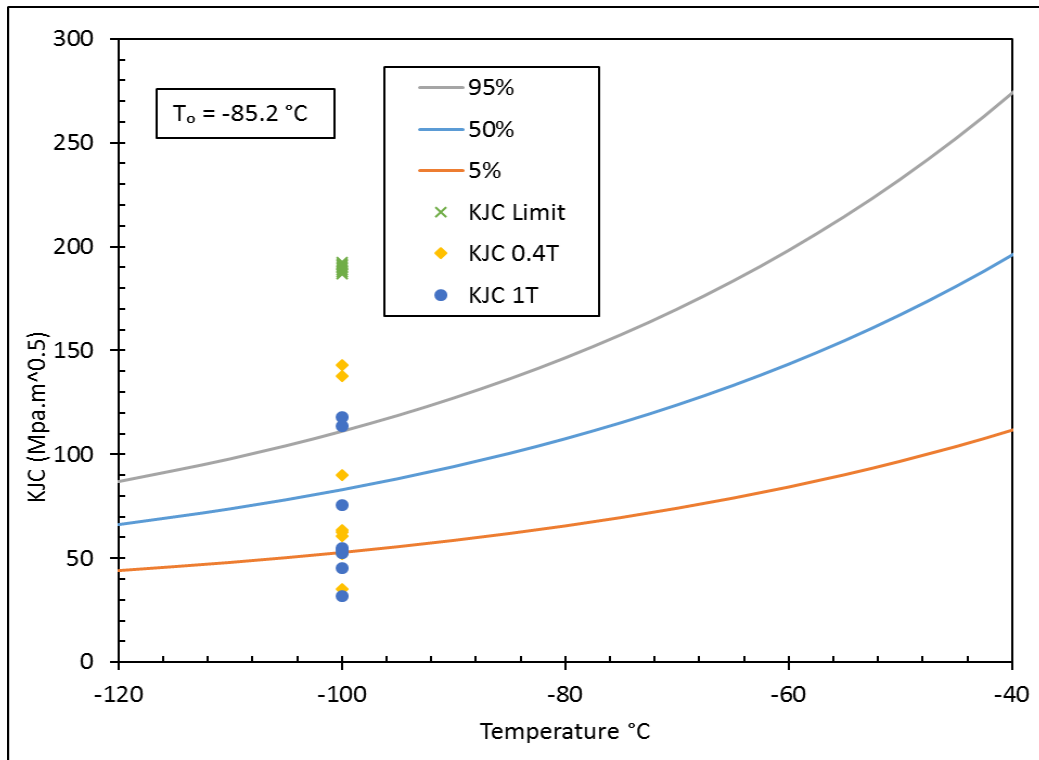
Figure 5.19   Intermediate Master Curve for 1T specimens based on 0.4T (10 mm)
a_0/W=0.52 data for S690QL with10^4 MPa√m.s^{-1} K-rate.
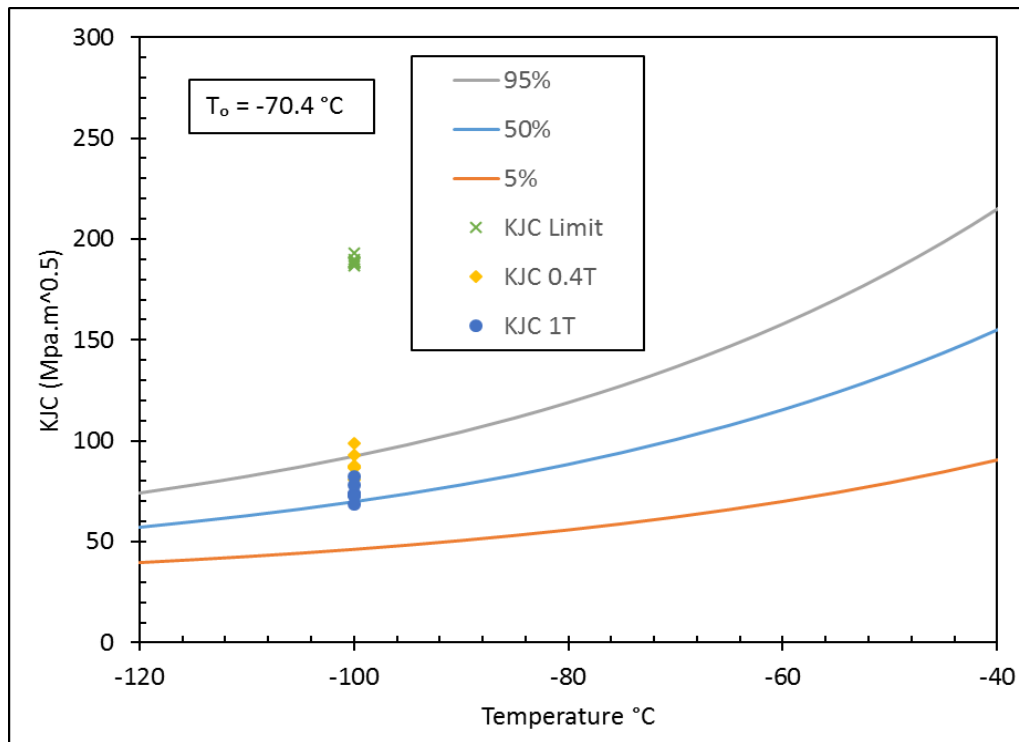
Figure 5.20   Dynamic Master Curve for 1T specimens based on 0.4T (10 mm), a_0/W=0.52
data for S690QL with10^6 MPa√m.s^{-1} K-rate.

Limited experimental data exist to determine $T_{0,d}$ for S960QL at the moment based on Master Curve approach. Given that the results of the S690QL tests show that the ASTM 1920-15a T_0 shift prediction with dynamic loading shows good comparison with the experimental estimation (MC), the ΔT_0 prediction for S960QL (which was not fracture toughness tested at dynamic loading rate) is estimated as 29 °C at 10^6 MPa√m.s^{-1} K-rate, based on QS T_0 value of 78 °C determined experimentally and yield strength at test temperature.

Therefore, as observed with the tensile test results, high strength structural steel is less affected by the effect of increased loading rates up to those studied (typical offshore in-service loading rate). S960QL shows less sensitivity to the effect of loading rate because of its higher strength when compared to S690QL. However, the cleavage fracture toughness still reduces for both steels when loading rate is increased. The Master Curve dynamic predictions have been shown to reasonably predict the transition fracture behaviour of S690QL at K-rates up to 10^6 MPa √m/s.

5.5   Tearing resistance (R) curve

5.5.1   Overview

Measurements of tearing resistance also known as the R-curve of a ferritic steel can be obtained either by unloading compliance (a single specimen), multiple specimen and normalisation methods to estimate the material's resistance to crack growth or resistance to tearing. The unloading compliance method is used when there is limited availability of test materials and often requires only one specimen to generate a valid R-curve. Unlike the unloading compliance which is loaded to the first point of interest, followed by partially unloading the specimen, and then reloaded again until all the data points are determined before the test is ended, the normalisation method requires only single specimen but requires the knowledge of the initial and final crack length measurements from the specimen fracture surface after the test together with the direct measurement of force-displacement recorded during the test.

The technique (normalisation method) provides effective way to estimate crack extension, and is mostly used where high loading rates are used or when testing at high temperatures. The crack extension cannot exceed the lesser of 4 mm or 15% of the initial cracked ligament (ASTM E1820). The multiple specimen methods use a minimum of 6 specimen to generate a valid R-

curve (BSI 1997). In this thesis, *J*-R curve using normalisation and multiple specimen methods have been employed at QS and elevated loading conditions, respectively.

5.5.2   *R-curve for S690QL*

The *R*-curve obtained for S690QL gives an estimate of the material's resistance to crack extension, instead of the single point value of J_m at the first attainment of a maximum force (ductile tearing) as the critical assessment point in a single point fracture toughness test earlier presented in sections 5.3. A typical force-displacement graph recorded during a fracture toughness SENB test for S690QL is shown in **Figure 5.3 and 5.4** at ambient temperature and under QS loading conditions. It should be noted that the plastic area is determined based on the entire graph and not on the first attainment of a maximum force in order to generate a *R*-curve.

The individual normalised curve for standard SENB specimen configuration (*B=W*=25 mm), functionally related for each S690QL specimen (M01-122 and M01-123) in reference to force-displacement records is presented in **Figure 5.21**, after the initial and final crack length measurements from the specimen fracture surface have been measured, **Figure 5.22**.
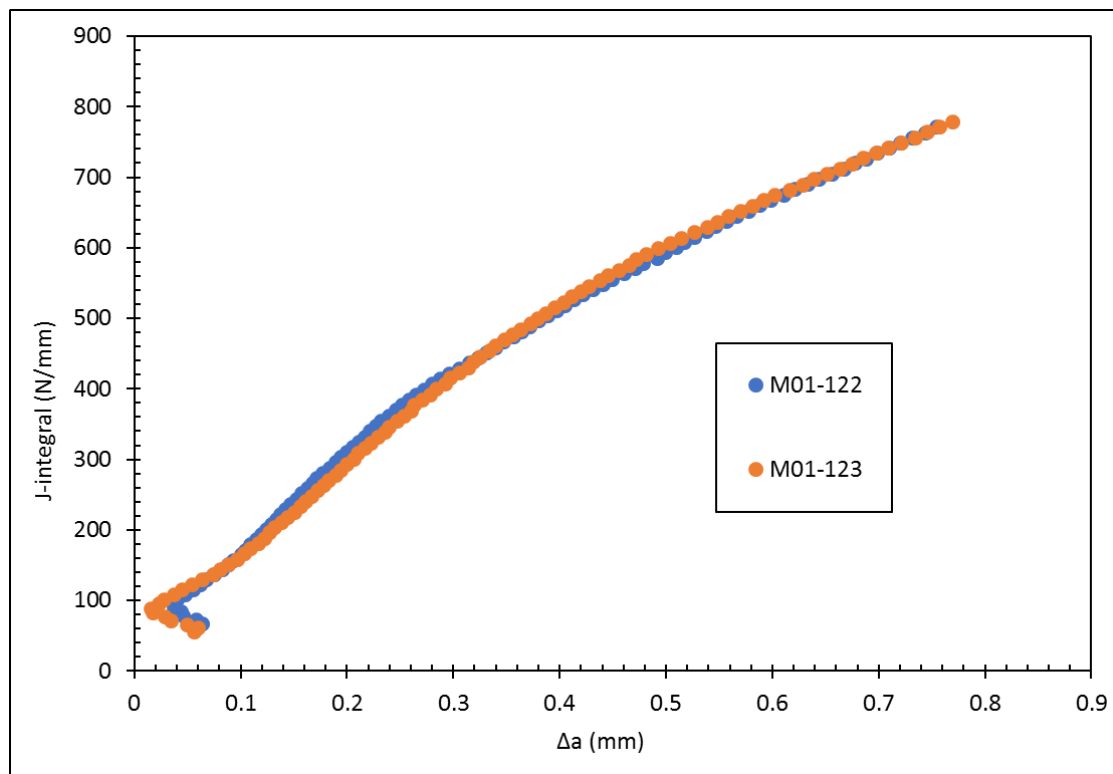
Figure 5.21   Normalisation curve from the force-displacement graph for 25 mm thick S690QL steel plate at QS with K-rate = 1 MPa√m.s^{-1}
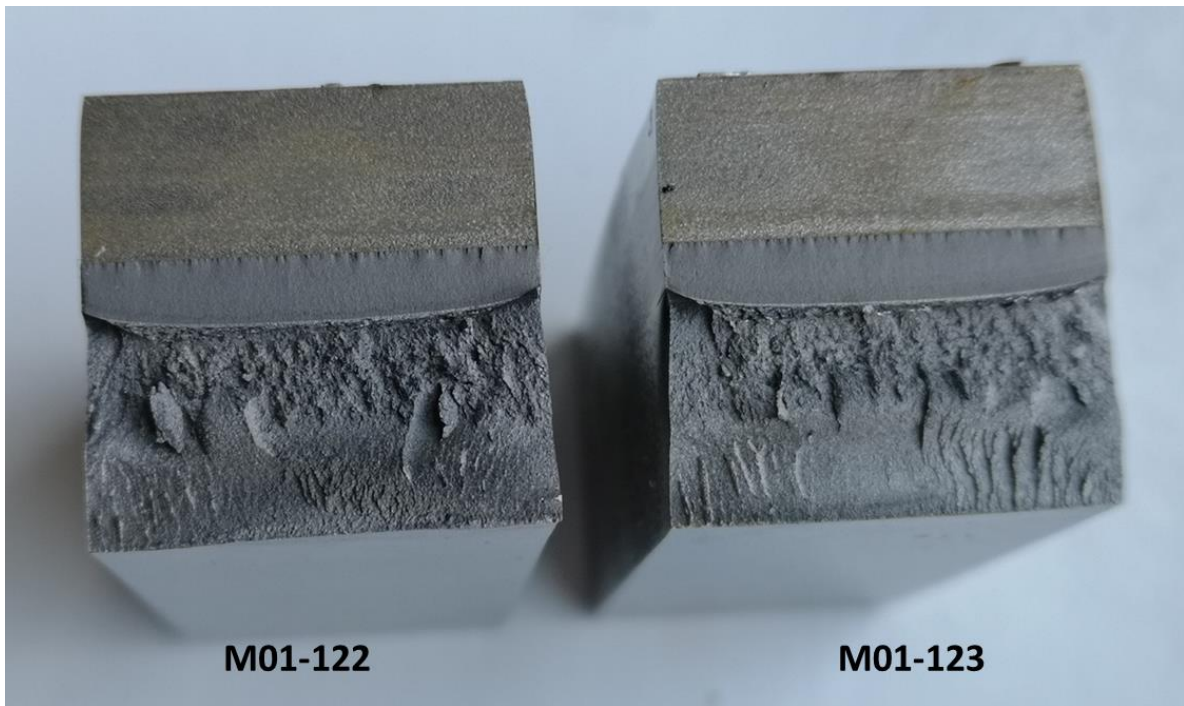
Figure 5.22   Fracture surface after the test showing the initial and final crack lengths of M01-122 and M01-123

Figures 5.23 and 5.24 show the *J-R* curve obtained for S690QL using the normalisation method for two specimens, M01-122 and M01-123, respectively. An average $J_{0.2}$ defined as the intersection of the *J-R* curve with an offset line of 0.2 mm from the two specimens is determined. The initiation fracture toughness J_{IC} which is size independent is defined as the *J*-integral value at a crack extension (Δa) given in Eq. (5.8), as specified by ASTM E1820, where σ_y represent the effective yield stress taken as 810 MPa.

$$\Delta a = {J_{IC}}/{2\sigma_Y} + 0.2 \ mm \qquad\qquad (5.8)$$

It follows that initiation toughness J_{IC} or $J_{0.2}$ at the onset of stable crack growth for S690QL which is size independent can be determined since the requirement that $B > 10J_Q/\sigma_Y$ is fulfilled in accordance with ASTM E1820. An average size independent initiation toughness J_{IC} value of 676.2 N/mm was estimated under QS loading conditions for M01-122 and M01-123.
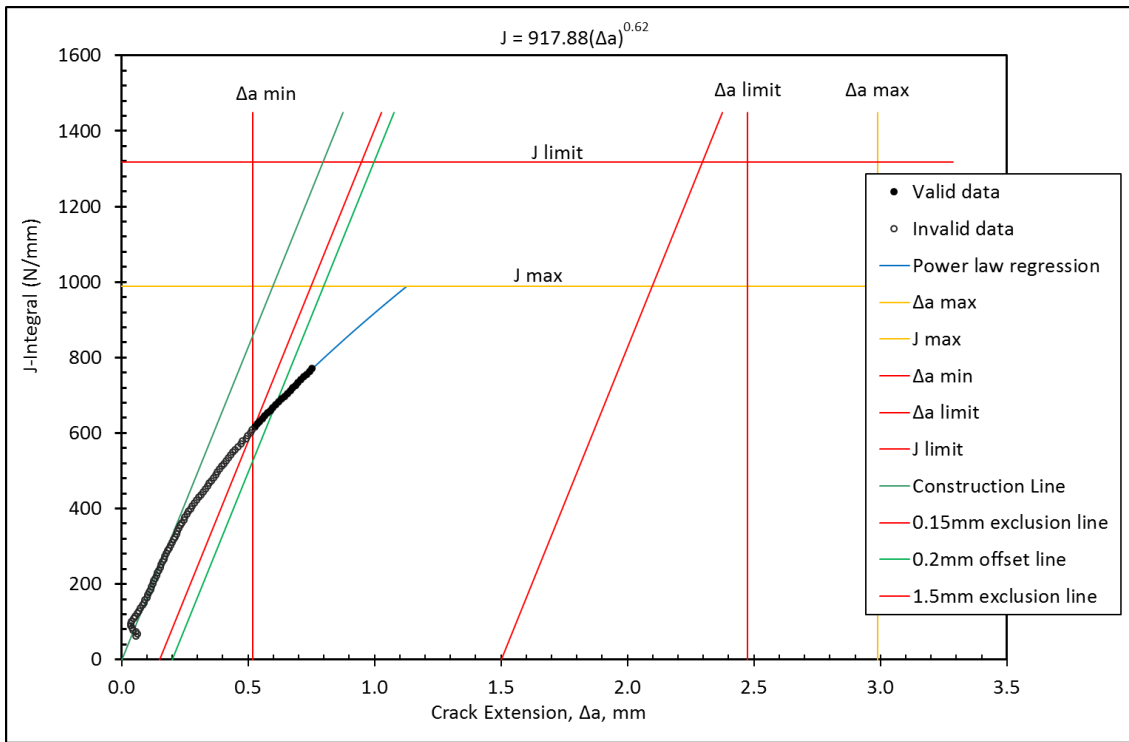
Figure 5.23   *J*-R curve for 25 mm thick S690QL steel plate using normalisation method under quasi-static conditions.
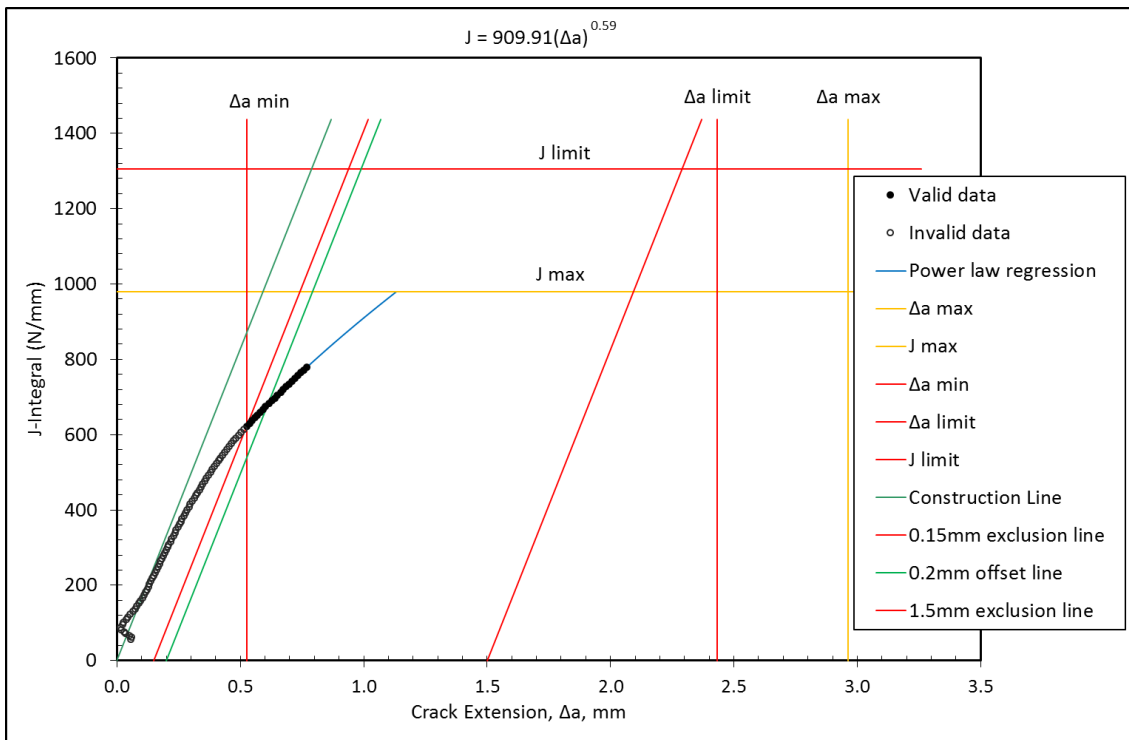
Figure 5.24   *J*-R curve for 25 mm thick S690QL steel plate using normalisation method under quasi-static conditions

The same normalisation method was used to generate a resistance curve for Charpy-sized pre-cracked SENB specimen ($B=W=10$ mm) for comparison with the standard SENB specimen configuration ($B=W=25$ mm). **Figure 5.25** shows the R-curve generated using $B=W=10$ mm under quasi-static loading condition. There are similarities between the R-curve generated for the two SENB specimen geometries ($B=W=25$ mm and $B=W=10$ mm).

It follows that a reduced initiation toughness J_{IC} or $J_{0.2}$ at the onset of stable crack growth of about 311.2 N/mm is observed using a Charpy-sized pre-cracked SENB specimen ($B=W=10$ mm) under QS loading conditions due to loss of crack tip constraint. This is almost half of the J_{IC} or $J_{0.2}$ obtained using a 1T specimen. The results show that a Charpy-sized pre-cracked SENB specimen ($B=W=10$ mm) can be used to generate the R-curve for ferritic steels but correction of the crack tip constraint will be needed (*Chao and Zhu 2000; He et al. 2018*). This is not discussed in this thesis but is considered for future work.
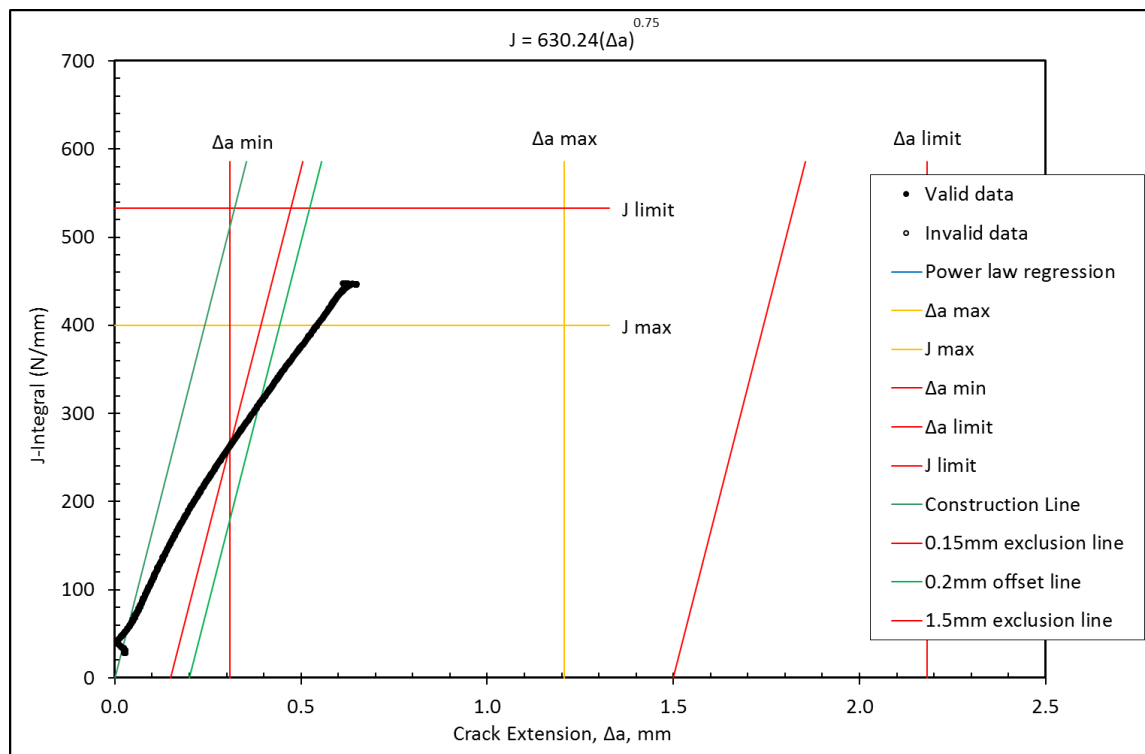
Figure 5.25   J-R curve by normalisation method for S690QL using Charpy-sized pre-cracked SENB specimen ($B=W=10$ mm) under quasi-static condition.

Assuring comparability, Charpy-sized pre-cracked SENB specimens ($B=W=10$ mm) have been employed to generate R-curve at dynamic loading rates. The multiple specimen methods which require a minimum of 6 specimens from low blow tests was used to generate a *J*-R curve at dynamic loading rates as shown in **Figure 5.26** with a $J_{0.2}$ value of about 456.3 N/mm. The

value of $J_{0.2}$ estimated at QS and dynamic loading rates using Charpy-sized pre-cracked SENB specimens ($B=W=10$ mm), show how the effect of loading rate enhances load bearing capacity of S690QL. Although the crack tip constraint correction is required for a valid size independent estimation of J_{IC} or $J_{0.2}$ using Charpy-sized pre-cracked SENB specimen ($B=W=10$ mm), this work thus gives an insight that sub-size specimen can be used to generate a valid J-R curve.
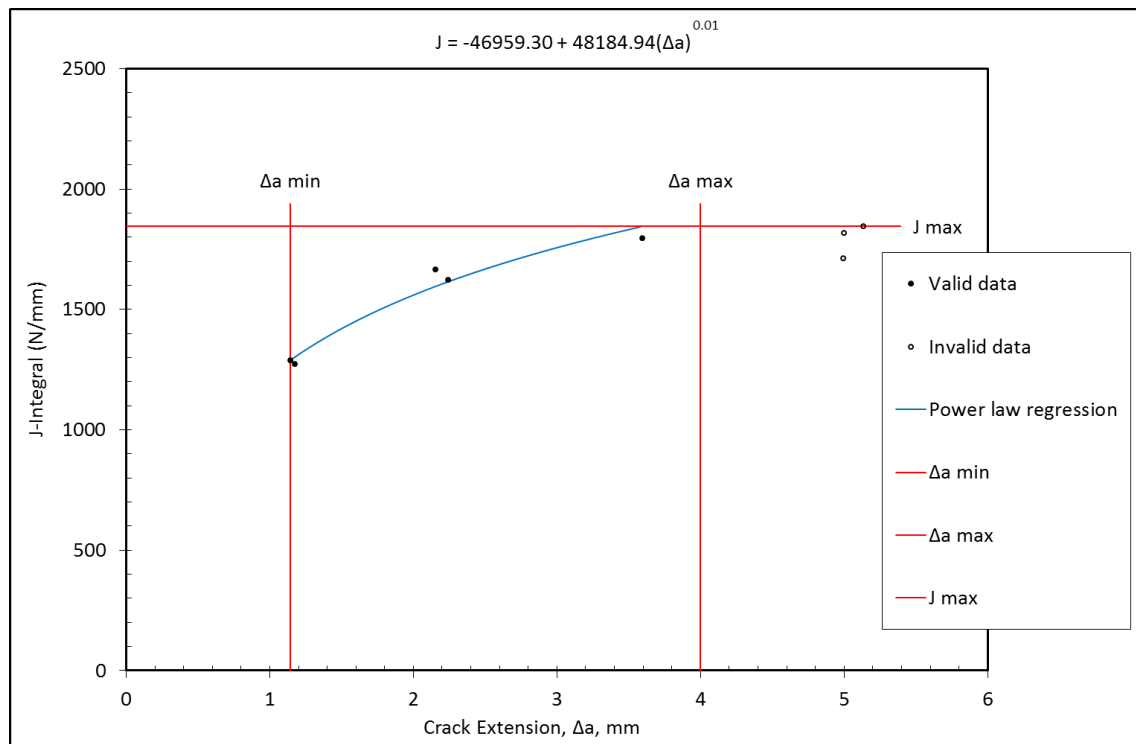
Figure 5.26 J-R curve obtained by multiple specimen method for S690QL using Charpy-sized pre-cracked SENB specimen ($B=W=10$ mm) at dynamic loading rate (5400 mm/s)

5.6   Structural implication of using CVN and fatigue pre-cracked Charpy-sized SENB specimens to qualify S690QL and S960QL fracture behaviour under impact loading.

5.6.1   *Overview*

Charpy V-Notch (impact energy) is a largely used criterion to classify structural steel grades as either brittle or ductile based on the absorbed energy recorded during an impact loading test. Ductile materials normally absorb more energy than brittle materials as illustrated in **Figure 5.27**, using real time CVN data of S690QL as an illustration. Like other ferritic (body-centred cubic crystal structure) steels, S690QL and S960QL experience a transition from the upper shelf (ductile) to the lower shelf (brittle) based on both CVN and Charpy-sized SENB impact

test results, fitted with *tanh* function. The transition from higher absorbed energy to lower impact resistance indicates a possible reduction in the amount of energy absorbed/resistance to fracture as the temperature decreases under impact loading.
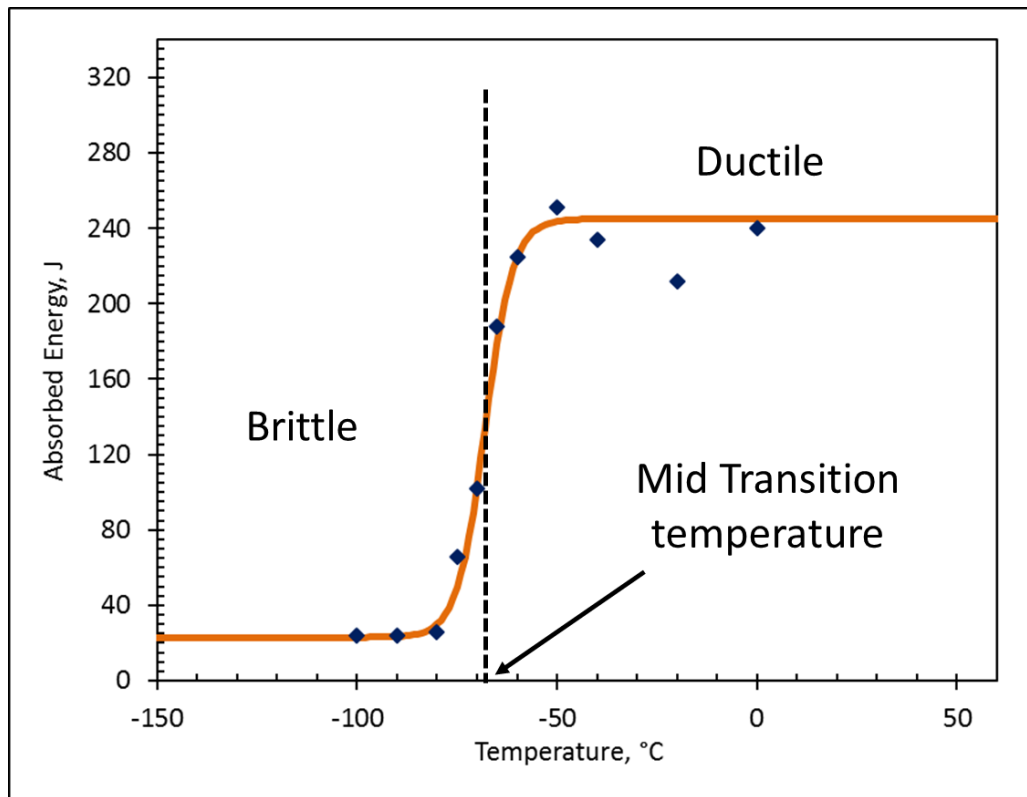
Figure 5.27   Illustration of the ductile-to-brittle transition curve using real time CVN data for S690QL

5.6.2   CVN and Charpy-sized SENB results

The full transition curve from using both CVN and Charpy-sized pre-cracked SENB impact test specimens for S690QL and S960QL are shown in **Figures 5.28 and 5.29**, respectively. The results from the Charpy-sized pre-cracked SENB impact tests indicate a possible reduction in the amount of energy absorbed/resistance to fracture when a sharp crack is introduced which is discussed further in the next sub-section. The full data are presented in the appendix.
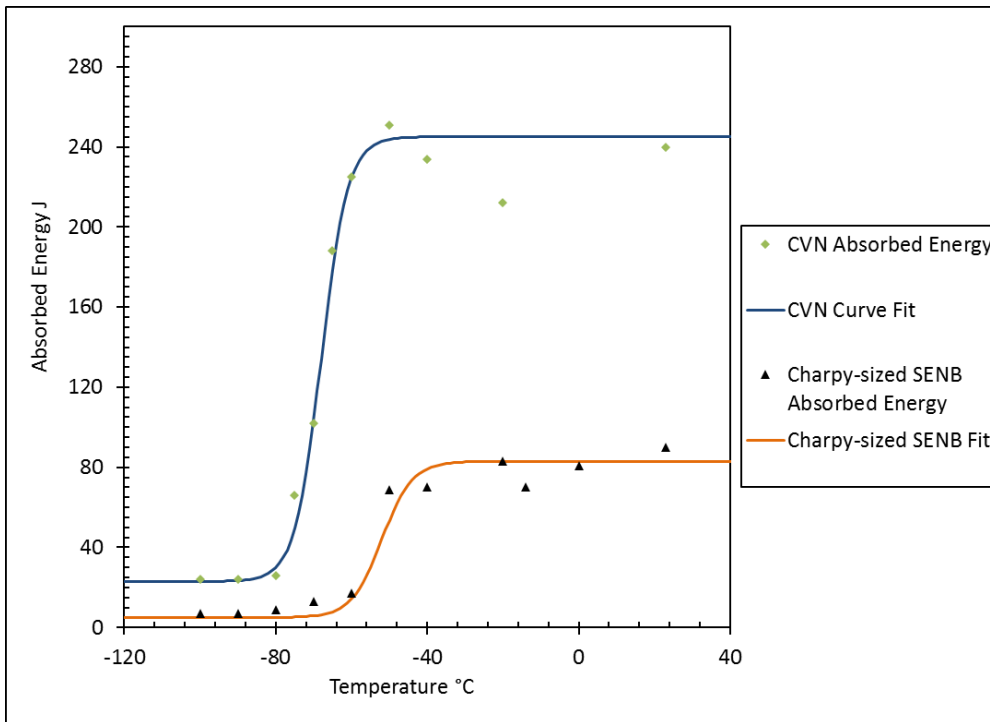
Figure 5.28   Full transition curves of S690QL in terms of Charpy V-Notch (CVN) and Charpy-sized pre-cracked SENB ($a_0/W = 0.5$).
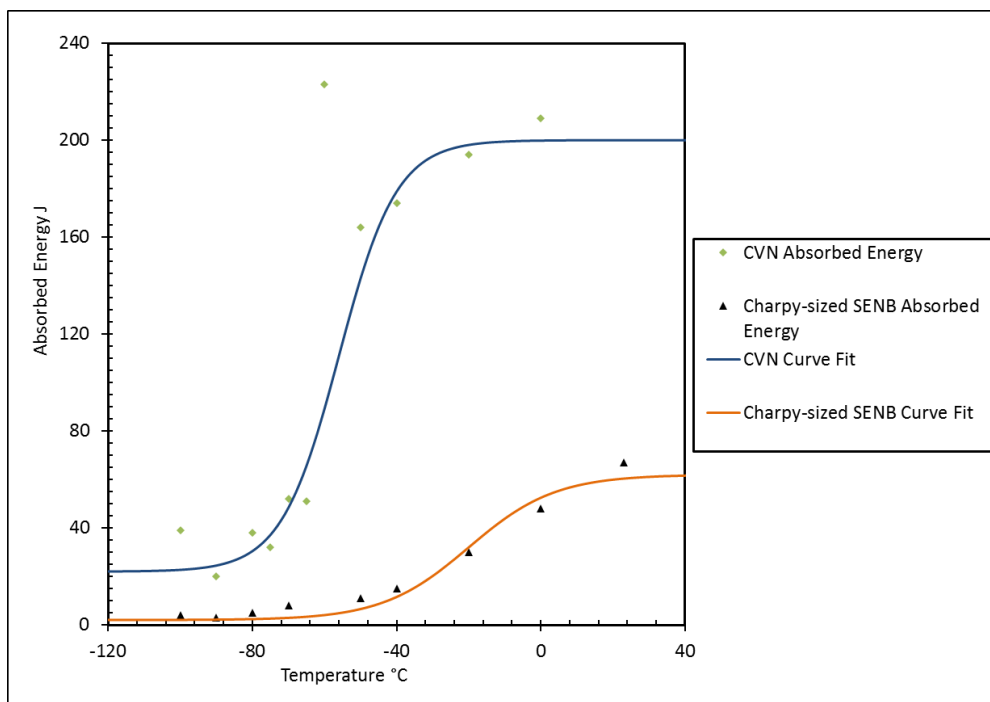
Figure 5.29   Full transition curves of S960QL in terms of Charpy V-Notch (CVN) and Charpy-sized pre-cracked SENB ($a_0/W = 0.5$).

The test data in terms of the mid-transition temperature (T_0) and temperature corresponding to 27 J (T_{27}) for S690QL and S960QL from **Figures 5.28 and 5.29** are summarised in **Tables 5.10 and 5.11,** respectively. It is important to mention that the data based on the *tanh* function curve fitting are considered as a conservative estimate.

Table 5.10 T_0 and T_{27} data for S690QL from Figure 5.28

Specimen	Mid transition temperature ($T_{0,m}$)	*Temperature corresponding to 27 J (T_{27})*
Charpy V-Notch (CVN)	-68	-82
Charpy-sized SENB ($a_0/W = 0.5$)	-52	-56

Table 5.11 T_0 and T_{27} data for S960QL from Figure 5.29

Specimen	Mid transition temperature ($T_{0,m}$)	*Temperature corresponding of 27 J (T_{27J})*
Charpy V-Notch (CVN)	-56	-84
Charpy-sized SENB ($a_0/W = 0.5$)	-20	-24

5.6.3   Discussion

The results show that these steels are predominantly ductile down to about -50 °C for S690QL, based on the CVN and Charpy-sized pre-cracked SENB results. If subjected to further reduction in temperature the steel enters the ductile to brittle transition, and at temperatures much below (around -75 °C for S690QL, CVN results), the brittle mode of failure occurs. The upper shelf region of the curve means these materials exhibit elastic-plastic behaviour with a ductile mode of failure, whereas the lower shelf indicates a brittle mode of failure. CVN impact tests may not be sufficient to directly analyse and assess the dynamic fracture toughness of a material, since the blunt notch of the specimen does not permit fracture mechanics calculations based on such test results. CVN results are often used as a qualitative proxy for the quasi-static fracture behaviour of steel.

The Charpy-sized pre-cracked SENB results are more representative of the fracture behaviour of these steels under dynamic loading. The introduction of a sharp crack/notch in the Charpy-

sized pre-cracked SENB means that they show a lower resistance in terms of the absorbed energy to impact loading on the lower shelf with 7 J recorded at -100 °C compared to CVN absorbed energy of 24 J for S690QL at the same temperature. The mid-transition temperature is estimated to be -52 °C and -20 °C for S690QL and S960QL, respectively. A difference of about 16 °C and 36 °C in the estimated transition temperature was recorded when comparing the results on blunt notch and sharp cracks for S690QL and S960QL, respectively.

The difference could be a result of the differences between extensional void growth exhibited by CVN specimens, in the direction of maximum plastic strain, rather than the dilatational growth as a result of high triaxial stress state at the crack tip, experienced by Charpy-sized pre-cracked SENB specimens (*Copper et al. 2017*). This explains why CVN specimens may not be appropriate to characterise the fracture behaviour under dynamic loading, but rather be used as qualification and for material selection purposes.

The fracture mechanics approach is the most appropriate method to characterise fracture behaviour of any ferritic steel irrespective of the strength level or Y/T ratio. Unlike the CVN impact testing, the fracture toughness test method introduces a sharp crack profile under high constraint in order to conservatively represent the different geometrical constraints a structural element may experience during in-service conditions. Performing the tests at different loading rates can help to understand the dynamic effects on the fracture performance, with an expected shift in the ductile-to-brittle transition temperature to higher temperature as discussed in section 5.4.

5.7   Fracture toughness SENB FEA model

5.7.1   Overview

This section presents the finite element analysis results and discussion from the fracture toughness SENB model developed to characterise the crack-tip stresses and strains in static linear analysis in order to determine the crack driving force which cannot be estimated or calculated during the fracture toughness tests, and to determine the effect of loading rate on the rate of crack mouth opening displacement

Also, the FEA was used to determine the best curve fitting method to be employed when the load and load line displacement (LLD) graph is generated from Instrumented Charpy test

results using Charpy-sized pre-cracked SENB impact test specimens and linear static analysis was also employed. Since a critical assessment point in a single point fracture toughness test J_m (ductile tearing) or J_c (brittle) is shown in the experimental fracture toughness test results, it is important to support the results with finite element analysis which is a good exercise for structural assessments.

In most structural assessments, crack driving force is widely determined numerically either using J-integral or CTOD fracture toughness parameter. A contour J-integral method has been employed in this analysis for crack driving force calculation due to its robust theoretical application, ease of calculation and for comparison with the experimental load versus load line displacement plot. A weighted method was employed to determine the average J-integral value from each load increment at the crack front.

The FE model was intended to be a representation of the test specimens, in order to extract crack driving force that could not be determined from the experiments. Therefore, direct experimental tensile test results validated via the material model were used for S690QL as discussed in section 4.5 and BS7910 (*BS 7910:2013+A1 2015*) was used to determine the tensile properties at low temperature based on the experimental tensile test results at ambient temperature. A rate dependent model was incorporated in the analysis using the yield stress ratio earlier discussed in section 3.3.1.

5.7.2 *Model generation and geometry*

The model was generated using the commercial FE modelling software, ABAQUS version 6.14 (*Simulia 2014*). The Charpy-sized pre-cracked SENB specimen ($B=W=10$ mm) geometry described earlier in this chapter was used as reference for the modelling. A three-dimensional symmetrical ¼ SENB was modelled for the quasi-static condition and this was unchanged for the elevated loading rate analysis. The deformable solid rectangular block measures 27.5 mm x 10 mm x 5 mm and this represent the ¼ SENB model used for the analysis.

The ¼ SENB model was modelled with an initial notch tip radius 2.5μm (blunt notch), **Figure 5.30** because in reality and in some materials, plastic deformation can cause blunting from the original sharp crack with the degree of blunting depending on the toughness (*Anderson 2005*). However, the results were compared with a ¼ SENB modelled without notch tip radius (sharp notch) as represented by a Charpy-sized pre-cracked SENB specimen. The block was partitioned to allow for the mesh density to be defined independently in different locations on

the block and with the symmetry plane in the Z direction, **Figure 5.31**. It is important to say that the ratio of the initial crack length and width (a_0/W) is taken for all models as 0.52 which is the average value from the experimental results.
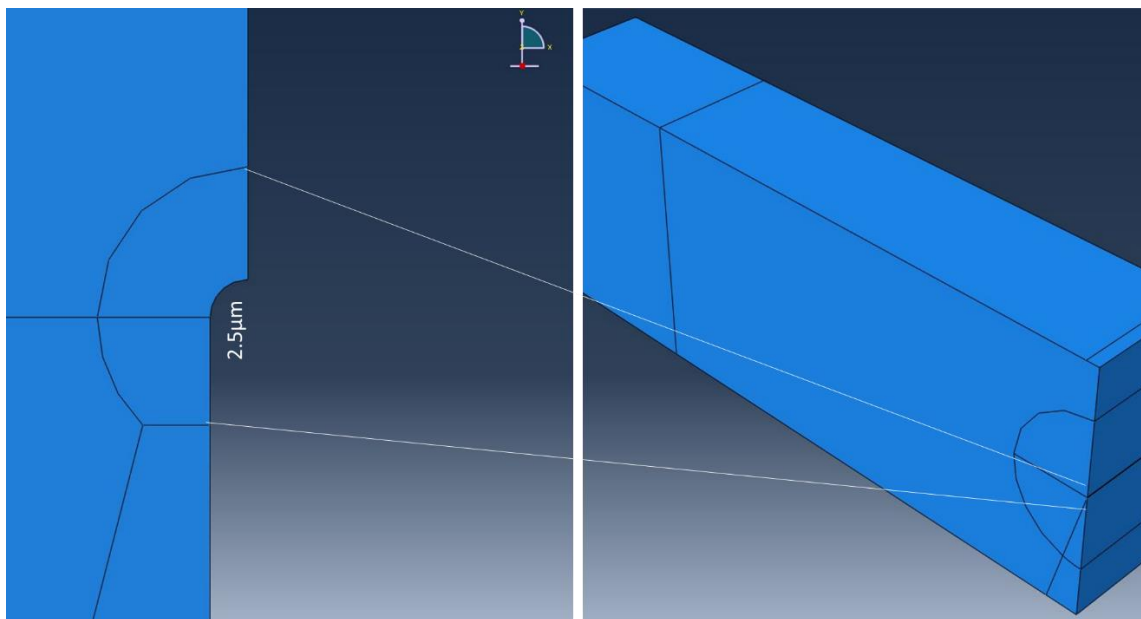
Figure 5.30   ¼ SENB model with an initial notch tip radius of 2.5µm
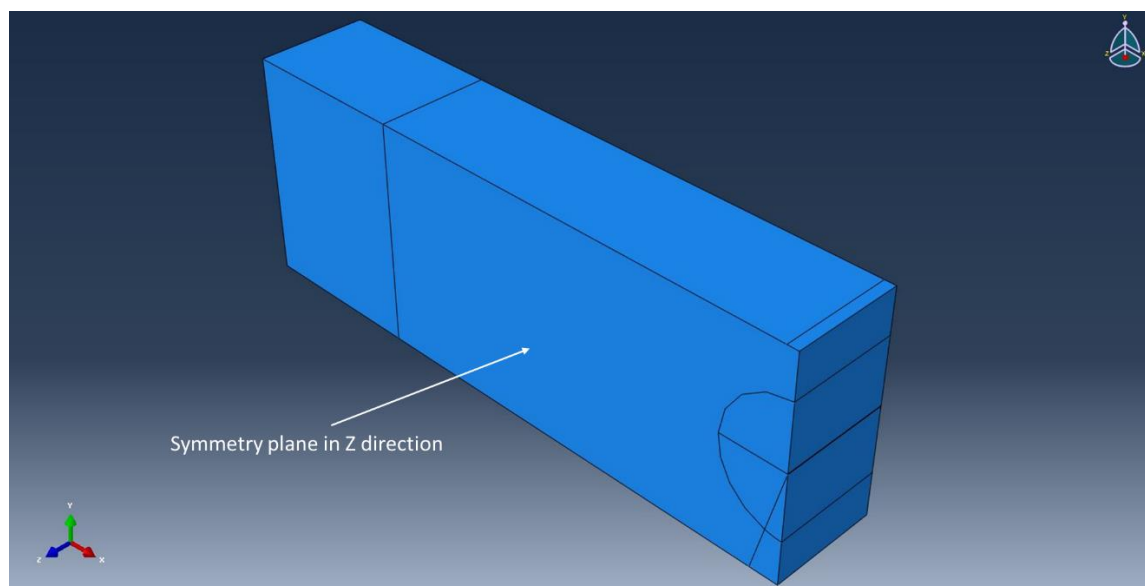
Figure 5.31   ¼ SENB model partitioning and the symmetric plane (Z direction)

5.7.3   *Meshing and boundary conditions*

The mesh arrangement used for this analysis is shown in **Figure 5.32**. Meshing was refined in the region of the crack tip with a higher mesh density applied to increase accuracy and improve

higher calculation definition. Reduced integration quadratic twenty node brick (C3D20R) elements were used to mesh the models with imposed displacement (DY) over an area in relation to the striker radius used in the experiment, and the boundary conditions (DX) also shown in **Figure 5.32**. The number of elements and imposed displacement applied to the model are summarised in **Table 3.6**.
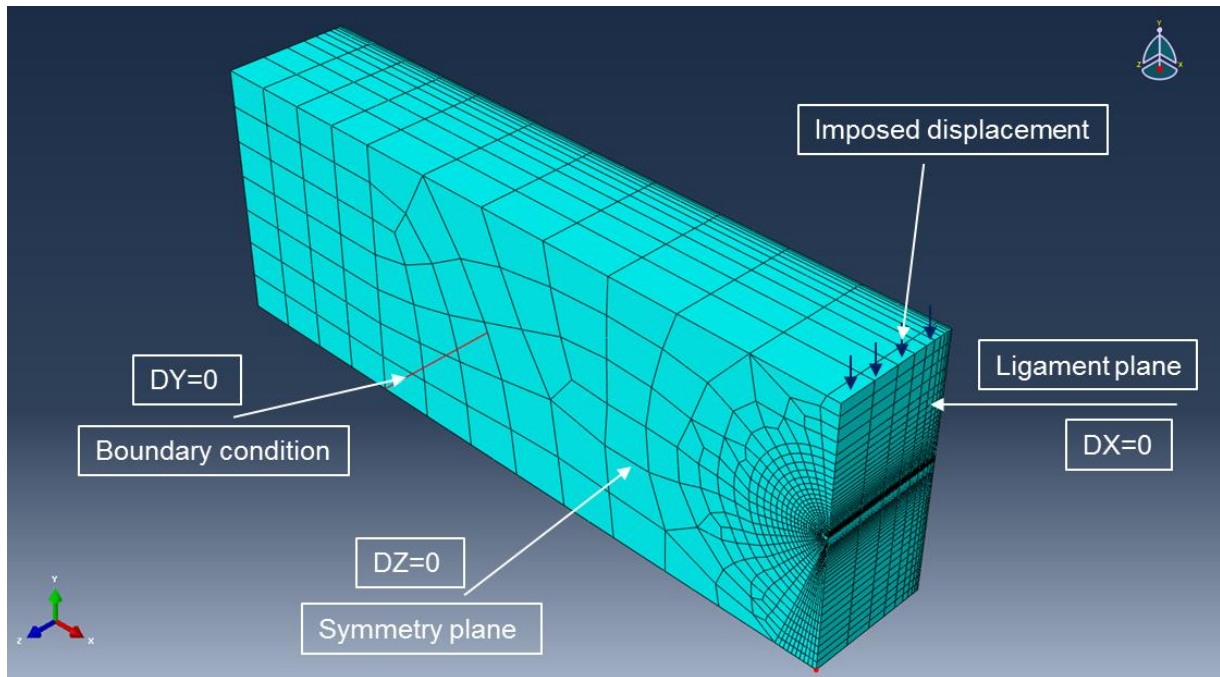
Figure 5.32   Mesh arrangement and boundary conditions used in the model

5.7.4   *Results and validation*

5.7.4.1 Quasi-static FEA loading condition

The results under QS condition at ambient and low temperatures with an initial notch tip radius 2.5μm (blunt notch) and without notch tip radius (sharp notch) were compared, **Figures 5.33 and 5.34**, respectively. The FEA results show good agreement with the experimental fracture toughness data at ambient temperature on a load versus CMOD plot. Marginal differences were observed between the results with an initial notch tip radius 2.5μm (blunt notch) and without notch tip radius. Subsequent analyses in this thesis use the model with an initial notch tip radius 2.5μm (blunt notch) for stress field analysis, which is influenced by crack blunting and reduces stress triaxiality locally.
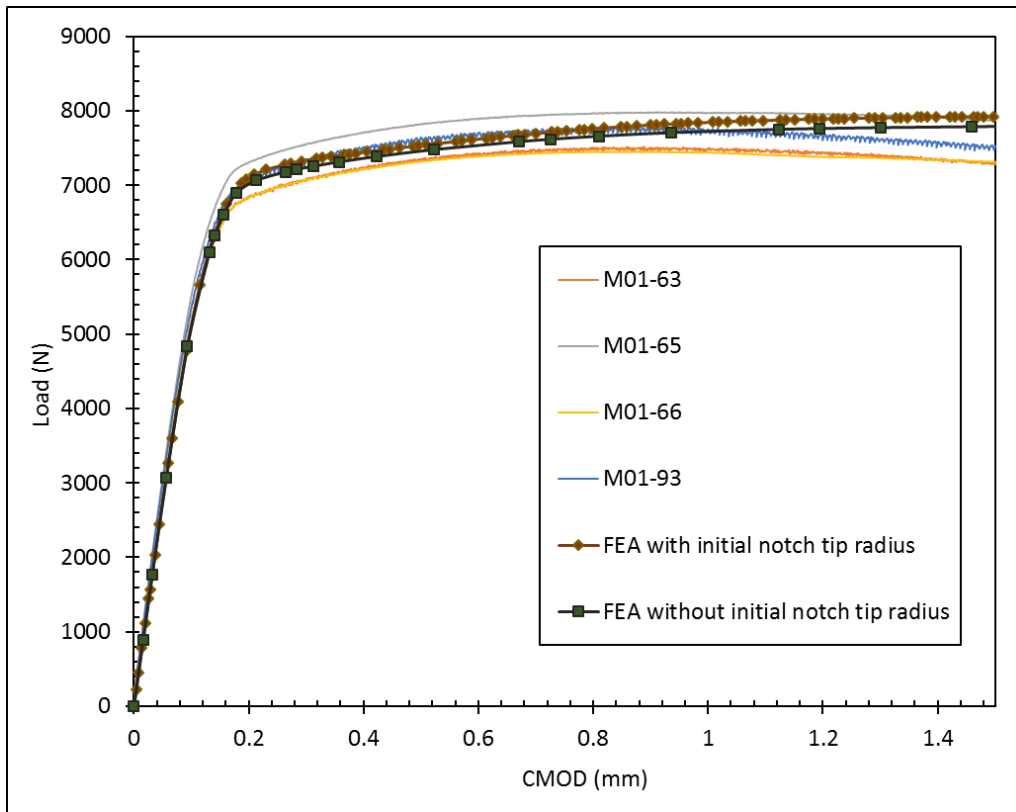
Figure 5.33   Load versus CMOD of S690QL at ambient temperature and QS condition
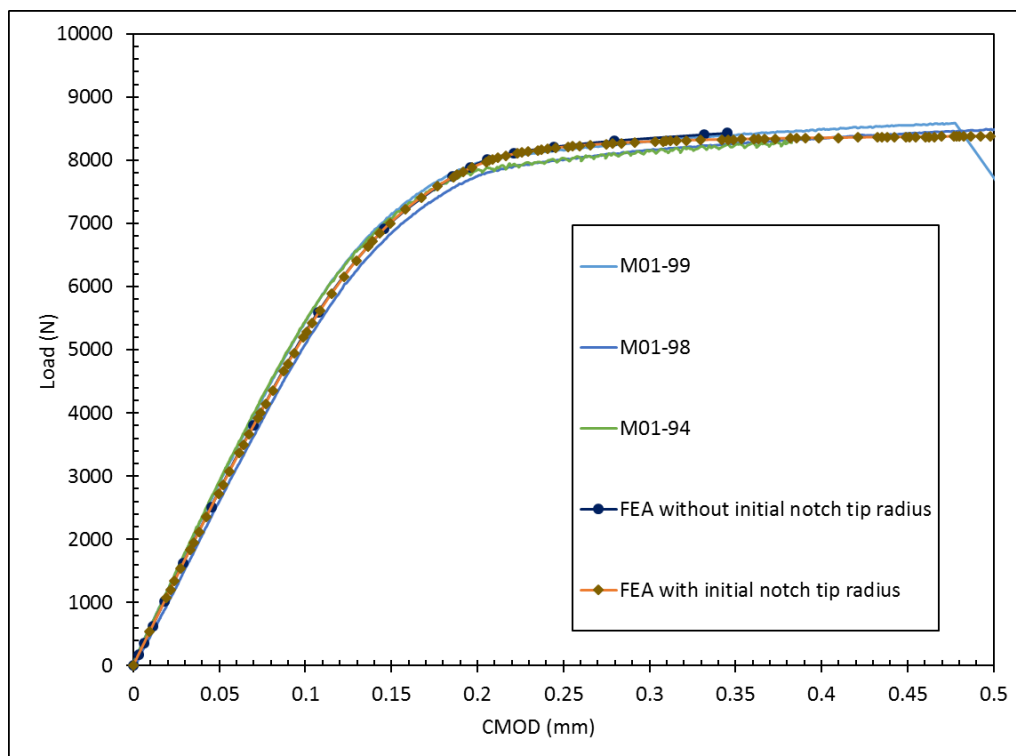
Figure 5.34   Load versus CMOD of S690QL at -100 °C and QS condition.

178

The FEA results at QS condition and ambient temperature were verified and validated in compliance with BS7448-4 given in section 3.3.2.1 as Eqs. (3.11-3.13). A weighted crack-front average J-integral (J_{avg}) value for each load increment was calculated from the model, and the load from the model was used to calculate the J-integral based on BS7448-4, **Figure 5.35**.

The circle on the graph shows the critical assessment point in a single point fracture toughness test, J_m (ductile tearing) at the first attainment of maximum load. This is commonly determined during a fracture toughness tests to represent the material resistance. The results on Figure 5.35 show how applied load drives crack opening which cannot be estimated during experimental fracture toughness tests. This is a very important exercise for structural assessment, and FEA has helped to determine the crack driving force for a ductile material like S690QL at ambient temperature and under QS condition.
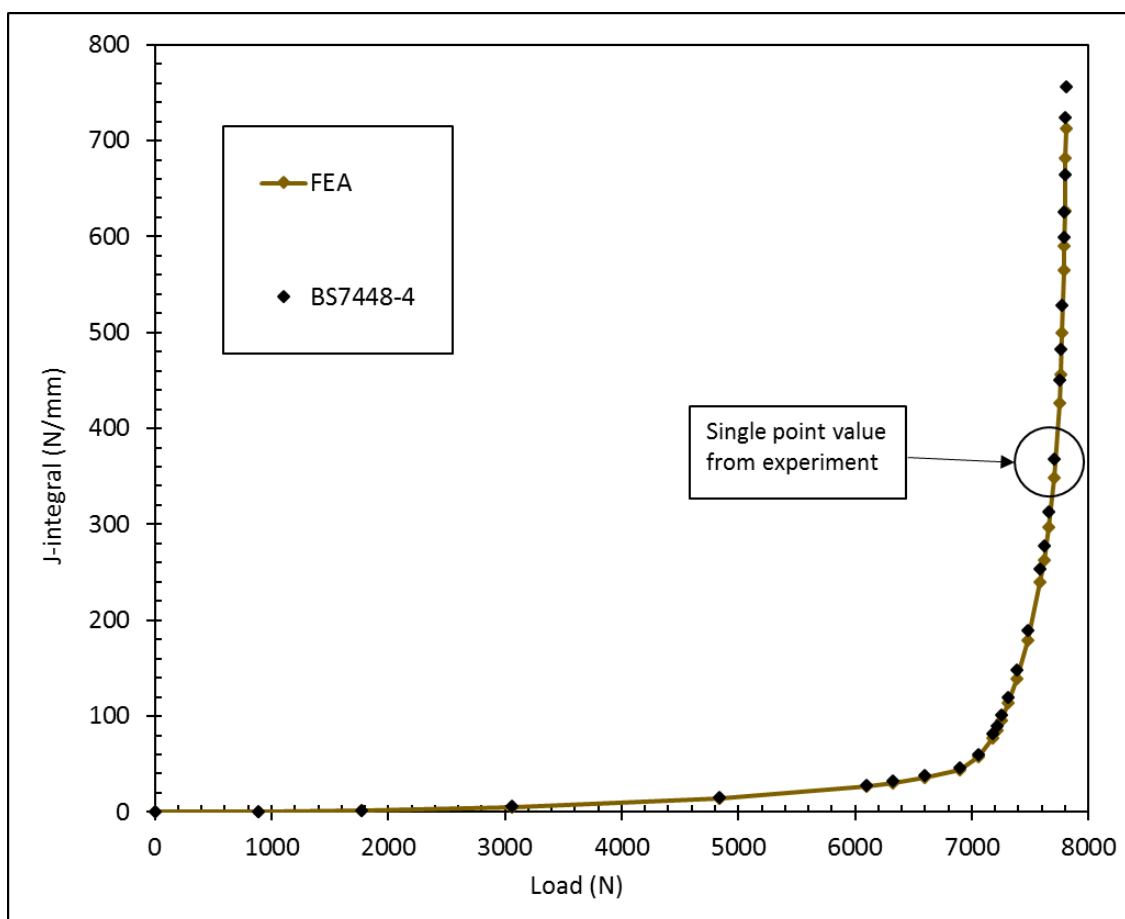
Figure 5.35   Compliance of the FEA model with BS7448-4 and validation of the J-integral of S690QL at ambient temperature and QS condition.

Compliance and validation of the FEA results with BS7448-4 was also carried out under QS condition at low temperature (-100 °C), **Figures 5.36 and 5.37**. The results compare the linearity between CTOD and the J-integral (discussed in section 2.3.2.3) **Figure 5.36**, and how applied load drives crack mouth opening displacement (CMOD) in compliance with BS7448-4, **Figure 5.37**.
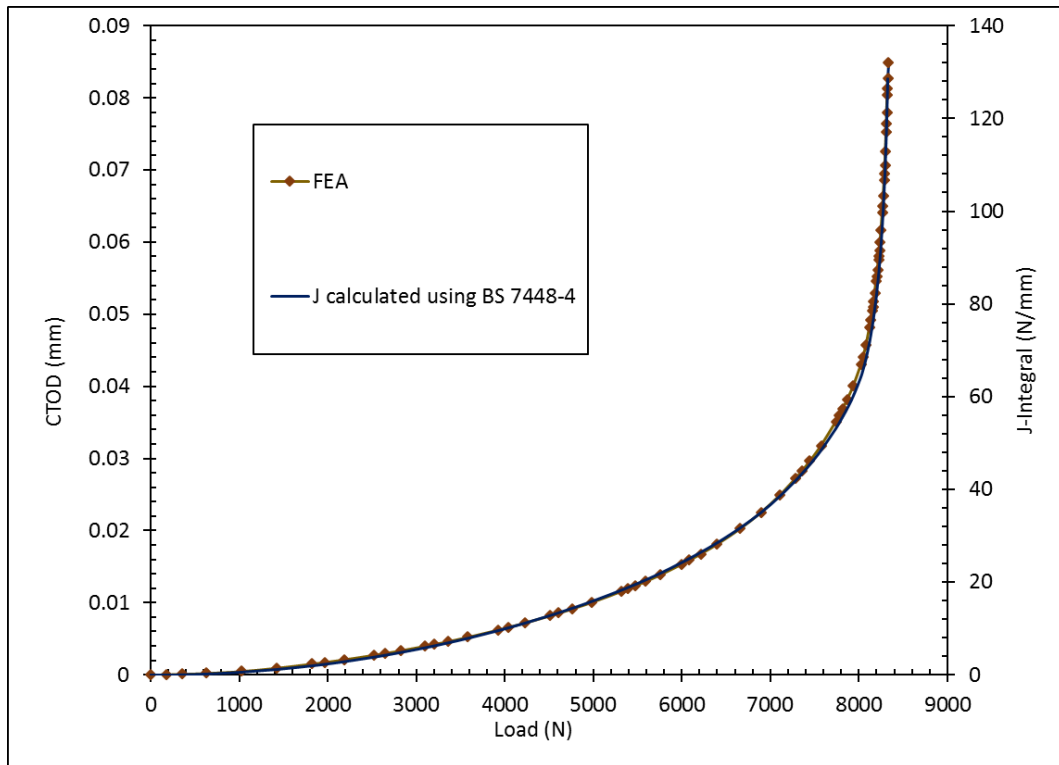
Figure 5.36   Compliance of the FEA model with BS7448-4 and validation of the *J*-integral and CTOD of S690QL at -100 °C and QS condition.
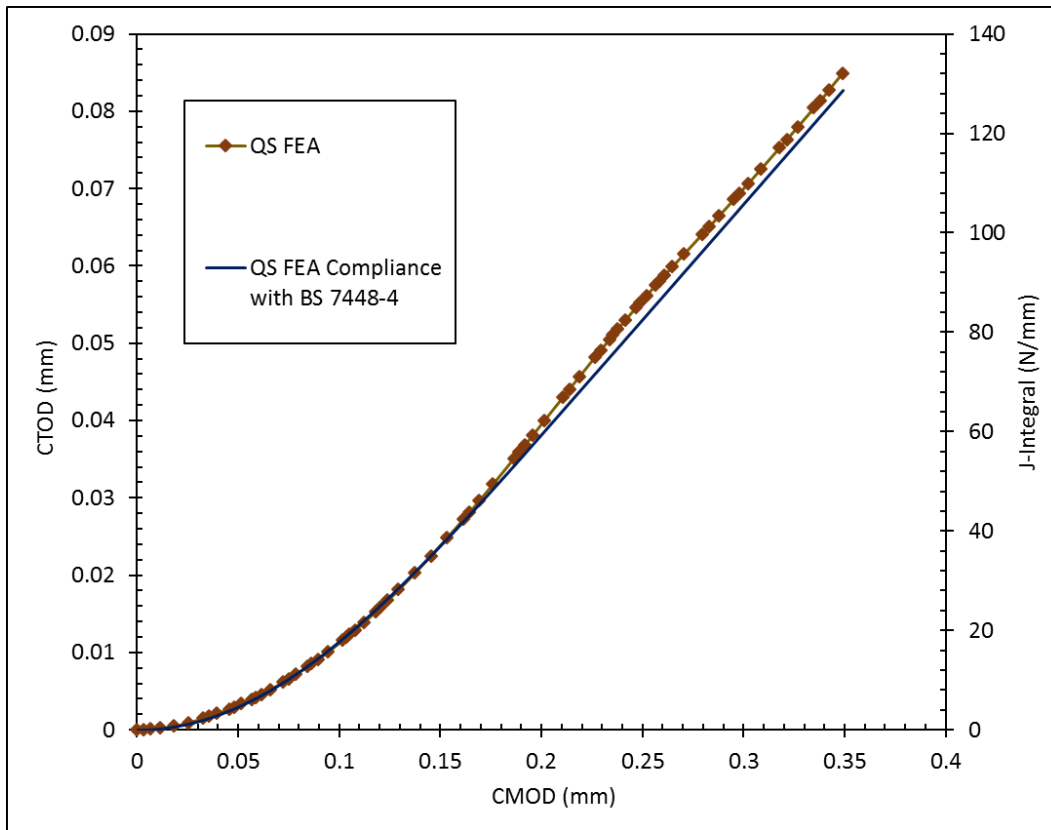
Figure 5.37   Comparison of CMOD from FEA and compliance of the FEA model with BS7448-4 of S690QL at -100 °C and QS condition.

Also, the model at low temperature (-100 °C) under quasi-static loading condition was validated with the HRR stress field as described in section 3.3.2.1. Stress field and *J*-integral from the model at each load increment is plotted in **Figure 5.38** to show convergence. The quasi-static HRR stress fields calculated for a mode I crack opening when $\theta = 0°$ are shown in **Figure 5.39**.

A good agreement with the theoretical HRR field was evident corresponding to the loading levels when *J* is >13.43 N/mm (**Figure 5.38**), where nodal mode I opening stress values were extracted (σ_{yy}) along the paths directly ahead of the model crack-tip different load increments. The radius, *r* (distance from the crack tip along the centre line) of each stress value at each load increment was normalised using $r\sigma_0/J$ to establish the similarity of the HRR stress fields and the FEA QS stress fields at -100 °C. The main input for the validation is summarised in Table 5.12.

Table 5.12   HRR stress field input data for validating the SENB model based on Eq. (3.14) (*Shih, 1983*)

n	I_n	E	σ_0 (-100 °C)	α	$\sigma_{\theta\theta}$	v
22	4.2	212000	949.4	1	2.68	0.3
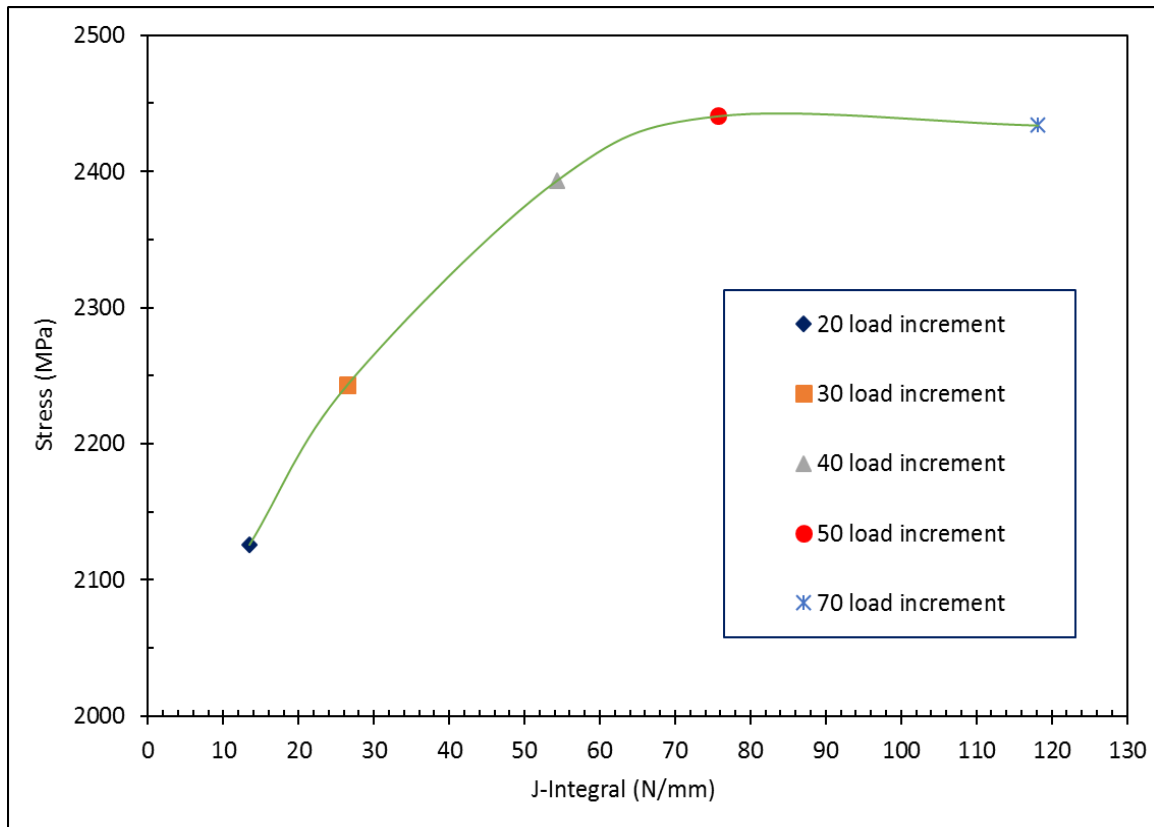
Figure 5.38   FEA QS Stress field versus *J*-integral at -100 °C for each load increment
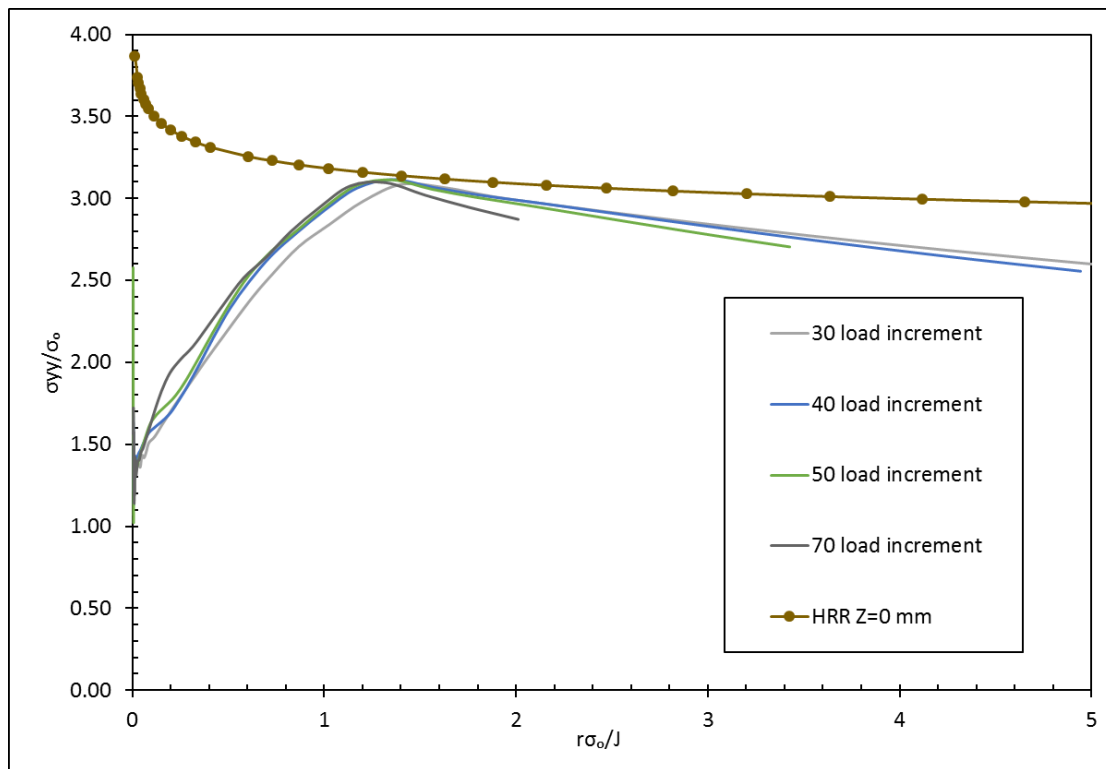
Figure 5.39   HRR stress field at $\theta = 0°$ at -100 °C under quasi-static condition

5.7.4.2 Elevated FEA loading condition

At elevated loading rates (in this case a loading rate of 5400 mm/s corresponding to a K-rate value of about 10^6 MPa$\sqrt{m}$/s) the model was unchanged, but a rate-dependent yield stress ratio was incorporated in the model. Displacement (DY) was applied in conjunction with the time period of the analysis (Δ) to achieve a crosshead speed of 5400 mm/s (assuming a constant speed). The mesh and boundary conditions under QS loading condition as discussed in sub-sections 5.7.2 and 5.7.3 were unchanged for the elevated loading rate FEA. A static linear analysis was carried out since the result from the time versus displacement plot shows a linear behaviour.

Since a major concern of the effect of loading rate on the DBTC of S690QL is a shift to higher transition temperature and possible reduction in the cleavage fracture toughness value, section 5.4, the simulation and analysis were conducted at low temperature. Due to the imbalance between the internal and external forces during high loading problems, the load signal as expected was noisy as a result of the stress wave propagation developed during the instrumented Charpy test, section 3.2.4. Therefore, it is imperative to validate the model at elevated loading rate with experimental results that exhibit some plastic deformation (ductile

tearing) before applying the methods to experimental data that failed by cleavage fracture with no ductile tearing, ($\Delta a = 0$ mm). The FEA results at -40 °C under elevated loading condition, **Figure 5.40** was verified and validated in compliance with BS7448-4 as shown in **Figure 5.41**.
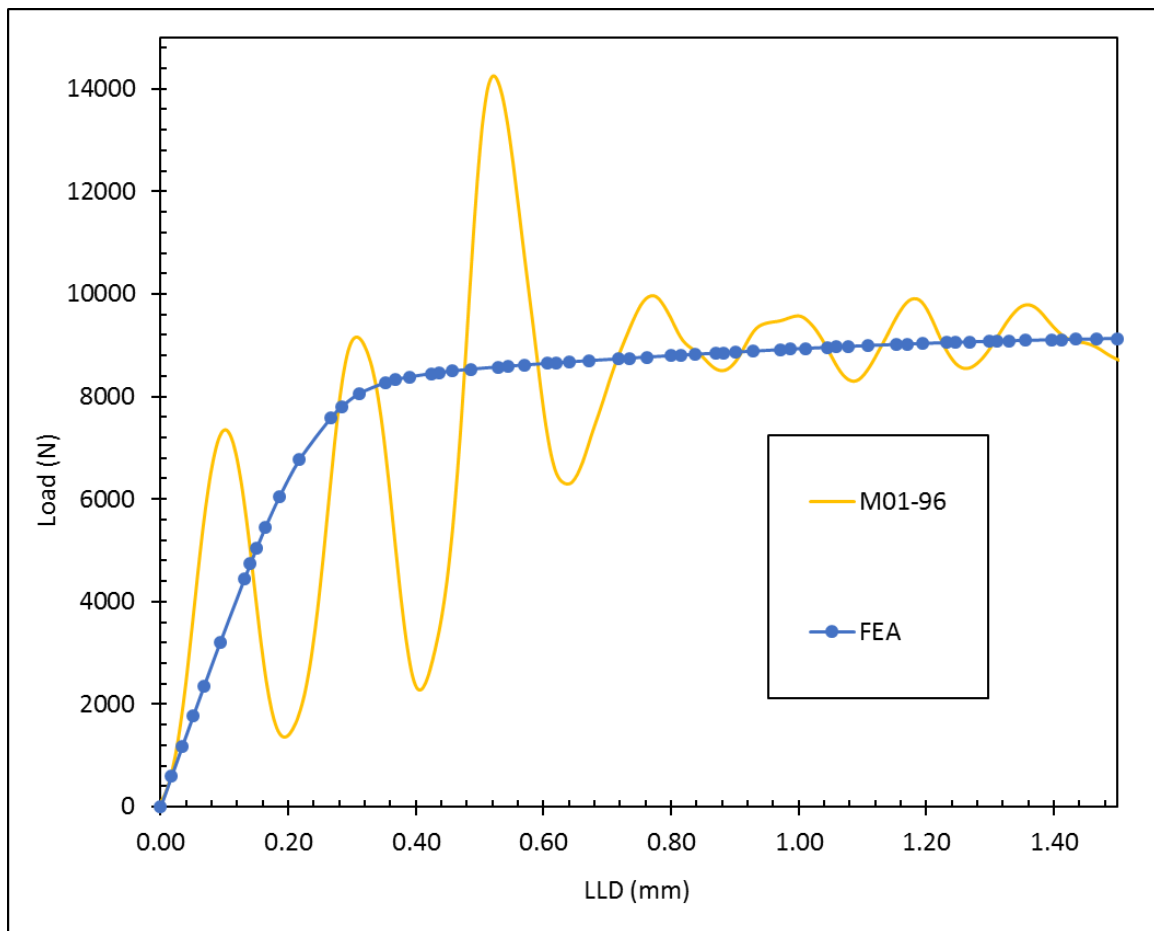
Figure 5.40   Load versus LLD of S690QL at -40 °C under elevated loading rate (K-rate = 10^6 MPa√m/s).

A good agreement is evident with the experimental fracture toughness data from the Instrumented Charpy test data at -40 °C on a load versus LLD plot, Figure 5.39. Crack mouth opening displacement (CMOD) increases as the loading rate increases at low temperature (**Figure 5.42**) when compared to the FEA results at QS at low temperature (Figure 5.37). CMOD increases from 0.35 at QS to 1.09 at elevated loading rates. The results show that the model can be used for further parametric study involving other steel grades with varying Y/T ratio in comparison to how CMOD and CTOD are affected.
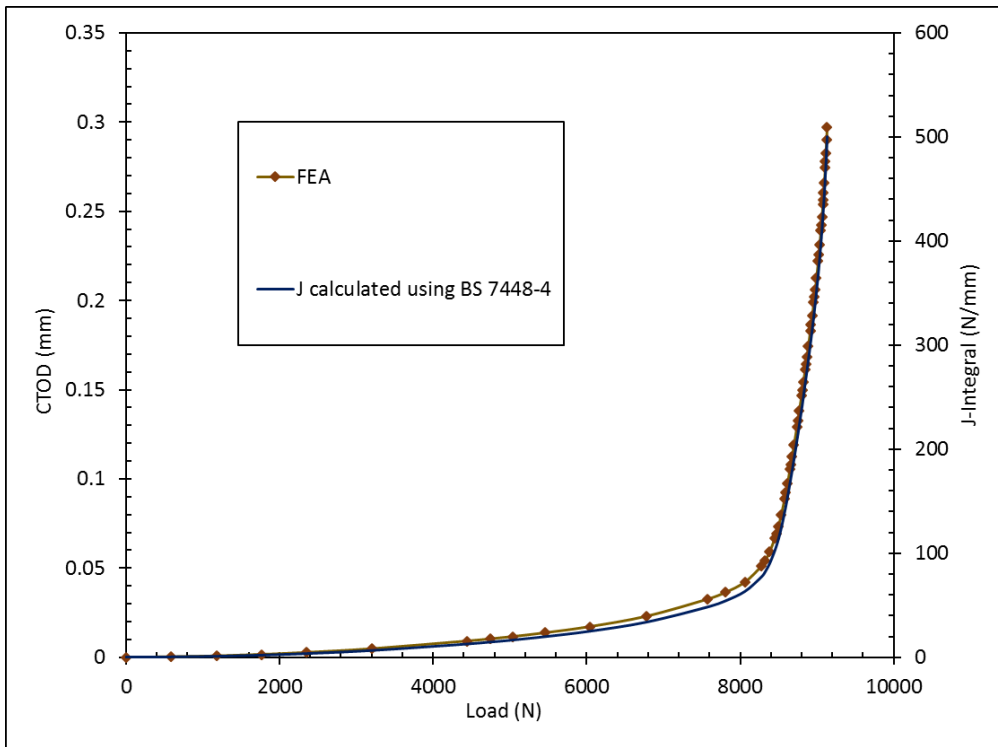
Figure 5.41   Compliance of the FEA model with BS7448-4 and validation of the *J*-integral and CTOD of S690QL at -40 °C under elevated loading rates (K-rate = 10^6 MPa√m/s).
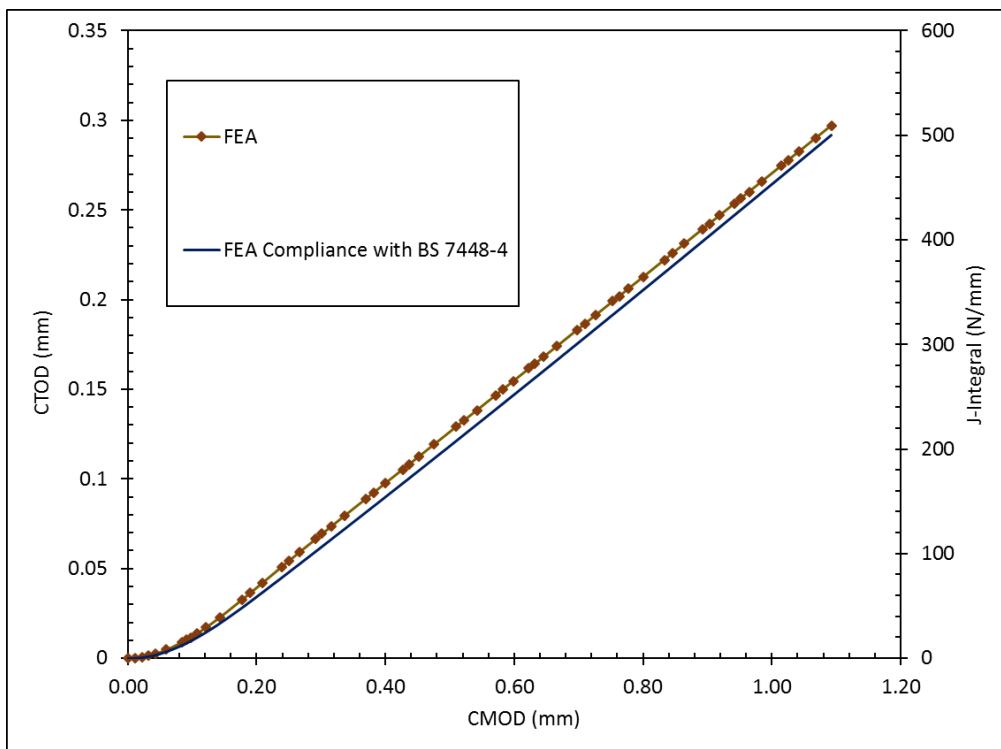
Figure 5.42   Comparison of CMOD from FEA and compliance of the FEA model with BS7448-4 of S690QL at -40 °C and elevated loading condition.

Another strong case from the FEA results at elevated loading rate when compared to results (FEA and experimental) under QS loading condition is the fitting method on the linear region when a load and load line displacement (LLD) graph is generated from an Instrumented Charpy test using Charpy-sized pre-cracked SENB impact test specimens. It is important to mention no clear guidance has been given in the international standards on fitting method to use when a Charpy-sized pre-cracked SENB impact test specimen is employed. Fitting the data/curve using mathematical methods such as spline or polynomial curve fitting techniques to generate an average data from the raw data could be non-representative of the material's elastic behaviour.

The experimental results at QS (ambient and low temperature) supported by the FEA results at elevated loading rates show that the linear (elastic) part of the load and load line displacement (LLD) graph generated from an Instrumented Charpy test using Charpy-sized pre-cracked SENB impact test specimen can be fitted using the experimental fracture toughness data at QS condition either at ambient or low temperature (with some ductile tearing). The plastic region can then be fitted using the mathematical fitting techniques as shown in **Figure 5.43** if a finite element analysis is not carried out. It is evident that in **Figure 5.43**, elevated FEA results show good agreement in the linear (elastic) part of the graph when compared to the experimental fracture toughness test result at both ambient (M01-63) and low temperature (M01-98) before showing a good agreement in the plastic region with the spline curve fitting method.
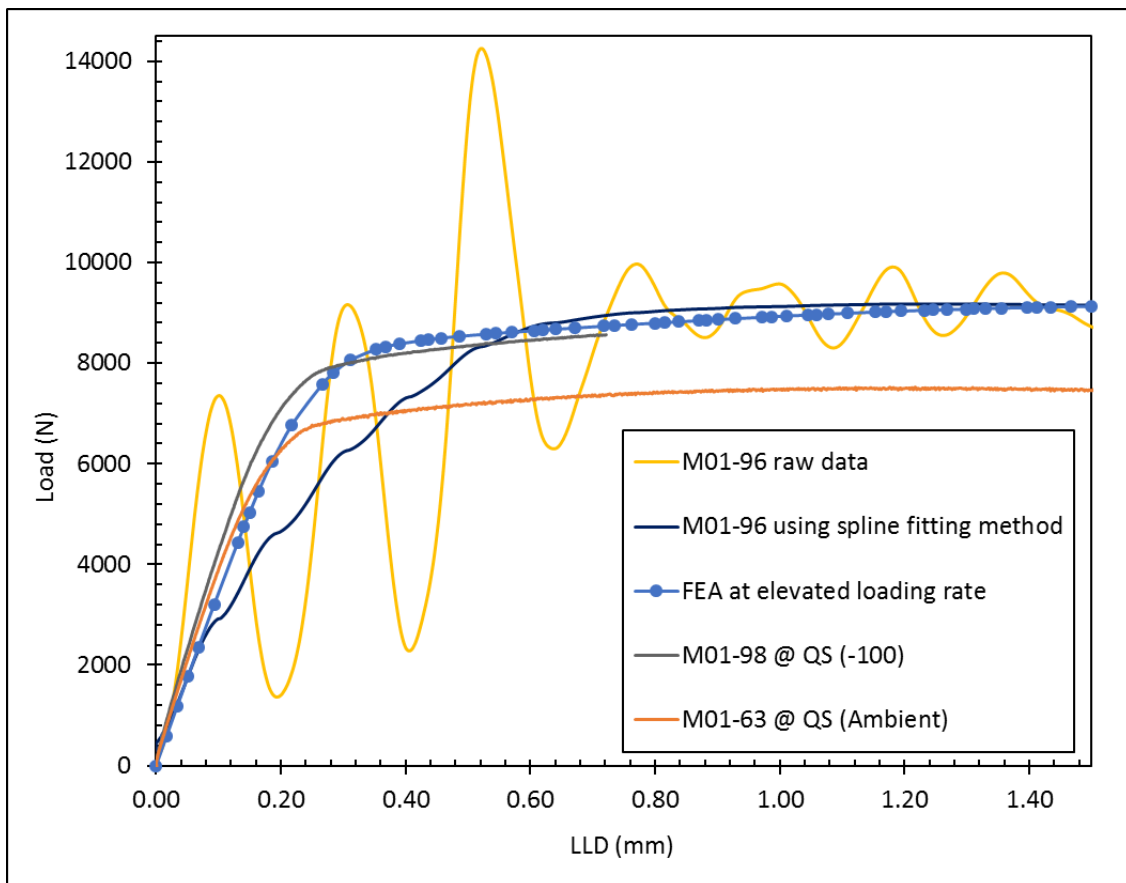
Figure 5.43   Use of FEA model at elevated loading rates to predict the best curve fitting method in the elastic region as compared with fracture toughness data at ambient and low temperature under quasi-static loading conditions.

5.8   Chapter summary

This section summarises the experimental fracture toughness test results of S690QL and S960QL at a range of loading rates. The loading rates considered represent the critical loading rate encountered in an offshore or marine in-service condition. The impact resistance full transition curve results of the CVN compared to Charpy-sized SENB impact tests on S690QL and S960QL are presented in this chapter. The structural implication of using a Charpy V-Notch (CVN) with blunt notch to characterise the dynamic behaviour in terms of the absorbed energy and to determine the mid-transition temperature on the DBTC is also discussed. The experimental test results of CVN and a similar Charpy-sized pre-cracked SENB geometry with crack depth $(a_0/W) = 0.5$ have been compared and discussed.

The experimental fracture toughness test results conducted at a range of temperatures between ambient and -120 °C represent test data from the following loading rates:

1. Standard or quasi-static (QS) loading rates at 0.005 mm/s, corresponding to an average K-rate value of about 1 MPa√m/s over the range of tests carried out using a single point measurement to determine the material fracture toughness. Standard SENB configuration ($B=W=25$ mm) and Charpy-sized pre-cracked SENB ($B=W=10$ mm) specimens were employed at this loading rate to characterise the fracture behaviour of S690QL and S960QL under normal loading conditions.

2. Intermediate loading rates at 200 mm/s – This corresponds to an average K-rate value of about 10^4 MPa√m/s over the range of tests conducted. The same test procedure used under QS loading conditions were used, and only Charpy-sized pre-cracked SENB ($B=W=10$ mm) specimens have been tested at ambient, -40 °C and -100 °C for this purpose.

3. High or dynamic loading rates at 5400 mm/s – At this loading condition, the Instrumented Charpy impact test results using the Charpy-sized pre-cracked SENB specimen at a range of temperatures are presented to determine the material resistance to impact loading. The crosshead speed corresponds to an average K-rate value of about 10^6 MPa√m/s over the range of tests.

Finally, the experimental fracture toughness results are supported by finite element analysis in order to evaluate the crack driving force and the effect of loading rate on the rate of crack mouth opening displacement. The SENB FEA model developed was validated using experimental data, BS 7448-4 and HRR stress field at ambient and low temperatures, and this was unchanged at elevated loading rates. The best curve fitting method to be employed when a load and load line displacement (LLD) graph is generated from Instrumented Charpy test results using Charpy-sized pre-cracked SENB impact test specimens are also discussed which will aid estimation of cleavage initiation point under impact loading.

Chapter 6   Effects of Dynamic Loading on Structural Integrity and Fitness-for-Service

6.1   Overview

Fracture-based engineering critical assessment (ECA) is introduced and discussed in this chapter. This is concerned with the structural implication of dynamic loading on the mechanical behaviour of HSS, by combining both the tensile properties and fracture toughness within an engineering critical assessment (ECA) when the assessment or behaviour is plotted on the failure assessment diagram (FAD) as the proximity to failure by fracture or plastic collapse. An assessment of how the properties of HSS under elevated loading rates presented in chapters 4 and 5 could affect the structural integrity of an offshore asset is conducted. The flaw case postulated represented on the FAD, conservatively considers a surface flaw in a 25 mm large plate to show how HSS will behave mechanically when loading rate might change a safe assessment to potentially unsafe ones when temperature decreases especially on the lower shelf of the ductile-to-brittle transition curve. To do this, a software developed by TWI Ltd CrackWISE® (CW5) has been used. The details of the software and application is discussed in section 6.3.

6.2   Introduction to fracture-based engineering critical assessment and failure assessment diagram

ECA provides guidance for failure avoidance and not failure prediction, but the assessment of ductile and brittle behaviour independently permits the effect of dynamic loading on both these failure modes to be somewhat quantified in relation to quasi-static performance. The ECA procedure is given in standards like British Standard BS 7910 for the assessment of flaws in metallic structures. Conventional design and fabrication practices only consider two parameters, material yield strength and applied stresses, without considering the actual condition (flaws or crack like defects) which limit the performance of structural components assumed to have been covered by fabrication quality standards.

Therefore, engineering critical assessment (ECA) is often used to supplement design and fabrication philosophy in order to assess whether structural components with a postulated or known flaw are safe from brittle fracture or plastic collapse under applied loads, graphically

represented on a failure assessment diagram (FAD). Three parameters are normally considered when carrying out an engineering critical assessment which forms the inputs to BS 7910. The first parameter is the material properties, which include tensile properties, fracture toughness, fatigue crack growth rate, etc. The second part constitute the flaws with varying size, position and orientation, while the last parameter is the stress or applied load acting on the region containing flaws, **Figure 6.1** (*Moore and Booth 2014*).

Understanding the interactions of flaws, material properties and applied stress helps to prevent major failure in-service. In this thesis, the interaction of the critical value of fracture toughness, tensile test results and flaw size of S690QL under different applied load and temperatures is studied using the FAD concept where assessment line and points are generated, the results of which are discussed further in section 6.4.
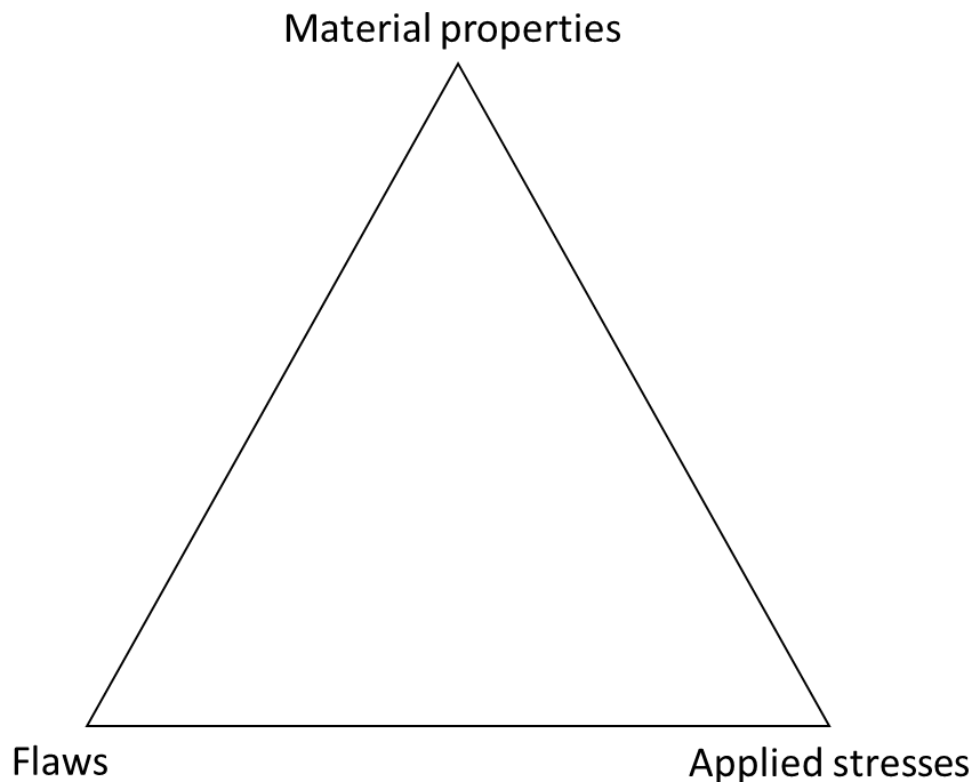
Figure 6.1   Three corner parameters used in ECA

FAD approach helps to determine the proximity to failure by fracture and plastic collapse where both failure modes are treated independently and plotted on orthogonal axes (*ATC65 2017*). The concept and background of FAD is based on the ratio of J_e and J_{ep} which represents the elastic (sufficient for brittle materials) and elastic-plastic (accounting for ductility),

respectively. The ratio of J_e and J_{ep} is unity at low loading, and slowly decreases with increasing loading towards yielding plotted as a square of J_e / J_{ep} in **Figure 6.2**. On a FAD-based fracture assessment, the assessment line shows how the failure modes interact in relation to predicted failure, where failures by fracture and plastic collapse can be considered as a balance between the structural driving force (J_{ep}) and the material's resistance in terms of fracture toughness designated as J_{mat}.

The assessment point on the other hand, helps to assess the significance of a flaw at given applied load which is re-arranged as the equivalent of the square root of J_e / J_{ep} (a function used to generate the failure assessment diagram line) in order to plot this assessment point on a FAD curve (*ATC65 2017*). When $J_{mat} > J_{ep}$, then flaw is deemed acceptable whereas, when $J_{mat} \leq J_{ep}$ then flaw is unacceptable as represented in **Figure 6.3**.
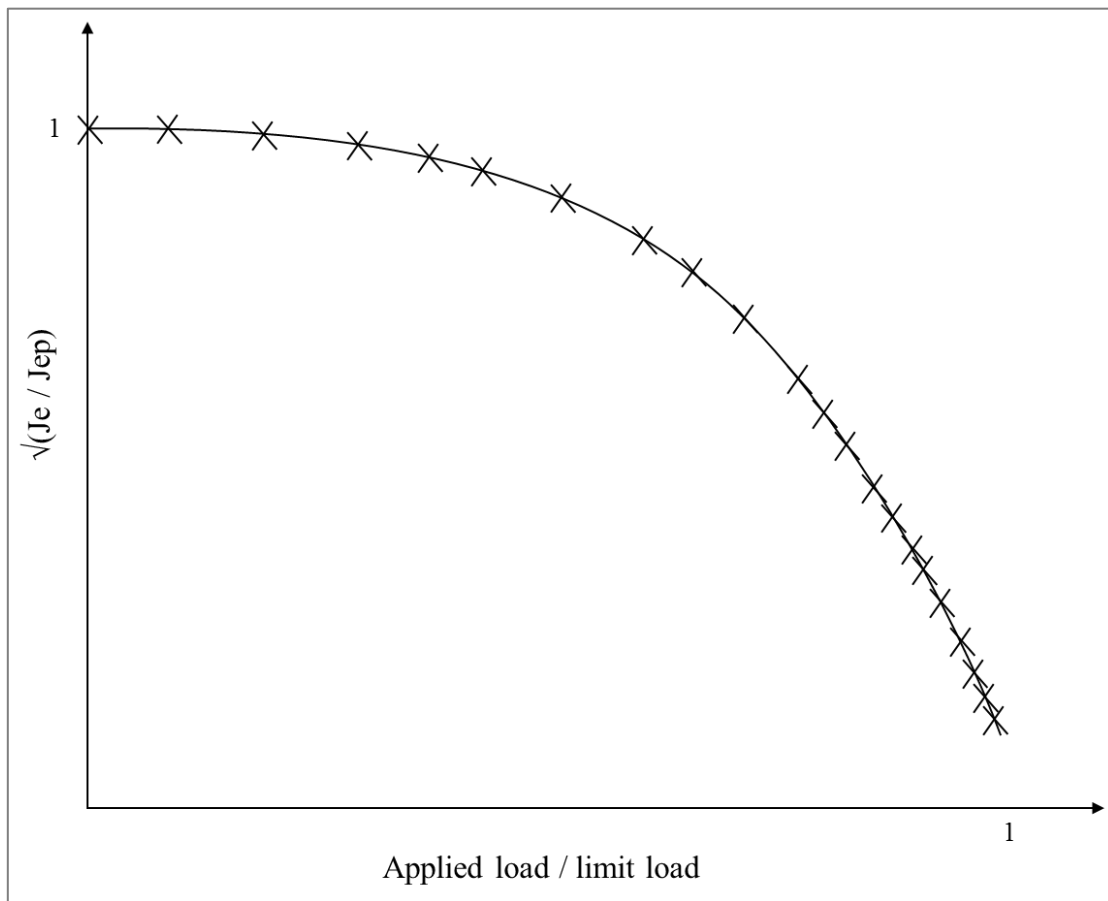
Figure 6.2   FAD approach showing the assessment line
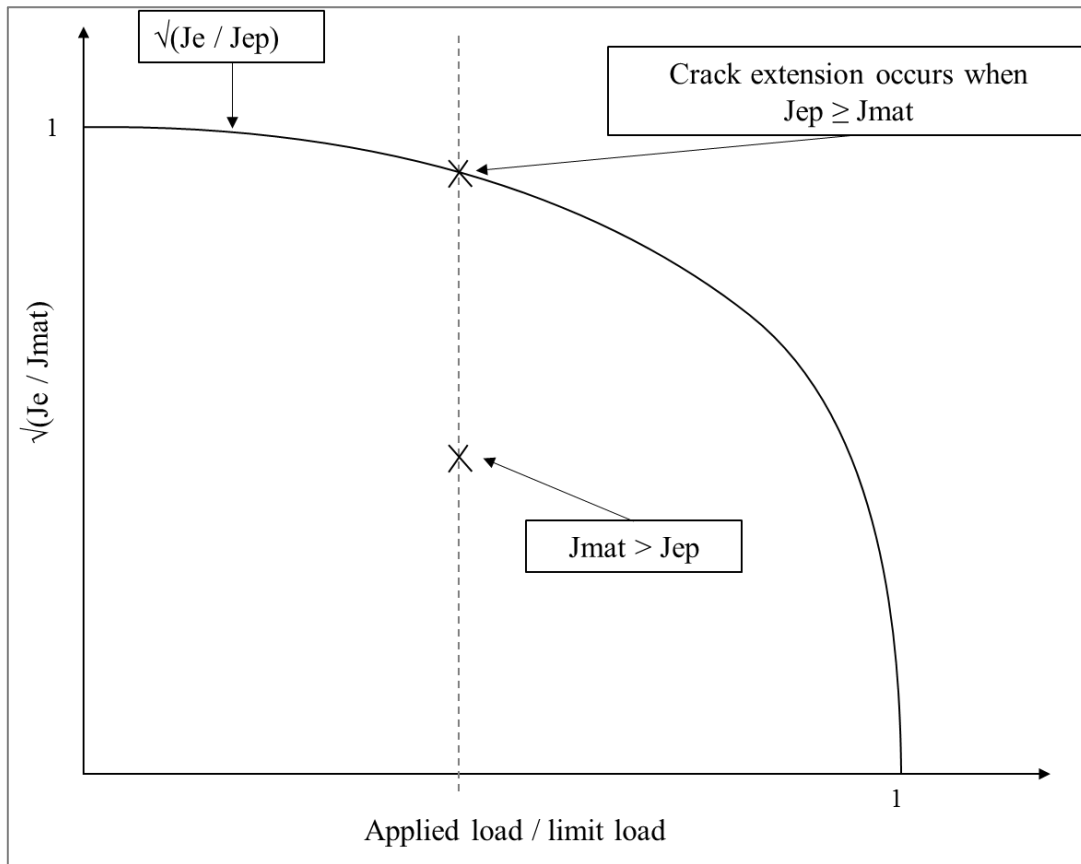
Figure 6.3　　　FAD-based fracture assessment

6.2.1　ECA and FAD in practise

In practice, FAD approach is used as a failure avoidance (rather than a failure prediction) tool plotted with an X-axis called L_r (the collapse ratio) and Y-axis called K_r (the fracture ratio). Fracture ratio (K_r) can be determined by Eqs. (6.1) or (6.2) with the inclusion V and ρ, respectively, in order to account for the interaction between primary and secondary crack-tip stress fields. It is important to mention that primary stresses designated as membrane stress (P_m) and bending stress (P_b) are stresses if sufficiently high contributes to plastic collapse such as dead weight in cranes, internal fluid pressure, pipe tension and bending. On the other hand, secondary stresses designated as thermal membrane stress (Q_{tm}) and thermal bending stress (Q_{tb}) do not contribute to plastic collapse. These stresses (secondary) are generally produced as a result of internal mismatch caused by welding processes and thermal gradient. The fracture ratio is both affected by primary and secondary stresses.

$$K_r = \frac{K_I^P + V K_I^S}{K_{mat}}$$
(6.1)

192

$$K_r = \frac{K_I^P + K_I^S}{K_{mat}} + \rho \qquad\qquad (6.2)$$

where,

K_r	is the fracture ratio on the vertical axis of FAD
K_I	is the stress intensity factor for the cracked geometry (MPa)
K_I^P	is the stress intensity factor from primary stresses based on the applied stress (σ) normal to the crack (MPa)
K_I^S	is the stress intensity from the secondary stresses (MPa)
K_{mat}	material fracture toughness measured by stress intensity factor (MPa)
V and ρ	are plasticity correction factor given in Annex R of BS7910

The collapse ratio (L_r) however, is only affected by primary stresses. L_r on the horizontal axis of FAD is the ratio of reference stress (σ_{ref}) and yield strength (σ_y) given in Eq. (6.3). It can also be defined as the ratio of the applied load and limit load. When $L_r = 1$, then σ_{ref} is equal to σ_y. The limit load in FAD assessments is required for the calculation of σ_{ref}. For example, the reference stress which characterises the increase in stress in the vicinity of a flaw for a through-thickness flaw in plates under combined tension and bending is calculated using Eq. (6.4) as given in Annex P of BS 7910. Please refer to Annex P of BS 7910 for other equations to calculate reference stress for other geometries.

$$L_r = \frac{\sigma_{ref}}{\sigma_y} = \frac{applied\ load}{limit\ load} \qquad\qquad (6.3)$$

$$\sigma_{ref} = \frac{P_b + (P_b^2 + 9P_m^2)^{0.5}}{3\left\{1 - \left(\frac{2a}{W}\right)\right\}} \qquad\qquad (6.4)$$

where,

L_r	is the collapse ratio on the horizontal axis of FAD
σ_y	is the yield strength taken as the lower yield strength or 0.2% proof strength (MPa)
σ_{ref}	is the reference stress (MPa)
P_b	is the primary stresses (MPa)
P_m	is the membrane stresses (MPa)

a half flaw length for through thickness flaw (mm)

W is the width (mm)

In FAD assessments, L_r serves two functions so that the limit load of the component containing the flaw under consideration is not exceeded as well as ensuring that the relationship between elastic-plastic driving force and proximity to plastic collapse is consistent with the relationship implied by the failure assessment curve (*ATC65 2017*)

6.3   Introduction to CrackWISE®

CrackWISE® is designed to assist industry experts with the evaluation of the integrity of various components such as offshore structures, pipelines, pressure equipment, storage tanks and structures containing flaws in line with BS 7910. It ensures safely operation of these structures, while reducing the potential cost of outages and other unforeseen problems. (*CW5-TWI software 2019*).

CrackWISE® comes with various features and benefits which has made it primary choice of industry experts in carrying out fitness-for-purpose procedure also known as engineering critical assessment (ECA) using fracture mechanics principles (*ATC65 2017; CW5-TWI software 2019*) as earlier discussed. Main features include automation of widely accepted flaw assessment procedure in line with BS 7910 which comprises of fracture assessment procedures and fatigue crack growth and fatigue life analysis. Another benefit of CrackWISE® is the wide range of flaw and structural geometries that can be assessed. Structural geometries such as flat plates, curved shell, cruciform joints, bars/bolts, including flaw geometries such as surface, edge, long surface, embedded and corner flaws. CrackWISE® is easy to use with user-friendly interface, intuitive to both existing and new users with software and technical support available anytime.

Another important feature of CrackWISE® is the electronic copy of BS 7910 which evolves with new changes/addition made to the standard with toolkits like Charpy toughness correlation, SI/US unit converter, yield strength calculator and Annex T flaw sizing calculator. Different analysis like known parameter analysis and critical parameter analysis can be performed with the software as represented on FAD in **Figures 6.4 and 6.5,** respectively (*ATC65 2017*). Others analysis include sensitivity parameter analysis, critical-sensitivity parameter analysis and crack growth and fatigue life analysis.
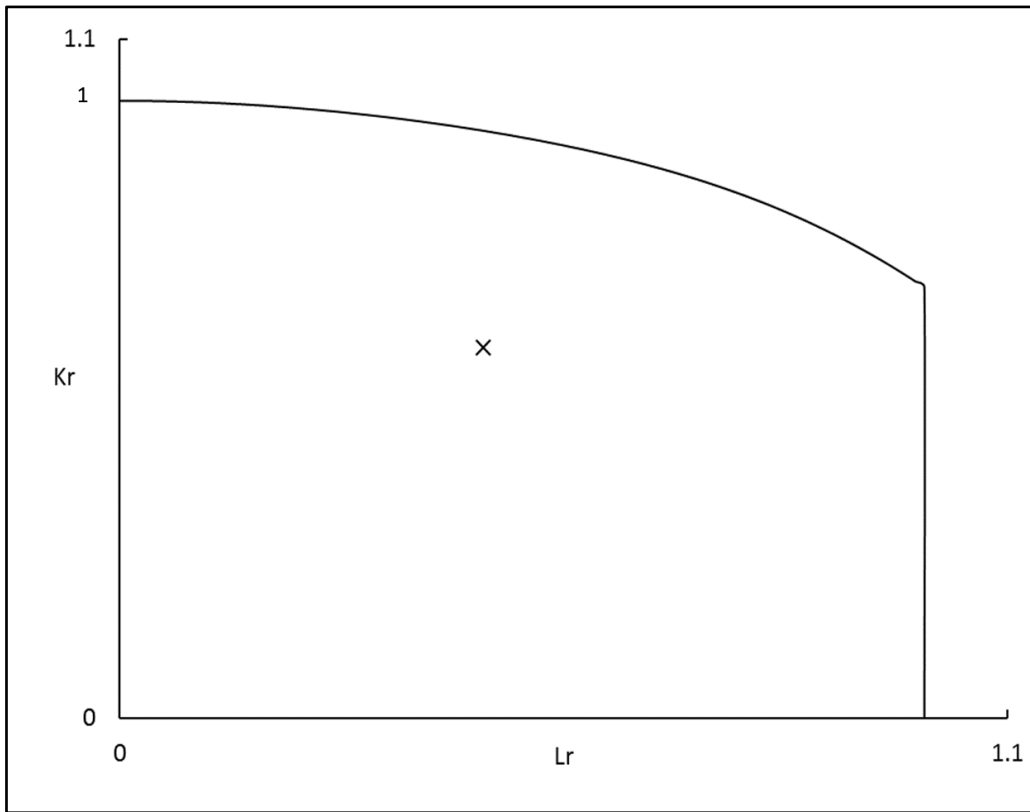
Figure 6.4   Example of known parameter analysis performed in CrackWISE®
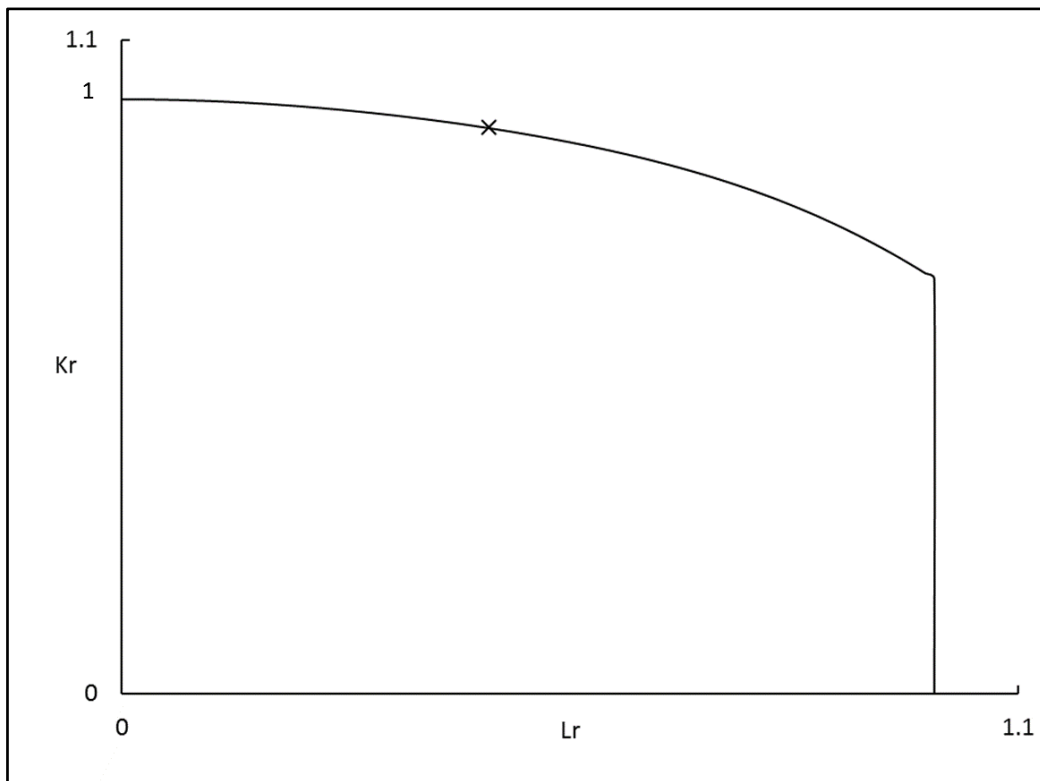
Figure 6.5   Example of critical parameter analysis performed in CrackWISE®

6.4   FAD-based fracture assessment of S690QL combining the test results

In this work, the interaction of the critical value of fracture toughness, tensile test results and flaw size of S690QL under different applied load and temperatures is presented as a case study on a failure assessment diagram (FAD) using CrackWISE®, a software developed by TWI for assessing the acceptability of flaws in metallic structures.

The summary of the input data, **Table 6.1** for the analysis include the single point critical fracture toughness values at ambient (upper shelf) and low temperatures (lower shelf) together with the tensile properties. The membrane stress which contributes to plastic collapse is taken as the 2/3 of the yield strength of 817 MPa. A flaw case is postulated in order to conservatively assess the effect of loading rate on the mechanical behaviour of S690QL on the upper shelf and lower shelf as a representation of a structural member in offshore structures. The flaw case assumes a surface flaw, **Figure 6.6** in a large plate where a represents the flaw height and $2c$ is the flaw length. W and B represent the width and thickness, respectively. The results of the assessment are presented in a FAD incorporating option 2 (full stress-strain curve of S690QL at QS and 4 s^{-1}, presented in chapter 4). The FAD adopted at QS loading conditions shows a comparison between using option 1 (basic tensile properties involving yield strength and ultimate tensile strength) and option 2 (full stress-strain curve) with option 2 allowing a more robust assessment as shown in **Figure 6.7**.

The assessment line using option 2 (full stress-strain curve) under ambient temperature of S690QL at quasi-static and elevated (4 s^{-1}) loading rates are compared on the FAD, **Figure 6.8**. This was used to determine the influence of elevated loading rate on the cut-off value of L_r. Since L_r is the ratio of the applied load and yield load as discussed earlier, section 6.2.1, it implies that L_r values based on the tensile behaviour of S690QL, which depends on the Y/T ratio, decrease by about 1.3% from 1.019584 to 1.006344 as the loading rate increases from QS to 4 s^{-1} strain rates as shown in Figure 6.8.

The procedure was repeated combining the assessment temperature, tensile properties and fracture toughness value in the FAD-based fracture assessment. The behaviour plotted on the failure assessment diagram (FAD) is allowed to conservatively represent the upper shelf and lower shelf behaviour of S690QL using the tensile and fracture toughness test data generated under QS and elevated loading rates, **Figure 6.9**.

Table 6.1   Summary of the inputs used in CrackWISE® to generate FAD for S690QL

FAD analysis method	Assessment temperature tensile properties (Option 2)		Fracture toughness parameters (J) N/mm	Flaw case (mm)	Geometry (mm)	Membrane Stress (MPa)
QS Upper Shelf (Ambient)	σ_y	817 (MPa)	344	$a = 4$ $2c = 100$	$B = 25$ $W = 2000$	545
	UTS	849 (MPa)				
Dynamic Upper Shelf (Ambient)	σ_y	867 (MPa)	411	$a = 4$ $2c = 100$	$B = 25$ $W = 2000$	545
	UTS	878 (MPa)				
QS Lower Shelf (-100 °C)	σ_y	949 (MPa)	48.8	$a = 4$ $2c = 100$	$B = 25$ $W = 2000$	545
	UTS	1036 (MPa)				
Dynamic Lower Shelf (-100 °C)	σ_y	1000 (MPa)	33.9	$a = 4$ $2c = 100$	$B = 25$ $W = 2000$	545
	UTS	1072 (MPa)				

Note: a represents the flaw height and $2c$ is the flaw length

Dynamic assessment line is based on full stress-strain curve of 4 s^{-1}
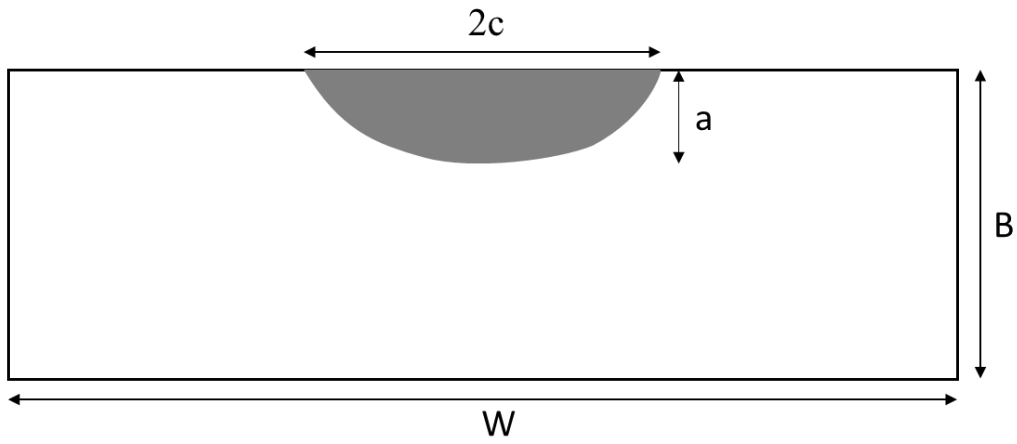
Figure 6.6   Surface flaw case assumed in the ECA analysis for S690QL
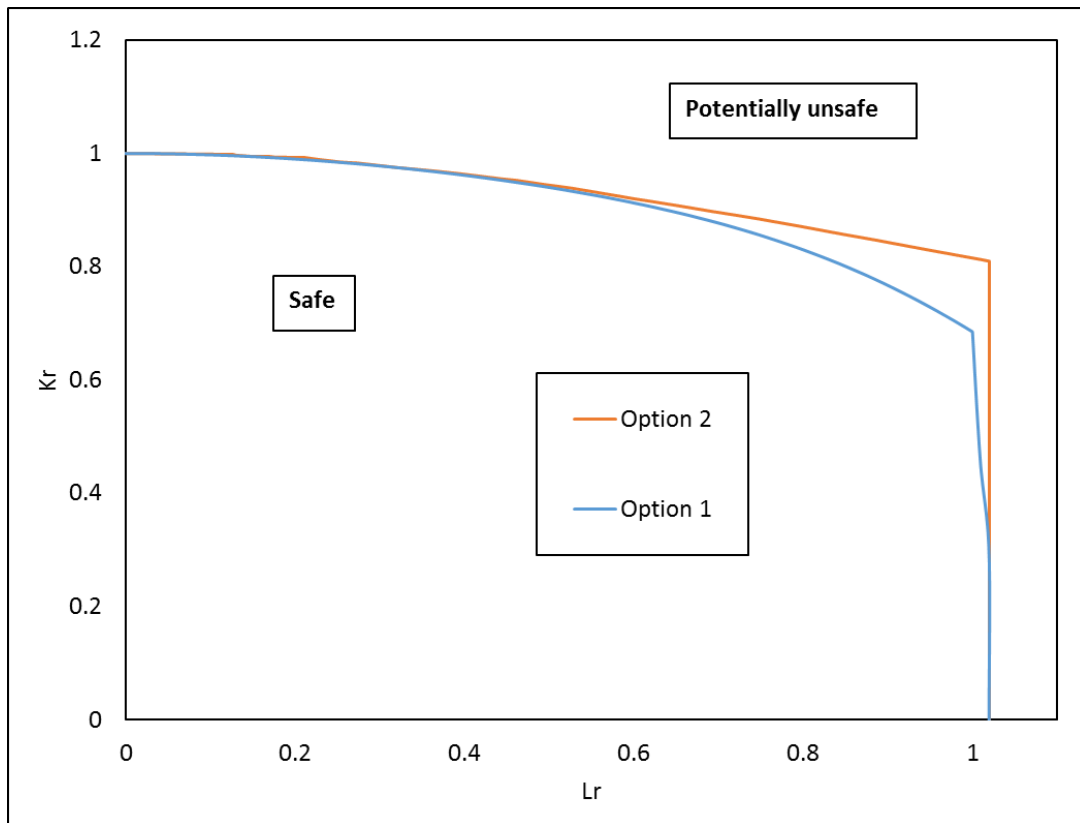
Figure 6.7   Comparison of Options 1 and 2 FADs for S690QL at ambient temperature under quasi-static loading condition.
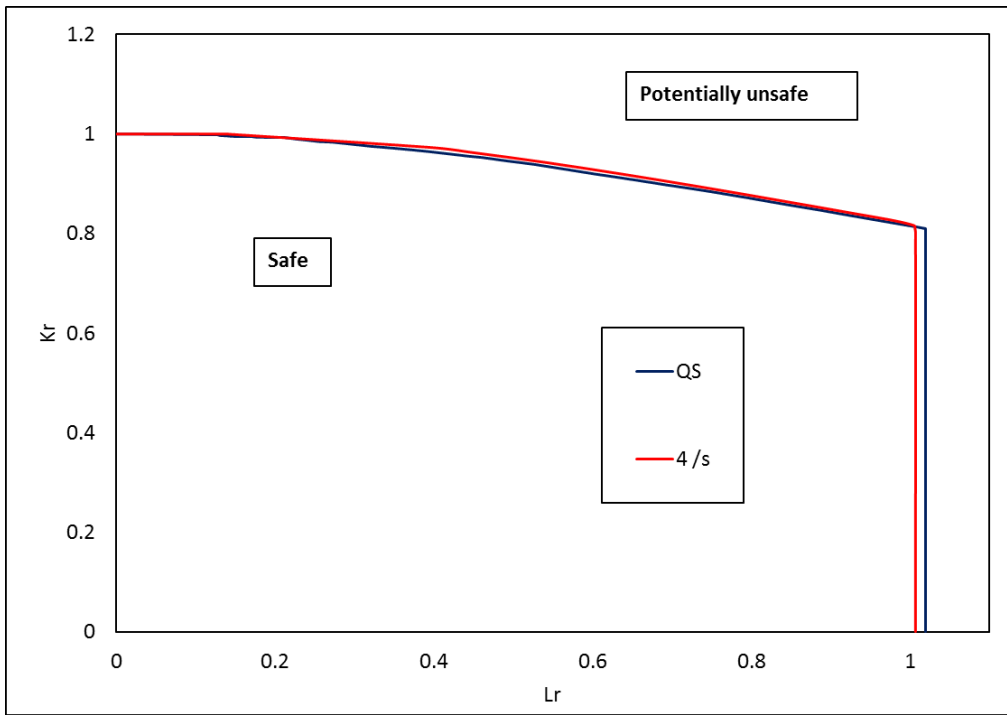
Figure 6.8   Influence of loading rate on the cut-off value of L_r value for S690QL on FAD at ambient temperature using option 2 (full stress-strain curve)
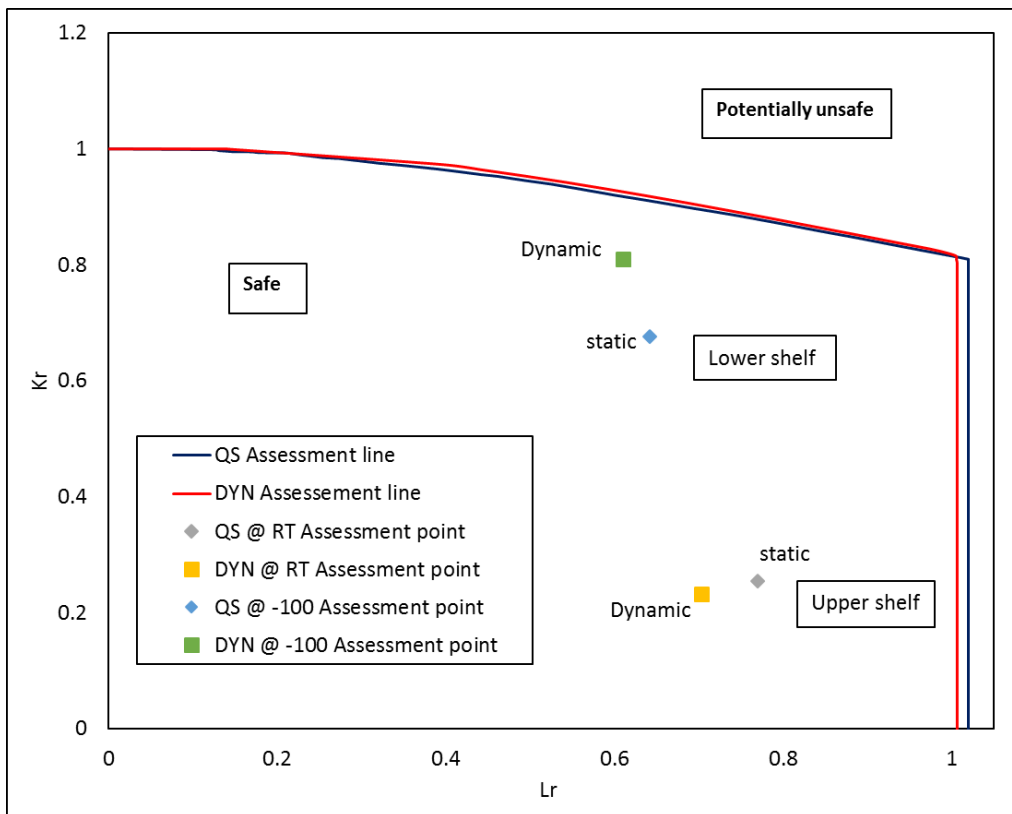
Figure 6.9   Conservatively representing the upper shelf and lower shelf behaviour of S690QL on FAD under quasi-static and dynamic loading rates.

On the upper shelf, the proximity to failure by plastic collapse and fracture decreases when the loading rate is increased, whereas on the lower shelf proximity to failure by fracture is increased. This shows that based on the conservative assessment carried out on the upper shelf and lower shelf behaviour of S690QL and the flaw case studied, it can be said that the effect of loading rate on the mechanical behaviour of HSS does not pose a major threat on the fracture behaviour on the upper shelf but may not be safe on the lower shelf.

It is important to also mention that the position of the assessment point on the FAD might change when other factors (fatigue, residual stresses, welding and actual structural geometry) are included in the analysis but would not change the assessment point on the upper shelf significantly. The purpose of this assessment is to show that HSS with high Y/T ratio can stand the test of time when used in an offshore environment, especially for offshore cranes that operate under air temperature between 29 °C and -6 °C, which falls on the upper shelf fracture behaviour of S690QL. Therefore, HSS can exploit its strength, but not rely on its ability to deform or locally yield under extreme loading for offshore and marine applications.

6.5   Chapter summary

The structural implication of dynamic loading on the mechanical behaviour of HSS, bringing together the tensile properties and fracture behaviour on the FAD-based fracture engineering critical assessment (ECA) is presented in this chapter. Engineering critical assessment is introduced, and the concept of FAD in practice discussed.

CrackWISE® software developed by TWI Ltd for the evaluation of the integrity of various components such as offshore structures, pipelines, pressure equipment, storage tanks and structures containing flaws in line with BS 7910 is also introduced. The software was used to postulate a flaw case that represents the mechanical behaviour of S690QL on the upper shelf and lower shelf at different loading conditions.

The results from the assessment shows that proximity to failure by plastic collapse and fracture on the upper shelf decreases when the loading rate is increased, whereas on the lower shelf, the proximity to failure by fracture is increased for S690QL assessed.

Chapter 7   Conclusion, recommendation and future work

7.1   Conclusion

This research provides a perspective combining the tensile and fracture toughness properties of modern high strength structural steel HSS (S690QL and S960QL) with high yield-to-tensile (Y/T) ratio under high loading rates applicable to offshore scenarios. This is supported by finite element analysis with a validated fracture toughness SENB model for the prediction of crack driving force and crack mouth opening displacement at elevated loading rates which cannot be determined during the fracture toughness tests using rate dependent model derived from the experimental tension tests.

The structural implication of dynamic loading on the mechanical behaviour of HSS, bringing together the tensile properties and fracture toughness data of S690QL is discussed and presented using a FAD-based fracture engineering critical assessment (ECA) method in this research. The results of the assessment as summarised on a failure assessment diagram achieves the main aim of this research which is to investigate and understand how high loading rate could affect the mechanical performance of an asset made from modern HSS with Y/T ratio >0.90 for an effective application of high strength structural steel in offshore structural members where reliability is important.

Major achievements include the followings:

7.1.1   Characterisation of S690QL and S960QL

- The tensile properties of S690QL and S960QL with Y/T ratio of about 0.95 are characterised at a range of strain rates up to 100 s^{-1} and these are compared with low strength structural steel with Y/T ratio <0.85 (S235 tested) and data taken from literature at a range of equivalent strain rates.

- High strength structural steels under consideration with Y/T ratio of about 0.95 are less sensitive to the effect of strain rate when compared to the low strength structural steels with low Y/T ratio <0.85 up to 100 s^{-1} strain rates studied. The effect of strain rates up to 100 s^{-1} on the yield stress of S690QL and S960QL is a moderate increase of about 9% and 6%, respectively, whereas about 66% increase in yield stress for S235 was observed at the same strain rate, similar to what is reported in the literature for mild or low strength structural

steel grades. It implies that, the degree of sensitivity is material dependent but decreases as the nominal yield strength increase as showcased by experimental test results for S690QL and S960QL.

- For S690QL and S960QL, the metallography examination shows that the finer-grained size microstructures were associated with the reduced degree of strain rate sensitivity which depends on the production routes, chemical compositions and size of the microstructure (grain size) with S960QL showing the lower grain size.

- The experimental data presented in this thesis shows that the tensile behaviour of modern HSS (like S690QL and S960QL studied) with high Y/T ratio >0.90 under quasi-static conditions is a reasonable prediction of the tensile performance at strain rates in-service of up to 4 s^{-1}, and this could be applied in offshore applications without necessarily requiring dynamic tensile testing.

7.1.2   *Fracture behaviour of S690QL and S960QL*

- Based on the experimental results and analysis of the fracture behaviour of S690QL and S960QL, the objective of determining how the loading rates affect the transition regime in the ductile-to-brittle transition curve (DBTC) of HSS has been realised. The estimated T_0 at -100 °C from both Charpy-sized pre-cracked SENB ($B=W=10$ mm) and standard SENB specimen configuration ($B=W=25$ mm) specimens are -116 °C and -108 °C, respectively, under QS conditions. The Master Curve theory should mean both datasets predict the same T_0, but it is important to mention that a difference of about 8 °C is observed due to the partial loss of crack-tip constraint which is within the limit given in ASTM E1921-15a when sub-size specimens are used to calculate T_0.

- The reference transition temperature (T_0) estimated for S690QL at QS, intermediate and dynamic loading conditions based on the Master Curve concept (experimental data), with tests performed at -100 °C using Charpy-sized pre-cracked SENB specimens, are -116 °C, -85.2 °C and -70.4 °C, respectively. Here the temperature shift (ΔT_0) from QS to intermediate loading conditions with K-rate of 10^4 MPa√m/s is 30.8 °C. If loading rate is increased to dynamic with K-rate of 10^6 MPa√m/s, the ΔT_0 increases to 45.6 °C.

- The experimental data presented show that the influence of loading rate on fracture toughness can be determined using Charpy-sized pre-cracked SENB specimens instead of

using the conventional Charpy V-Notch (CVN) method to determine the material resistance at impact loading. The T_0 estimated from the CVN tests is not conservative when compared to Charpy-sized pre-cracked SENB tests with sharp notch ($a_0/W = 0.5$).

- A possible temperature shift ΔT_0 of about 40 °C for S690QL is predicted for QS conditions up to a K-rate of magnitude of 10^6 MPa√m/s, based on ASTM E1921-15a with prior knowledge of T_0 under QS conditions. This shows that the ASTM E1921 made reasonable, but slightly non-conservative, predictions of temperature shift (ΔT_0) for a K-rate up to magnitude of 10^6 MPa√m/s for HSS provided T_0 is known under QS conditions.

- An average initiation toughness J_{IC} value of 676.2 N/mm was estimated under QS loading conditions for S690QL in 25 mm specimens. A material initiation toughness J_{IC} or $J_{0.2}$ at the onset of stable crack growth of about 311.2 N/mm is observed using a Charpy-sized pre-cracked SENB specimen ($B=W=10$ mm) under QS loading conditions due to loss of crack tip constraint. Although these parameters are considered "size-independent", these results show they are not truly independent of the specimen dimensions and geometry.

- A $J_{0.2}$ material initiation toughness at the onset of stable crack growth of 456.3 N/mm is estimated using a Charpy-sized pre-cracked SENB specimen ($B=W=10$ mm) under dynamic loading conditions, using the low blow testing method. The value shows how the effect of loading rate enhances the load bearing capacity of S690QL. Although the crack tip constraint correction is required for a valid size-independent estimation of J_{IC} or $J_{0.2}$ using Charpy-sized pre-cracked SENB specimen ($B=W=10$ mm), this work thus gives an insight that sub-size specimens can be used to generate a valid J-R curve.

7.1.3 *Structural implication of dynamic loading on the mechanical properties of S690QL and S960QL*

- The structural implication of dynamic loading on the mechanical behaviour of HSS, based on flaw case assessed on S690QL using FAD-based fracture engineering critical assessment technique, shows that HSS can exploit its strength, provided it does not rely on its ability to deform or locally yield under extreme loading, for offshore and marine applications intended for dynamic service operating predominantly on the upper shelf to upper transition region of the DBTC like the temperatures between 29 °C and -6 °C where offshore cranes predominantly operate for this steel grade.

- On the upper shelf, the proximity to failure by plastic collapse and fracture decreases when the loading rate is increased, whereas on the lower shelf proximity to failure by fracture is increased. This shows that based on the conservative assessment carried out on the upper shelf and lower shelf behaviour of S690QL and the flaw case studied, it can be said that the effect of loading rate on the mechanical behaviour of HSS does not pose a major threat on the fracture behaviour on the upper shelf but may not be safe on the lower shelf.

- Therefore, HSS such as S690QL and S960QL intended for dynamic service operating predominantly on the upper shelf to upper transition region of the DBTC can be characterised using the experimental data under quasi-static loading regimes. However, care must be taken when the dynamic service is intended for the lower shelf to lower transition region of the DBTC. Fracture toughness tests can be carried out at the assessment temperature using Charpy-sized pre-cracked SENB specimen on an instrumented Charpy machine to determine the dynamic transition temperature $T_{0,d}$.

7.1.4   Finite element analysis

The FEA was successfully used to determine the crack driving force and the effect of loading rate on the rate of crack mouth opening displacement at QS and elevated loading rates for S690QL supported by a validated material model developed for S690QL. The equivalent J corresponding to QS and elevated loading conditions was generated from the model developed and validated using an analytical method in accordance with BS 7448-4 in conjunction with the experimental data. The FEA accurately represents the experimental test results at QS rates using linear static analysis and this model can be used for further parametric studies on other grades with different Y/T ratio to determine the rate of crack opening and crack driving force provided the material properties are known. Assessment of the stress field was conducted using the Hutchinson-Rice-Rosengren (HRR) field equations, and good agreement with the theoretical HRR field was evident corresponding to the loading levels when J is >13.43 N/mm at QS rates.

The FEA results at elevated loading rates supported the validation of the best method to fit dynamic loading rate test data generated from Instrumented Charpy test results. To generate a sufficiently smooth data trace from a load and load line displacement (LLD) graph generated from Instrumented Charpy Impact test results, it is important to first fit through the linear (elastic) part of experimental data using the experimental fracture toughness data at equivalent

temperature under quasi-static loading conditions, before using a curve fitting technique such as a spline or polynomial to generate a fit through the plastic region of the dynamic data. This will aid estimation of cleavage initiation point under impact loading.

7.2 Future work and recommendation

The application of high strength structural steel (yield strength >690MPa) with high yield-to-tensile ratio >0.90 is still relatively limited in offshore applications compared to conventional low strength structural steel with yield strengths up to around 500 MPa with yield-to-tensile ratio <0.85.

To fully understand the mechanical performance of HSS with a range of Y/T ratio above 0.85 under in-service loading conditions, more research is still needed. Following the scope of this research which represents HSS with an average Y/T ratio value of 0.95, research on fatigue and weldments capacity of HSS with high Y/T ratio which is not covered in this research is required. Moreso, research on a range of HSS with Y/T ratios between 0.85 and 0.95 is important in order to increase confidence and usage of HSS for different applications, especially marine/offshore application.

Concerning the experimental methodology and development for determining HSS steel grade fracture toughness using Charpy-sized pre-cracked SENB impact test results, the following future work is recommended:

1. The accuracy of using a Charpy-sized pre-cracked SENB specimens to generate the *J*-R curve of ferritic steel depends on the correction for crack tip constraints. A family of constraint corrected *J*-R curves within a wider range of HSS grade fracture toughness data sets is needed, supported by FEA, for the purpose of evaluating the extent of the dependency of the crack tip constraint on specimen size and microstructure. This will aid the development of a model within existing structural integrity assessments to generate a size-independent resistance curve (R-curve) for HSS material under impact loading using a Charpy-sized pre-cracked SENB specimen.

2. The existing statistical and empirical relationship based on the Master Curve (MC) concept, and the transition temperature shift prediction based on ASTM E1921-15a[e1] which uses the Master Curve approach to assess cleavage fracture in the transition and

lower shelf regions of DBTC represents a significant advancement in the quantification of most ferritic steel transition behaviour on the DBTC. It is recommended that correlating the dependence on HSS microstructure using a large data set would be a valuable exercise that will improve structural integrity assessments of HSS for different applications.

3. Also, further work is necessary to correlate Charpy V-notch and Charpy-sized pre-cracked SENB impact test results. This will aid the development of a model that can be used to qualify fracture behaviour of ferritic steel especially HSS grade at impact loading within the context of existing FAD-based fracture engineering critical assessment.

In conclusion, the structural implication of dynamic loading on the mechanical behaviour of HSS, means that HSS with high yield-to-tensile ratio can exploit its strength, but not rely on its ability to deform or locally yield under extreme loading for offshore and marine applications. It is recommended to characterise the dynamic fracture behaviour (material resistance under impact loading) on the lower shelf region of HSS experimentally using Charpy-sized pre-cracked SENB specimens tested on an instrumented Charpy machine to determine $T_{0,d}$, rather than using the conventional CVN methods to determine T_0 from transition curve based on absorbed energy. A transition temperature (T_0) estimated from the conventional Charpy V-Notch impact tests is non-conservative when compared to the T_0 generated from Charpy-sized pre-cracked SENB tests with sharp notch ($a_0/W = 0.5$) as discussed in this research.

References

Anderson, T., L., (2005). "*Fracture Mechanics - Fundamental and Applications*" 3rd Edition, CRC Press, Taylor & Francis Group, Boca Raton.

API 2A-WSD, (2014)*. "Planning, designing, and constructing fixed offshore platforms – Working Stress Design" American Petroleum Institute recommended practice 21st Edition.*

ANSI/AISC 360-16, (2016). "*Specification for Structural Steel Buildings*" AISC, Chicago USA.

AS 4100, (1998). "*Steel structures*" Australian standard, published by Standards Association of Australia, Homebush, NSW 2140.

ASTM STP1130 (1992). *"Rapid Load Fracture Testing"* American **Society** for Testing and Materials International United States.

ASTM E23-07a[e1] (2007). *"Standard Test Methods for Notched Bar Impact Testing of Metallic Materials"* American Society for Testing and Materials International United States.

ASTM E399-12e[3] (2013). *"Standard Test Method for Linear – Elastic Plane Strain Fracture Toughness K of Metallic Materials"* American Society for Testing and Materials International United States.

ASTM E1820-17e[2] (2013). *"Standard Test Method for Measurement of Fracture Toughness"* American Society for Testing and Materials International United States.

ASTM E112 (2013) *"Standard test methods for determining average grain size"* American Society for Testing and Materials International United States. https://doi.org/10.1520/E0112-13.

ASTM E2298-15 (2015) *"Standard test method for instrumented impact testing of metallic materials"* American Society for Testing and Materials International United States.

ASTM E1921-15[e1] (2016). *"Standard Test Method for Determination of Reference Temperature, T_0, for Ferritic Steels in the Transition Range[1]"* ASTM International, United States.

ATC65 Course, (2017). *"Structural integrity assessment and practical application of BS 7910 procedures for the assessment of flaws in metallic structures"* Training course delivered at TWI Ltd, Granta Park, Cambridge, UK.

Ban H. Y., Shi G., Shi Y. J., Wang Y. Q., (2011). *"Research progress on the mechanical property of high strength structural steels"* Advanced Materials Research 250-253(1-4): 640-648.

Ban H., Y., Shi G., (2017). "*A review of research on high-strength steel structures*" Structures and Buildings, Proceeding of the Institution of Civil Engineers (URL http://dx.doi.org/10.1680/jstbu.16.00197)

Bannister, A., C., Trail, S., J., (1996). *"The Significance of the Yield Stress / Tensile Stress Ratio to Structural Integrity"* SINTAP Sub-Task 2.1 Report, August 1996.

Bannister, A., C., (1999). *"Yield Stress / Tensile Stress Ratio: Results of Experimental Programme"* SINTAP Sub-Task 2.3 Report, February 1999.

Bannister, A., C., Ruiz Ocejo, J., Gutierrez-Solana, F., (2000). *"Implications of the yield stress/tensile stress ratio to the SINTAP failure assessment diagrams for homogeneous materials"* Engineering Fracture Mechanics 67, pp 547-562, Elsevier Science Ltd.

Billingham, J., Healy, J., Bolt, H., (1997). *"High strength steels – The significance of yield ratio and work-hardening for structural performance"* Marine Technology Directorate (MTD), Marine Research Review 9, 1997 36 pages, ISBN 1-870553-27-6.

Billingham, J., Sharp, J., V., Spurrier, J., Kilgallon, P., J., (2003). *"Review of the performance of high strength steels used offshore"* HSE research report 105, 2003 (URL http://www.hse.gov.uk/research/rrpdf/rr105.pdf).

Breuk, D., (2003). *"Flow stress and ductile failure at varying strain rates"*, ISBN 90-9016534-7, 2003.

Brockenbrough, R., L., and Associates Inc., (1995). *"Effect of Yield-Tensile Ratio on Structural Behaviour – High Performance Steels for Bridge Construction"* Expanded Draft Final Report, ONR-AISI Agreement No. N00014-94-2-0002.

BS 7448-1: (1991). *"Fracture mechanics toughness tests — Part 1: Method for determination of K_{IC}, critical CTOD and critical J values of metallic materials"*

BS 7448-3: (2005). *"Fracture mechanics toughness tests — Part 3: Method for determination of fracture toughness of metallic materials at rates of increase in stress intensity factor greater than 3.0 MPa√ms^{-1}"*

BS 7448-4 (1997). *"Fracture mechanics toughness tests — Part 4: Method for determination of fracture resistance curves and initiation values for stable crack extension in metallic materials"*

BS EN ISO 6507-1 (2005). *"Metallic materials - Vickers hardness test - Part 1: Test method"*

BS EN ISO 6892-1 (2009). *"Metallic materials – Tensile testing Part 1: Method of test at ambient temperature"*

BS EN ISO 148-1 (2010). *"Metallic materials – Charpy pendulum impact test Part 1: Test method"*

BS EN 10025:6: +A1 (2009). Hot rolled products of structural steels – Part 6 *"Technical delivery conditions for flat products of high yield strength structural steels in the quenched and tempered condition"*

BS ISO 26843: (2015). *"Metallic materials — Measurement of fracture toughness at impact loading rates using pre-cracked Charpy-type test pieces"*

BS 7910:2013+A1 (2015). *"Guide to methods for assessing the acceptability of flaws in metallic structures"*

Burdekin, F., M., Zhao, W., Tkach, Y., Wiesner, C., S., Xu, W., (2004). *"The effects of dynamic loading on structural integrity assessments"* HSE research report 208, (URL http://www.hse.gov.uk/research/rrpdf/rr208.pdf).

Campbell, J., D., Ferguson, W., G., (1970). *"The temperature and strain-rate dependence of the shear strength of mild steel"* Philosophical Magazine, vol. 21, iss.169, pp 63-82, (URL http://dx.doi.org/10.1080/14786437008238397).

Chao Y., J., Zhu, X., K., (2000). "*Constraint-modified J-R curves and its application to ductile crack growth*" International Journal of Fracture 106, 135-160.

Choung, J., Nam, W., Lee, J-Y., (2013). *"Dynamic hardening behaviours of various marine structural steels considering dependencies on strain rate and temperature"* Marine Structures vol. 32, (2013) 46-67, (URL https://doi.org/10.1016/j.marstruc.2013.02.001)

Commissions of the European Communities, (1988). "*High strength structural steels – A European Review*" Technical Steel Research GT ASSOCIATES Contract No ECI 1467-86 UK.

Cooper, A., J., Smith, R., J., Sherry A., H., (2017). *"An assessment of the ductile fracture behaviour of hot isostatically pressed and forged 304L stainless steel"* Metallurgical and Materials Transactions A, Volume 48, Issue 5, pp 2207–2221 https://link.springer.com/article/10.1007/s11661-017-4005-1.

Cutter, J., Flanagan, J., W., Brown, P., Rando, M., Mo, G., (2011). "*Samuel Beckett Bridge, Dublin, Ireland*" Proceeding of the Institution of Civil Engineers, Bridge Engineering, Vol 164, Issue BE3, pp. 133-144 (http://dx.doi.org/10.1680/bren.2011.164.3.133).

Davis, J., R., (2004). "*Tensile Testing*" 2nd Edition, ASM International. OH 44073–0002, 2004 ISBN: 0-87170-806-X.

Dexter, R., J., Ferrell, M., (1995). Optimum Weld-Metal Strength for High-Strength Steel Structures, ATLSS Report No. 95-08, Sponsored by Ship Structure Committee, U.S. Coast Guard, July 1995 (URL https://preserve.lehigh.edu/engr-civil-environmental-atlss-reports/210).

Dillinger Hütte GTS downloaded in 2019 *"The Samuel Beckett cable-stayed bridge"* Steel for construction steelwork, AG der Dillinger Hüttenwerke Marketing, D-66748 Dillingen/Saar, Postfach 1580. https://www.dillinger.de/imperia/md/content/dh/referenzen/stahlbau/samuel_beckett_en.pdf

Eurocode 3, Design of steel structures: Part 1-12, (2007). *"Additional rules for the extension of EN 1993 up to steel grades S 700"*

Faridmehr, I., Osman, M.H., Adnan, A.B., Nejad, A.F., Hodjati, R., Azimi, M., (2014). *"Correlation between Engineering Stress-Strain and True Stress-Strain Curve"* American Journal of Civil Engineering and Architecture, Vol. 2, No. 1, pp. 53-59

Francis, P., H., Cook, T., S., Nagy, A., (1978). *"The Effect of Strain Rate on The Toughness of Ship Steels"* Ship Structure Committee Report 275 (SSC-275) under project SR-1231, July 1978.

GB/T19879, (2015). "*Steel plate for building structures*" National Standard of the People's Republic of China (Translated English of Chinese Standard version).

Gotoh, k., (2015). "*Practical Evaluation of the Strain Rate and Temperature effects on Fracture Toughness of Steels"* OMAE2015 – 41982, Newfoundland, Canada.

GL Rules IV – Industrial Services, Part 6 – Offshore Technology (Structural Design) (2007). "*Rules for Classification and Construction*" Germanischer Lloyd Aktiengesellschaft, Edition 2007.

Griffith, A., A., (1921). *"The phenomena of rupture and flow in solids"* Philosophical Transactions of Royal Society of London, Series A, Vol. 221, pp. 163-198, doi: 10.1098/rsta.1921.0006

Hai, L-T., Sun, F-F., Zhao, C., Li, G-Q., Wang, Y-B., (2018). *"Experimental cyclic behaviour and constitutive modelling of high strength structural steels"* Construction and Building Materials, Vol. 189, pp.1264-1285 https://doi.org/10.1016/j.conbuildmat.2018.09.028

Healy, J., Billingham, J., Billington, C., Bolt, H., (1995). *"Design Implications of the High Yield to Ultimate Ratio of High Strength Steels in Offshore Engineering"* OMAE1995, Volume III, Materials Engineering, ASME 1995, pp. 271-277.

Healy, J., Billingham, J., (1995). *"Metallurgical Considerations of the High Yield to Ultimate Ratio in High Strength Steels for use in Offshore Engineering"* OMAE1995, Volume III, Materials Engineering, ASME 1995, pp 365-370.

He, G., W., Bao, C., Cai, L., X., Wu, Y., J., Zhao X., H., (2018). *"Estimation of J-resistance curves of SA-508 steel from small sized specimens with the correction of crack tip constraint"* Engineering Fracture Mechanics, Vol. 200, pp. 125-133.

HSE report (1999). *"The behaviour of carbon steels at high strain rates and strain limits"* Offshore Technology Report – OTO 1999/018, produced by Bomel Limited for HSE, HSE Books.

HSE report (2001). *"Elevated temperature and high strain rate properties of offshore steels"* Offshore Technology Report (OTO 2001/020), HSE, 2001 (URL http://www.hse.gov.uk/research/otopdf/2001/oto01020.pdf).

ISO 19902 (2007). "*Petroleum and natural gas industries - Fixed steel offshore structures*"

Johnson, G., R., Cook, W., H., (1983). *"A constitutive model and data for metals subjected to large strains, high strain rates and high temperatures"* Proceedings of the 7th International Symposium on Ballistics in the Netherlands pp 541-547.

Johnson, G., R., Cook, W., H., (1985). *"Fracture characteristics of three metals subjected to various strain, strain rates, temperature and pressures"* Engineering Fracture Mechanics vol. 21, No.1, (1985) 31-48, http://dx.doi.org/10.1016/0013-7944(85)90052-9 (URL http://www.sciencedirect.com/science/article/pii/0013794485900529?via%3Dihub).

Joyce, J., A., Tregoning, R., L., (2005). *"Determination of constraint limits for cleavage initiated toughness data"* Engineering Fracture Mechanics 72 (2005) 1559-1579

Loveday, M., S., Gray, T., Aegerter, J., (2004). *"Tensile testing of metallic materials: A review"*, EU Funded Project, TENSTAND-Work Package 1, final report with Contract Number G6RD-2000-00412.

Lucon, E., (2008). *"Influence of striking edge radius (2 mm versus 8 mm) on Instrumented Charpy data and absorbed energies"* open report of the Belgian Nuclear Research Centre, ISSN 1379-2407.

Miki, C., Homma, K., Tominaga, T., (2002). *"High strength and high performance steels and their use in bridge structures"* Journal of Constructional Steel Research 58, pp. 3-20, Elsevier Science Ltd.

Moore, P., Booth, G., (2014) *"The Welding Engineer's Guide to Fracture and Fatigue"* Woodhead Publishing Series in Metals and Surface Engineering (Hardback) ISBN: 9781782423706

Moore, P., (2015). *"Fracture mechanics testing"* Material Joining and Engineering Technologies Training Course Note held at TWI, Granta Park, Cambridge UK.

NagarajaRao, N., Lohrmann, M., Tall, L., (1966). *"Effect of strain rate on the yield stress of structural steel"* ASTM Journal of Materials, vol. 1, No. 1, Publication No. 293 Fritz Laboratory Reports, Paper 1684 1966 http://preserve.lehigh.edu/engr-civil-environmental-fritz-lab-reports/1684.

Priest, A., H., (1977). *"Influence of strain rate and temperature on the fracture and tensile properties of several metallic materials"* Welding Institute, Cambridge, Paper 10, pp 95-111.

Ramberg, W., Osgood, W., R., (1943). *"Description of stress-strain curves by three parameters"* Technical note No. 902, Technical Advisory Committee for Aeronautics, Washington DC.

Rice, J., R., (1968). "*A Path Independent Integral and the Approximate Analysis of Strain Concentration by Notches and Cracks*". Journal of Applied Mechanics, Vol 35, No. 2, pp. 379-386. https://pdfs.semanticscholar.org/8b99/bfb8fc11ff6285f9863788fe537c48764428.pdf

Seven Borealis, (2019). Downloaded in 2019 *https://www.subsea7.com/content/dam/subsea7corporate2018/Datasheets/Vessel/rigid-pipelay-heavy lift/Seven%20Borealis.pdf.downloadasset.pdf*

Shoemaker, A., K., (1981). *"Fracture characteristics of ship steel under extremely high loading rates"* paper presented at Extreme Loads Response Symposium, Arlington, VA, USA.

Shi, G., Hu, F., Shi Y., (2014). *"Recent Research Advances of High Strength Steel Structures and Codification of Design Specification in China"* International Journal of Steel Structures, Vol 14, No 4, pp. 873-887. DOI 10.1007/s13296-014-1218-7

Shi, G., Zhu, X., Ban, H., (2016). *"Material properties and partial factors for resistance of high-strength steels in China"* Journal of Constructional Steel Research Vol. 121, pp. 65-79 http://dx.doi.org/10.1016/j.jcsr.2016.01.012

Shih, C., F., (1983). *"Tables of Hutchinson-Rice-Rosengren singular field quantities"* Materials research laboratory, Brown University.

Simulia, (2014)*,* ABAQUS CAE Version 6.14

SSAB Technology AB (2011). *"041-General product information Weldox, Hardox, Armox and Toolox"* downloaded in 2018 http://www.aemach.com/hardox/pdf/041_SSAB_plate_general_product_information_UK.pdf

SSAB media (2019). Downloaded in 2019 https://e-lass.eu/media/2019/01/SSAB-Ramsses-Elass-meeting-in-Pite%C3%A5.pdf

SSAB offshore brochure (2019). *"SSAB products for offshore and marine industries" downloaded in 2019* https://www.ssab.com/products/industries/offshore-marine-energy

Subsea 7 (2015). *"Seven Borealis – Pipelay and heavy lift vessel Subsea 7"* https://www.subsea7.com/content/dam/subsea7/documents/whatwedo/fleet/rigidpipelay/Seven%20Borealis.pdf

Tagawa, T., Kawabata, T., Sakimoto, T., Kayamori, Y., Ohata, M., Yamashita, Y., Tamura, E., Yoshinari, H., Aihara, S., Minami F., Mimura H., Hagihara, Y., (2014). *"Experimental Measurements of Deformed Crack tips in different Yield-to-Tensile ratio Steels"* Engineering Fracture Mechanics, http://dx.doi.org/10.1016/j.engfracmech.2014.07.012

TNO Report (2010). *"Offshore application of High Strength Steel: a problem and a challenge"* Report of MIF seed money study

TWI software 2019, CrackWISE® Version 5.0 R32544 http://www.twisoftware.com/EasySiteWeb/GatewayLink.aspx?alId=1901825

UK National Annex to Eurocode 3, Design of steel structures: Part 1-12, (2007). *"Additional rules for the extension of EN 1993 up to steel grades S 700"*

Van Es, S., Slot, H., Steenbergen, H., Maljaars, J., Pijpers, R., (2018). *"Use of HSS and VHSS in steel structures in civil and offshore engineering: Requirements regarding material properties"* Steel Construction, Vol. 11, No. 4, pp. 249-256, https://onlinelibrary.wiley.com/doi/epdf/10.1002/stco.201800018

Wang, J., Afshan, S., Schillo, N., Theofanous, M., Feldmann, M & Gardner, L., (2017). *"Material properties and compressive local buckling response of high strength steel square and rectangular hollow sections",* Engineering Structures, vol. 130, pp. 297-315. https://doi.org/10.1016/j.engstruct.2016.10.023

Wallin, K., Mahidhara, R., K., (1997). *"Effect of Strain Rate on the Fracture Toughness Reference Temperature T_o for Ferritic Steels"* TMS Publisher

Wallin, K., (2011). *"Fracture Toughness of Engineering Materials – Estimation and Application"* EMAS Publishing, Birchwood Park, Warrington, UK.

Walters, C., L., Przydatek, J., (2014). "*Relating Structural Loading Rate to Testing Rate for Fracture Mechanics Specimens"* OMAE2014 – 23962, San Francisco, California, USA.

Wells, A., A., (1969). "*Crack opening displacements from elastic-plastic analyses of externally notched tension bars*". Engineering Fracture Mechanics, Volume 1, No. 3, pp. 399-410.

Wiesner, C., S., MacGillivray, H., (1999). *"Loading Rate Effects on Tensile Properties and Fracture Toughness of Steel"* Paper Presented at TAGSI Seminar - 'Fracture, Plastic Flow and Structural Integrity' (dedicated to Sir Alan Cottrell in the year of his Eightieth Birthday), Held at TWI, Cambridge, UK, 29 April 1999

Willms, R., (2009). *"High strength steel for steel constructions"* Marketing Department, AG der Dillinger Hüttenwerke, Dillingen, Germany, 2009.

Xu, Z., Li, Y., (2011). "*A novel method in determination of dynamic fracture toughness under mixed mode I/II impact loading"* International Journal of Solids and Structures 49, pp 366-376, Elsevier Ltd.

Zhou, D; (2007): *"Numerical Determination of Dynamic Fracture Toughness from Measured Time-to-Fracture"* Research Report 891/2007 for Industrial Members of TWI Ltd.

Zhu, X., K., Joyce, J., A., (2012). *"Review of fracture toughness (G, K, J, CTOD, CTOA) testing and standardization"* U.S. Navy Research. Paper 49, Elsevier Ltd. http://digitalcommons.unl.edu/usnavyresearch/49 Engineering Fracture Mechanics 85, pp. 1-46, doi:10.1016/j.engfracmech.2012.02.001.

Appendices

CTOD test data not reported in the text for S690QL and S960QL at quasi-static loading rate

Table A1   CTOD test data at ambient temperature under quasi-static condition for S690QL

Specimen No	CTOD (mm)	Specimen geometry (mm)	Initial crack length (a₀) (mm)	Maximum load (kN)
M01-63	0.218	$B=W=10$	5.169	7.52
M01-65	0.234	$B=W=10$	5.040	7.98
M01-66	0.218	$B=W=10$	5.199	7.45
M01-93	0.236	$B=W=10$	5.096	7.78
M01-122	0.405	$B=W=25$	13.088	43.55
M01-123	0.416	$B=W=25$	13.181	43.11

Table A2   CTOD test data at low temperatures under quasi-static conditions for S690QL

Specimen No	CTOD (mm)	Specimen geometry (mm)	Test temperature (°C)	Initial crack length (a₀) (mm)	Fracture load (kN)
*M01-86	0.216	$B=W=10$	-100	5.156	8.54 (J_m)
M01-87	0.034	$B=W=10$	-100	5.123	7.64
M01-94	0.086	$B=W=10$	-100	5.093	8.31
M01-98	0.136	$B=W=10$	-100	5.094	8.57
M01-99	0.112	$B=W=10$	-100	5.112	8.58
M01-100	0.056	$B=W=10$	-100	5.168	7.77
M01-106	0.008	$B=W=10$	-120	4.954	5.59
M01-112	0.028	$B=W=10$	-120	4.989	8.07
M01-113	0.026	$B=W=10$	-120	5.278	7.15

M01-114	0.025	$B=W=10$	-120	5.202	7.30
M01-115	0.045	$B=W=25$	-100	13.313	38.54
M01-116	0.037	$B=W=25$	-100	13.271	36.50
M01-117	0.073	$B=W=25$	-100	13.280	43.34
M01-118	0.013	$B=W=25$	-100	13.239	23.87
M01-119	0.023	$B=W=25$	-100	13.196	31.11
M01-120	0.018	$B=W=25$	-100	13.151	29.15
M01-121	0.033	$B=W=25$	-100	13.317	34.93

Table A3   CTOD test data at ambient temperature under quasi-static condition for S960QL

Specimen No	CTOD (mm)	Specimen geometry (mm)	Initial crack length (a_0) (mm)	Maximum load (kN)
M03-46	0.140	$B=W=10$	5.147	8.60
M03-48	0.160	$B=W=10$	5.078	8.84
M03-49	0.176	$B=W=10$	5.098	8.82
M03-60	0.163	$B=W=10$	5.240	8.29
M03-62	0.207	$B=W=10$	5.134	8.01
M03-63	0.163	$B=W=10$	5.244	8.29
M03-66	0.169	$B=W=10$	5.156	8.05

Table A4   CTOD test data at -100 °C under quasi-static condition for S960QL

Specimen No	CTOD (mm)	Specimen geometry (mm)	Test temperature (°C)	Initial crack length (a_0) (mm)	Fracture load (kN)
M03-67	0.028	$B=W=10$	-100	5.147	6.55
M03-68	0.018	$B=W=10$	-100	5.163	6.66
M03-69	0.027	$B=W=10$	-100	5.098	7.92

M03-86	0.050	B=W=10	-100	5.177	8.11
M03-89	0.008	B=W=10	-100	5.089	5.23
M03-90	0.014	B=W=10	-100	5.142	5.54

CTOD test data not reported in the text for S690QL at intermediate loading rate

Table A5   CTOD test data at -100 °C under intermediate loading condition for S690QL

Specimen No	CTOD (mm)	Specimen geometry (mm)	Test temperature (°C)	Initial crack length (a_0) (mm)
M01-125	0.042	B=W=10	-100	5.141
M01-126	0.009	B=W=10	-100	5.019
M01-127	0.022	B=W=10	-100	5.111
M01-128	0.022	B=W=10	-100	5.206
M01-129	0.009	B=W=10	-100	4.992
M01-130	0.026	B=W=10	-100	5.259
M01-139	0.018	B=W=10	-100	4.955
M01-140	0.017	B=W=10	-100	5.081

Charpy V-Notch test data for S690QL

Table A6   CVN results with notch in the transverse direction for S690QL

Specimen	Size (mm)	Charpy notch	Test Temp (° C)	Results (Joules KV)	Crystallinity %
M01-20	10 x 10	2 mm V	-40	234	0
M01-21	10 x 10	2 mm V	-50	251	0
M01-22	10 x 10	2 mm V	-60	225	0
M01-23	10 x 10	2 mm V	-70	102	0
M01-24	10 x 10	2 mm V	-80	26	79

M01-25	10 x 10	2 mm V	-100	24	85
M01-27	10 x 10	2 mm V	-65	188	0
M01-28	10 x 10	2 mm V	-20	212	0
M01-30	10 x 10	2 mm V	0	240	0
M01-31	10 x 10	2 mm V	-75	66	70
M01-32	10 x 10	2 mm V	-90	24	85

Table A7   CVN results with notch in the rolling/longitudinal direction for S690QL

Specimen	Size (mm)	Charpy notch	Test Temp (° C)	Results (Joules KV)	Crystallinity %
M01-05	10 x 10	2 mm V	-40	189	0
M01-06	10 x 10	2 mm V	-50	187	0
M01-07	10 x 10	2 mm V	-60	174	0
M01-08	10 x 10	2 mm V	-70	172	0
M01-09	10 x 10	2 mm V	-80	58	5
M01-10	10 x 10	2 mm V	-100	16	87
M01-12	10 x 10	2 mm V	-20	219	0
M01-13	10 x 10	2 mm V	0	237	0
M01-14	10 x 10	2 mm V	-75	42	0
M01-15	10 x 10	2 mm V	-90	18	87

Charpy V-Notch test data for S960QL

Table A8   CVN results with notch in the transverse direction for S960QL

Specimen	Size (mm)	Charpy notch	Test Temp (° C)	Results (Joules KV)	Crystallinity %
*M03-26	10 x 10	2 mm V	-50	164	0
*M03-27	10 x 10	2 mm V	-60	223	0

*M03-28	10 x 10	2 mm V	-70	52	71
*M03-29	10 x 10	2 mm V	-80	38	80
*M03-30	10 x 10	2 mm V	-100	39	80
**M03-31	10 x 10	2 mm V	-75	32	75
**M03-32	10 x 10	2 mm V	-20	194	0
**M03-33	10 x 10	2 mm V	-40	174	0
**M03-34	10 x 10	2 mm V	0	209	0
**M03-35	10 x 10	2 mm V	-65	51	61
**M03-36	10 x 10	2 mm V	-90	20	90

Note:

* specimens are machined within 2 mm of the upper surface of 60 mm thickness of S960QL

** specimens are machined within 17 mm of the upper surface of 60 mm thickness of S960QL

Charpy-sized pre-cracked SENB test data for S690QL

Table A9   Charpy-sized pre-cracked SENB absorbed energies at different test temperatures for S690QL at full striker angle (160°)

Specimen	Size (mm)	Notch details	Test Temp (° C)	Results (Joules KV)	Crystallinity %
M01-95	10 x 10	3.08 mm deep x 0.3 mm wide EDM notch with a fatigue crack length of 4.89 mm	23	90	0
M01-108	10 x 10	3.08 mm deep x 0.3 mm wide EDM notch with a fatigue crack length of 4.79 mm	23	91	0
M01-109	10 x 10	3.08 mm deep x 0.3 mm wide EDM notch with a fatigue crack length of 4.89 mm	23	98	0
M01-111	10 x 10	3.08 mm deep x 0.3 mm wide EDM notch with a fatigue crack length of 4.86 mm	23	95	0

M01-69	10 x 10	3.08 mm deep x 0.3 mm wide EDM notch with a fatigue crack length of 4.86 mm	0	81	0
M01-70	10 x 10	3.08 mm deep x 0.3 mm wide EDM notch with a fatigue crack length of 4.88 mm	-20	83	0
M01-71	10 x 10	3.08 mm deep x 0.3 mm wide EDM notch with a fatigue crack length of 4.89 mm	-14	70	0
M01-72	10 x 10	3.08 mm deep x 0.3 mm wide EDM notch with a fatigue crack length of 4.89 mm	-60	17	59
M01-73	10 x 10	3.08 mm deep x 0.3 mm wide EDM notch with a fatigue crack length of 4.87 mm	-50	69	0
M01-96	10 x 10	3.08 mm deep x 0.3 mm wide EDM notch with a fatigue crack length of 4.87 mm	-40	70	0
M01-74	10 x 10	3.08 mm deep x 0.3 mm wide EDM notch with a fatigue crack length of 4.88 mm	-70	13	68
M01-75	10 x 10	3.08 mm deep x 0.3 mm wide EDM notch with a fatigue crack length of 4.76 mm	-80	9	68
M01-76	10 x 10	3.08 mm deep x 0.3 mm wide EDM notch with a fatigue crack length of 4.87 mm	-90	7	72
M01-88	10 x 10	3.08 mm deep x 0.3 mm wide EDM notch with a fatigue crack length of 4.84 mm	-100	5	73
M01-89	10 x 10	3.08 mm deep x 0.3 mm wide EDM notch with a fatigue crack length of 4.85 mm	-100	6	71
M01-90	10 x 10	3.08 mm deep x 0.3 mm wide EDM notch with a fatigue crack length of 4.86 mm	-100	7	70

Specimen	Size (mm)	Notch details	Test Temp (° C)	Results (Joules KV)	Striker angle (°)
M01-91	10 x 10	3.08 mm deep x 0.3 mm wide EDM notch with a fatigue crack length of 4.88 mm	-100	5	72
M01-92	10 x 10	3.08 mm deep x 0.3 mm wide EDM notch with a fatigue crack length of 4.82 mm	-100	5	75
M01-97	10 x 10	3.08 mm deep x 0.3 mm wide EDM notch with a fatigue crack length of 4.82 mm	-100	7	88
M01-104	10 x 10	3.08 mm deep x 0.3 mm wide EDM notch with a fatigue crack length of 4.86 mm	-100	4	76
M01-105	10 x 10	3.08 mm deep x 0.3 mm wide EDM notch with a fatigue crack length of 4.86 mm	-100	6	75

Table A10   Low blow Charpy-sized pre-cracked SENB absorbed energies at ambient temperature for S690QL

Specimen	Size (mm)	Notch details	Test Temp (° C)	Results (Joules KV)	Striker angle (°)
M01-142	10 x 10	3.08 mm deep x 0.3 mm wide EDM notch with a fatigue crack length of 4.82 mm	23	36	25
M01-143	10 x 10	3.08 mm deep x 0.3 mm wide EDM notch with a fatigue crack length of 4.77 mm	23	36	25
M01-144	10 x 10	3.08 mm deep x 0.3 mm wide EDM notch with a fatigue crack length of 4.88 mm	23	51	30
M01-145	10 x 10	3.08 mm deep x 0.3 mm wide EDM notch with a fatigue crack length of 4.84 mm	23	52	30
M01-146	10 x 10	3.08 mm deep x 0.3 mm wide EDM notch with a fatigue crack length of 4.80 mm	23	49	30

Specimen	Size (mm)	Notch details	Test Temp (° C)	Results (Joules KV)	Crystallinity %
M01-147	10 x 10	3.08 mm deep x 0.3 mm wide EDM notch with a fatigue crack length of 4.80 mm	23	69	35
M01-148	10 x 10	3.08 mm deep x 0.3 mm wide EDM notch with a fatigue crack length of 4.77 mm	23	88	40
M01-149	10 x 10	3.08 mm deep x 0.3 mm wide EDM notch with a fatigue crack length of 4.76 mm	23	94	45
M01-150	10 x 10	3.08 mm deep x 0.3 mm wide EDM notch with a fatigue crack length of 4.74 mm	23	103	45

Charpy-sized pre-cracked SENB test data for S960QL

Table A11   Charpy-sized pre-cracked SENB absorbed energies at different test temperatures for S960QL at full striker angle (160°)

Specimen	Size (mm)	Notch details	Test Temp (° C)	Results (Joules KV)	Crystallinity %
M03-74	10 x 10	3.08 mm deep x 0.3 mm wide EDM notch with a fatigue crack length of 4.86 mm	23	67	0
M03-87	10 x 10	3.08 mm deep x 0.3 mm wide EDM notch with a fatigue crack length of 4.87 mm	23	61	0
M03-88	10 x 10	3.08 mm deep x 0.3 mm wide EDM notch with a fatigue crack length of 4.86 mm	23	50	0
M03-59	10 x 10	3.08 mm deep x 0.3 mm wide EDM notch with a fatigue crack length of 4.86 mm	0	48	31
M03-52	10 x 10	3.08 mm deep x 0.3 mm wide EDM notch with a fatigue crack length of 4.87 mm	-20	30	44

M03-75	10 x 10	3.08 mm deep x 0.3 mm wide EDM notch with a fatigue crack length of 4.88 mm	-40	15	53
M03-77	10 x 10	3.08 mm deep x 0.3 mm wide EDM notch with a fatigue crack length of 4.87 mm	-50	11	64
M03-78	10 x 10	3.08 mm deep x 0.3 mm wide EDM notch with a fatigue crack length of 4.86 mm	-70	8	73
M03-79	10 x 10	3.08 mm deep x 0.3 mm wide EDM notch with a fatigue crack length of 4.86 mm	-80	5	79
M03-80	10 x 10	3.08 mm deep x 0.3 mm wide EDM notch with a fatigue crack length of 4.77 mm	-90	3	81
M03-76	10 x 10	3.08 mm deep x 0.3 mm wide EDM notch with a fatigue crack length of 4.88 mm	-100	4	90
M03-70	10 x 10	3.08 mm deep x 0.3 mm wide EDM notch with a fatigue crack length of 4.85 mm	-100	4	74
M03-71	10 x 10	3.08 mm deep x 0.3 mm wide EDM notch with a fatigue crack length of 4.88 mm	-100	4	76
M03-72	10 x 10	3.08 mm deep x 0.3 mm wide EDM notch with a fatigue crack length of 4.86 mm	-100	4	72
M03-73	10 x 10	3.08 mm deep x 0.3 mm wide EDM notch with a fatigue crack length of 4.85 mm	-100	4	70
M03-83	10 x 10	3.08 mm deep x 0.3 mm wide EDM notch with a fatigue crack length of 4.88 mm	-100	4	76
M03-84	10 x 10	3.08 mm deep x 0.3 mm wide EDM notch with a fatigue crack length of 4.79 mm	-100	4	75

Table A12   Low blow Charpy-sized pre-cracked SENB absorbed energies at ambient temperature for S960QL

Specimen	Size (mm)	Notch details	Test Temp (° C)	Results (Joules KV)	Striker angle (°)
M03-110	10 x 10	3.08 mm deep x 0.3 mm wide EDM notch with a fatigue crack length of 4.86 mm	23	36	25
M03-111	10 x 10	3.08 mm deep x 0.3 mm wide EDM notch with a fatigue crack length of 4.81 mm	23	36	25
M03-112	10 x 10	3.08 mm deep x 0.3 mm wide EDM notch with a fatigue crack length of 4.81 mm	23	52	30
M03-113	10 x 10	3.08 mm deep x 0.3 mm wide EDM notch with a fatigue crack length of 4.88 mm	23	52	30
M03-114	10 x 10	3.08 mm deep x 0.3 mm wide EDM notch with a fatigue crack length of 4.86 mm	23	70	35
M03-115	10 x 10	3.08 mm deep x 0.3 mm wide EDM notch with a fatigue crack length of 4.83 mm	23	70	35
M03-116	10 x 10	3.08 mm deep x 0.3 mm wide EDM notch with a fatigue crack length of 4.80 mm	23	77	40
M03-117	10 x 10	3.08 mm deep x 0.3 mm wide EDM notch with a fatigue crack length of 4.85 mm	23	79	45
M03-118	10 x 10	3.08 mm deep x 0.3 mm wide EDM notch with a fatigue crack length of 4.88 mm	23	75	45

Test certificates

Fracture toughness test certificates

- Standard SENB specimen configuration (*B=W=25* mm) test certificates for S690QL at ambient temperature.

TWI

SENB FRACTURE TEST 25463 M01-122

Client		
Project leader	Aderinkola Alabi	Signed:

Data source

Data logging program	LVGENLOG V 1.44 30-Oct-2017	
Program used to calculate CTOD/J	LVGENPLOT V 1.54 09-Feb-2018	
Calculation date of CTOD/J	07 Mar 2018	

Specimen details

Material	S 690 QL	
Specimen type	Full thickness, SENB	
Crack plane orientation	Y-X	
Type of notch tip	Fatigue	
Notch tip location	Parent material	
Specimen width	25.040	mm
Specimen thickness	25.150	mm
Initial crack length	13.088	mm
Side-grooved?	NO	

Test details

Test standard(s)	BS 7448: Part 1: 1991	
Test date	26/02/2018	
Test time	13:54:00	
Test technician	Phillip Cossey	Signed:
Test machine	INSTRON 8500 B107	
Test environment	AIR	
Test temperature	21.0	°C
Soak time @ test temperature	25.0	minutes
Knife edge heights	2.500, 12.500	mm
Knife edge attachment spacing	2.00	mm
Initial K-rate	0.6	$MPa.m^{1/2}/s$
Loading span	100.0	mm
Double roller diameter	18.00	mm
Single roller diameter	12.00	mm
Crosshead displacement rate	0.30	mm/min

LVGENPLOT V 1.54 09-Feb-2018   Page 1 of 5   SI/FRA/F/1 Rev0.1 March 2017

Material properties

Yield strength for pre-cracking	810.0 MPa	Measured at RT
Tensile strength for pre-cracking	843.5 MPa	Measured at RT
Yield strength for testing	810.0 MPa	Measured at RT
Tensile strength for testing	843.5 MPa	Measured at RT
Poisson's ratio	0.3	Assumed
Young's modulus	213 GPa	Assumed

Fatigue details

Stress ratio, R	0.100	
Final force, F_f	8.00	kN
Final K	23.0	$MPa.m^{1/2}$
Fatigue temperature	21.0	°C
Loading span, S	100.0	mm

Analysis details

Method of determining Load Point Displacement, q	DOUBLE CLIP	
Lower knife edge height check	OK	

Compiled by:	Phillip Cossey	**Signed:**	

LVGENPLOT V 1.54 09-Feb-2018   Page 2 of 5   SI/FRA/F/1 Rev0.1 March 2017

SENB FRACTURE TEST 25463 M01-122

Qualification checks to	BS 7448: Part 1: 1991			Value	Allowed
(5.1.3)					
Knife edge attachment spacing		**Pass**		2.00	12.52
(6.4.5,6.4.6)					
The final fatigue precracking force <= F_f (a)		**Pass**		8.00	14.85
$\Delta K/E$ below limit (b)		**Pass**		0.003	0.010
(6.4.7)					
Initial/Final K ratio during precracking < 1.3 (a)		**Pass**		1.09	1.30
(7.5.1)					
Single roller diameter		**Pass**		12.00	8.35 - 25.04
Double roller diameter		**Pass**		18.00	12.52 - 25.04
Loading span		**Pass**		100.0	95.2 - 105.2
(8.5)					
Initial K-rate between 0.5 $MPa.m^{0.5}s^{-1}$ and 3.0 $MPa.m^{0.5}s^{-1}$		**Pass**		0.64	0.5 - 3.0
(10.2.2)					
Minimum surface crack length (a)		**Pass**		11.97	11.27
Minimum crack extension at surface (b)		**Pass**		2.40	1.30
Difference in surface crack measurements (c)		**Pass**		0.20	1.81
Surface fatigue cracks in envelope (d)		**Pass**			
Crack plane within 10° (e)		**Pass**			
(10.2.3)					
Multiplane cracking (a)		**Pass**			
a_0/W check 0.45-0.55 (b)		**Pass**		0.52	0.45-0.55
Crack shape (c)		**Pass**		1.10	1.31
Minimum crack length (d)		**Pass**		2.60	1.30
(10.3)					
The stress ratio <= 0.1 (c)		**Pass**		0.10	

TWI

SENB FRACTURE TEST 25463 M01-122

Test date	26/02/2018			Client	00/01/1900		
Technician	Phillip Cossey			Project leader	Aderinkola Alabi		
Test machine	INSTRON 8500 B107			Investigator's signature			
Control mode	Displacement			Compiled by	Phillip Cossey		

Selected point coordinates for plot	
	1.550
	1.932
	0.000
	43.553

SPECIMEN DETAILS		
Force, F	43.55	kN
Width, W	25.040	mm
Thickness, B	25.150	mm
Crack length, a_0	13.088	mm
Loading span, S	100.00	mm
Yield strength	810	MPa
Young's modulus	213	GPa
Poisson's ratio	0.300	
Test temperature	21.0	°C

RESULTS		
δ	0.405	mm
K @ calculation point	125.2	MPa.m$^{1/2}$
F_{max}/F_Q	1.70	
K_Q	73.56	MPa.m$^{1/2}$
Total area under Force v q	85.72	kNmm
J0 from q from DOUBLE CLIP	567.75	kJ/m² (N/mm)
Plastic area Force vs q	75.26	kNmm
Type of result	δ/J_m	
Test standard(s)	BS 7448: Part 1: 1991	
Result qualified to standard(s)	YES	

Slope for clip 1	0.008785
Clip 1 offset	-0.00237
Slope for clip 2	0.013198
Clip 2 offset	-0.004079
Yfunc	2.865225
Ctod from upper clip	0.397775
Fq	25.5835
Q type	2
Number of clips	2
Area under load v Q	75.260397
Number of pop-ins	0
K Units	0
Stress units	0
E units	1
J units	0
Sample type	0
Type of result	8
Type of test	1
Hide UCAS logo	0
Graph X axis title	Clip gauge, mm

LOWER CLIP GAUGE VALUES		
Knife edge height	2.50	mm
Vg	1.932	mm
Vp	1.550	mm

UPPER CLIP GAUGE VALUES		
Knife edge height	12.50	mm
Vg	2.839	mm
Vp	2.264	mm
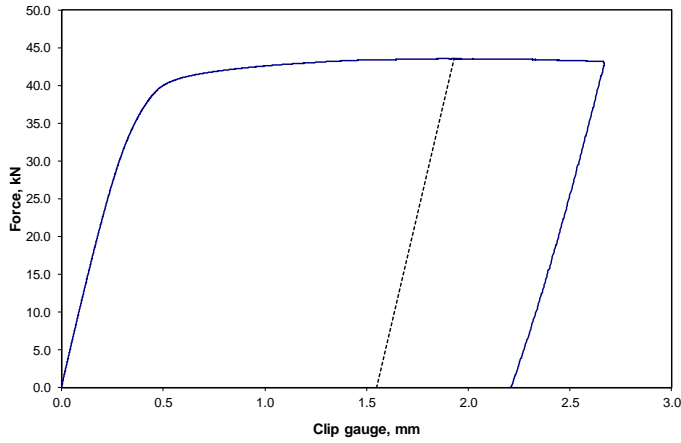
SENB FRACTURE TEST 25463 M01-122

Diagram of fracture face

Specimen width, W	25.040	mm
Specimen thickness, B	25.150	mm
Machined notch depth, M	9.610	mm
Surface crack length, a_{S1}	0.360	mm
Surface crack length, a_{S2}	12.150	mm
Net section thickness, B_N	11.970	mm
a_{max}	13.340	mm
a_{min}	12.170	mm

Comments

Measurement Line	Fatigue crack length a_0, mm	Slow stable crack extension + fatigue crack a_p, mm	Slow stable crack extension including stretch zone, Δ_a, mm
1	12.560	12.560	0.000
2	13.070	14.070	1.000
3	13.290	14.330	1.040
4	13.330	14.250	0.920
5	13.340	14.130	0.790
6	13.260	14.090	0.830
7	13.150	14.010	0.860
8	12.900	13.650	0.750
9	12.170	12.170	0.000
Weighted Average	**13.088**	**13.862**	**0.774**

Measured by: Phillip Cossey   **Signed:**

- Standard SENB specimen configuration (*B=W=*25 mm) test certificates for S690QL at -100 °C.

SENB FRACTURE TEST 25463 M01-115

Client	TWI
Project leader	Aderinkola Alabi Signed:

Data source

Data logging program	LVGENLOG V 1.44 30-Oct-2017
Program used to calculate CTOD/J	LVGENPLOT V 1.54 09-Feb-2018
Calculation date of CTOD/J	07 Mar 2018

Specimen details

Material	S 690 QL	
Specimen type	Full thickness, SENB	
Crack plane orientation	Y-X	
Type of notch tip	Fatigue	
Notch tip location	Parent material	
Specimen width	25.020	mm
Specimen thickness	25.130	mm
Initial crack length	13.313	mm
Side-grooved?	NO	

Test details

Test standard(s)	BS 7448: Part 1: 1991	
Test date	23/02/2018	
Test time	11:11:00	
Test technician	Phillip Cossey Signed:	
Test machine	INSTRON 8500 B107	
Test environment	ENVIRONMENTAL CHAMBER	
Test temperature	-100.0	℃
Soak time @ test temperature	25.0	minutes
Knife edge heights	2.500, 12.500	mm
Knife edge attachment spacing	2.00	mm
Initial K-rate	0.6	MPa.m$^{1/2}$/s
Loading span	100.0	mm
Double roller diameter	18.00	mm
Single roller diameter	12.00	mm
Crosshead displacement rate	0.30	mm/min

LVGENPLOT V 1.54 09-Feb-2018   Page 1 of 5   SI/FRA/F/1 Rev0.1 March 2017

Material properties

Yield strength for pre-cracking	810.0	MPa	Measured at RT
Tensile strength for pre-cracking	843.5	MPa	Measured at RT
Yield strength for testing	942.5	MPa	Estimated from measured value with temperature correction
Tensile strength for testing	1030.0	MPa	Assumed from material specification
Poisson's ratio	0.3		Assumed
Young's modulus	213	GPa	Assumed

Fatigue details

Stress ratio, R	0.100	
Final force, F$_f$	8.00	kN
Final K	23.8	MPa.m$^{1/2}$
Fatigue temperature	21.0	℃
Loading span, S	100.0	mm

Analysis details

Method of determining Load Point Displacement, q	DOUBLE CLIP
Lower knife edge height check	OK

Compiled by: Phillip Cossey   Signed:

LVGENPLOT V 1.54 09-Feb-2018   Page 2 of 5   SI/FRA/F/1 Rev0.1 March 2017

SENB FRACTURE TEST 25463 M01-115

Qualification checks to	BS 7448: Part 1: 1991		Value	Allowed
(5.1.3)				
Knife edge attachment spacing		**Pass**	2.00	12.51
(6.4.5,6.4.6)				
The final fatigue precracking force <= F_f (a)		**Pass**	8.00	14.24
$\Delta K/E$ below limit (b)		**Pass**	0.003	0.010
(6.4.7)				
Initial/Final K ratio during precracking < 1.3 (a)		**Pass**	1.07	1.30
(7.5.1)				
Single roller diameter		**Pass**	12.00	8.34 - 25.02
Double roller diameter		**Pass**	18.00	12.51 - 25.02
Loading span		**Pass**	100.0	95.1 - 105.1
(8.5)				
Initial K-rate between 0.5 MPa.m$^{0.5}$s^{-1} and 3.0 MPa.m$^{0.5}$s^{-1}		**Pass**	0.59	0.5 - 3.0
(10.2.2)				
Minimum surface crack length (a)		**Pass**	12.12	11.26
Minimum crack extension at surface (b)		**Pass**	2.50	1.30
Difference in surface crack measurements (c)		**Pass**	0.10	1.82
Surface fatigue cracks in envelope (d)		**Pass**		
Crack plane within 10° (e)		**Pass**		
(10.2.3)				
Multiplane cracking (a)		**Pass**		
a_0/W check 0.45-0.55 (b)		**Pass**	0.53	0.45-0.55
Crack shape (c)		**Pass**	1.00	1.33
Minimum crack length (d)		**Pass**	2.90	1.30
(10.3)				
The stress ratio <= 0.1 (c)		**Pass**	0.10	

DRAFT

TWI

SENB FRACTURE TEST 25463 M01-115

Test date	23/02/2018		Client	TWI			Selected point coordinates for plot	
Technician	Phillip Cossey		Project leader	Aderinkola Alabi			0.069	
Test machine	INSTRON 8500 B107		Investigator's signature				0.420	
Control mode	Displacement		Compiled by	Phillip Cossey			0.000	
							38.536	

SPECIMEN DETAILS			RESULTS					
Force, F	38.54	kN	δ	0.045	mm	Slope for clip 1	0.009117	
Width, W	25.020	mm	K @ calculation point	114.5	MPa.m$^{1/2}$	Clip 1 offset	-0.003096	
Thickness, B	25.130	mm	F_{max}/F_Q	1.53		Slope for clip 2	0.013116	
Crack length, a_0	13.313	mm	K_Q	75.07	MPa.m$^{1/2}$	Clip 2 offset	-0.002765	
Loading span, S	100.00	mm	Total area under Force v q	9.29	kNmm	Yfunc	2.956307	
Yield strength	943	MPa	J0 from q from DOUBLE CLIP	68.78	kJ/m² (N/mm)	Ctod from upper clip	0.043712	
Young's modulus	213	GPa	Plastic area Force vs q	1.87	kNmm	Fq	25.253841	
Poisson's ratio	0.300		Type of result	δ / J_c		Q type	2	
Test temperature	-100.0	°C				Number of clips	2	
			Test standard(s)	BS 7448: Part 1: 1991		Area under load v Q	1.870715	
			Result qualified to standard(s)	YES		Number of pop-ins	0	
						K Units	0	
						Stress units	0	
LOWER CLIP GAUGE VALUES			UPPER CLIP GAUGE VALUES			E units	1	
Knife edge height	2.50	mm	Knife edge height	12.50	mm	J units	0	
Vg	0.420	mm	Vg	0.596	mm	Sample type	0	
Vp	0.069	mm	Vp	0.091	mm	Type of result	0	
						Type of test	1	
						Hide UCAS logo	0	
						Graph X axis title	Clip gauge, mm	

SENB FRACTURE TEST 25463 M01-115

Diagram of fracture face

Specimen width, W	25.020	mm
Specimen thickness, B	25.130	mm
Machined notch depth, M	9.610	mm
Surface crack length, a_{S1}	0.380	mm
Surface crack length, a_{S2}	12.190	mm
Net section thickness, B_N	12.120	mm
a_{max}	13.540	mm
a_{min}	12.510	mm
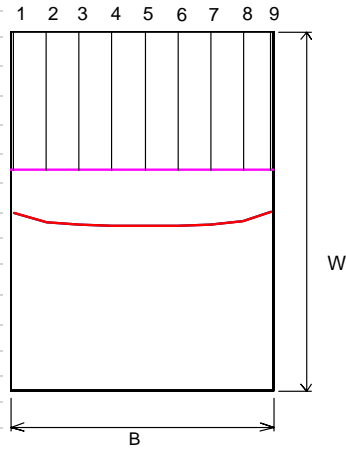
Comments

Measurement Line	Fatigue crack length a_0, mm	Slow stable crack extension + fatigue crack a_p, mm	Slow stable crack extension including stretch zone, Δ_a, mm
1	12.620	12.620	0.000
2	13.250	13.250	0.000
3	13.450	13.450	0.000
4	13.540	13.540	0.000
5	13.540	13.540	0.000
6	13.530	13.530	0.000
7	13.440	13.440	0.000
8	13.190	13.190	0.000
9	12.510	12.510	0.000
Weighted Average	**13.313**	**13.313**	**0.000**

Measured by: Phillip Cossey   **Signed:**

- Charpy-sized pre-cracked SENB specimen configuration (B=W=10 mm) test certificates for S690QL at ambient temperature.

TWI

SENB FRACTURE TEST 25463 M01-66

Client		TWI		
Project leader			Signed:	

Data source

Data logging program	LVGENLOG V 1.42 14-Jul-2017	
Program used to calculate CTOD/J	LVGENPLOT V 1.45 02-Jun-2017	
Calculation date of CTOD/J	20 Jul 2017	

Specimen details

Material		
Specimen type	Subsize, SENB	
Crack plane orientation	Y-X	
Type of notch tip	Fatigue	
Notch tip location	Parent material	
Specimen width	10.030	mm
Specimen thickness	10.010	mm
Initial crack length	5.199	mm
Side-grooved?	NO	
Original PM 1 thickness	20.00	mm

DRAFT

Test details

Test standard(s)	BS 7448: Part 1: 1991	
Test date	17/07/2017	
Test time	14:15:00	
Test technician	Phillip Cossey	Signed:
Test machine	INSTRON 8801 B909	
Test environment	AIR	
Test temperature	21.0	ºC
Soak time @ test temperature	0.0	minutes
Knife edge heights	2.500, 8.500	mm
Knife edge spacing	2.00	mm
Initial K-rate	1.0	MPa.m$^{1/2}$/s
Loading span	40.0	mm
Double roller diameter	8.00	mm
Single roller diameter	8.00	mm

LVGENPLOT V 1.45 02-Jun-2017	Page 1 of 5	SI/FRA/F/1 Rev0.1 March 2017

Material properties

Yield strength for pre-cracking	810.0	MPa	Measured at RT
Tensile strength for pre-cracking	843.5	MPa	Measured at RT
Yield strength for testing	810.0	MPa	Measured at RT
Tensile strength for testing	843.5	MPa	Measured at RT
Poisson's ratio	0.3		Assumed
Young's modulus	213	GPa	Assumed

Fatigue details

Stress ratio, R	0.100	
Final force, F$_f$	2.00	kN
Final K	22.5	MPa.m$^{1/2}$
Fatigue temperature	21.0	ºC
Loading span, S	40.0	mm

DRAFT

Analysis details

Method of determining Load Point Displacement, q	SINGLE CLIP
Lower knife edge height check	Warning !!! z/a > 0.2

Compiled by:	Phillip Cossey	**Signed:**

LVGENPLOT V 1.45 02-Jun-2017	Page 2 of 5	SI/FRA/F/1 Rev0.1 March 2017

SENB FRACTURE TEST 25463 M01-66

Qualification checks to	**BS 7448: Part 1: 1991**			Value	Allowed
(5.1.3)					
Knife edge attachment spacing		**Pass**		2.00	5.02
(6.4.5,6.4.6)					
The final fatigue precracking force <= F_f (a)		**Pass**		2.00	2.41
$\Delta K/E$ below limit (b)		**Pass**		0.003	0.010
(6.4.7)					
Initial/Final K ratio during precracking < 1.3 (a)		**Pass**		1.07	1.30
(7.5.1)					
Single roller diameter		**Pass**		8.00	3.34 - 10.03
Double roller diameter		**Pass**		8.00	5.01 - 10.03
Loading span		**Pass**		40.0	38.1 - 42.1
(8.5)					
Initial K-rate between 0.5 MPa.m$^{0.5}$s^{-1} and 3.0 MPa.m$^{0.5}$s^{-1}		**Pass**		0.99	0.5 - 3.0
(10.2.2)					
Minimum surface crack length (a)		**Pass**		4.87	4.51
Minimum crack extension at surface (b)		**Pass**		1.80	1.30
Difference in surface crack measurements (c)		**Pass**		0.00	0.73
Surface fatigue cracks in envelope (d)		**Pass**			
Crack plane within 10° (e)		**Pass**			
(10.2.3)					
Multiplane cracking (a)		**Pass**			
a_0/W check 0.45-0.55 (b)		**Pass**		0.52	0.45-0.55
Crack shape (c)		**Pass**		0.40	0.52
Minimum crack length (d)		**Pass**		1.90	1.30
(10.3)					
The stress ratio <= 0.1 (c)		**Pass**		0.10	

DRAFT

SENB FRACTURE TEST 25463 M01-66

Test date	17/07/2017
Technician	Phillip Cossey
Test machine	INSTRON 8801 B909
Control mode	Displacement

Client	TWI
Project leader	Aderinkola Alabi
Investigator's signature	
Compiled by	Phillip Cossey

Selected point coordinates for plot	
0.997	
1.179	
0.000	
7.448	

SPECIMEN DETAILS

Force, F	7.45	kN
Width, W	10.030	mm
Thickness, B	10.010	mm
Crack length, a_0	5.199	mm
Loading span, S	40.00	mm
Yield strength	810	MPa
Young's modulus	213	GPa
Poisson's ratio	0.300	
Test temperature	21.0	°C

RESULTS

δ	0.218	mm
K @ calculation point	83.7	MPa.m$^{1/2}$
F_{max}/F_Q	1.76	
K_Q	47.53	MPa.m$^{1/2}$
Total area under Force v q	8.14	kNmm
J0 from q from SINGLE CLIP	337.21	kJ/m² (N/mm)
Plastic area Force vs q	7.43	kNmm
Type of result	δ/J_m	

Test standard(s)	BS 7448: Part 1: 1991
Result qualified to standard(s)	YES

Slope for clip 1	0.024521
Clip 1 offset	-0.002605
Slope for clip 2	0.04101
Clip 2 offset	-0.00366
Yfunc	2.824399
Ctod from upper clip	0.212049
Fq	4.23024
Q type	0
Number of clips	2
Area under load v Q	7.430413
Number of pop-ins	0
K Units	0
Stress units	0
E units	1
J units	0
Sample type	0
Type of result	8
Type of test	1
Hide UCAS logo	1

LOWER CLIP GAUGE VALUES

Knife edge height	2.50	mm
Vg	1.179	mm
Vp	0.997	mm

UPPER CLIP GAUGE VALUES

Knife edge height	8.50	mm
Vg	1.871	mm
Vp	1.566	mm

Force, kN vs Clip gauge, mm
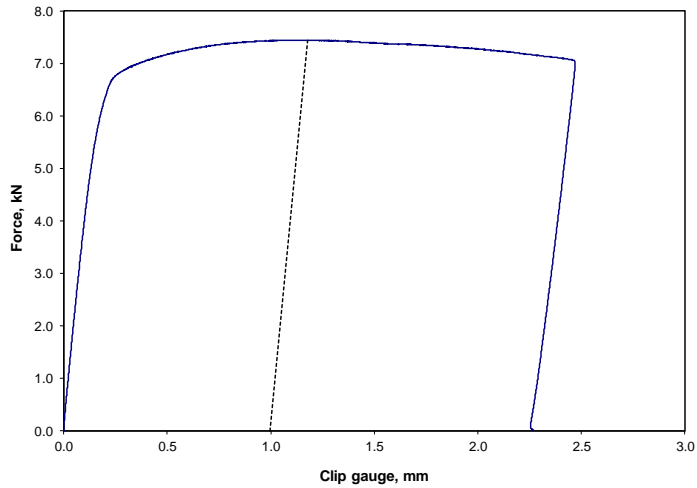
SENB FRACTURE TEST 25463 M01-66

Diagram of fracture face

Specimen width, W	10.030	mm
Specimen thickness, B	10.010	mm
Machined notch depth, M	3.060	mm
Machined notch width, N	0.300	mm
Surface crack length, a_{S1}	4.890	mm
Surface crack length, a_{S2}	4.870	mm
a_{max}	5.290	mm
a_{min}	4.940	mm

Comments
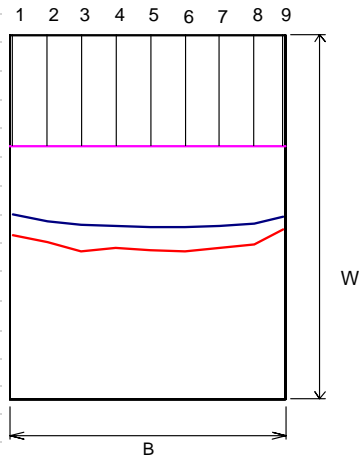
Measurement Line	Fatigue crack length a_0, mm	Slow stable crack extension + fatigue crack a_p, mm	Slow stable crack extension including stretch zone, Δ_a, mm
1	4.940	5.510	0.570
2	5.120	5.700	0.580
3	5.220	5.960	0.740
4	5.250	5.880	0.630
5	5.290	5.920	0.630
6	5.290	5.950	0.660
7	5.260	5.880	0.620
8	5.190	5.780	0.590
9	5.000	5.370	0.370
Weighted Average	5.199	5.814	0.615

Measured by: Phillip Cossey

Signed:

- Charpy-sized pre-cracked SENB specimen configuration (B=W=10 mm) test certificates for S690QL at -100 °C and -120 °C.

TWI

SENB FRACTURE TEST 25463 M01-98

Client	TWI	
Project leader		Signed:

Data source

Data logging program	LVGENLOG V 1.43 22-Aug-2017	
Program used to calculate CTOD/J	LVGENPLOT V 1.47 17-Aug-2017	
Calculation date of CTOD/J	08 Nov 2017	

Specimen details

Material	S 690 QL	
Specimen type	Subsize, SENB	
Crack plane orientation	Y-X	
Type of notch tip	Fatigue	
Notch tip location	Parent material	
Specimen width	10.060	mm
Specimen thickness	10.040	mm
Initial crack length	5.094	mm
Side-grooved?	NO	
Original PM 1 thickness	20.00	mm

Test details

Test standard(s)	BS 7448: Part 1: 1991	
Test date	06/11/2017	
Test time	16:24:00	
Test technician	Phillip Cossey	Signed:
Test machine	ESH B296	
Test environment	ENVIRONMENTAL CHAMBER	
Test temperature	-100.0	°C
Soak time @ test temperature	10.0	minutes
Knife edge heights	2.500, 8.500	mm
Knife edge spacing	2.00	mm
Initial K-rate	1.1	MPa.m$^{1/2}$/s
Loading span	40.0	mm
Double roller diameter	8.00	mm
Single roller diameter	8.00	mm
	0.29	

LVGENPLOT V 1.47 17-Aug-2017   Page 1 of 5   SI/FRA/F/1 Rev0.1 March 2017

Material properties

Yield strength for pre-cracking	810.0	MPa	Measured at RT
Tensile strength for pre-cracking	843.5	MPa	Measured at RT
Yield strength for testing	810.0	MPa	Measured at RT
Tensile strength for testing	843.5	MPa	Measured at RT
Poisson's ratio	0.3		Assumed
Young's modulus	207	GPa	Measured

Fatigue details

Stress ratio, R	0.100	
Final force, F$_f$	2.00	kN
Final K		MPa.m$^{1/2}$
Fatigue temperature		°C
Loading span, S		mm

Analysis details

Method of determining Load Point Displacement, q	DOUBLE CLIP
Lower knife edge height check	Warning !!! z/a > 0.2

Compiled by:	Phillip Cossey	**Signed:**

LVGENPLOT V 1.47 17-Aug-2017   Page 2 of 5   SI/FRA/F/1 Rev0.1 March 2017

SENB FRACTURE TEST 25463 M01-98

Qualification checks to	**BS 7448: Part 1: 1991**			Value	Allowed
(5.1.3)					
Knife edge attachment spacing		**Pass**		2.00	5.03
(6.4.5,6.4.6)					
The final fatigue precracking force <= F_f (a)		**Pass**		2.00	2.56
$\Delta K/E$ below limit (b)		**Pass**		0.003	0.010
(6.4.7)					
Initial/Final K ratio during precracking < 1.3 (a)		**Pass**		1.13	1.30
(7.5.1)					
Single roller diameter		**Pass**		8.00	3.35 - 10.06
Double roller diameter		**Pass**		8.00	5.03 - 10.06
Loading span		**Pass**		40.0	38.2 - 42.3
(8.5)					
Initial K-rate between 0.5 MPa.m$^{0.5}$s^{-1} and 3.0 MPa.m$^{0.5}$s^{-1}		**Pass**		1.12	0.5 - 3.0
(10.2.2)					
Minimum surface crack length (a)		**Pass**		4.87	4.53
Minimum crack extension at surface (b)		**Pass**		1.80	1.30
Difference in surface crack measurements (c)		**Pass**		0.00	0.73
Surface fatigue cracks in envelope (d)		**Pass**			
Crack plane within 10° (e)		**Pass**			
(10.2.3)					
Multiplane cracking (a)		**Pass**			
a_0/W check 0.45-0.55 (b)		**Pass**		0.51	0.45-0.55
Crack shape (c)		**Pass**		0.40	0.51
Minimum crack length (d)		**Pass**		1.70	1.30
(10.3)					
The stress ratio <= 0.1 (c)		**Pass**		0.10	

SENB FRACTURE TEST 25463 M01-98

Test date	06/11/2017		Client	TWI			Selected point coordinates for plot	
Technician	Phillip Cossey		Project leader	00/01/1900			0.545	
Test machine	ESH B296		Investigator's signature				0.753	
Control mode	Displacement		Compiled by	Phillip Cossey			0.000	
							8.565	

SPECIMEN DETAILS			RESULTS					
Force, F	8.57	kN	δ	0.136	mm		Slope for clip 1	0.024384
Width, W	10.060	mm	K @ calculation point	91.9	MPa.m$^{1/2}$		Clip 1 offset	0.000421
Thickness, B	10.040	mm	F_{max}/F_Q	1.67			Slope for clip 2	0.03862
Crack length, a_0	5.094	mm	K_Q	54.89	MPa.m$^{1/2}$		Clip 2 offset	-0.002444
Loading span, S	40.00	mm	Total area under Force v q	5.09	kNmm		Yfunc	2.717408
Yield strength	810	MPa	J0 from q from DOUBLE CLIP	206.49	kJ/m² (N/mm)		Ctod from upper clip	0.131988
Young's modulus	207	GPa	Plastic area Force vs q	4.22	kNmm		Fq	5.115561
Poisson's ratio	0.300		Type of result	δ/J_c			Q type	2
Test temperature	-100.0	℃					Number of clips	2
			Test standard(s)	BS 7448: Part 1: 1991			Area under load v Q	4.221617
			Result qualified to standard(s)	YES			Number of pop-ins	0
							K Units	0
							Stress units	0
LOWER CLIP GAUGE VALUES			UPPER CLIP GAUGE VALUES				E units	1
Knife edge height	2.50	mm	Knife edge height	8.50	mm		J units	0
Vg	0.753	mm	Vg	1.186	mm		Sample type	0
Vp	0.545	mm	Vp	0.856	mm		Type of result	0
							Type of test	1
							Hide UCAS logo	0
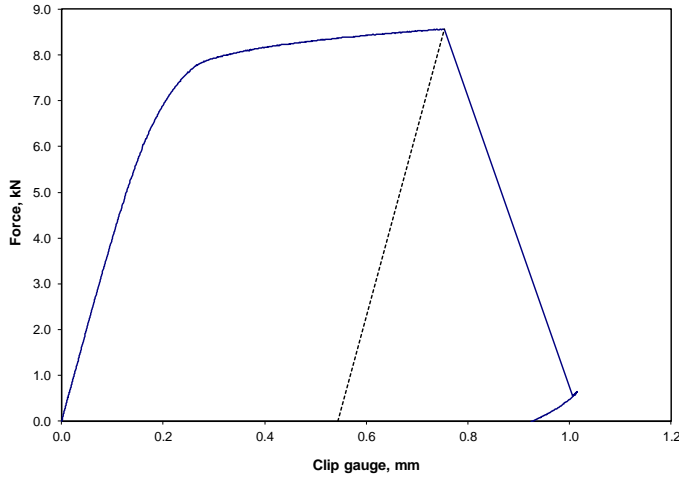
SENB FRACTURE TEST 25463 M01-98

Diagram of fracture face

Specimen width, W	10.060	mm
Specimen thickness, B	10.040	mm
Machined notch depth, M	3.070	mm
Machined notch width, N	0.320	mm
Surface crack length, a_{S1}	4.870	mm
Surface crack length, a_{S2}	4.900	mm
a_{max}	5.180	mm
a_{min}	4.790	mm
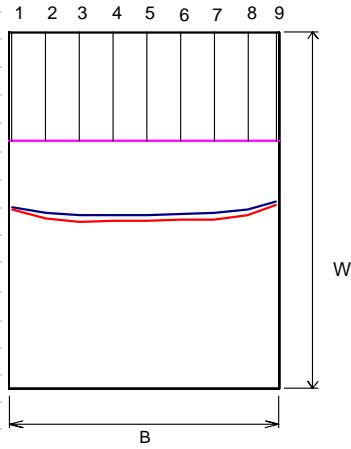
Comments

DRAFT

Measurement Line	Fatigue crack length a_0, mm	Slow stable crack extension + fatigue crack a_p, mm	Slow stable crack extension including stretch zone, Δ_a, mm
1	4.940	5.000	0.060
2	5.110	5.270	0.160
3	5.180	5.360	0.180
4	5.170	5.330	0.160
5	5.170	5.340	0.170
6	5.150	5.300	0.150
7	5.110	5.280	0.170
8	5.000	5.160	0.160
9	4.790	4.890	0.100
Weighted Average	**5.094**	**5.248**	**0.154**

Measured by: Phillip Cossey   **Signed:**

TWI

SENB FRACTURE TEST 25463 M01-112

Client		
Project leader	Aderinkola Alabi	Signed:

Data source

Data logging program	LVGENLOG V 1.46 15-Feb-2018	
Program used to calculate CTOD/J	LVGENPLOT V 1.54 09-Feb-2018	
Calculation date of CTOD/J	07 Mar 2018	

Specimen details

Material	S 960 QL	
Specimen type	Subsize, SENB	
Crack plane orientation	Y-X	
Type of notch tip	Fatigue	
Notch tip location	Parent material	
Specimen width	10.040	mm
Specimen thickness	10.020	mm
Initial crack length	4.989	mm
Side-grooved?	NO	
Original PM 1 thickness	20.00	mm

Test details

Test standard(s)	BS 7448: Part 1: 1991	
Test date	27/02/2018	
Test time	15:32:00	
Test technician	Phillip Cossey	Signed:
Test machine	INSTRON 8500 B107	
Test environment	ENVIRONMENTAL CHAMBER	
Test temperature	-120.0	°C
Soak time @ test temperature	10.0	minutes
Knife edge heights	2.500, 8.500	mm
Knife edge attachment spacing	2.00	mm
Initial K-rate	1.0	$MPa.m^{1/2}/s$
Loading span	40.0	mm
Double roller diameter	8.00	mm
Single roller diameter	8.00	mm
Crosshead displacement rate	0.29	mm/min

LVGENPLOT V 1.54 09-Feb-2018	Page 1 of 5	SI/FRA/F/1 Rev0.1 March 2017

Material properties

Yield strength for pre-cracking	810.0	MPa	Measured at RT
Tensile strength for pre-cracking	843.5	MPa	Measured at RT
Yield strength for testing	987.5	MPa	Estimated from measured value with temperature correction
Tensile strength for testing	1076.0	MPa	Estimated from measured value with temperature correction
Poisson's ratio	0.3		Assumed
Young's modulus	215	GPa	Assumed

Fatigue details

Stress ratio, R	0.100	
Final force, F_f	2.00	kN
Final K	20.9	$MPa.m^{1/2}$
Fatigue temperature	21.0	°C
Loading span, S	40.0	mm

Analysis details

Method of determining Load Point Displacement, q	DOUBLE CLIP
Lower knife edge height check	Warning !!! z/a > 0.2

Compiled by:	Phillip Cossey	**Signed:**

LVGENPLOT V 1.54 09-Feb-2018	Page 2 of 5	SI/FRA/F/1 Rev0.1 March 2017

SENB FRACTURE TEST 25463 M01-112

Qualification checks to	BS 7448: Part 1: 1991			Value	Allowed
(5.1.3)					
Knife edge attachment spacing		**Pass**		2.00	5.02
(6.4.5,6.4.6)					
The final fatigue precracking force <= F_f (a)		**Pass**		2.00	2.64
$\Delta K/E$ below limit (b)		**Pass**		0.003	0.010
(6.4.7)					
Initial/Final K ratio during precracking < 1.3 (a)		**Pass**		1.16	1.30
(7.5.1)					
Single roller diameter		**Pass**		8.00	3.35 - 10.04
Double roller diameter		**Pass**		8.00	5.02 - 10.04
Loading span		**Pass**		40.0	38.2 - 42.2
(8.5)					
Initial K-rate between 0.5 MPa.m$^{0.5}$s^{-1} and 3.0 MPa.m$^{0.5}$s^{-1}		**Pass**		1.04	0.5 - 3.0
(10.2.2)					
Minimum surface crack length (a)		**Pass**		4.75	4.52
Minimum crack extension at surface (b)		**Pass**		1.70	1.30
Difference in surface crack measurements (c)		**Pass**		0.10	0.72
Surface fatigue cracks in envelope (d)		**Pass**			
Crack plane within 10° (e)		**Pass**			
(10.2.3)					
Multiplane cracking (a)		**Pass**			
a_0/W check 0.45-0.55 (b)		**Pass**		0.50	0.45-0.55
Crack shape (c)		**Pass**		0.40	0.50
Minimum crack length (d)		**Pass**		1.60	1.30
(10.3)					
The stress ratio <= 0.1 (c)		**Pass**		0.10	

TWI

SENB FRACTURE TEST 25463 M01-112

Test date	27/02/2018		Client	00/01/1900	
Technician	Phillip Cossey		Project leader	Aderinkola Alabi	
Test machine	INSTRON 8500 B107		Investigator's signature		
Control mode	Displacement		Compiled by	Phillip Cossey	

Selected point coordinates for plot
0.058
0.252
0.000
8.073

SPECIMEN DETAILS

Force, F	8.07	kN
Width, W	10.040	mm
Thickness, B	10.020	mm
Crack length, a_0	4.989	mm
Loading span, S	40.00	mm
Yield strength	988	MPa
Young's modulus	215	GPa
Poisson's ratio	0.300	
Test temperature	-120.0	°C

RESULTS

δ	0.028	mm
K @ calculation point	84.5	MPa.m$^{1/2}$
F_{max}/F_Q	1.50	
K_Q	56.53	MPa.m$^{1/2}$
Total area under Force v q	1.04	kNmm
J0 from q from DOUBLE CLIP	43.44	kJ/m² (N/mm)
Plastic area Force vs q	0.34	kNmm
Type of result	δ/J_c	

Test standard(s)	BS 7448: Part 1: 1991	
Result qualified to standard(s)	YES	

Slope for clip 1	0.024031
Clip 1 offset	-0.002399
Slope for clip 2	0.037027
Clip 2 offset	-0.004405
Yfunc	2.636398
Ctod from upper clip	0.026287
Fq	5.403091
Q type	2
Number of clips	2
Area under load v Q	0.335134
Number of pop-ins	0
K Units	0
Stress units	0
E units	1
J units	0
Sample type	0
Type of result	0
Type of test	1
Hide UCAS logo	0
Graph X axis title	Clip gauge, mm

LOWER CLIP GAUGE VALUES

Knife edge height	2.50	mm
Vg	0.252	mm
Vp	0.058	mm

UPPER CLIP GAUGE VALUES

Knife edge height	8.50	mm
Vg	0.383	mm
Vp	0.084	mm

LVGENPLOT V 1.54 09-Feb-2018	Page 4 of 5

SI/FRA/F/1 Rev0.1 March 2017
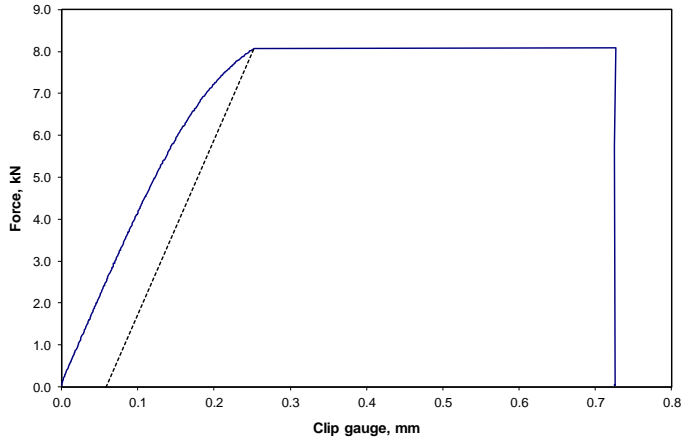
SENB FRACTURE TEST 25463 M01-112

Diagram of fracture face

Specimen width, W	10.040 mm
Specimen thickness, B	10.020 mm
Machined notch depth, M	3.060 mm
Surface crack length, a_{S1}	0.330 mm
Surface crack length, a_{S2}	4.810 mm
Net section thickness, B_N	4.750 mm
a_{max}	5.080 mm
a_{min}	4.700 mm

Comments

Measurement Line	Fatigue crack length a_0, mm	Slow stable crack extension + fatigue crack a_p, mm	Slow stable crack extension including stretch zone, Δ_a, mm
1	4.740	4.740	0.000
2	4.960	4.960	0.000
3	5.040	5.040	0.000
4	5.050	5.050	0.000
5	5.080	5.080	0.000
6	5.080	5.080	0.000
7	5.030	5.030	0.000
8	4.950	4.950	0.000
9	4.700	4.700	0.000
Weighted Average	**4.989**	**4.989**	**0.000**

Measured by: Phillip Cossey   **Signed:**

LVGENPLOT V 1.54 09-Feb-2018   Page 5 of 5   SI/FRA/F/1 Rev0.1 March 2017

HRR stress fields and the FEA QS stress fields validation for S690QL at ambient temperature under quasi-static loading condition.

E	v	σo	n	α	ln	σθθ	J20	J30	J40	J50	J70
211920	0.3	942.5	22	1	4.2	2.68	13.43042	26.439	54.283	75.63	96.14

$$\sigma_{yy} = \sigma_o\,(EJ/\alpha\sigma_o^2 Inx)^{1/(n+1)}\,\sigma\theta\theta(n,\theta)$$

20 Increment / HRR

r	σyy	σyy/σo	σyy	σyy/σo	r*σo/J
0.00	1240.64	1.32	0	0	0
0.00	1278.67	1.36	3440.14	3.65	0
0.00	1372.49	1.46	3342.11	3.55	0
0.00	1419.74	1.51	3307.06	3.51	0
0.00	1468.97	1.56	3275.82	3.48	0
0.00	1526.01	1.62	3247.48	3.45	0
0.00	1577.05	1.67	3221.50	3.42	0
0.00	1632.46	1.73	3198.54	3.39	0
0.00	1691.97	1.80	3176.54	3.37	0
0.01	1818.62	1.93	3139.32	3.33	0
0.01	1958.24	2.08	3105.45	3.29	0
0.01	2101.81	2.23	3074.67	3.26	1
0.01	2255.58	2.39	3046.57	3.23	1
0.01	2421.79	2.57	3020.60	3.20	1
0.02	2571.91	2.73	2996.38	3.18	1
0.02	2836.00	3.01	2952.26	3.13	1
0.02	2907.99	3.09	2931.97	3.11	2
0.03	2863.37	3.04	2912.66	3.09	2
0.03	2804.52	2.98	2894.21	3.07	2
0.04	2754.10	2.92	2876.51	3.05	3
0.04	2702.23	2.87	2859.43	3.03	3
0.05	2647.84	2.81	2842.90	3.02	4
0.06	2591.01	2.75	2826.85	3.00	4
0.07	2532.22	2.69	2811.20	2.98	5
0.07	2472.25	2.62	2795.92	2.97	5
0.08	2410.75	2.56	2780.97	2.95	6
0.09	2347.77	2.49	2766.30	2.93	7
0.11	2282.91	2.42	2751.90	2.92	7
0.12	2217.19	2.35	2737.72	2.90	8
0.13	2154.42	2.29	2723.76	2.89	9
0.15	2066.41	2.19	2710.00	2.88	11
0.17	1966.80	2.09	2696.41	2.86	12
0.19	1864.48	1.98	2682.98	2.85	13
0.21	1758.59	1.87	2669.71	2.83	15
0.24	1649.79	1.75	2656.58	2.82	17
0.27	1539.02	1.63	2643.57	2.80	19
0.30	1427.46	1.51	2630.69	2.79	21

30 Increment / HRR

r	σyy	σyy/σo	σyy	σyy/σo	r*σo/J
0	1469.96	1.56			
0.00032	1305.99	1.39	3645.71	3.868	0.012
0.0007	1315.16	1.40	3526.44	3.7414	0.025
0.00088	1303.43	1.38	3491.43	3.7043	0.031
0.00108	1294.39	1.37	3459.78	3.6707	0.039
0.00132	1362.43	1.45	3429.66	3.6387	0.047
0.00161	1348.48	1.43	3400.49	3.6078	0.057
0.00193	1379.98	1.46	3373.97	3.5797	0.069
0.00232	1434.64	1.52	3347.12	3.5512	0.083
0.00317	1470.72	1.56	3301.73	3.503	0.113
0.00426	1540.85	1.63	3259.69	3.4584	0.152
0.00561	1623.58	1.72	3220.91	3.4173	0.2
0.00723	1718.94	1.82	3185.70	3.3799	0.258
0.00912	1827.71	1.94	3153.62	3.3459	0.325
0.01133	1953.09	2.07	3124.05	3.3145	0.404
0.01685	2251.14	2.39	3070.57	3.2578	0.601
0.02025	2410.71	2.56	3046.14	3.2318	0.722
0.02412	2572.18	2.73	3023.02	3.2073	0.86
0.02852	2698.81	2.86	3001.10	3.1841	1.017
0.03348	2835.05	3.01	2980.24	3.1619	1.194
0.03906	2932.04	3.11	2960.32	3.1408	1.393
0.04532	2912.74	3.09	2941.27	3.1206	1.615
0.0523	2860.99	3.04	2923.00	3.1012	1.864
0.06009	2817.92	2.99	2905.41	3.0825	2.142
0.06877	2773.04	2.94	2888.41	3.0645	2.452
0.07845	2725.53	2.89	2871.92	3.047	2.797
0.08924	2675.11	2.84	2855.87	3.03	3.181
0.10127	2621.34	2.78	2840.22	3.0134	3.61
0.11468	2564.7	2.72	2824.91	2.9971	4.088
0.12961	2505.95	2.66	2809.91	2.9812	4.621
0.14626	2445.19	2.59	2795.18	2.9656	5.214
0.16481	2382.21	2.53	2780.71	2.9502	5.875
0.18548	2316.96	2.46	2766.46	2.9351	6.612
0.20852	2249.37	2.39	2752.42	2.9202	7.434
0.23418	2180.47	2.31	2738.56	2.9055	8.349
0.26278	2114.37	2.24	2724.87	2.891	9.368
0.29465	2013.06	2.14	2711.35	2.8766	10.5

Chart — σyy/σo versus Rσo/J, legend: 30 load increment; 40 load increment; 50 load increment; HRR Z=0 mm; 70 load increment.

40 Increment / HRR

r	σyy	σyy/σo	σyy	σyy/σo	r*σo/J
0	1443.99	1.53			
0.000177	1587.03	1.68	3862.40	4.097862	0.003068
0.000335	1403.81	1.49	3756.50	3.985502	0.005816
0.000342	1231.51	1.31	3753.19	3.981993	0.005935
0.000363	1081.76	1.15	3743.31	3.971508	0.006306
0.000409	1403.19	1.49	3724.04	3.951069	0.0071
0.000479	1230.7	1.31	3698.54	3.924016	0.008316
0.000577	1223.63	1.30	3668.64	3.89229	0.010023
0.00073	1358.05	1.44	3631.47	3.852851	0.012669
0.001079	1292.97	1.37	3570.18	3.787827	0.018739
0.001614	1362.66	1.45	3508.30	3.722172	0.028016
0.002399	1394.39	1.48	3448.29	3.658503	0.041662
0.003458	1441.37	1.53	3393.91	3.600811	0.06005
0.004808	1491.48	1.58	3345.63	3.549585	0.083491
0.006447	1520.8	1.61	3303.24	3.504619	0.11194
0.010602	1591.99	1.69	3232.57	3.429636	0.184086
0.01321	1662.09	1.76	3201.81	3.396999	0.229366
0.01628	1759.01	1.87	3172.84	3.366271	0.28268
0.019901	1886.83	2.00	3145.26	3.337007	0.34555
0.024153	2044.11	2.17	3118.89	3.309031	0.419376
0.02911	2212.08	2.35	3093.68	3.28228	0.505457
0.034846	2367.29	2.51	3069.58	3.256714	0.605052
0.041425	2516.57	2.67	3046.59	3.232318	0.719284
0.04891	2646.21	2.81	3024.67	3.209061	0.849241
0.057374	2778.91	2.95	3003.75	3.186868	0.996207
0.06691	2905.37	3.08	2983.74	3.165634	1.161787
0.077617	2955.42	3.14	2964.54	3.145269	1.347704
0.089595	2909.73	3.09	2946.10	3.125704	1.555685
0.102961	2866.07	3.04	2928.34	3.106865	1.787758
0.117864	2827.69	3.00	2911.18	3.088658	2.046525
0.134479	2783.45	2.95	2894.54	3.070999	2.335019
0.153003	2733.54	2.90	2878.34	3.053816	2.656659
0.17365	2678.96	2.84	2862.55	3.037055	3.015163
0.196662	2620.39	2.78	2847.10	3.020667	3.41473
0.22231	2558.27	2.71	2831.97	3.004611	3.860068
0.250893	2493.02	2.65	2817.11	2.988851	4.356367
0.282745	2425.32	2.57	2802.51	2.97336	4.909428

50 Increment / HRR

r	σyy	σyy/σo	σyy	σyy/σo	r*σo/J
0	2061	2.19			
0.000489	2446.41	2.60	3748.94	3.97749	0.006091
0.000528	1490.37	1.58	3736.42	3.964199	0.006579
0.0006	1345.09	1.43	3715.65	3.942171	0.007478
0.00064	971.212	1.03	3705.21	3.931088	0.007979
0.000664	1402.95	1.49	3699.31	3.924832	0.008276
0.000681	1113.49	1.18	3695.53	3.920606	0.008484
0.000696	1190.06	1.26	3691.73	3.916793	0.008676
0.000743	1334.62	1.42	3681.32	3.905748	0.009258
0.000844	1222.99	1.30	3661.03	3.88422	0.010513
0.001067	1314.55	1.39	3623.78	3.844701	0.013301
0.001448	1302.12	1.38	3575.99	3.793988	0.018052
0.002014	1294.64	1.37	3525.09	3.739994	0.025101
0.002807	1336.23	1.42	3474.60	3.686418	0.03498
0.003875	1389.96	1.47	3426.23	3.6351	0.048289
0.006986	1525.73	1.62	3339.54	3.543127	0.087062
0.009079	1577.27	1.67	3301.70	3.502982	0.113149
0.011579	1617.04	1.72	3266.97	3.46613	0.144308
0.014562	1655.46	1.76	3234.58	3.431765	0.181477
0.018129	1708.43	1.81	3203.91	3.399224	0.225937
0.022404	1796.17	1.91	3174.55	3.368081	0.279206
0.027497	1920.48	2.04	3146.40	3.338217	0.342679
0.033499	2070.95	2.20	3119.51	3.309682	0.417482
0.040496	2237.76	2.37	3093.89	3.282499	0.504681
0.048573	2404.58	2.55	3069.52	3.256645	0.605344
0.057806	2542.35	2.70	3046.38	3.232099	0.720402
0.068265	2659.9	2.82	3024.43	3.208813	0.850751
0.080048	2797.04	2.97	3003.57	3.186674	0.997603
0.093286	2923.05	3.10	2983.65	3.165541	1.162577
0.108123	2954.18	3.13	2964.56	3.145291	1.347484
0.124704	2899.88	3.08	2946.23	3.125841	1.554125
0.143201	2852.88	3.03	2928.57	3.1071	1.784645
0.163826	2807.73	2.98	2911.48	3.088976	2.041684
0.186819	2755.48	2.92	2894.91	3.071388	2.328235
0.21245	2697.18	2.86	2878.77	3.054267	2.647661
0.241019	2634.01	2.79	2863.02	3.037558	3.003703
0.272859	2567.03	2.72	2847.62	3.021215	3.400509

70 Increment / HRR

r	σyy	σyy/σo	σyy	σyy/σo	r*σo/J
0	2746.41	2.91			
0.000679	1484.39	1.57	3734.56	3.962229	0.006654
0.000855	1628.33	1.73	3697.23	3.922627	0.008384
0.001044	1226.49	1.30	3665.32	3.888771	0.010234
0.001146	1497.2	1.59	3650.48	3.873025	0.011235
0.001281	1097.51	1.16	3632.83	3.854303	0.012559
0.0014	1201.38	1.27	3618.83	3.839443	0.013726
0.001491	1351.62	1.43	3608.94	3.828948	0.014618
0.001597	1130.59	1.20	3598.18	3.817535	0.015657
0.001731	1323.22	1.40	3585.59	3.804175	0.016972
0.001785	1142.33	1.21	3580.86	3.799156	0.017495
0.001785	1287.35	1.37	3580.85	3.799154	0.017495
0.001898	1349.23	1.43	3571.24	3.788956	0.018611
0.002133	1307.83	1.39	3553.21	3.769826	0.020909
0.002475	1244.28	1.32	3530.30	3.745521	0.024263
0.003658	1328.61	1.41	3470.84	3.682428	0.035862
0.004554	1335.24	1.42	3437.93	3.647514	0.044647
0.005683	1379.22	1.46	3405.00	3.612574	0.055711
0.007114	1404.46	1.49	3371.89	3.577453	0.069747
0.008973	1457.97	1.55	3338.03	3.541528	0.08797
0.011433	1526.48	1.62	3303.05	3.504419	0.112087
0.014697	1621.84	1.72	3267.18	3.466361	0.144088
0.01899	1733.12	1.84	3230.98	3.42795	0.186179
0.02449	1838.42	1.95	3195.45	3.390256	0.240091
0.031256	1915.47	2.03	3161.74	3.354484	0.30643
0.039307	1990.14	2.11	3130.39	3.321224	0.385358
0.048717	2103.66	2.23	3101.31	3.290375	0.477617
0.059634	2239.22	2.38	3074.17	3.261577	0.58464
0.072219	2387.03	2.53	3048.68	3.234537	0.708018
0.086588	2503.64	2.66	3024.72	3.209118	0.848895
0.102827	2655.11	2.82	3002.20	3.185224	1.008098
0.121065	2791.64	2.96	2980.96	3.162692	1.1869
0.141517	2919.06	3.10	2960.80	3.141301	1.387408
0.164423	2937.42	3.12	2941.55	3.120878	1.611975
0.19001	2865.22	3.04	2923.11	3.101314	1.862825
0.218549	2794.87	2.97	2905.38	3.082502	2.142617
0.250365	2725.73	2.89	2888.26	3.064341	2.454535

Published papers

Journal of Constructional Steel Research

Contents lists available at ScienceDirect

Journal of Constructional Steel Research

ELSEVIER

Tensile behaviour of S690QL and S960QL under high strain rate

A.A. Alabi [a,b,*], P.L. Moore [c], L.C. Wrobel [a], J.C. Campbell [a,b], W. He [d]

[a] Department of Mechanical and Aerospace Engineering, Brunel University London, Uxbridge, UK
[b] National Structural Integrity Research Centre (NSIRC), Granta Park, Great Abington, Cambridge, UK
[c] TWI Ltd, Granta Park, Great Abington, Cambridge, UK
[d] Lloyds Register Global Technology Centre, Southampton, UK

A B S T R A C T

Despite offering significant strength-to-weight advantages, high-strength structural steels, such as S690QL and S960QL, are used only in limited offshore applications. This is due to the lack of material characterisation in regard to their tensile behaviour, with little data available on loading rates other than those typically experienced offshore. The concern is that high strength structural steels with high yield-to-tensile ratio >0.90 are obtained at the expense of ductility and strain-hardening capacity. In this paper the tensile properties from two high strength structural steels were studied and characterised over a range of strain rates and, the results are compared against the performance of mild steel. High strength structural steels with yield-to-tensile ratios in excess of 0.90 were significantly less sensitive to the effect of strain rate than mild steel with yield-to-tensile <0.85 at ambient temperature. The yield stress of S690QL and S960QL moderately increase to about 9% and 6% respectively from quasi-static to 100 s^{-1} strain rate, which is within typical strain rates encountered in primary offshore structural applications.

© 2018 Elsevier Ltd. All rights reserved.

1. Introduction

The main driving force in the development and usage of high strength structural steel (HSSS) in offshore applications is the need to reduce weight and cost over structures manufactured from conventional low strength structural grades. Modern production routes for HSSS grades deliver high yield strengths, but with much higher yield-to-tensile (Y/T) ratios than in lower strength structural steel grades (LSSS). This high Y/T ratio results in existing standards lacking clear guidance for the application and performance of modern high strength steel. Eurocode 3 (Design of Steel Structures), EN 1993: Part 1–12 [1] recommends a limit of 0.95 Y/T ratio, whereas the UK National Annex of the same standard proposed a value of 0.91 [2] due to lack of confidence regarding the performance of HSSS with high Y/T ratio in the standards. Most design codes and standards relate the design formulae to mild strength steel with low Y/T ratio < 0.85 and yield strength <500 MPa for offshore design requirement [3,4], limiting the overall usage of HSSS in offshore steel structural applications. This is because the performance of LSSS is well established, and also provides an enhanced safety margin (a proportion of the yield strength against the ultimate tensile strength) with which the same confidence with HSSS is not known. A concern is that higher yield strength with Y/T > 0.9 may be obtained at

the expense of ductility and strain-hardening capacity, compromising the post-yield strength upon which design criteria depend when compared to LSSS with Y/T < 0.8 [4,5]. As confidence in the characterisation and performance of steels with Y/T ratios in excess of 0.90 is established, they will become more accepted into design codes and standards. HSSS would then be exploited for its strength, but not rely on its ability to deform or locally yield under extreme loading because HSSS steel structures offer significant benefits which include a greater reduction in capital cost (economy), improved mechanical properties (safety), and development of special aesthetic and elegant designs with reduced structural section (architecture).

Hence, the motivation of this research is to reverse the under-utilization of HSSS for various applications through developing a better understanding and characterisation of the behaviour of HSSS grades with high Y/T ratios >0.90 under different loading conditions and determine their sensitivity to in-service loading rates, such as those given in Table 1 where there is a chance of reduced ductility at dynamic loading rates. For example, Eurocode 3 (Design of Steel Structures) now has an extension up to S700 (S690QL equivalent) in EN 1993: Part 1–12 [1] due to the need to reduce weight with increased strength capacity, coupled with the cost effectiveness. This standard allows S700 utilization but with a limitation of Y/T ratio between 0.91 and 0.95 for bridges, buildings and other steel structures [1,2].

Compared with other published data and experimental results from conventional low strength carbon steel tensile tests, modern high strength steel possesses a different stress-strain characteristic, reduced

---

* Corresponding author at: National Structural Integrity Research Centre (NSIRC), Granta Park, Great Abington, Cambridge CB21 6AL, UK.
  E-mail address: aderinkola.alabi@brunel.ac.uk (A.A. Alabi).

Table 1
Typical strain rates in some engineering components. Data from [11–13].

Application	Strain rate $(\dot{\varepsilon})$ s^{-1}
Storage tanks, buried pipelines, pressure vessels	10^{-6} to 10^{-4}
Self-weight, wind and wave loading	10^{-4} to 10^{-2}
Bridges, cranes, earthmoving	10^{-2} to 0.1
Earthquake loading, marine collisions	0.1 to 10
Land transport, aircraft undercarriage	10 to 10^3
Explosion, ballistics	10^4 to 10^{6+}

Table 2
Treatment of Y/T ratio in accordance with various design codes taken from [1,2,4,22].

Code	Limitation (YS as proportion of UTS)	Application
API 2A-WSD	0.67	Tubular joints, 500 MPa
	0.80[a]	$< \sigma_y \leq 800$ MPa
HSE guidance notes (offshore)	0.70	Tubular joints
BS 5950 (buildings)	0.84	All components
NS 3472 (NPD) (offshore)	0.83	All components
EC3 (buildings, bridges and other steel structures)	0.91[b]/0.95	All components ($\varepsilon_{UTS} \geq 15\sigma_y/E$)
DnV (offshore)	0.85	Except tubular joints
	0.75	Tubular joints ($\sigma_y > 500$ N/mm^2)
AISC (buildings)	0.90	Grade 50 ksi beams

[a] New Y/T ratio for joints provided adequate ductility is demonstrated in both HAZ and parent metal [4].
[b] Recommended Y/T ratio in the UK National Annex to Eurocode 3 [2].

elongation and low strain-hardening capacity and, generally, has high Y/T ratio [6,7]. In addition, very little information is available on the performance of HSSS (specifically, with Y/T in excess of 0.90) subjected to high loading rate scenarios. It is noteworthy that the effect of high loading rates is generally known to affect the strength and fracture performance of steels [8–17]. Invariably, the effect of loading rates on the tensile properties or strength of a steel is predicted to be specifically dependent on a particular steel grade [8,9] with the sensitivity depending on the strength level itself. The degree of sensitivity, however, on the low strength carbon steels is high compared to quenched and tempered and High Strength Low Alloyed (HSLA) steels, which are relatively unaffected [10]. Typical examples of engineering loading rates expressed in terms of strain rate are given in Table 1. These values are taken from the information given by [11–13], and should be used as estimates only since the exact values will depend largely on loading configuration, local geometry, and flaw dimensions [12]. Whilst the fracture mechanical loading rate is mostly expressed in terms of stress intensity factor loading rate for linear elastic conditions, the loading rates in structural engineering are usually considered in terms of strain rates [8]. Therefore, for the purpose of this paper, loading rates in terms of strain rate have been considered.

The effect of loading rates on the tensile properties of typical high strength structural steels, namely S690QL and S960QL, produced via quenched and tempered (QT) processing routes has been studied. The degree of strain rate sensitivity is compared with the performance of low strength conventional structural steel, S235 at ambient temperature. It should be noted that the main purpose of this work is to study

the tensile behaviour of HSSS with high Y/T ratio > 0.90 and not LSSS grades with low Y/T ratio < 0.80. The conventional structural steel S235 was used as an example of low Y/T ratio grade that has been previously well characterised for dynamic behaviour, although not used significantly in offshore applications. The findings and data generated would help to better understand the structural performance of HSSS with high Y/T ratio and, thus, reduce the misconceptions of its performance in design guidelines and in-service.

2. Review of strain rate effects on the tensile properties of structural steels

The major strain rate effect on the tensile properties of steel is the amplification of the yield and tensile strengths, considered as a positive strain rate dependence [12]. On the other hand, the increment could result in a shift in the Ductile-to-Brittle Transition Curve (DBTC) leading to a reduced fracture toughness value at the lower shelf as a result of material strengthening during an increase in strain rate (negative strain rate dependence) [8,12]. The behaviour of carbon steels at high strain
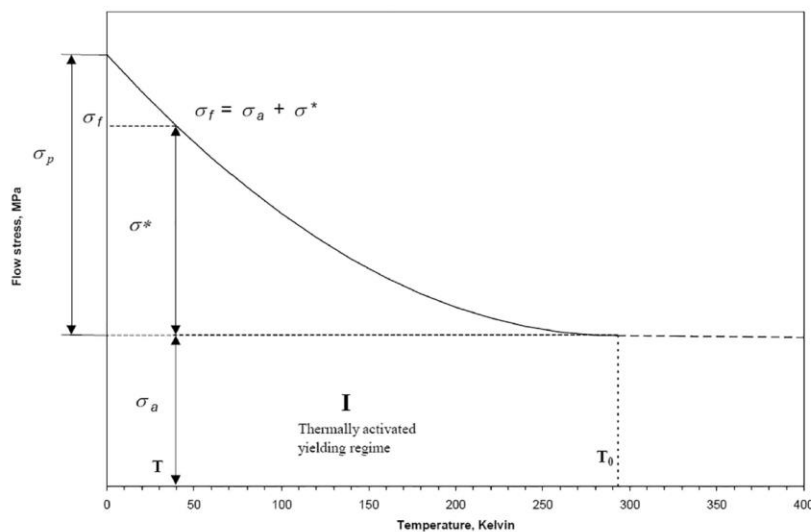

Fig. 1. Flow stress partitions of an effective stress and internal stress with temperature of interest less 300 K [13]. Courtesy of TWI Ltd.
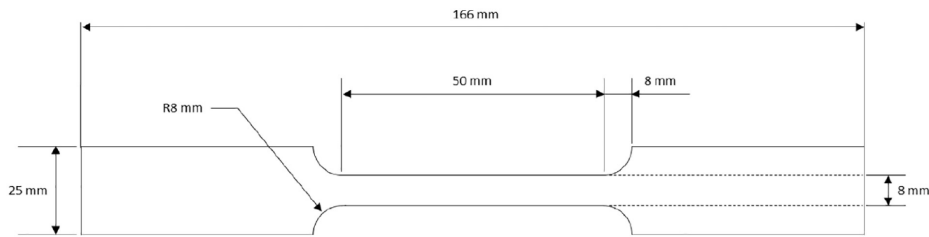
248

Fig. 2. Quasi-static tensile test specimen geometry. Courtesy of TWI Ltd.

rates shows that both the upper and lower yield stresses and strains increase with increasing strain rates [9]. However, the ultimate stress and strain are less sensitive at high strain rates, whereas the strain at initiation of strain hardening is the most sensitive parameter to the effect of strain rate [9]. Another important aspect of strain rate effect on the tensile properties of steel is the temperature dependence. The effect of high strain rate and consequently, the dynamic amplification on yield strength is temperature dependent, being increased at lower temperature [8–10,12–18]. In general terms, the yield strength of a particular material under dynamic loading (high strain rate) is strain rate and temperature dependent, linearly related to the logarithm of the strain rate and inversely proportional to the absolute temperature as expressed in Eq. (1) [10].

The dynamic yield strength was observed to be equal to the static yield strength plus a factor which causes an increase (or decrease) in the tensile properties called the dynamic over stress [10]. The dynamic over stress is temperature dependent and implies that at low temperature, the dynamic over stress increases owing to the strain rate effects, but decreases with thermal softening at high temperature.

$$\sigma_{yd} = \sigma_y\,(T, \dot{\varepsilon}) \approx \frac{\ln(\dot{\varepsilon})}{T} \qquad (1)$$

This is explained by the mechanism of thermal activation of dislocations over short-range barriers [13,18]. Since a dislocation is obstructed in its movement by the interstitial atoms (such as, carbon, nitrogen, boron or hydrogen) or grain boundaries in steel, it means that a higher force is required to overcome this obstruction. A stress (flow stress) is required to sustain plastic deformation by moving dislocations via both short and long range barriers, with its magnitude depending on the temperature [13]. Over short-range barriers, there exists an initial stress large enough to enable the dislocations to move past these barriers without the aid of thermal fluctuations associated with yield stress at absolute zero temperature. It follows that at stresses greater than the initial stress, the barriers are ineffective and the strain rate is then controlled by a different mechanism (dissipative mechanism), such as the interaction of dislocations with electrical and thermal waves in the crystal lattice [18]. If deformation is thermally activated Fig. 1, the effective stress σ^* is strain rate and temperature dependent due to short-range

barriers that can be cut or passed by thermal activation, which is characterised by activation enthalpy, Eq. (2) [13].

The value of flow stress can therefore be characterised varying from a maximum value ($\sigma_p + \sigma_a$) to an athermal internal stress value σ_a at temperature T_0, Fig. 1 [13]. At athermal (long range barriers) condition, the increased amplitude of atomic thermal vibrations produces an effective vibration of the dislocation line, and this permits it to cut through barriers that could not be bypassed by the stress alone and, thus σ_a is not temperature or strain rate sensitive [13,19]. From Eq. (2), flow stress as a function of strain rate and temperature can therefore be written as Eq. (3) [13].

$$H = kT\,\ln(A/\dot{\varepsilon}) \qquad (2)$$

$$\sigma_f = \sigma_a + \sigma_p\left\{1 - \frac{kT\,\ln(A/\dot{\varepsilon})}{H_0}\right\}^{\frac{1}{1-m}} \qquad (3)$$

where:

σ_a = internal stress, MPa
σ_p = Peierls stress (MPa) at $T = 0$ in K
k = gas constant, $1.38E^{-23}$ JK^{-1}
T = temperature in K
A = frequency factor taken as 10^8
$\dot{\varepsilon}$ = strain rate s^{-1}
H_0 = activation enthalpy associated with local barriers in J
m = material constant.

Temperature rise is inherent at high strain rates owing to the short time available to conduct the heat generated during plastic work deformation in which there is no significant local heat exchange with the environment (adiabatic effect). Whereas, at low or quasi-static strain rates, the heat conduction time increases and thus, operates solely on a non-adiabatic condition because of the available time for heat conduction, leading to a lower rise in temperature [17,20]. Considering this fact, the strength model developed by Johnson-Cook [21] shows that in all cases (strain rates at $1\,s^{-1}$, $10\,s^{-1}$, $100\,s^{-1}$), the adiabatic stress-strain curve increased to a maximum then decreased with increasing strain.
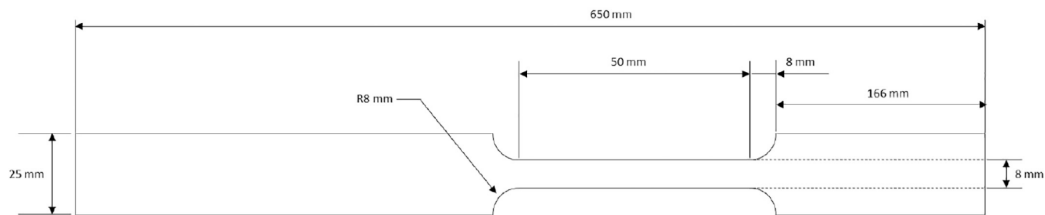

Fig. 3. Dynamic tensile test specimen geometry for strain rate above $4\,s^{-1}$. Courtesy of TWI Ltd.
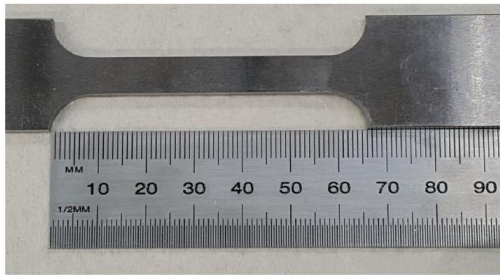
Fig. 4. Photograph of specimen before test. Courtesy of TWI Ltd.

Table 3a
Chemical composition of S690QL 25 mm plate (%).

Element	C	Si	Mn	P	S	Ni	V	Nb	CEV
% (m/m)	0.14	0.29	1.19	0.008	<0.002	0.084	0.031	0.016	0.42

Table 3b
Chemical composition of S960QL 60 mm plate (%).

Element	C	Si	Mn	P	S	Ni	V	Nb	CEV
% (m/m)	0.16	0.21	1.39	0.008	<0.002	0.077	0.021	0.013	0.55

At approximately strain rate beyond 0.1 s^{-1}, adiabatic deformation dominates [17]. Whether this has significant impact on the flow stress of HSSS compared to LSSS at room temperature is a point of discussion in this paper.

3. Significance of Y/T ratio on the structural design and performance of HSSS

In engineering terms, the Y/T ratio provides the basis for measuring the deformation (strain-hardening) capacity of a material which normally increases as the static yield strength increases. This is related to the strain-hardening exponent (n), which is used to qualify the plastic deformation performance of a metal [22,23]. Usually, a higher Y/T ratio leads to a decrease in yield point elongation (Lüders Plateau) and decrease in strain-hardening exponent [22]. It means that steels with low Y/T ratios, typically in the range 0.5 to 0.85, associated with conventional low and medium strength steels have high strain-hardening exponent (extra safety margin). Whereas, modern high strength steels inherent with high Y/T ratios in excess of 0.90 exhibit low strain-hardening exponent. Hence the treatment and limitation of high Y/T ratio in design codes, Table 2, based on the notion that a high Y/T ratio connotes a poor fracture performance [24].

In principle, for designs based on elastic loading, i.e. stresses kept below yield, the strain-hardening characteristics beyond yield should not matter strongly in the design. This conventional approach has guided the traditional structural design methodologies where the working stress is usually taken as a proportion of the yield stress, with typical values around 60% of yield strength in normal loading and up to 80% in severe loading [5]. This concept ensures that load resistance falls within the linear region of the stress-strain curve of the component, making the Y/T ratio irrelevant in such elastic case. More recently, plastic design concepts have been incorporated. This design approach is an additional safety precaution in steel structures in which the structure is able to yield (absorb energy) and redistribute load (work hardening) without

major failure or total collapse. This design methodology has helped shape modern structural designs in defining, assessing and determining the mechanical response of steel structures under different loading conditions. In this case, the Y/T ratio becomes applicable in the post-yield behaviour of steel. Therefore, in engineering terms, the Y/T ratio can be said to be the parameter which represents the ability to withstand plastic loading and the basic measure of deformation capacity of a material [5].

Studies [7,22–27] show that the application of high Y/T ratio in HSSS has been successful in some bridge and building applications but limited in other engineering applications (especially offshore applications) due to the lack of characterisation data on their structural performance. Although the Y/T ratio only becomes relevant in the post-yield behaviour of steels, which represents the ability to withstand plastic loading and basic measure of deformation capacity, other related characteristics such as strain-hardening exponent, ductile tearing resistance, and overall global deformation are important factors to consider when considering the practicality of using high Y/T ratio as a measure of plastic strain capacity of cracked components [23].

Therefore, the successful application of HSSS with high Y/T ratio in bridges and buildings means HSSS can exploit its strength, but not rely on its ability to deform or locally yield under extreme loading.
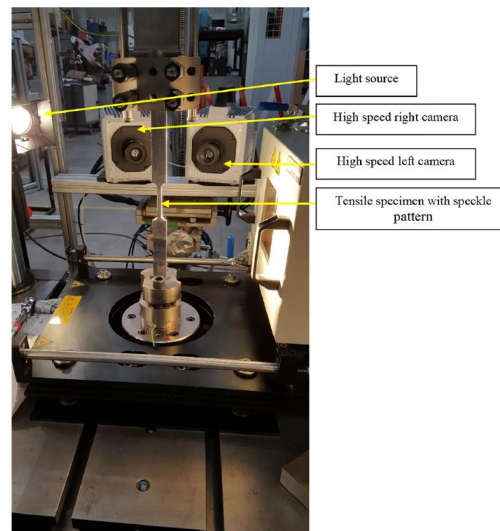

Fig. 6. DIC system setup with the VHS test machine with view from behind (facing the camera). Courtesy of TWI Ltd.

Fig. 5. Photograph of specimen after test. Courtesy of TWI Ltd.

4. Experimental methods

4.1. Materials and specimen geometries

In this paper, a program of tensile testing was developed to provide characterisation data for two high strength structural steels S690QL (WELDOX 700 EZ) and S960QL (WELDOX 960HZ) with high Y/T ratios in excess of 0.95 at a range of strain rates. The as-received delivery properties was in accordance with BS EN 10025:6+A1 (2009) [28]. According to the standard, 690 MPa is the minimum yield strength and 940 MPa as the maximum tensile strength for nominal thickness ≤ 50 mm for S690QL. Since production route and/or chemical compositions have less effect on the tensile strength, the production process have incremental effect on the nominal yield strength when strength-to-weight ratio is important, hence the high Y/T ratio that comes with it. This is discussed in Sections 1 and 5.3.

The data generated was compared with that of low strength structural steel (S235) as a representative of LSSS which has Y/T ratio < 0.80. For the purpose of easy machining, comparison and setup during quasi-static and high strain rates tension tests, flat dog-bone shaped tensile specimens were employed. The choice of flat dog-bone specimens was informed due to the recommended specimen geometry for the high speed dynamic fast jaw grip hydraulic machine. In order to make sure that the collapse load falls within the machine capacity (100 kN), the ratio between the width of the gauge area (W_a) and the shoulder width (W_s) was set at <0.33.

Also, for a better understanding and comparison of the change of the mechanical behaviour of the materials over a range of strain rates, the aspect ratio (ratio between the width and the 3 mm specimen thickness) was kept constant. The specimen geometries employed during the quasi-static and high strain rates tensile tests are shown in Figs. 2 and 3, and photographs of specimens before and after the test are
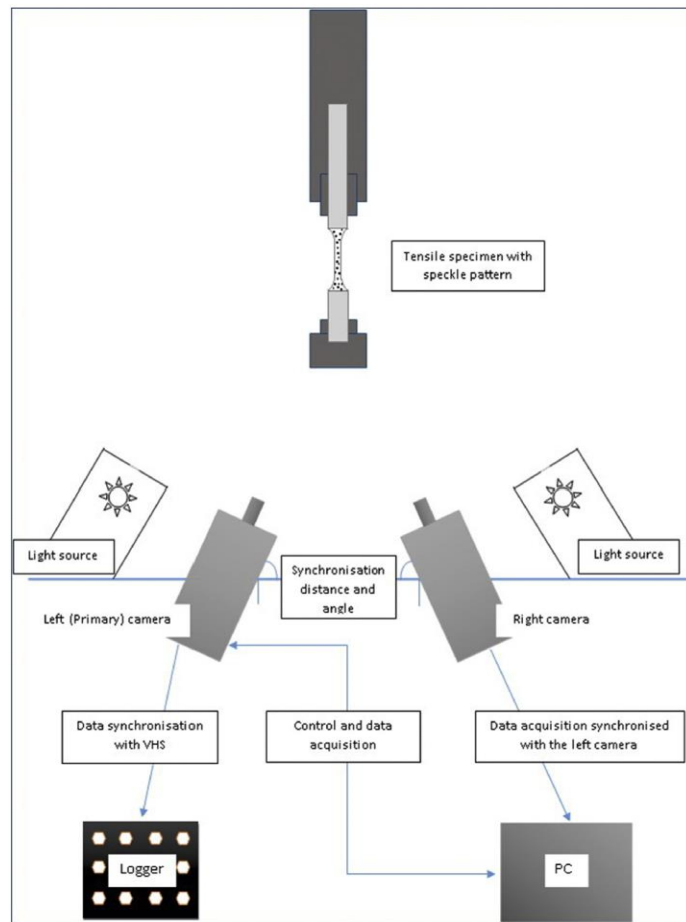

Fig. 7. A simple schematic representation of the DIC setup and framework with the VHS machine. Courtesy of TWI Ltd.

shown in Figs. 4 and 5 respectively. It is worth pointing out that the specimen type for the high strain rate tests requires one end to be longer, because of the testing machine requirement discussed in Section 4.2. A total number of 18 specimens each were investigated for both materials. Specimens were prepared from S690QL and S960QL high strength steel plates, with load axis aligned with the rolling direction.

The choice of taking the samples in the rolling (parallel) direction was made because it is more conservative (with slightly lower differences in the yield stress) compared to samples taken in the transverse (perpendicular) direction [17]. It should be noted that the S690QL and S960QL specimens were machined from the as-received plate and supplied in thicknesses of 25 mm and 60 mm respectively. The grade designation stands for the following:

S – Structural Steel

690 – Minimum Yield Strength (MPa)
Q – Quenching and Tempering (Production process)
L – Low Notch Toughness Testing Temperature (Impact energy at minimum temperature).

The chemical compositions of the materials are summarized in Tables 3a and 3b.

4.2. Setup and test procedures

Dynamic tests require a special machine capable of high speed loading and data recording along with skilled and experienced personnel for the experimental procedures and setup. This has made dynamic testing over the years very expensive and, as such, has made quasi-static testing conditions generally accepted for design purposes. This is why most offshore and marine structures such as ships and fixed structures are often designed for quasi-static loading conditions despite that there are occasions when dynamic loading such as impact from ship collision or dropped objects could affect the response of the structure. It is therefore imperative to quantify the mechanical response in terms of in-service loading conditions since structures do not always operate under quasi-static loading conditions. To bridge this gap, tests were carried at quasi-static and in-service loading rate scenarios, especially those experienced by offshore cranes (Table 1). Instron Machine B909 was employed for tests from quasi-static up to 4 s^{-1} strain rates with the use of extensometer and load cell to measure the stress-strain characteristics of the material at room temperature. Tests above 4 s^{-1} strain rates were carried out at room temperature on an Instron VHS 160 Dynamic Test Machine. The machine is a special dynamic testing machine with capacity of 100 kN with speed up to 20 m/s, utilising advanced servohydraulic and control technologies alongside patented FastJaw gripping techniques. The gripping techniques require one end of the flat tensile specimen longer than the other in order to give room for travel. All tests were performed at TWI, Cambridge.

To maintain accuracy and precision at strain rate above 10 s^{-1}, high speed recording equipment is required. The use of a Digital Image Correlation (DIC) system has proven to be a suitable option for the measurement of the strain profile experienced by the specimen under high loading conditions. Since the purpose of the test is to determine the effects of high loading rates in terms of strain rate, DIC was employed with the VHS high speed test machine. The DIC system is calibrated to measure within a certain measuring volume which takes a trigger pulse from the VHS test machine to start the camera and data logger. The DIC system required a high speed camera to capture about 70,000 frames/s number of data points along the gauge length of the specimen. The camera setup (field of view used, frame rate and standoff distance) all contribute to the number of data points. The setup of the test machine and DIC system is shown in Figs. 6 and 7, respectively. For the purpose of this paper emphasis will be made on tests from quasi-static up to 100 s^{-1} strain rates and at ambient temperature.
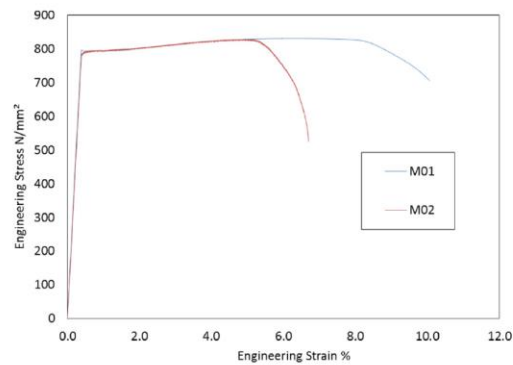

Fig. 8. Effect of specimen geometry on S690 at quasi-static loading condition. Courtesy of TWI Ltd.

In order to achieve the required overall precision, it is noteworthy that the experience of the technician played an important role. Whilst the use of DIC at high loading rate required skilled and experienced personnel, the test-setup and accuracy at strain rate below 10 s^{-1} also require a well calibrated machine, experienced personnel and accurate stress-strain measurements (with the use of an extensometer attached to the specimen gauge length). At the end of each test, both cross-section reduction and gauge length extension were measured.

5. Results and discussion

5.1. Initial uniaxial tensile test results on S690QL at quasi-static strain rate

Initial uniaxial tensile tests at room temperature were carried out to determine how material geometry and/or cross-sections affect the overall plastic deformation (uniform and localised) under quasi-static condition as shown in Fig. 8 using designations M01 and M02 to represent samples with cross sectional areas 24 mm^2 and 38 mm^2, respectively. Within the elastic limit, no notable change is observed but a significant difference is noticed in the plastic work. Although for low cross sectional area (M01) a reduced value of about 20% in strain-hardening exponent (n) compared to high cross sectional area (M02) is obtained as shown in Table 4, there is a similarity in the plastic work shape prior to necking. A low cross section gave enhanced percentage reduction in area after necking (non-uniform plastic work deformation or local elongation). The Y/T ratio in Table 4 is taken as the ratio of the 0.2% proof stress and ultimate tensile strength from engineering stress-strain curve. Also, the linear fit from the logarithmic relationship of the true stress-strain curve ($\sigma = K\varepsilon^n$) where σ is the stress, ε is the strain, n is the strain-hardening exponent and K is the strength coefficient represents the value of the strain-hardening exponent used for the analysis. These definitions and approach to determining the values of Y/T ratio and n have been employed in this paper.

Table 4
Effect of specimen geometry on strain-hardening exponent (n).

Specimen no	CSA[a]	Strain-hardening exponent (n)	Y/T ratio	Strain rate (s^{-1})
M01	24 mm^2	0.044	0.956	2×10^{-4}
M02	38 mm^2	0.053	0.955	2×10^{-4}

[a] CSA is cross sectional area.

Fig. 9. S235 result at strain rate of $100\,\mathrm{s}^{-1}$. Courtesy of TWI Ltd.
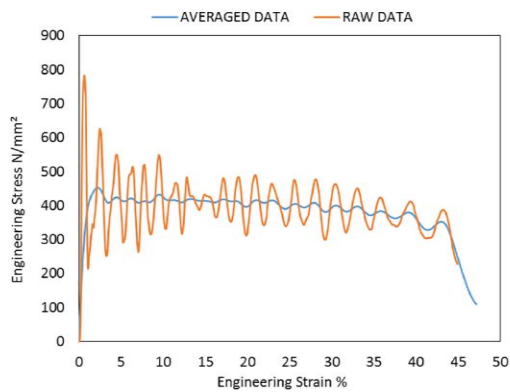

Fig. 11. S960 result at strain rate of $100\,\mathrm{s}^{-1}$. Courtesy of TWI Ltd.

The result means that elongation and reduction in area is a measure of different responses in the mechanical behaviour of a material and should not be generalized as a means of measuring ductility. Uniform plastic elongation is highly influenced by plastic work hardening, whereas reduction in area is a representation of a local plastic work deformation before fracture. As such, reduction in area is influenced by the necking process and is the most structure-sensitive ductility factor in detecting quality changes in a material behaviour after necking [29,30]. Therefore, the extent of plastic work deformation does not only depend on the strain-hardening curve but also depends on the specimen geometry and the shape (cross sections) prior to necking formation.

Specimens with a cross sectional area of 24 mm^2 are used for all subsequent tests so that comparisons could be made at different strain rates, but conclusions based on absolute values cannot be drawn.

5.2. Characterisation of S690QL and S960QL

Based on the initial tests, comprehensive uniaxial tensile tests were performed to characterise the mechanical behaviour of S690QL and S960QL high strength structural plates at a range of strain rate up to $100\,\mathrm{s}^{-1}$. Strain rates from quasi-static (QS) (0.0002 s^{-1}) to high/dynamic (~100 s^{-1}) extend over the primary strain rate range encountered in an offshore or marine in-service conditions, Table 1. Yield

stress is defined as the 0.2% proof strength for all samples, to enable the yield-to-tensile ratio to be determined. Information regarding offshore structures in-service scenarios under normal and high strain rate conditions revealed that time at maximum force could be around 1.3 s and 0.25 s, respectively [11]. For the tensile tests carried out, the corresponding time to maximum force and fracture at 1 s^{-1} strain rate (the critical strain rate for offshore cranes) falls around 0.08 s and 0.12 s, respectively. This is slightly lower but similar to those given by Walters et al. [11] for offshore structures. Based on this understanding more emphasis will be made for strain rates from QS to 4 s^{-1}, however discussion will still include the strain rate at 100 s^{-1}.

It is worth noting that the measurement of load signal at 100 s^{-1} was challenging due to the requirements for accuracy and precision. DIC was employed for this purpose and the results from tests at 100 s^{-1} strain rate are presented in Figs. 9, 10 and 11 for LSSS (S235) and HSSS (S690 and S960), respectively. The raw data represents the load cell signal syncronised with the reading from the DIC. The strain measurement was taken from the DIC, which records the strain profile on the sample. Due to the imbalance between the internal and external forces during high strain problems, the load signal was noisy as a result of stress wave propagation developed during the test. To reduce the noise in the data, averaged data using moving average technique in
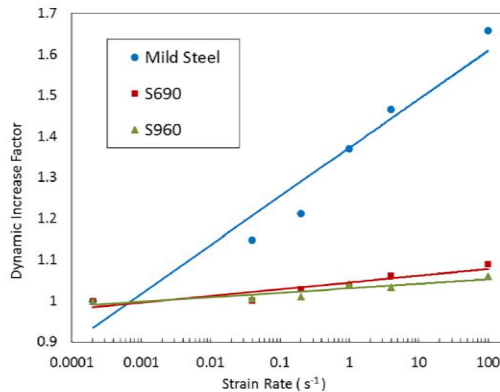

Fig. 10. S690 result at strain rate of $100\,\mathrm{s}^{-1}$. Courtesy of TWI Ltd.

Fig. 12. The effect of strain rate on the yield true stress of S235, S690 and S960 from QS to $100\,\mathrm{s}^{-1}$. Courtesy of TWI Ltd.
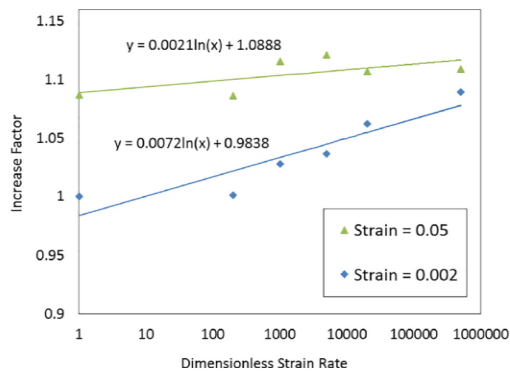
Fig. 13. Flow stress increase factor (σ_d/σ_0) dependence on the dimensionless strain rate ($\dot{\varepsilon}_p/\dot{\varepsilon}_0$) for S690. Reference strain $\dot{\varepsilon}_0$ taken as $2 \times 10^{-4}\,s^{-1}$. Courtesy of TWI Ltd.
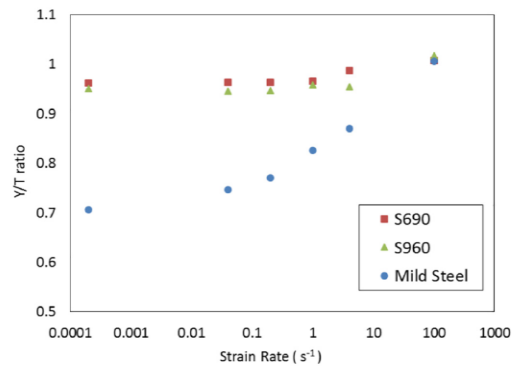

Fig. 15. The effect of strain rate on the Y/T ratio of mild steel and high strength steels. Courtesy of TWI Ltd.

matlab was employed and, this was used to quantify the effect of strain rate at $100\,s^{-1}$ for the three materials under consideration.

The results show that the dynamic amplification as a result of strain rate effect on the yield stress of LSSS with Y/T ratio < 0.8 (S235) is high. The degree of sensitivity of HSSS with Y/T ratio > 0.95 (S690QL and S960QL) is relatively unaffected by the strain rate effect. About 66% amplification was observed on the yield stress of low strength steel (S235) from quasi-static to $100\,s^{-1}$ strain rates. This is an equivalent of about 1.66 dynamic increase factor as shown in Fig. 12. On the other hand, this effect (strain rate sensitivity) is less notable on the HSSS (S690QL and S960QL) whose dynamic amplification effect on yield stress from QS to $100\,s^{-1}$ is <10%. This is due to the fact that the degree of sensitivity of steel decreases with increasing nominal yield strength. For this reason, the metallurgical and production techniques used to achieve the strength level of S690QL and S960QL were studied and discussed in the next section. Also noted is the high sensitivity of the strain at the initiation of strain hardening. This shows that the degree of sensitivity is high at 0.2% proof stress or zero plastic strain. Since yield strength is linearly related to the logarithm of the strain rate [10], it follows that a semi-logarithmic graph can be used to represent the flow stress increase factor dependence on dimensionless strain rate, Figs. 13 and 14, using Eq. (4) [17,21]. The sensitivity decreases as the plastic strain

increases at ambient temperature.

$$F = 1 + C \, \ln(\dot{\varepsilon}^*) \qquad (4)$$

where:

F = flow stress increase factor σ_d/σ_0
C = sensitivity parameter.
$\dot{\varepsilon}^*$ = dimensionless strain rate $\dot{\varepsilon}_p / \dot{\varepsilon}_0$

The Y/T ratio only becomes relevant in the post-yield behaviour of steels, which represents the ability to withstand plastic loading and as a measure of deformation capacity. Designs based on elastic loading, i.e. stresses kept below yield, the strain-hardening characteristics beyond yield should not matter strongly in the design. Fig. 15 shows that the Y/T ratio for S235 grade mild steel increased from around 0.7 at quasi-static loading rates, steadily up to around 1 at $100\,s^{-1}$. The S690 and S960 Y/T ratio kept fairly constant, ranging between 0.95 and 1 throughout the strain rate range tested. Also, since the strain-hardening exponent (n) determines the plastic deformation performance of steel, the strain-hardening exponent was determined using the power law approach ($\sigma = K\varepsilon^n$). A downward trend was observed on the n value
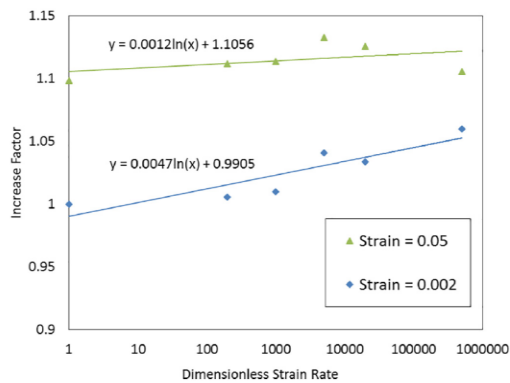

Fig. 14. Flow stress increase factor (σ_d/σ_0) dependence on the dimensionless strain rate ($\dot{\varepsilon}_p/\dot{\varepsilon}_0$) for S960. Reference strain $\dot{\varepsilon}_0$ taken as $2 \times 10^{-4}\,s^{-1}$. Courtesy of TWI Ltd.
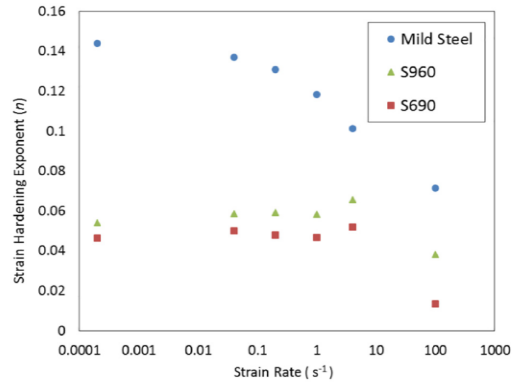

Fig. 16. Effect of strain rate on the strain-hardening exponent (n) of LSS (mild steel) and HSSS. Courtesy of TWI Ltd.
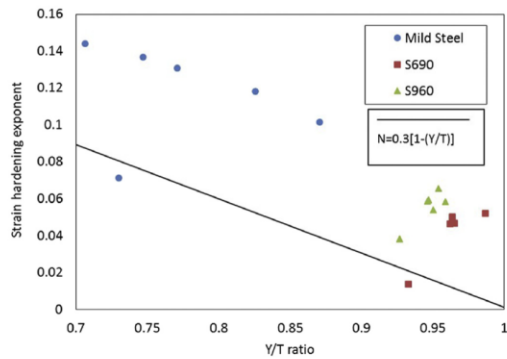
Fig. 17. A conservative lower bound fit for calculating strain hardening exponent (N) from Y/T ratio using SINTAP approach, Eq. (5) [24]. Courtesy of TWI Ltd.
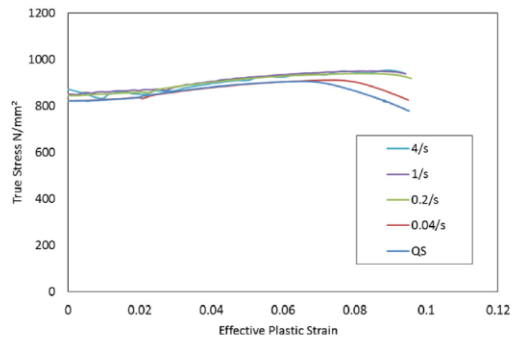

Fig. 19. Flow stress for S690QL generated up to 4 s^{-1} strain rate. Courtesy of TWI Ltd.

of S235 as the strain rate increases from QS to 100 s^{-1}. For the HSSS (S690 and S960), n kept fairly constant at up to 4 s^{-1} strain rate but dropped at 100 s^{-1}, Fig. 16. A relationship between Y/T ratio and n has been developed [23–24]. The expression in Eq. (5) provides a conservative lower bound fit for calculating n from Y/T ratio, Fig. 17, where N represents strain-hardening exponent. From Fig. 17, it is important to point out that the materials may look the same, but they are not of the same tensile properties. S690QL, delivered in 25 mm thickness has nominal yield strength of about 817 MPa and 0.96 Y/T ratio, whereas and S960QL delivered in 60 mm has nominal yield strength of about 906 MPa and Y/T ratio 0.95. This is important to point out because it would help the users to have clear information about the tensile performance of these steel grades with varying thickness delivery conditions.

$$N = 0.3[1 - (Y/T)] \tag{5}$$

The flow stresses of S690QL and S960QL from QS up to 4 s^{-1} are shown in Figs. 19 and 20, respectively, with increased ductility at moderately high strain rates. This is compared with mild steel (S235) as shown in Fig. 18. The effective plastic strain here is the total true strain minus the recoverable strain (ratio of true stress and elastic Young Modulus). It is worth pointing out that, from Figs. 19 and 20, the material
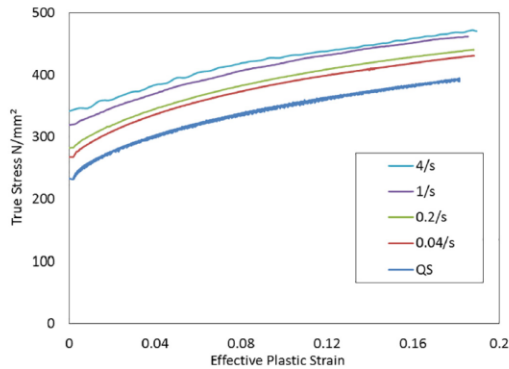
shows peak effect as the strain rate increases, and this is not considered in the analysis as 0.2% proof stress was taken as the yield strength for all.

5.3. Metallographic examination

Traditionally, alloying elements such as carbon and manganese added to steel increase nominal yield strength, with detrimental effects on the fabrication properties of steels, in particular, weldability. To avert this effect, carbon contents in modern steels are limited, along with a high degree of cleanliness and typical sulphur and phosphorus levels of <0.005% and <0.010% respectively implemented for good toughness and through-thickness homogeneity [25]. Modern production routes such as Quenched and Tempered (QT), Thermomechanically Controlled Rolled (TMCR) or Accelerated Cooled (AC/TMCP) were developed to promote fine-grained and homogeneous structures with higher strength, thereby improving the combination of strength level and toughness in modern and high performance HSSS. These production processes and/or compositions have less effect on the ultimate tensile strength but an incremental effect on the nominal yield strength, and consequently high Y/T ratio. The increase in nominal yield strength of steel predominantly achieved via alloying and heat treatment, affect the degree of sensitivity to strain rate because of the fine-grain size achieved during the process. Metallographic examination was carried out to determine to some extent the effect of grain size on the strain rate sensitivity. The metallographic examination shows a variation in grain size of the three materials (S235, S690 and S960) under consideration. It is seen that the examination from S235 micrograph, Fig. 21,
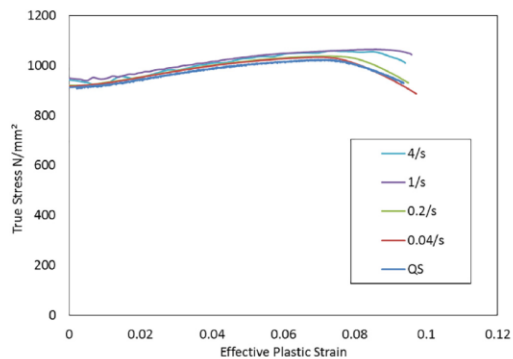

Fig. 18. Flow stress for mild steel (S235) generated up to 4 s^{-1} strain rate. Courtesy of TWI Ltd.

Fig. 20. Flow stress for S960QL generated up to 4 s^{-1} strain rate. Courtesy of TWI Ltd.
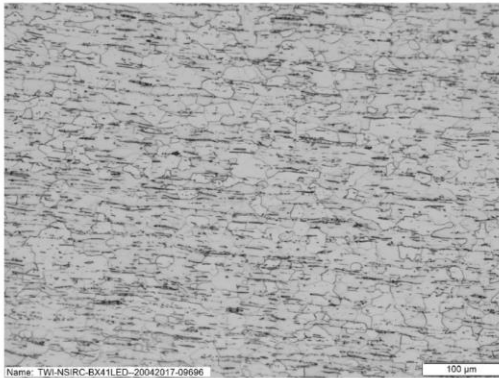
Fig. 21. Micrograph of Mild Steel (S235) etched with 2% Nital. Courtesy of TWI Ltd.
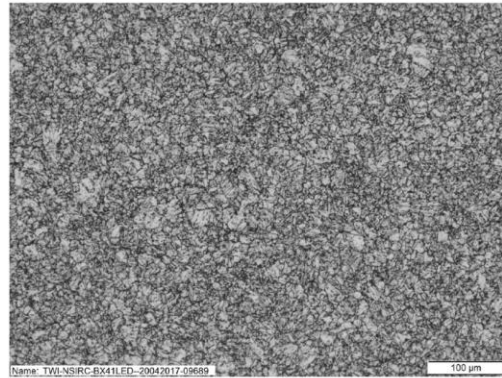

Fig. 23. Micrograph of S960 etched with 2% Nital. Courtesy of TWI Ltd.

shows coarse grain size and inclusions as a result of large concentrations of impurities (high sulphur content). On the other hand, S690QL and S960QL showed a fine-grained size structure and high degree of cleanliness with typical sulphur and phosphorus levels of <0.002% and < 0.009%, Figs. 22 and 23. There is no doubt that the tempered martensite structure, such as achieved in S690QL and S960QL quenched after austenising above room temperature and rapid cooling in water, would have a different degree of rate sensitivity compared to steel grades produced via a Normalised (N) heat treatment route, heated slightly above the temperature where its austenite totally changes to a ferritic-perlitic structure followed by slow cooling. It should be noted that the micrographs shown in Figs. 21 to 23 refer to as as-received grain size material properties.

The grain size was determined according to ASTM E112 [31], as given in Table 5. From the results, the grain size varies from 0.021 mm to 0.008 mm; a larger grain size was observed in S235 while S960 has the smallest. Obviously, the production routes have an effect on the grain size and the grain size influences the strength level. Therefore, it can be said that among other factors the degree of strain rate sensitivity depends on the production routes, chemical compositions and consequently a finer-grained structure with less sensitivity is recorded when the nominal yield strength increases.
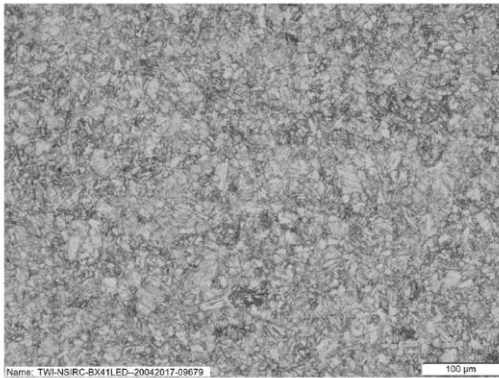
6. Conclusions and recommendations

The effect of strain rate on the tensile properties of HSSS compared to LSSS has been studied. Major findings include the following:

- The high strength structural steels with Y/T ratio > 0.90 are less sensitive to the effect of strain rate when compared to the LSSS structural steels with low Y/T ratio < 0.8.
- The extent of plastic work deformation does not only depend on the strain hardening curve but also depends on the specimen geometry and the shape (cross-section) prior to necking formation.
- The yield stress for S235 mild steel grade increased by about 66% from quasi-static to $100 \ s^{-1}$ strain rate. The effect of strain rate up to 100 s^{-1} on the yield stress of S690QL and S960QL moderately increase to about 9% and 6%, respectively.
- In terms of strain-hardening exponent (n), the value of n for S235 decreases as the strain rate increases whereas for S690 and S960, n kept fairly constant at up to $4 \ s^{-1}$ strain rate but decrease drastically at 100 s^{-1}.
- Finer-grained size microstructures were associated with a reduced degree of strain rate sensitivity. The degree of strain rate sensitivity in the tensile properties therefore depends on the production routes, chemical compositions and microstructure.
- The strain rate effect on the HSSS at strain rates from $4 \ s^{-1}$ to $100 \ s^{-1}$ should be characterised with a larger data set to increase confidence in the trends within this loading rate range.
- The tensile performance of HSSS under quasi-static conditions gives a reasonably accurate prediction of its behaviour under high loading up to $4 \ s^{-1}$ strain rate without requiring any specialist tensile testing for its characterisation.
- In the absence of high strain rate test data, quasi-static test data of S690QL and S960QL can be used to characterise its tensile behaviour up to $4 \ s^{-1}$ strain rate at room temperature.

As the experimental tensile test results show that S690QL and S960QL are relatively unaffected by the effect of structural loading rate

Fig. 22. Micrograph of S690 etched with 2% Nital. Courtesy of TWI Ltd.

Table 5
Calculated grain size according to ASTM E112 [31].

Materials	ASTM grain size	Mean grain diameter (mm)
S235	8	0.021
S690	10	0.011
S960	11	0.008

from quasi-static up to $100\ s^{-1}$ strain rates (typical strain rate that off-shore or marine structures may be subjected to), fracture toughness values at different structural loading and temperature conditions encountered in primary offshore structural applications would help to better understand the mechanical response and performance of these materials even in the presence of flaws. Further research is required to establish the Ductile-to-Brittle Transition Curve (DBTC) of these materials (S690QL and S960QL) where a shift from the upper shelf to lower shelf could be unsafe. To this end, ongoing experimental fracture toughness investigation is expected to play an important role in predicting the mechanical behaviour of high strength structural steels with high yield-to-tensile ratio in addition to the finite element analysis and design optimisation.

Acknowledgements

References

[1] Eurocode 3, Design of Steel Structures: Part 1–12, Additional Rules for the Extension of EN 1993 Up to Steel Grades S 700, 2007.

[2] UK National Annex to Eurocode 3, Design of steel structures: Part 1–12, Additional rules for the extension of EN 1993 up to steel grades S 7002007.

[3] J. Billingham, J.V. Sharp, J. Spurrier, P.J. Kilgallon, Review of the performance of high strength steels used offshore, HSE Res. Rep. 105 (2003)http://www.hse.gov.uk/research/rrpdf/rr105.pdf.

[4] API 2A-WSD, Planning, Designing, and Constructing Fixed Offshore Platforms – Working Stress Design, American Petroleum Institute recommended practice 21st Edition, 2014.

[5] J. Healy, J. Billingham, C. Billington, H. Bolt, Design implications of the high yield to ultimate ratio of high strength steels in offshore engineering, OMAE1995, Mater. Eng., ASME 3 (1995) 271–277.

[6] R. J. Dexter, M. Ferrell, Optimum weld-metal strength for high-strength steel structures, ATLSS Report No. 95–08, Sponsored by Ship Structure Committee, U.S. Coast Guard, July 1995 (https://preserve.lehigh.edu/engr-civil-environmental-atlss-reports/210).

[7] H.Y. Ban, G. Shi, A review of research on high-strength steel structures, Structures and Buildings, Proceeding of the Institution of Civil Engineers, 2017https://doi.org/10.1680/jstbu.16.00197.

[8] K. Wallin, Fracture Toughness of Engineering Materials – Estimation and Application, EMAS Publishing, Birchwood Park, Warrington, UK, 2011.

[9] Bomel Limited, The behaviour of carbon steels at high strain rates and strain limits, Offshore Technology Report OTO 1999/018, HSE, 1999http://www.hse.gov.uk/research/otopdf/1999/oto99018.pdf.

[10] P.H. Francis, T.S. Cook, A. Nagy, The effect of strain rate on the toughness of ship steels, Ship Structure Committee Report (SSC-275) under project SR-1231, 1978http://www.shipstructure.org/pdf/275.pdf.

[11] C.L. Walters, J. Przydatek, Relating structural loading rate to testing rate for fracture mechanics specimens, OMAE2014–23962, Materials Technology, Petroleum Technology, Vol. 5, ASME, 2014https://doi.org/10.1115/OMAE2014-23962 V005T03A028 http://proceedings.asmedigitalcollection.asme.org/proceeding.aspx?articleid=1911751.

[12] C.S. Wiesner, H. MacGillivray, Loading rate effects on tensile properties and fracture toughness of steel, Paper Presented at TAGSI Seminar – Fracture, Plastic Flow and Structural Integrity (dedicated to Sir Alan Cottrell in the year of his Eightieth Birthday), held at TWI, Cambridge, UK, 1999http://www.twi-global.com/technical-knowledge/published-papers/loading-rate-effects-on-tensile-properties-and-fracture-toughness-of-steel-april-1999/.

[13] F.M. Burdekin, W. Zhao, Y. Tkach, C.S. Wiesner, W. Xu, The effects of dynamic loading on structural integrity assessments, HSE Research Report 208, 2004http://www.hse.gov.uk/research/rrpdf/rr208.pdf.

[14] B. Burgan, Elevated temperature and high strain rate properties of offshore steels, Offshore Technology Report (OTO 2001/020), HSE, 2001http://www.hse.gov.uk/research/otopdf/2001/oto01020.pdf.

[15] J. Choung, W. Nam, J.-Y. Lee, Dynamic hardening behaviours of various marine structural steels considering dependencies on strain rate and temperature, Marine Structures, Vol. 32, 2013, pp. 46–67, https://doi.org/10.1016/j.marstruc.2013.02.001www.sciencedirect.com/science/article/pii/S0951833913000154.

[16] N. NagarajaRao, M. Lohrmann, L. Tall, Effect of strain rate on the yield stress of structural steel, ASTM J. Mater. 1 (1) (1966) Publication No. 293 Fritz Laboratory Reports, Paper 1684 http://preserve.lehigh.edu/engr-civil-environmental-fritz-lab-reports/1684.

[17] D. Breuk, Flow Stress and Ductile Failure at Varying Strain RatesISBN 90-9016534-7 2003.

[18] J.D. Campbell, W.G. Ferguson, The temperature and strain-rate dependence of the shear strength of mild steel, Philos. Mag. 21 (1970) 63–82, https://doi.org/10.1080/14786437008238397 169 http://www.tandfonline.com/doi/pdf/10.1080/14786437008238397?needAccess=true.

[19] J.W. Morris, Overview of dislocation plasticity, Int. Mater. Sci. I (2007) 1–36http://www.mse.berkeley.edu/groups/morris/MSE205/Extras/dislocationplasticity.pdf.

[20] A. Trondl, D.-Z. Sun, Modelling of strain rate dependence of deformation and damage behaviour of HSS and UHSS at different loading states, 10th European LS-DYNA Conference, Würzburg, Germany, 2015http://www.dynalook.com/10th-european-ls-dyna-conference/2%20Crash%20I%20-%20Failure/03-Trondl-FraunhoferIWM-P.pdf.

[21] G.R. Johnson, W.H. Cook, Fracture characteristics of three metals subjected to various strain, strain rates, temperature and pressures, Eng. Fract. Mech. 21 (1) (1985) 31–48, https://doi.org/10.1016/0013-7944(85)90052-9http://www.sciencedirect.com/science/article/pii/0013794485900529?via%3Dihub.

[22] A.C. Bannister, S.J. Trail, The significance of the yield stress/tensile stress ratio to structural integrity, SINTAP Sub-Task 2.1 Report, 1996http://www.eurofitnet.org/sintap_BRITISH_STEEL_The_Significance_of_y-t_ratio.pdf.

[23] A.C. Bannister, Yield stress/tensile stress ratio: Results of experimental programme, SINTAP Sub-Task 2.3 Report, 1999http://www.eurofitnet.org/sintap_BRITISH_STEEL_BS-25.pdf.

[24] A.C. Banister, J. Ruiz Ocejo, F. Gutierrez-Solana, Implications of the yield stress/tensile stress ratio to the SINTAP failure assessment diagrams for homogeneous materials, Eng. Fract. Mech. 67 (2000) 547–562https://doi.org/10.1016/S0013-7944(00)00073-4http://www.sciencedirect.com/science/article/pii/S0013794400000734.

[25] J. Healy, J. Billingham, Metallurgical considerations of the high yield to ultimate ratio in high strength steels for use in offshore engineering, 14th International Conference OMAE1995, vol. 3: Materials Engineering, ASME 1995, pp. 365–370.

[26] R. L. Brockenbrough & Associates Inc., Effect of yield-tensile ratio on structural behaviour – High performance steels for bridge construction, Expanded Draft Final Report, ONR-AISI Agreement No. N00014-94-2-0002, 1995. (http://www.smdisteel.org/~/media/Files/SMDI/Construction/Bridges%20-%20HPS%20-%20Report%20%20Effect%20of%20Yield%20Tensile%20Ratio%20on%20Structural%20Behavior%20-%2006–06-1995.pdf).

[27] J. Billingham, J. Healy, H. Bolt, High strength steels – The significance of yield ratio and work-hardening for structural performance, Marine Technology Directorate (MTD), Mar. Res. Rev. 9 (1997) (36 pages, ISBN 1-870553-27-6).

[28] BS EN 10025:6: +A1: 2009, Hot rolled products of structural steels – Part 6 Technical delivery conditions for flat products of high yield strength structural steels in the quenched and tempered condition, 2009.

[29] J.R. Davis, Tensile Testing, 2nd Edition ASM International, Materials Park, OH 44073–0002, 2004 ISBN: 0-87170-806-X.

[30] M.S. Loveday, T. Gray, J. Aegerter, Tensile testing of metallic materials: A review, EU Funded Project, TENSTAND-Work Package 1, final report with Contract Number G6RD-2000-00412, 2004.

[31] A.S.T.M. E112, Standard test methods for determining average grain size, ASTM (2013)https://doi.org/10.1520/E0112-13.

ECF22 - Loading and Environmental effects on Structural Integrity

Influence of Loading Rate on the Fracture Toughness of High Strength Structural Steel

A. A. Alabi[a,b,*], P. L. Moore[c], L. C. Wrobel[d], J. C. Campbell[a,b], W. He[e]

[a]*Department of Mechanical and Aerospace Engineering, Brunel University London, Uxbridge, UB8 3PH, UK*
[b]*National Structural Integrity Research Centre, Granta Park Great Abington, Cambridge, CB21 6AL, UK*
[c]*TWI Ltd, Granta Park Great Abington, Cambridge CB21 6AL, UK*
[d]*Institute of Materials and Manufacturing, Brunel University London, Uxbridge, UB8 3PH, UK*
[e]*Lloyds Register Global Technology Centre, Southampton, SO16 7QF, UK*

Abstract

It is known that rates of loading influence the fracture behaviour of most ferritic steels. High loading rates could change a stable ductile tearing behaviour to an unstable brittle fracture by altering the ductile-to-brittle transition curve. This is predicted to be material dependent, with lower strength structural steels showing a larger tensile property loading rate sensitivity compared to high strength structural steels. A programme of mechanical testing was carried out on S690QL and S960QL to determine the influence of loading rate on the fracture behaviour of high strength structural steels with yield strength > 690 MPa and yield-to-tensile ratio above 0.90. The loading rates considered are those anticipated in offshore in-service conditions, with K-rates up to the order of magnitude of 10^6 MPa√m/s. Results from tensile tests show that the strengths of these grade of steels are relatively unaffected by the effect of loading rate. However, brittle fracture, which is controlled by material strengthening as a result of principal stress in front of the crack, is both loading rate and temperature dependent. Results from tests at quasi-static and elevated loading rates show changes in the fracture behaviour in terms of transition temperature. A shift to a higher ductile-to-brittle transition temperature was observed as the loading rate increases. This was associated with a reduction in the fracture toughness value on the lower transition region. The reference temperature, T_0, at a K-rate of 1 MPa √m/s using Master Curve concepts is estimated to be around -116 °C and -108 °C for Charpy-sized pre-cracked and standard (25x25 mm) SENB specimens respectively, under quasi-static conditions for S690QL. The dynamic $T_{0,d}$ is -70.4 °C in the same steel for Charpy-sized pre-cracked specimens at K-rates up to 10^6 MPa √m/s.

* Corresponding author. Tel.: +447572141987
 E-mail address: aderinkola.alabi@brunel.ac.uk

1. Introduction

Often, an understanding of fracture behaviour of steel during experimental testing at different loading regimes helps to prevent some of the potential catastrophic accidents during in-service conditions. It is assumed that a single fracture toughness value (critical value) controls the fracture behaviour of a material [*Wallin (2011)*]. This value describes the crack initiation and subsequent propagation behaviour of the material (the driving force and the material resistance). The driving force is the combination of material flaw size and loading conditions, while the material resistance is the ability of the material to resist propagation of these flaws or cracks [*Wallin (2011)*]. The strain-hardening exponent (n) influences fracture behaviour [*Bannister and Trail (1996)*]. It has been demonstrated that crack opening is enhanced by a high yield-to-tensile (Y/T) strength ratio and, hence low strain-hardening capacity [*Bannister (1999)*].

The effect of loading rates on the difference in the dynamic and quasi-static fracture toughness values for a steel material relies mainly on the material's deformation properties, with the brittle cleavage fracture process remaining the same, but the difference in fracture toughness predicted to be material dependent [*Wallin (2011)*]. In some cases, ductile fracture is considered to have a positive rate dependence with an enhancement of dynamic ductile fracture toughness, however this factor is considered negligible when performing structural analysis [*Walters and Przydatek (2014)*]. Brittle fracture toughness of ferritic steels generally reduces in value with increasing loading rate (a negative rate dependence) [*Wiesner and MacGillivray (1999), Wallin (2011)*]. The mechanism of brittle fracture is mainly controlled by the stress state in front of the crack, and less affected by adiabatic heating because its initiation is in the region of high stresses where the plastic strains are relatively small, further away from the crack tip [*Wallin (2011)*]. This implies that the yield strength and strain-hardening properties of a steel material have an effect on the brittle fracture toughness resistance.

A significant impact may be experienced on the ductile-to-brittle-transition curve where a brittle fracture toughness may drop up to 80% from the measured toughness at quasi-static conditions [*Wallin (2011)*]. Thus, the effect of loading rate must be accounted for in the estimation of brittle fracture toughness resistance of high strength structural steel (HSSS) with high Y/T ratio above 0.90. In this paper, a short survey and outlook of the effect of loading rate on fracture toughness of ferritic steel is presented alongside the structural implication of high Y/T ratio in ferritic steel. Finally, test data at quasi-static and elevated loading rates show how fracture toughness behaviour in terms of the transition temperature of S690QL and S960QL with Y/T ratio above 0.90 changes due to elevated loading rate.

Nomenclature

a_0	initial crack length (mm)
n	Strain-hardening exponent
σ_y	Yield strength (MPa or N/mm²)
B	specimen thickness (mm)
Y/T	ratio of yield to tensile strength
HAZ	Heat affected zone
1T	specimen size at 1 in thickness, i.e. B = 25.4 mm
E	Modulus of elasticity (GPa)
K	Stress intensity factor (MPa√m)
$\dot{K}$	Stress intensity factor loading rate (MPa√m/s)
K_{JC}	elastic-plastic equivalent stress intensity factor derived from J-integral at onset of cleavage fracture
$\dot{\varepsilon}$	Strain rate (s⁻¹)
a_0/W	ratio of the initial crack growth to the width
SENB	single edge notched bend
W	specimen width, measured in the direction of the notch (mm)
ΔT	Temperature shift (°C)
T_0	quasi-static reference transition temperature (°C)
$\sigma_y^{T_0}$	Yield strength estimated at T_0 (MPa)

$T_{0,d}$	dynamic master curve reference temperature (°C)

2. Outlook of high strength structural steel and loading rate effect on fracture toughness of ferritic steel

2.1. Application and structural implication of high Y/T ratio in high strength structural steel

High strength structural steels (HSSS) are often preferred to conventional lower strength structural steels (LSSS) for special structural element designs when sectional weight reduction of heavy steel structures, as used in offshore industry (lifting appliances, topsides), construction industry (bridges and buildings) and off-highway equipment (fixed and mobile cranes, excavators, earthmoving), is important, *Commissions of the European Communities (1988), Willms (2009)*. The fracture behaviour and performance of LSSS is well known and established in the standards. In fact, most of the design codes relate the design formulae to LSSS with Y/T ratio below 0.85 and yield strength up to 500 MPa for offshore design requirements, *Billingham et al. (1997) and Billingham et al. (2003)*. The same level of confidence is yet to be achieved for HSSS and, the high Y/T ratio that comes with it. The concern is that these HSSS grades obtained their strength at the expense of ductility and strain-hardening capacity; properties which provide a sense of extra safety in avoidance of failure should service loads exceed yield. So design codes that utilise these properties to deliver safety when using low strength structural steel grades, with a Y/T ratio below 0.85, may not currently be applicable for modern high strength steels. An example of the approach to HSSS is the American Petroleum Institute (API) practice which recommends a value for certain tubular joints yield level of 66% (two-thirds) tensile strength with yield strength property up to 500 MPa [*API 2A-WSD (2014)*]. However, a re-evaluation conducted and incorporated into the newest edition of the standard suggested that a Y/T ratio of 0.80 for joints could be used provided that an adequate ductility is demonstrated in both HAZ and parent metal with 500 MPa < σ_y ≤ 800 MPa [*API 2A-WSD (2014)*]. Also, Eurocode 3 (Design of steel structures), allows a Y/T value up to 0.95, whereas the UK Annex of the same standard recommends 0.91 as a maximum [*Eurocode 3: Part 1-12 (2007), UK National Annex to Eurocode 3: Part 1-12 (2007)*]. As confidence in the structural performance of these grades is established they become more accepted into the standards. Ttypical stress-strain curves for modern high strength steel and conventional low strength steel are given in Fig. 1.
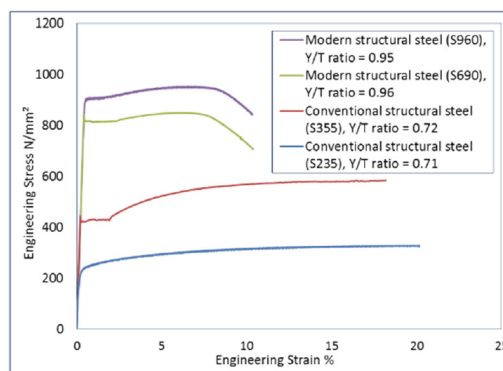

Fig. 1. Stress-strain characteristics of modern QT high strength structural steel and conventional low strength structural steel. Courtesy of TWI Ltd)

In an elastic design approach, the working stress is usually taken as a proportion of the yield stress, with typical values around 60% of yield strength in normal loading and up to 80% in severe loading, ensuring that load resistance falls within the linear region of the stress-strain curve of the component, making the Y/T ratio irrelevant in such elastic cases [*Healy et al. (1995)*]. However, in the case of plastic design (design concept in which the structure is able to locally yield and redistribute load without major failure or total collapse), the Y/T ratio becomes relevant in the post-yield behaviour of steel [*Healy et al. (1995)*]. Therefore, in engineering terms, the Y/T ratio can be said to be the parameter which represents the ability to withstand plastic loading and the basic measure of deformation capacity of a material [*Bannister and Trail (1996)*]. The increase in nominal yield strength affects the extent of plastic stability in the form of reserve strength induced

by strain-hardening indicated by an increased Y/T ratio [*Healy et al. (1995), Bannister and Trail (1996)*]. To this end, a maximum Y/T ratio is imposed in design codes to ensure steel structures have adequate room to redistribute load before major failure [*Bannister and Trail (1996)*].

However, integrity performance of HSSS with Y/T ratios between 0.8 and 0.95 in structural designs such as pipelines, pressure vessels, building constructions, shows that high Y/T ratio does not necessarily signify poor fracture performance, which depends on a number of other factors [*Brockenbrough, R. L. and Associates Inc., (1995), Bannister and Trail (1996), Willms (2009)*]. The Y/T ratio per se is not the only governing parameter that influences the plastic response of a material, other related characteristics such as strain-hardening exponent, ductile tearing resistance, and overall global deformation are important factors to take into account when considering the practicality of using high Y/T ratio as a measure of plastic strain capacity of a cracked component [*Bannister (1999)*].

2.2. Reference survey on the effect of loading rate on the fracture toughness of ferritic steel

The one common effect of loading rate on the fracture toughness of most ferritic steels is the increase in the transition temperature [*Francis et al. (1978), Wiesner and MacGillivray (1999), HSE report, OTO (1999), Burdekin et al. (2004), Wallin (2011), Walters and Przydatek (2014), Gotoh (2015)*]. The extent of the shift is highly dependent on the nominal yield strength [*Wiesner and MacGillivray (1999), HSE report, OTO (1999)*]. Perhaps one of the reasons why toughness requirements must be adjusted according to the yield strength of the steel for normal or extreme loading conditions [*Shoemaker (1981)*]. The effect of increasing loading rate is more pronounced on the lower strength steel grades, whereas, high strength steel exhibits less loading rate sensitivity depicted by the shift in transition temperature [*Wiesner and MacGillivray (1999)*]. The increasing loading rate does not necessarily mean an increase in ductile toughness on the upper shelf [*Wiesner and MacGillivray (1999)*].

The effect of loading rate on the fracture toughness is more sensitive to temperature and the rate of change of the crack tip stress intensity factor loading rate ($\dot{K}$) rather than the overall strain rate ($\dot{\varepsilon}$) of the material in a cracked component [*Francis et al. (1978)*]. It is important to note that whilst the fracture mechanical loading rate is mostly approximated and expressed in terms of stress intensity factor loading rate for linear elastic conditions, the loading rates in structural engineering are usually considered in terms of strain rates [*Wallin (2011)*]. The use of the strain rate to determine a single effective loading rate value in a cracked specimen could lead to a crude estimation in a real scenario [*Wallin (2011)*]. Hence, the use of stress intensity factor loading rate as a mean of expressing fracture mechanical loading rate. However, a relationship exist between $\dot{K}$ and $\dot{\varepsilon}$, Eq 1, for a cracked component within the elastic region just outside of the crack tip plastic zone [*Burdekin et al. (2004)*].

$$\dot{\varepsilon} = \frac{2\sigma_y}{E} \frac{\dot{K}}{K} \tag{1}$$

In summary, the general trend shows that the effect of loading rate on the fracture toughness of ferritic steels was mainly concerned with defining the fracture transition temperature shift (ΔT_0) to a higher temperature value using an empirical approach [*Burdekin et al. (2004)*]. The Master Curve is a statistical method describing the fracture characteristics in the transition region based on the reference transition temperature T_0, and this forms the basis of ASTM 1921 testing standard [*ASTM 1921-15a$^{\varepsilon 1}$*]. The concept has been applied to a wide range of yield strengths from 200 to 1000 MPa to predict ΔT_0, Eq 2, as a result of loading rate induced temperature shift [*Wallin and Mahidhara (1997)*].

$$\Delta T_0 = \frac{T_0 \cdot \ln(\dot{K}_I)}{\Gamma - \ln(\dot{K}_I)} \tag{2}$$

The function Γ is the loading rate effect fitting parameter given in Eq 3, and $\dot{K}_I$ is the average loading rate of the elevated rate tests.

$$\Gamma = 9.9 \cdot exp\left[\left(\frac{T_0 + 273.15}{190}\right)^{1.66} + \left(\frac{\sigma_y^{T_0}}{722}\right)^{1.09}\right] \tag{3}$$

261

3. Materials and experimental methods

3.1. Materials

The materials studied are S690QL (WELDOX 700 EZ) and S960QL (WELDOX 960 HZ) with Y/T ratio in the region of 0.96 and 0.95 respectively, which are typical high strength structural steel grades used in offshore applications. These two materials were delivered in quenched and tempered conditions, and satisfy the -40 °C minimum impact energy requirement in the transverse direction. The delivery condition was in accordance with BS EN 10025:6: +A1 (2009). The grade designation stands for the following: S – Structural Steel, 690/960 – Minimum Yield Strength (MPa), Q – Quenched and Tempered production process, L – Low Notch Toughness Testing Temperature at -40 °C.

3.2. Experimental methods

Single edge notched bend (SENB) specimens were prepared and tested to BS EN 7448 part 1 in the case of quasi-static condition and BS EN 7448 part 3 and BS ISO 26843:2015 in the case of elevated loading rate. Specimens were taken at ¼ depth of full thickness and notched through thickness in the Y-X orientation. The specimens were fatigue pre-cracked with the nominal a_0/W of 0.5. Two datasets were generated for S690QL tests, a standard specimen configuration (WxB=25x25 mm) and a Charpy-sized pre-cracked specimen (WxB=10x10 mm). For S960QL, only Charpy-sized pre-cracked specimens (WxB=10x10 mm) were tested. In this paper, tests done at 0.005 mm/s refer to quasi-static (QS) loading rates, and 5400 mm/s describes tests carried out at elevated loading rates (dynamic). In terms of fracture mechanical loading rate expressed as K-rate, the QS K-rate is within the range 0.5 to 3 MPa√m/s specified by BS EN 7448 part 1. In order to simulate the possible loading rates that offshore and marine structures could be subjected to in-service, Table 1, the average elastic stress intensity factor loading rate (K-rate) was calculated by fitting the linear part of the data describing the stress intensity factor-time trace. An order of magnitude of 10^6 MPa√m/s was achieved for the 5400 mm/s test speed.

Table 1. Typical loading rates in some engineering components. Data taken from *Wiesner and MacGillivray (1999, Burdekin et al. (2004), Walters and Przydatek (2014)*

Applications	Strain Rate $\dot{\varepsilon}$ (s^{-1})	Stress Intensity Factor Loading Rate $\dot{K}$ (MPa√m/s)
Storage tanks, buried pipelines, pressure vessels	10^{-6} to 10^{-4}	10^{-2} to 1
Self-weight, wind and wave loading	10^{-4} to 10^{-2}	1 to 10
Bridges, cranes and earthmoving	10^{-2} to 0.1	10 to 10^3
Earthquake loading and marine collision	0.1 to 10	100 to 10^4
Land transport and aircraft undercarriage	10 to 1000	10^3 to 10^6
Explosion and ballistics	10^4 to 10^{6+}	10^7 to 10^{10+}

4. Results and Discussion

4.1. Tensile properties

Initial stress-strain curves generated from the tension tests, Figs. 2a and 2b, shows that the tensile properties of high strength steels are relatively unaffected by the effect of strain rate. This is discussed in detail by *Alabi et al. (Journal paper under review)*. Yield strength amplification of only about 6% and 3% were recorded for S690QL and S960QL at 4 s^{-1} strain rate respectively when compared to quasi-static (0.0002 s^{-1}) strain rate tests [*Alabi et al. (Journal paper under review)*]. Therefore, it could be said that strain rate sensitivity of ferritic steels decreases as the nominal yield strength increases.
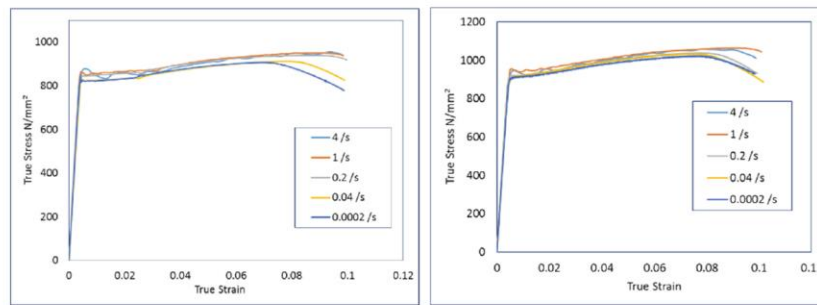
Fig. 2. (a) Effect of strain rate on the stress-strain characteristics of S690QL; (b) S960QL between 0.0002 s^{-1} and 4 s^{-1} strain rates.
(Courtesy of TWI Ltd)

4.2. Fracture toughness results

Fracture toughness results at quasi-static loading conditions (QS) for 10x10 mm and 25x25 mm SENB tests are summarised in Tables 2a and 2b respectively.

Table 2a. Fracture toughness data for S690QL at QS using Charpy-sized pre-cracked (10x10 mm) SENB

S690QL	Test temperature (°C)	J (N/mm)	K_{JC} 1T (MPa √m/s)	Test speed (mm/s)
M01-87	-100	48.82	88.89	0.005
M01-94	-100	131.18	143.09	0.005
M01-98	-100	206.49	178.48	0.005
M01-99	-100	174.72	164.51	0.005
M01-100	-100	79.14	112.06	0.005
M01-106	-120	15.17	51.51	0.005
M01-112	-120	43.44	84.33	0.005
M01-113	-120	41.09	82.13	0.005
M01-114	-120	39.34	80.45	0.005

Table 2b. Fracture toughness data for S690QL at QS using standard (25x25 mm) SENB

S690QL	Test temperature (°C)	J (N/mm)	K_{JC} (MPa √m/s)	Test speed (mm/s)
M01-115	-100	68.78	126.55	0.005
M01-116	-100	57.72	115.94	0.005
M01-117	-100	111.08	160.83	0.005
M01-118	-100	20.78	69.56	0.005
M01-119	-100	38.97	95.26	0.005
M01-120	-100	35.45	90.86	0.005
M01-121	-100	51.29	109.29	0.005

4.3. Master Curve predictions

The Master Curve concept is only intended for describing materials fracture toughness in the transition region of the ductile-to-brittle transition curve (DBTC). Therefore, data from tests at -100 °C and -120 °C have been considered for the calculation. The estimated T_0 determined from both Charpy-sized pre-cracked and 25 mm thick specimens are -116 °C and -108 °C respectively, Figs. 3a and 3b under QS conditions. The master curve theory should mean both datasets predict the same T_0, but it is important to mention that a difference of about 8 °C is observed due to the partial loss of crack-tip constraint. This effect is described by *Joyce and Tregoning (2005)*.

For this work, a comparison between QS and dynamic results is being sought, so the same Charpy-sized pre-cracked specimens were used throughout to avoid the influence on the shift in transition temperature. The dynamic master curve reference temperature $T_{0,d}$ calculated is -70.4 °C, Fig. 4. A shift of about 45.6 °C is therefore observed for S690QL.
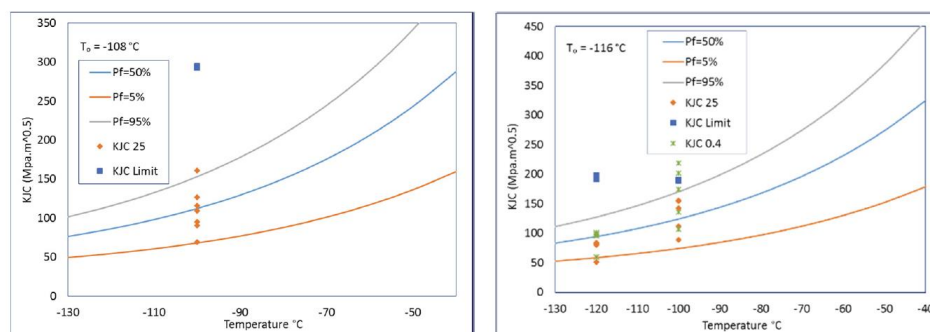
Fig. 3. (a) QS Master Curve for 1T specimens for S690QL; (b) QS Master Curve for 1T specimens based on 0.4T (10 mm) data for S690QL. (Courtesy of TWI Ltd)
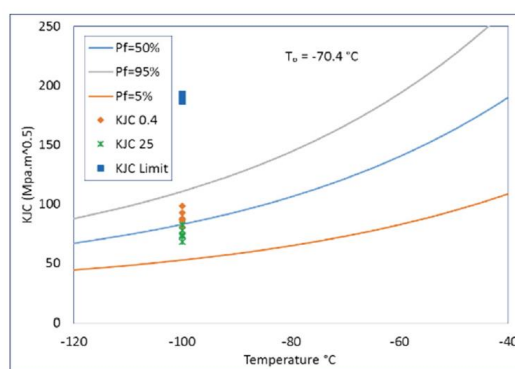

Fig. 4. Dynamic Master Curve for 1T specimens based on 0.4T data for S690Q. (Courtesy of TWI Ltd)

Given that the results of the S690QL tests shows that the ASTM 1920-15a T_0 shift prediction with dynamic loading compares well the experimental estimation, the ΔT_0 prediction for S960QL (which was not fracture toughness tested at elevated loading rate) is 29 °C. Therefore, as observed with the tensile test results, high strength steel is less affected by the effect of increased loading rates up to those studied (typical offshore in-service loading rate). S960QL shows less sensitivity to the effect of loading rate because of its higher strength when compared to S690QL. However, the cleavage fracture toughness still reduces for both steels when loading rate is increased. The Master Curve dynamic predictions have been shown to reasonably predict the transition fracture behaviour of S690QL at K-rates up to 10^6 MPa √m/s.

5. Conclusions

The effect of loading rate on the fracture toughness of S690QL and S960QL has been studied. Based on the investigation, it can concluded that:

- The T_0 estimated for S690QL at QS and dynamic conditions based on the Master Curve, with tests performed at -100 °C using Charpy-sized pre-cracked SENB specimens, is -116 °C and -70.4 °C respectively. Here the ΔT_0 from QS conditions to 10^6 MPa√m/s is 45.6 °C
- The influence of loading rate on fracture toughness can be determined using Charpy-sized pre-cracked SENB specimens.

- A temperature shift of about 40 °C and 29 °C for S690QL and S960QL respectively is predicted for QS conditions up to a K-rate with an order of magnitude of 10^6 MPa√m/s, based on ASTM E1921-15a with prior knowledge of T_0 under QS conditions.
- Although, the tensile properties of very high HSSS is fairly insensitive to strain rates up to 4 s^{-1}, the fracture toughness behaviour is affected by dynamic loading.

Acknowledgements

References

Alabi, A., A., Moore, P., L., Wrobel, L., C., Campbell, J., C., He, W., *"Tensile Behaviour of S690QL and S960QL under High Strain Rate"* (Journal Paper under review for publication in the Journal of Constructional Steel Research submitted in Nov 2017)

API 2A-WSD, 2014. *"Planning, Designing, and Constructing Fixed Offshore Platforms – Working Stress Design"* American Petroleum Institute recommended practice 21st Edition.

ASTM E1921-15^{e1}, 2016. *"Standard Test Method for Determination of Reference Temperature, T_0, for Ferritic Steels in the Transition Range^1"* ASTM International, United States.

Bannister, A., C., Trail, S., J., 1996. *"The Significance of the Yield Stress / Tensile Stress Ratio to Structural Integrity"* SINTAP Sub-Task 2.1 Report, August 1996.

Bannister, A., C., 1999. *"Yield Stress / Tensile Stress Ratio: Results of Experimental Programme"* SINTAP Sub-Task 2.3 Report, February 1999.

Billingham, J., Healy, J., Bolt, H., 1997. *"High Strength Steels – The Significance of Yield Ratio and Work-hardening for Structural Performance"* Marine Technology Directorate (MTD), Marine Research Review 9, 1997 36 pages, ISBN 1-870553-27-6.

Billingham, J., Sharp, J., V., Spurrier, J., Kilgallon, P., J., 2003. *"Review of the Performance of High Strength Steels used Offshore"* HSE research report 105, 2003 (URL http://www.hse.gov.uk/research/rrpdf/rr105.pdf).

Brockenbrough, R., L., and Associates Inc., 1995. *"Effect of Yield-Tensile Ratio on Structural Behaviour – High Performance Steels for Bridge Construction"* Expanded Draft Final Report, ONR-AISI Agreement No. N00014-94-2-0002.

BS EN 10025'6: +A1: 2009. Hot rolled products of structural steels – Part 6 *"Technical Delivery Conditions for Flat Products of High Yield Strength Structural Steels in the Quenched and Tempered Condition"*.

Burdekin, F., M., Zhao, W., Tkach, Y., Wiesner, C., S., Xu, W., 2004. *"The Effects of Dynamic Loading on Structural Integrity Assessments"* HSE research report 208, (URL http://www.hse.gov.uk/research/rrpdf/rr208.pdf).

Commissions of the European Communities, 1988. *"High Strength Structural Steels – A European Review"* Technical Steel Research GT ASSOCIATES Contract No ECI 1467-86 UK.

Eurocode 3, Design of steel structures: Part 1-12, 2007. *"Additional Rules for the Extension of EN 1993 up to Steel Grades S 700"*

Francis, P., H., Cook, T., S., Nagy, A., 1978. *"The Effect of Strain Rate on The Toughness of Ship Steels"* Ship Structure Committee Report 275 (SSC-275) under project SR-1231, July 1978.

Gotoh, k., 2015. *"Practical Evaluation of the Strain Rate and Temperature effects on Fracture Toughness of Steels"* OMAE2015 – 41982, Newfoundland, Canada.

Healy, J., Billingham, J., Billington, C., Bolt, H., 1995. *"Design Implications of the High Yield to Ultimate Ratio of High Strength Steels in Offshore Engineering"* OMAE1995, Volume III, Materials Engineering, ASME 1995, pp 271-277.

Health and Safety Executive 1999. *"The Behaviour of Carbon Steels at High Strain Rates and Strain Limits"* Offshore Technology Report – OTO 1999/018, produced by Bomel Limited for HSE, HSE Books.

Joyce, J., A., Tregoning, R., L., 2005. *"Determination of Constraint Limits for Cleavage Initiated Toughness Data"* Engineering Fracture Mechanics 72 (2005) 1559-1579

Shoemaker, A., K., 1981. *"Fracture Characteristics of Ship Steel under Extremely High Loading Rates"* paper presented at Extreme Loads Response Symposium, Arlington, VA, USA

UK National Annex to Eurocode 3, Design of steel structures: Part 1-12, 2007. *"Additional Rules for the Extension of EN 1993 up to Steel Grades S 700"*

Wallin, K., Mahidhara, R., K., 1997. *"Effect of Strain Rate on the Fracture Toughness Reference Temperature T_o for Ferritic Steels"* TMS Publisher

Wallin, K., 2011. *"Fracture Toughness of Engineering Materials – Estimation and Application"* EMAS Publishing, Birchwood Park, Warrington, UK.

Walters, C., L., Przydatek, J., 2014. *"Relating Structural Loading Rate to Testing Rate for Fracture Mechanics Specimens"* OMAE2014 – 23962, San Francisco, California, USA

Wiesner, C., S., MacGillivray, H., 1999. *"Loading Rate Effects on Tensile Properties and Fracture Toughness of Steel"* Paper Presented at TAGSI Seminar - 'Fracture, Plastic Flow and Structural Integrity' (dedicated to Sir Alan Cottrell in the year of his Eightieth Birthday), Held at TWI, Cambridge, UK, 29 April 1999

Willms, R., 2009. *"High Strength Steel for Steel Constructions"* Marketing Department, AG der Dillinger Hüttenwerke, Dillingen, Germany, 2009.